Department of Chemical and Process Engineering

University of Strathclyde

Efficient Utilisation of Biochar for Water Remediation and Soil Amendment— Towards a Circular Economy

Michaela Anne McFadden

This thesis is submitted for the degree of Doctor of Philosophy

September 2025

Declaration of Authenticity and Author's Rights

This thesis is the result of the author's original research. It has been composed by the author and has not been previously submitted for examination which has led to the award of a degree.

Michaela Anne McFadden

September 2025

Dedication

In loving memory of my grandmother, Mary McMahon, and all the other generations of women who would have surely also accomplished this achievement had they been fortunate enough to have been afforded the opportunities I am today.

Acknowledgements

The completion of this thesis would not have been possible without the support and guidance of many people.

I would like to firstly acknowledge the contributions of my supervisors. I would like to thank my primary supervisor, Dr Xiaolei Zhang, for providing me with crucial feedback, guidance, and support throughout my PhD. I am incredibly grateful for the opportunity to learn from her expertise and experience her encouragement and patience, which have helped me to develop my skills and confidence as a researcher. I would like to thank my second supervisor, Prof Ashleigh Fletcher, for sharing her invaluable expertise in adsorption, and being a consistent source of motivation and inspiration. She has always provided an unwavering source of confidence in my abilities, even when my own was lacking. I have become a more resilient person from experiencing her understanding and determination. I would like to thank my third supervisor, Christine Davison, for her support in tackling an area of science which was new to me. Her patience, guidance, and expertise throughout various aspects of my PhD have helped me become a more well-rounded researcher, and I am grateful to have benefited from her diligent supervision. I would also like to thank my industrial supervisor, Sean Kerr, for providing materials used in this work, sharing his network, and his infectious passion for helping both people and the environment.

I wish to thank the members (both current and past) of the supportive and collaborative Fletcher and Zhang research groups for many brainstorming sessions, presentation sessions, and their company, which kept me sane during long hours in the lab.

I also wish to thank the laboratory technicians for their help in my experimental work. In particular, I would like to thank Mr Christopher Jones, Mr Ian Airdire, Mrs Mara Knapp, and Dr Tanya Peshkur for their assistance in training and

troubleshooting within the lab, as well as their kindness and conversation which enriched my experience in the labs immensely.

I would like to express my extreme gratitude for the personal support I have received from my family, my partner's family, and my close friends. To my partner, Andrew Coll, for always providing an unwavering stream of love and encouragement and allowing all of my goals to become our goals— without this support, my PhD would have felt like an insurmountable task, and I will forever be profoundly grateful. Finally, I reserve my most significant thanks for my parents, Marie & William McFadden, for encompassing every part of the phrase “unconditional love”, believing in me even when I didn’t believe in myself, nurturing my passions, and instilling in me a deep appreciation for my education. Everything I have ever achieved is supported by the foundations they built for me and still maintain. Without their encouragement, care, and many, many, FaceTime calls the completion of this PhD would not have been possible.

Abstract

In recent years, an increasing volume of work has been conducted on the use of modified biochar for the recovery of phosphorus (P) from aqueous systems, with potential applications in the treatment of waterbodies with excessive plant and algal growth due to detrimentally high nutrient levels. Considering biochar's suitability for use in soil systems, the opportunity exists to create a circular economy framework by utilising biochar for the recovery of aqueous P with subsequent recycling back to soil. However, further clarification is needed in the literature regarding the optimal process for producing functionalised biochar for the discussed purpose, with an enhanced understanding of biochar's aqueous P-recovery mechanisms and resilience to environmental factors required before implementing the process in real systems. This thesis presents the optimisation of Ca-biochar (calcium salt functionalised biochar) production for aqueous P-removal using a design of experiments (DoE) methodology to understand the effect of two key functionalisation parameters (pyrolysis temperature and chemical loading ratio (CLR)) on the physicochemical properties and aqueous P-removal of biochars. Aqueous P-removal mechanisms are discussed, and the performance of Ca-biochars in conditions reflective of real wastewaters is presented, alongside pot trials demonstrating the suitability of P-charged biochar as a soil amendment.

Biochar functionalised using calcium chloride demonstrated a superior P-removal capacity compared to biochar functionalised using magnesium chloride. Pre-pyrolysis particle size control and activation were found to increase uptake of calcium salt, and subsequently the aqueous P-removal of biochar samples, compared to post-pyrolysis particle size control or activation. Optimal P-removal was achieved when impregnating particle-size-controlled wood flakes pre-pyrolysis with $CaCl_2$.

A DoE methodology successfully determining the relationship between functionalisation conditions (pyrolysis temperature and CLR) and key

physicochemical characteristics (yield, surface area, average pore volume, and mass ratio of Cl:Ca) of biochar is presented. A mechanism for the transformation of $CaCl_2$ to $CaCO_3$ during pyrolysis is proposed. Aqueous P-removal by Ca-biochars synthesised in this work was found to occur via a dual mechanism of bulk precipitation and adsorption.

The Ca-biochar samples produced demonstrated excellent total P-removal, achieving up to 97% removal in a 20 mg_P/L solution and 79 % in a 200 mg_P/L solution. Adsorption alone was able to remove up to 43.7 % of P in a 20 mg_P/L solution, with regression analysis successfully determining a quadratic relationship between P-adsorption and functionalisation conditions. Biochars' P-adsorption was shown to be subject to synergistic effects of functionalisation conditions, with optimal CLR increasing with rising pyrolysis temperature.

The Ca-biochar samples displayed excellent resilience to changes in pH and the presence of coexisting ions. However, the samples experienced a significant decrease in P-recovery at low initial concentrations, removing up to 27% of P from a 1 mg_P/L solution, with initial concentrations <1.21 mg_P/L preventing precipitation and reducing adsorption. Biochar produced would be suitable for the remediation of eutrophic waters via waterbed sediment inactivation and the prevention of eutrophication via the treatment of municipal wastewaters and trade effluents. Pot trials demonstrate the use of P-charged Ca-biochars to be suitable as a soil amendment capable of increasing germination and growth rate compared to control samples.

The work presented in this thesis helps establish a best practice for the production of Ca-biochar for aqueous P recovery, providing key insights into the effects of the functionalisation process on the physicochemical properties and aqueous P-removal of biochars. A dual P-removal mechanism considering the effects of bulk precipitation is presented for the first time in the literature, providing essential insight into the P-cycling potential of biochar. The suitability of Ca-biochar for use in real water systems and supporting plant growth is

demonstrated. These results provide proof of concept for a biochar circular process capable of recovering and recycling P within the environment.

List of Abbreviations

ACP- Amorphous Calcium Phosphate

ANOVA- Analysis of Variance

BE- Binding Energy

BET- Brunauer-Emmet-Teller

BJH-Barret, Joyner, and Halenda

Ca-Calcium

CCC- Circumscribed Central Composite (Design)

CCD-Central Composite Design

CCI- Inscribed Central Composite (Design)

C_i= Initial Concentration

CLR- Chemical Loading Ratio

C.V.- Coefficient of Variance

DFFITS- Difference in Fits (Plot)

DO- Dissolved Oxygen

DoE- Design of Experiments

DW- Dry Weight

FCC- Face-Centred Central Composite (Design)

FTIR- Fourier Transform Infrared Spectroscopy

FW- Fresh Weight

HAP- Hydroxyapatite

IC- Ion Chromatography

ICP-AES- Inductively Coupled Plasma Atomic Emission Spectroscopy

IUPAC- International Union of Pure and Applied Chemistry

IPD- Intra Particle Diffusion (Model)

LDH- Layered Double Hydroxide

Mg- Magnesium

P-Phosphorus

PFO- Pseudo First Order (Model)

pHi- Initial pH

pH_{pzc}- Point of Zero Charge

PSO- Pseudo Second Order (Model)

nZVI- Nano Zero Valent Iron

RSM-Response Surface Methodology

SEM-EDS- Scanning Electron Microscope-Energy Dispersive Spectroscopy

SEPA- Scottish Environmental Protection Agency

T-Temperature

TP- Total Phosphorus

XRD- X-ray Diffraction

XRF- X-Ray Fluorescence Spectroscopy

XPS- X-ray Photoelectron Spectroscopy

2FI – Two Factor Interaction

Contents

List of Figures

List of Tables

1 Introduction

This chapter will outline the global pursuit of net-zero and emphasise the importance of adopting a circular economy to reach this goal, followed by the potential role of biochar in supporting a circular economy. It will conclude with the aims and objectives of the research, as well as a detailed description of the thesis outline.

1.1 Net-Zero and Circular Economy

Currently, 129 parties have signed the Paris Agreement—a legally binding international treaty that aims to "substantially reduce global greenhouse gas (GHG) emissions to hold global temperature increase to well below 2 °C above pre-industrial levels and pursue efforts to limit it to 1.5 °C above pre-industrial levels"[1]. To achieve the goal of limiting global warming to 1.5 °C, it is necessary to cut GHG emissions by 43% (compared to 2019 levels) by 2030 and reach net-zero emissions by 2050. Currently, the world is not on track to meet this target. Based on available national action plans, emissions are projected to be only 2.6 % lower in 2030 compared to 2019 [2]. The G20 group (including the UK and European Union) accounts for 77 % of global GHG emissions and must begin taking significant steps toward reducing emissions immediately [3].

Much discussion regarding the reduction of GHG emissions often focuses on improving energy efficiency and replacing fossil fuels with renewable energy. Whilst extremely important, this only accounts for around 55 % of global GHG emissions, with the remaining 45 % attributed to food, materials, and products [4]. To tackle the remaining 45 %, waste and pollution must be eliminated by circulating materials and products and regenerating nature. Currently, the world operates under a predominantly linear economy, in which raw materials are extracted from the earth, used to produce products, and eventually discarded as waste. In contrast, a circular economy is one in which there is no waste and products are kept in a closed loop in which they are reused, repaired, remanufactured, recycled, or recovered.

Figure 1.1 illustrates the current and projected 2050 embedded carbon demand (total GHG emissions for a products entire life cycle) of key sectors, indicating that decarbonisation is expected to significantly reduce demand in the energy and transport sectors, while demand in the chemicals and materials sector is expected to double [5]. Currently, the demand for embedded carbon in organic materials is met by fossil fuels (85 %), biomass (10 %), and recycling (5 %). There is potential for the use of fossil carbon to be substituted using three main sources: biomass, recycling, and captured CO_2. Valorisation of biomass waste plays a crucial role in a circular economy, helping to reduce emissions linked to food and material production, while also contributing to increased demand for chemicals and materials.

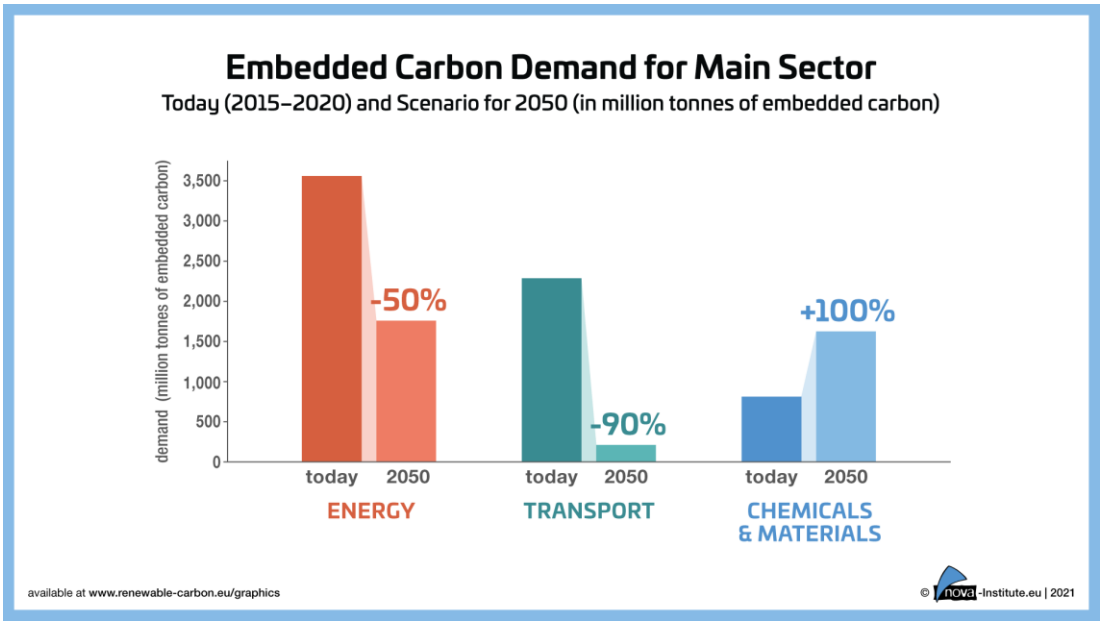

Figure 1.1: The current and future trends in global carbon demand for three key sectors: energy, transport, and chemicals & materials [2].

1.2 Biochar and Phosphorus Recovery

Biochars are a class of porous, carbonaceous materials and the solid product associated with the thermochemical conversion of biomass in an oxygen-deficient atmosphere. Biochar can be utilised for both energy and material

purposes. Biochar's porous nature and suitability as a sorbent make it appropriate for use in a wide range of applications, including carbon sequestration, soil amendment, and water remediation. The production of biochar supports all three key principles of a circular economy by eliminating biomass waste, valorising this waste to circulate materials, and regenerating nature.

Biochar has been reported to be suitable for use in water bodies as an adsorbent for various pollutants, including heavy metals, organic pollutants, nutrients, and agricultural or pharmaceutical residues [5]. Biochar is particularly desirable as a sustainable adsorbent due to its low cost and compatibility with existing infrastructure. The benefits of biochar for soil amendment are wide and varied including: improving plant growth and yield [7]; enhancing soil fertility and water retention [8], [9]; remediating and immobilising pollutants [10], [11]; and providing nutrients [12].

It is possible to create a circular economy framework by using biochar in both water remediation and soil amendment. However, there are challenges to achieving this. Pollutants removed from water should not be harmful to soil systems, and the biochar use in water should not degrade its performance in soil. In recent years, an increasing amount of research has been carried out on utilising biochar for phosphorus (P) recovery from aqueous systems [13], [14]. Biochar’s suitability as both an adsorbent and a potential soil amendment makes it particularly promising for the recovery of P and its subsequent recycling back to the soil.

Phosphorus is both an essential macronutrient required for plant growth and a key cause of eutrophication in water bodies. Eutrophication is the detrimental surplus of plant nutrients in water, primarily inorganic forms of phosphorus and nitrogen [15]. Eutrophication is associated with increased growth of phytoplankton (algal blooms) on a water body's surface or increased growth of aquatic plants on the waterbed. The overgrowth of these phytoplankton and

plants decreases the water's dissolved oxygen (DO), which is needed by fish and other aquatic organisms, reducing the biodiversity of the water body [16]. High levels of P is the most common reason for water quality failures in England, with 55 % of rivers and 75 % of lakes failing to meet phosphorus standards set out under the Water Framework Directive [17]. Similarly, the most common causes of poor water quality in Scotland are high P concentrations and periods of low rainfall and warm weather [18].

Currently, the most significant pressure affecting both Europe's ground and surface water is diffuse pollution from agriculture— responsible for around a third of pollution in both water types [19]. Diffuse pollution of P from agriculture to surface and groundwater is a result of the intensive use of fertilisers and pesticides. Due to low efficiency, chemical fertilisers used during farming are loaded with excess nutrients, which are transported into water bodies. Recently, studies on the application of biochar as a slow-release fertiliser replacement have been carried out, but few have considered the potential of using spent biochar charged by the removal of nutrients from water.

The use of biochar for recycling P not only helps create a circular economy but also addresses a key environmental problem, P loss. Phosphorus is mined from phosphate rock, a finite resource estimated to run out within 50-100 years [20]. Phosphorus, due to its importance in various sectors including agriculture, has been classified by the European Commission as a critical raw material (CRM) [21] . CRMs are raw materials of high economic importance within the EU which due to low concentrations of sources and absence of appropriate substitutes face a high risk of supply disruption [22]. To prevent the damage caused by P pollution in water and secure food production for future generations, it is essential that both P management and recycling be drastically improved. The Our Phosphorus Future report (produced from the input of all UN nations) calls for an ambitious "50 % reduction in global phosphorus pollution and a 50 % increase in the recycling of phosphorus lost in residues and wastes, by 2050" [23].

1.3 Research Focus of This Thesis

Motivated by the pressing need for a sustainable bioeconomy to support a circular economy and achieve net-zero goals, this thesis presents the results of a testbed study aimed at addressing key research gaps within the literature preventing the utilisation of biochar to its full potential in addressing agricultural and environmental issues. The key research focus is the examination of how to technically achieve the production of biochar for the removal of aqueous P from water and subsequent use of the P-charged biochar in soil systems as a slow-release fertiliser replacement. In detail, as illustrated in *Figure 1.2*, an optimal process for the production of functionalised biochar needs to be developed, and the synergistic effects of functionalisation conditions need to be examined. Then, the P-recovery performance of this optimal biochar in environmentally relevant conditions needs to be tested, and the ability of recovered P to be returned to soil in bioavailable forms needs to be investigated and examined.

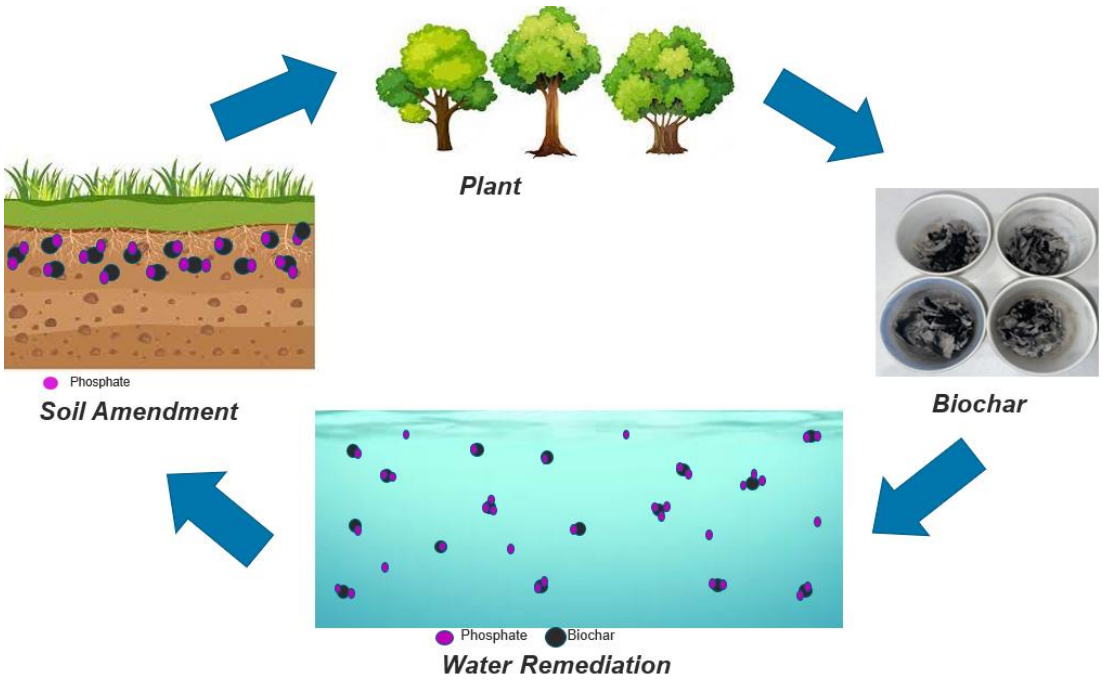

Figure 1.2: Biochar circular economy proposed in this thesis

This thesis aims to develop a proof of concept for a biochar circular process capable of being scaled up for real-life use, which integrates waste utilisation,

water remediation, and soil amendment to create a circular economy. This overall aim will be achieved by meeting the following objectives:

1. Examine and compare existing pre-treatment, biochar production and modification methods to identify the most effective process for producing biochar with high aqueous P-removal.
2. Utilise a design of experiments (DoE) methodology to examine the synergistic effects of functionalisation conditions (pyrolysis temperature and chemical loading ratio) on biochar's physiochemical properties, optimising for high aqueous P-recovery.
3. Investigate the mechanisms of P-recovery by biochar in aqueous systems, with a focus on the relationships among P-removal, adsorption, and precipitation.
4. Test the suitability of produced biochar for P recovery in conditions reflective of those achieved in real-life eutrophication-causing water streams and conduct pot trials to assess the performance of P-charged biochar as a fertiliser alternative.

1.4 Thesis Outline

Chapter 1 of this thesis outlines the aim and objectives of this thesis and provides the background and motivation for this work. Chapter 2 offers a comprehensive review of the existing literature on the modification and application of biochar for aqueous P recovery, as well as its role as a P-releasing soil amendment. This chapter also identifies critical research gaps and introduces the novel contributions of the presented study. Chapter 3 details the research methodology and theoretical background, covering key techniques, including DoE, adsorption, and physicochemical characterisation. Chapter 4 focuses on establishing an optimal functionalisation process for biochar production, including comparative analyses of magnesium chloride and calcium chloride activation, pre- versus post-pyrolysis treatments, and the effects of grinding biochar versus raw biomass. Chapter 5 focuses on the optimisation of functionalisation parameters, evaluating their impact on biochar's

physicochemical properties and subsequent P-recovery performance. Chapter 6 explores the mechanisms behind aqueous P-recovery to provide a deeper understanding of the involved phenomena. Chapter 7 examines biochar P-recovery under conditions relevant to eutrophic water and wastewater systems and assesses the effectiveness of P-loaded biochar as a soil amendment to enhance plant growth. Finally, Chapter 8 summarises the main conclusions of this thesis and offers recommendations for future research.

References

[1] "The Paris Agreement | United Nations." Accessed: Feb. 24, 2025. [Online]. Available: https://www.un.org/en/climatechange/paris-agreement

[2] United Nations Climate Change, "2024 NDC Synthesis Report," Nov. 2024.

[3] U. N. E. Programme, "Emissions Gap Report 2024: No more hot air … please! With a massive gap between rhetoric and reality, countries draft new climate commitments," 2024, doi: 10.59117/20.500.11822/46404.

[4] "Climate and a circular economy | Ellen MacArthur Foundation." Accessed: Feb. 25, 2025. [Online]. Available: https://www.ellenmacarthurfoundation.org/topics/climate/overview

[5] F. Kahler, M. Carus, O. Porc, and C. vom Berg, "Turning off the Tap for Fossil Carbon - Future Prospects for a Global Chemical and Derived Material Sector Based on Renewable Carbon," Apr. 2021. Accessed: Jun. 02, 2025. [Online]. Available: https://renewable-carbon.eu/publications/product/turning-off-the-tap-for-fossil-carbon-future-prospects-for-a-global-chemical-and-derived-material-sector-based-on-renewable-carbon/

[6] O. Porc, M. Carus, F. Kahler, and C. Vom Berg, "Embedded Carbon Demand for Main Sector - Today and 2050 (PNG) | Renewable Carbon Publications," Jun. 2021, *Renewable Carbon*. Accessed: Feb. 25, 2025. [Online]. Available: https://renewable-carbon.eu/publications/product/embedded-carbon-demand-for-main-sector-today-and-2050-png/

[7] T. Abbas *et al.*, "Biochar application increased the growth and yield and reduced cadmium in drought stressed wheat grown in an aged contaminated soil," *Ecotoxicol Environ Saf*, vol. 148, pp. 825–833, Feb. 2018, doi: 10.1016/J.ECOENV.2017.11.063.

[8] F. Razzaghi, P. B. Obour, and E. Arthur, “Does biochar improve soil water retention? A systematic review and meta-analysis,” *Geoderma*, vol. 361, p. 114055, Mar. 2020, doi: 10.1016/J.GEODERMA.2019.114055.

[9] J. Lehmann, M. C. Rillig, J. Thies, C. A. Masiello, W. C. Hockaday, and D. Crowley, “Biochar effects on soil biota – A review,” *Soil Biol Biochem*, vol. 43, no. 9, pp. 1812–1836, Sep. 2011, doi: 10.1016/J.SOILBIO.2011.04.022.

[10] M. A. Rao, G. Di Rauso Simeone, R. Scelza, and P. Conte, “Biochar based remediation of water and soil contaminated by phenanthrene and pentachlorophenol,” *Chemosphere*, vol. 186, pp. 193–201, Nov. 2017, doi: 10.1016/J.CHEMOSPHERE.2017.07.125.

[11] M. Uchimiya, S. C. Chang, and K. T. Klasson, “Screening biochars for heavy metal retention in soil: Role of oxygen functional groups,” *J Hazard Mater*, vol. 190, no. 1–3, pp. 432–441, Jun. 2011, doi: 10.1016/J.JHAZMAT.2011.03.063.

[12] M. Z. Hossain *et al.*, “Biochar and its importance on nutrient dynamics in soil and plant,” *Biochar 2020 2:4*, vol. 2, no. 4, pp. 379–420, Sep. 2020, doi: 10.1007/S42773-020-00065-Z.

[13] I. W. Almanassra, G. Mckay, V. Kochkodan, M. Ali Atieh, and T. Al-Ansari, “A state of the art review on phosphate removal from water by biochars,” *Chemical Engineering Journal*, vol. 409, p. 128211, Apr. 2021, doi: 10.1016/J.CEJ.2020.128211.

[14] T. Vijay *et al.*, “Scotland’s Rural College Phosphorus adsorption by functionalized biochar Phosphorus adsorption by functionalized biochar: a review,” *Environ Chem Lett*, doi: 10.1007/s10311-022-01519-5.

[15] M. Devlin and J. Brodie, “Nutrients and Eutrophication,” in *Marine Pollution- Monitoring, Management and Mitigation*, Springer, Cham, 2023, pp. 75–100. doi: 10.1007/978-3-031-10127-4_4.

[16] D. A. Vallero, “Watershed Events,” *Paradigms Lost*, pp. 163–196, Jan. 2006, doi: 10.1016/B978-075067888-9/50006-5.

[17] Environment Agency, “Phosphorous and freshwater eutrophication: challenges for the water environment,” Dec. 2022. Accessed: Feb. 28, 2025. [Online]. Available: https://view.officeapps.live.com/op/view.aspx?src=https%3A%2F%2Fassets.publishing.service.gov.uk%2Fmedia%2F64b50abe0ea2cb001315e366%2FPhosphorus-challenges-for-the-water-environment.odt&wdOrigin=BROWSELINK

[18] L. May *et al.*, “Mitigating Climate Change Impacts on the Water Quality of Scottish Standing Waters,” Mar. 2022. Accessed: Feb. 28, 2025. [Online]. Available: crew.ac.uk/publication/mitigating-climate-change-phase-2

[19] European Environment Agency, “Europe’s state of water 2024 : the need for improved water resilience,” Publications Office of the European Union, Luxembourg, Jul. 2024.

[20] D. Cordell, J. O. Drangert, and S. White, “The story of phosphorus: Global food security and food for thought,” *Global Environmental Change*, vol. 19, no. 2, pp. 292–305, May 2009, doi: 10.1016/J.GLOENVCHA.2008.10.009.

[21] “Critical raw materials - Internal Market, Industry, Entrepreneurship and SMEs.” Accessed: Dec. 04, 2025. [Online]. Available: https://single-market-economy.ec.europa.eu/sectors/raw-materials/areas-specific-interest/critical-raw-materials_en

[22] “Critical raw materials act - Consilium.” Accessed: Dec. 04, 2025. [Online]. Available: https://www.consilium.europa.eu/en/infographics/critical-raw-materials/

[23] W. J. Brownlie, M. A. Sutton, K. V Heal, D. S. Reasy, and B. M. Spears, “Our Phosphorus Future Towards global phosphorus sustainability With support from the Natural Environment Research Council, The United Nations Environment Programme, The Global Environment Facility, through the International Nitrogen Management System project and the

European Sustainable Phosphorus Platform," Edinburgh, 2022. doi: 10.13140/RG.2.2.17834.08645.

2 Literature Review

This chapter will provide a critical review of the current literature on utilising biochar for aqueous P removal and the subsequent use of spent biochar in soil systems to promote a circular economy. First, the key physicochemical characteristics of biochar and their effect on aqueous phosphate recovery are discussed; the impact of pyrolysis conditions on these characteristics is also reviewed. The need for biochar functionalisation is analysed, and various options for types of biochar decoration and production of decorated biochar are discussed and compared. Next, the key factors affecting biochars' ability to recover aqueous phosphorus (P) in conditions reflective of eutrophic and waste waters (pH, aqueous P concentration, and coexisting ions) are presented. Following this, the suitability of biochar for soil amendment and as a slow-release P fertiliser substitute is examined. Lastly, the key research gaps currently present in the literature and the novel aspects of this work are discussed.

2.1 Biochar

Biochars are carbon rich, porous solid materials produced from the thermochemical conversion of biomass in an oxygen-deficient atmosphere. Biochar is often suitable for use in soil amendment, carbon capture, and water remediation due to high surface areas and functional groups present on the material surface. Biochar is most commonly formed via pyrolysis, the thermal decomposition of materials at high temperature in the absence of oxygen resulting in biochar, bio-oil, and syngas [1]. Typically, biomass feedstock used is composed primarily of 3 main constituents: cellulose, hemicellulose, and lignin, alongside mineral components. During thermal degradation of biomass moisture first evaporates (below 200 °C), then hemicellulose begins to decompose (200-300 °C), followed by cellulose decomposition (300-400 °C), and slow lignin decomposition (300-600 °C) while mineral compounds (often referred to as ash) remain [2], [3], [4], [5]. During biomass degradation volatiles are released including permanent gases (commonly H_2O, H_2, CO, CO_2, CH_4, and light

hydrocarbons) and condensable vapours (commonly acids, aldehydes, ketones, phenolic compounds, and aromatic hydrocarbons) [6], [7], [8], [9]. The release of volatiles during pyrolysis produces bio-oil from condensable vapours and syngas from gaseous products, while the remaining carbon framework—known as biochar—develops a porous structure as volatiles escape.

2.1.1 Physicochemical Properties

Key physicochemical properties influence biochar's suitability for various applications. The suitability of biochar for use as an adsorbent typically depends on its surface charge, surface area, and porosity, with the ability of biochar to adsorb aqueous phosphate primarily dependant on surface functionality. These physicochemical properties can be affected by feedstock selection and pyrolysis conditions.

2.1.1.1 Surface Area

Adsorption is the adhesion of an adsorbate on the surface of an adsorbent; as such, it follows that the larger the surface area of an adsorbent, the higher the adsorption capacity [10]. A high adsorption capacity is favourable when using biochar to remove pollutants from either gaseous or aqueous systems. However, not all of an adsorbent surface is always equally attractive to an adsorbate—in these cases, the surface area of favourable adsorption sites is more important than the total surface area [11]. The availability of surface charges varies with changing surface area, which influences the cation exchange capacity—an important factor for applications in both water and soil [12]. When biochar is used as a soil amendment, increasing surface area enhances the number of surface sites available for nutrient fixation and microbial colonization [13].

2.1.1.2 Porosity

A key characteristic influencing surface area is the porosity of biochar. Pores form in biochar when water and volatiles are released from the biomass during pyrolysis [11]. Increasing the pore volume of biochar will, in turn, enhance its surface area and create more potential sites for adsorption. The distribution of pore sizes is another important factor, as different sizes offer various advantages

and challenges. For use in water systems, mesopores of 10-50 nm are considered desirable, since smaller pores may be too small to allow water particles entry to the pore, and too many large macropores can decrease the total surface area [14], [15]. For carbon capture purposes, microporosity is more advantageous due to increased surface area [11]. Pore size has also been used to increase biochar's selectivity toward specific compounds, with pore size distribution potentially creating a "sieving" effect. One study utilising biochar to remove anions from water demonstrated that biochar with pore sizes large enough for nitrate ions (0.29 nm) to enter, but not sulphate (0.46 nm) or phosphate (0.476 nm) ions, produced an ion-sieve effect [16]. When used as a soil amendment, porosity and pore interconnectivity are important in determining biochar's water-holding capacity [17].

2.1.1.3 Surface Charge and Functionality

Key factors influencing biochar's surface charge are surface functional groups and, for aqueous systems, the biochar's point of zero charge (pH_{pzc}). The pH_{pzc} of biochar is the pH at which its net charge is zero- both negatively and positively charged surface sites will still be present [18]. When the pH of solution is less than the pH_{pzc} the biochar will have a positively charged surface; conversely, when the solution's pH exceeds pH_{pzc}, the biochar will have a negatively charged surface [19]. Biochar's surface charge varies with feedstock; however, it is normally net negative, reducing its affinity for anions [20]. Surface functional groups determine the attractiveness of biochars surface for a target pollutant and the mechanism by which adsorption occurs. Functional groups on biochars surface also affect how hydrophobic or hydrophilic a biochar is in nature with high quantities of polar oxygen-containing groups increasing biochars hydrophilicity, while biochar surfaces dominated by nonpolar aromatic carbon structures with few oxygen containing groups are more hydrophobic [21].

2.1.2 Pyrolysis

Biochar can be produced using various technologies such as pyrolysis, torrefaction, gasification, and hydrothermal carbonisation [22]. Pyrolysis is the

most commonly used technique, yielding more biochar than gasification and producing biochar with a higher degree of carbonisation than torrefaction and hydrothermal carbonisation [23], [24], [25]. Operating conditions such as pyrolysis temperature, heating rate, residence time, gas flow rate, and pressure can all have a significant effect on the resulting biochar.

2.1.2.1 Pyrolysis Temperature

Pyrolysis temperature is the main factor affecting the porosity and surface area of biochar; it also influences the surface functional groups present [11], [26], [27]. Low pyrolysis temperatures produce biochars of low porosity. At temperatures below 400°C, the degree of devolatilization of gases from biochar is significantly reduced. This prevents the cracking and formation of new pores, as well as potentially blocking existing pores [28]. Above 400 °C, a greater number of volatiles (primarily permanent gases) are released from the char, and amorphous carbons begin to increase the degree of crystallinity in their structures [29]. Lower pyrolysis temperatures favour the presence of hydrophilic anionic groups on the biochar surface, while higher temperatures increase hydrophobicity [30]. The pH_{pzc} of biochar can also be affected by pyrolysis temperature, with higher temperatures usually resulting in higher pH_{pzc} values due to an increased decomposition of acidic functional groups and increase in the formation of alkaline minerals [19].

Zhou *et al*. compared biochar produced from five different plant waste feedstocks and found that surface area, total pore volume, and alkalinity of biochar samples increased with rising temperature between 300-700 °C for all feedstocks [31]. The study showed that phosphate adsorption increased with increasing pyrolysis temperature for unmodified eggshell. Similar results were observed when Thalia dealbata Fraser-derived unmodified biochar was produced at temperatures of 300, 500, and 700 °C [32]. Biochar surface area, porosity, and sorption capacity for phosphate all increased with rising temperature at low temperature ranges. The ash content of biochar also increased, which is commonly observed with rising temperature [11]. However,

porosity and surface area do not increase indefinitely with temperature. There are 'inflection' points at which surface area and pore volume start to decrease as temperature rises. It is important to note that these inflection points may occur at different temperatures for surface area and pore volume. As temperatures continue to increase, pores may widen, reducing surface area, or begin to collapse, lowering porosity. The optimum temperature for high porosity and surface area varies between feedstocks. Inflection points often appear around 500-600 °C for various biomass sources, with higher temperatures observed at higher lignin contents [11].

2.1.2.2 Heating Rate

Heating rate plays an important role in determining biochar yield, with low heating rates associated with high yield [33]. At low heating rates, there is high resistance to heat and mass transfer within biomass particles, resulting in reduced volatile release and subsequently decreased porosity and surface area [34]. However, when the heating rate is too high biomass components (cellulose, hemicellulose, and lignin) may thermally degrade faster than they can release volatiles, softening and demonstrating thermoplastic behaviour, forming viscous intermediates prior to carbonisation and leading to a coalescence of particles which smooth out the biochar surface reducing its surface area [35]. Additionally, if the heating rate is too low to allow volatile matter to diffuse fully, then pore blocking may occur [36]. A comparison carried out of 9 studies indicated high surface area and pore volume to be achieved at heating rates between 5 °C/min and 30 °C/min [11].

2.1.2.3 Residence Time

Residence time is an important factor to ensure biomass fully pyrolyzes and enough time is given for devolatilization without the biochar melting and destroying the pore structure [37], [38]. Selection of a favourable residence time is highly dependent on pyrolysis temperature and heating rate. When examining the effects of residence time on rapeseed stem-derived biochar, the surface area

increased between 10 and 60 minutes but decreased between 60 and 100 minutes [39]. Commonly used residence times range from 30-120 minutes [11].

2.1.2.4 Carrier Gas

A carrier gas is required during pyrolysis to purge volatiles released from the biomass and prevent any secondary reactions affecting the biochar composition or surface chemistry. Nitrogen is the most commonly used purge gas due to its low cost and high availability compared to other inert gases such as argon [40]. Increasing the gas flow rate can lead to a slight decrease in biochar yield due to the inhibition of repolymerization reactions [41], [42]. Enhancing the release of volatiles also promotes pore formation, increasing surface area and porosity. However, overly high carrier gas flow rates can cause cooling of the char, reduce volatile release, and therefore decrease porosity and surface area [43]. Moderate flow rates are recommended to increase char surface area and porosity [11], [43].

2.1.2.5 Pressure

Pyrolysis is typically carried out at atmospheric pressure [44], [45]. Raising pyrolysis operating pressure increases biochar yield by enhancing volatile activity in the gas phase and promoting secondary reactions [46]. Whilst the yield of biochar may increase, the quality is often decreased with various studies showing surface area decrease with pressure increase up to 20bar [47], [48].

2.1.3 Summary

Prior to selecting pyrolysis conditions, it is important to understand the desired application of biochar. Desired characteristics may differ depending on the application; this should be considered when selecting pyrolysis conditions. In summary, biochar's performance as an adsorbent can be enhanced by optimising key physiochemical characteristics such as high surface area and porosity, and a favourable surface charge to promote interactions with adsorbate; pyrolysis conditions greatly influence these traits. Suitable pyrolysis conditions to produce biochar for use in aqueous systems include moderate to high temperatures, with moderate heating rates, residence times, and carrier gas flow rates.

2.2 Biochar Modification

Biochar can be modified through various modification methods (illustrated in *Figure 2.1*) to achieve desired characteristics, such as enhanced porosity or desired surface functionality. Activation is the process of physically or chemically treating biochar to enhance its physicochemical properties (surface area, pore volume, and surface functionality) for a specific application. Both physical and chemical activation can be used to improve biochar's surface area and porosity. Physical activation generally involves the use of oxidising gases, such as CO_2 or steam, at high temperatures to remove carbon and eliminate volatiles. Chemical activation with acids or alkalis can be used to increase surface area by removing ash, and unblocking and expanding pores [49]. Functionalisation involves the introduction or enrichment of specific functional groups on the biochars surface, engineering the surface chemistry of the final biochar without necessarily enhancing physical characteristics [50]. Functionalisation can be used to increase or decrease biochar's surface charge, add desired surface functional groups, or magnetise biochar. Functionalisation methods used to alter the surface chemistry of biochar include chemical doping (incorporation of foreign atoms into the carbon lattice), formation of biochar–metal composites via decoration (attachment of metal species onto the biochar surface), oxidation, and treatment with acids or alkalis [49][51], [52] .

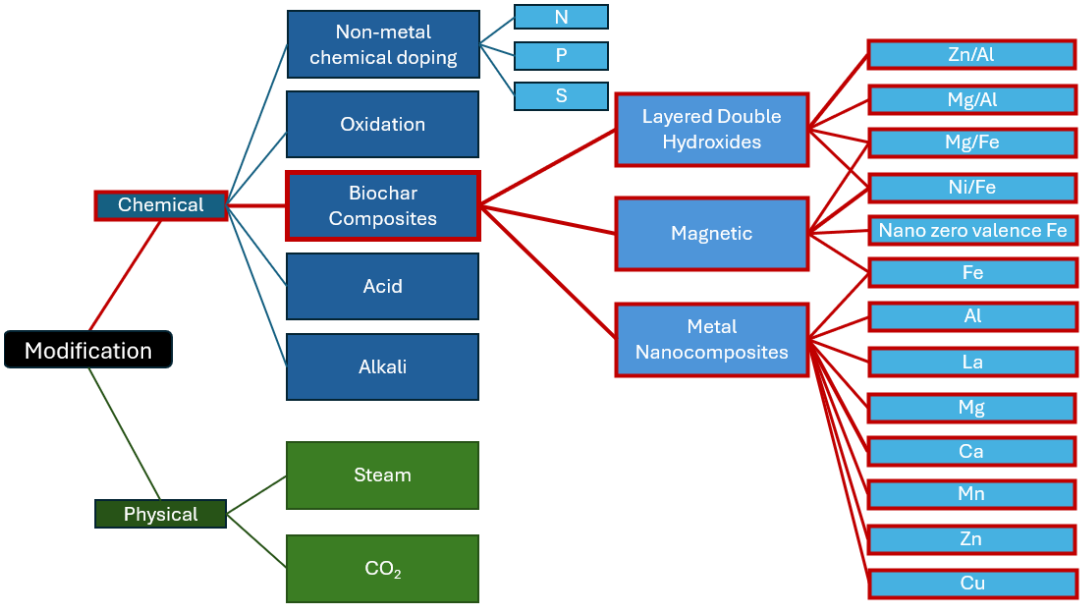

Figure 2.1: Tree diagram illustrating different options for physical (green) and chemical (blue) biochar modification with methods suitable to achieve aqueous phosphate recovery outlined in red.

When aiming to adsorb oxyanions such as phosphate, it is reportedly necessary to increase the positive surface charge of negatively charged biochar, as such modification should focus on functionalisation to achieve the desired surface chemistry. Phosphate in aqueous environments may exist in various forms: dihydrogen phosphate ($H_2PO_4^-$), hydrogen phosphate (HPO_4^{2-}), and phosphate (PO_4^{3-}). However, PO_4^{3-} is not typically present within the pH range characteristic of eutrophic conditions [53], [54], [55]. Adsorption of phosphate can occur through either chemisorption or physisorption, with surface precipitation being the primary mechanism reported in the literature [56]. Surface precipitation occurs when phosphate ions react with metal atoms on the biochar surface, depositing metal phosphates. Electrostatic repulsion from the negatively charged surfaces of unmodified biochar can often result in low phosphate sorption capacities, demonstrating the need for chemical functionalisation of the biochar; adsorption capacities of ~3 mg_P/L, 0.5 mg_P/L, and 5.2 mg_P/L have been seen from biochar derived from soybean straw, orange peel, and jackfruit

peel respectively [57], [58], [59]. Improving the phosphate sorption capacity of biochar can be achieved via functionalisation to produce layered double hydroxide (LDH) biochar, metallic biochar, or other metal nanocomposite biochar.

2.2.1 Metal Nanocomposite Biochar

Functionalising biochar using metal compounds allows for protonation of the biochar surface, addition of surface functional groups, and enhancement of biochar's porosity. Favourable biochars for aqueous P recovery are often created via the addition or formation of metal oxides or carbonates onto the biochar surface.

2.2.1.1 Aluminium

Much success has been seen using aluminium oxide decorated biochars produced from feedstock impregnated with aluminium chloride prior to pyrolysis. When soybean straw was used as a feedstock, aluminium oxide decoration increased the phosphate adsorption capacity of biochar from 0.82 to 15 mg_P/g_{BC} [57]. Impregnating soybean straw with aluminium chloride reportedly more than doubled the surface area of biochar; it was hypothesised that high pH_{pzc} and small AlOOH particle size were the leading causes of the increased adsorption. Most studies report achieving a max P adsorption capacity for Al-modified biochar within the range of 11.29 to 31.28 mg_P/g_{BC} [60], [61], [62]. Al has been shown to be a beneficial addition to biochar already modified with other metals. Various studies have demonstrated favourable sorption capacities achieved through the modification of biochar with Al alongside other metals such as Mn and Fe, with particularly high sorption capacities (up to 289 mg_P/g_{BC}) reported when mixed with Mg. [57],[63], [64], [65].

While Al-modified biochars are highly suitable for water remediation, aluminium can be very toxic to plants. In small concentrations, aluminium may promote plant growth by enhancing resistance to stress and improving nutrient uptake [66]. However, excessive aluminium, such as levels commonly found in acidic

soils, can inhibit root growth and be highly toxic [67]. Aluminium is considered to be the primary factor limiting plant growth in acidic soils, indicating that Al-modified biochar may not be suitable for circular use in often acidic Scottish soils.

2.2.1.2 Lanthanum

Significant improvement in adsorption of phosphate has also been reported using La-modified biochars. Lanthanum has been reported to increase the pH_{pzc} of biochar, with Tang *et al*. reporting the maximum phosphate adsorption capacity of three La-modified biochars, produced from precipitation of $La(OH)_3$ onto the biochar surface, to increase up to 45.6 mg_P/g_{BC} with increasing pH_{pzc} [68]. Adsorption capacities of biochars produced from impregnation of feedstock with $La(NO_3)_3$ prior to pyrolysis have been reported as 36.06, 148.11, and 312.55 mg_P/g_{BC} for biochar derived from wetland plant waste, plantus ball fibre, and sewage sludge, respectively [69], [70], [71]. Despite variations in adsorption capacities, all studies reported mechanisms including ligand exchange, electrostatic attraction between phosphate and lanthanum hydroxide crystals, and surface complexation with La^{2+} ions.

A clear consensus is missing on the effect of lanthanum on plant growth. Results from studies vary widely: lanthanum promotes the growth of some plants [72], decreases the growth of others (such as corn and mung beans)[73], and has no significant effect on plants such as bell peppers [74]. The risk of lanthanum being harmful to plant growth has been shown to rise in increasingly acidic soils [75]. Furthermore, lanthanum has been classified by the EU commission as a critical raw material, as such its use may not be suitable for large scale use [76].

2.2.1.3 Magnesium

Decorating biochar with magnesium oxide has been consistently reported to produce composites with high aqueous phosphate removal capacities in the range of 89-380 mg_P/g_{BC}, as seen in *Table 2.1* below. Key P adsorption mechanisms for magnesium oxide decorated-biochar are surface precipitation and electrostatic attraction. Whilst Mg salts are reliable functionalisation agents

for producing biochar with high P recovery, optimal production conditions remain unclear.

Table 2.1: Comparison of aqueous P removal capacities of Mg-biochars from various feedstocks.

Feedstock	**Chemical Agent**	**Surface Area (m^2/g)**	**Pore Volume (cm^3/g)**	**Mg Content (wt%)**	**Max Adsorption Capacity (mg_P/g_{BC})**	**Ref.**
Poplar chips	$MgCl_2$	254	0.13	9.3	89	[77]
Phragmites australis	$MgCl_2$	90	0.09	16.2	100	[78]
Sugarcane harvest residue	$MgCl_2$	41	0.37	23.1	129.7	[79]
Rice straws	$MgCl_2$	145	0.26	11.6	136	[80]
Rice Straw	$Mg(CH_3COO)_2$	57	0.09	-	171.5	[81]
Corn	$MgCl_2$	490	-	-	239	[82]
Poultry manure	$MgCl_2$	-	-	8.31	250.8	[83]
Sugar beet tailings	$MgCl_2$	70		15.7	272.2	[84]
Anaerobic fermentation sludge	$Mg(CH_3COO)_2$	93	0.17	18.8	379.5	[85]

The importance of Mg content for P-adsorption potential in magnesium oxide decorated biochars is unclear from the current literature. Zhang *et al*. examined the P removal capacity of five MgO decorated biochars produced from pre-pyrolysis $MgCl_2$ impregnation of different feedstocks; whilst the best performing biochar (66.7% P-removal) had a reportedly significantly higher Mg content than the worst performing biochar (0.5% P-removal), there was a lack of clear

correlation between Mg content and P-adsorption [84]. Similarly, Jiang *et al*. tested the performance of MgO decorated biochar produced from the impregnation of six different types of straw feedstock with $MgCl_2$ prior to pyrolysis and reported that both the highest (31.15 mg_P/g_{BC}) and lowest (6.77 mg_P/g_{BC}) maximum adsorption capacities of Mg-biochars occurred in biochars with the highest Mg contents [86]. Instead, MgO decorated biochars adsorption capacity was seen to correlate with pH_{pzc}. When a constant feedstock is used, biochar's affinity for aqueous P has been observed to increase with rising Mg content; however, some studies show there to be an inflection point at which adding excess Mg reduces P adsorption due to aggregation of MgO crystals over blocking pores and decreasing potential adsorption sites [88],[81], [81]. The potential for overloading of biochar may help explain the discrepancy in the effects of Mg content between different feedstocks, as the optimal chemical loading rate is likely to vary depending on the structural properties of the feedstock. This variability makes it challenging to compare functionalised biochar derived from diverse sources.

There remains some debate in the literature regarding the effects of pyrolysis temperature on the P-removal capacity of MgO decorated biochar, with many studies reporting that the P-removal performance increases with rising pyrolysis temperatures, while others report it decreases [77], [81], [82], [83]. Increasing pyrolysis temperature has been shown to promote the agglomeration of MgO crystals, increasing the surface area of favourable adsorption sites; however, if crystal clusters grow too large, there is a greater risk of detrimental pore blocking [84][87]. As such, synergistic effects of functionalisation and pyrolysis conditions should be studied.

Magnesium is an essential macronutrient for plant growth. It plays a vital role in photosynthesis, the activation of many plant enzymes, and increasing crop yield and quantity [88]. Magnesium deficiency is a common problem that limits crop production in acidic soils [89], [90]. Its non-toxic nature, widespread availability,

and low cost make magnesium modification of biochar an economically feasible solution [56].

2.2.1.4 Calcium

Calcium-rich biomass has been used alongside other biomass sources to produce Ca-biochars via co-pyrolysis. Oyster shell has been employed for co-pyrolysis with peanut shell and tobacco shell to produce biochar with reported removal capacities of 168.2 and 88.64 mg_P/g_{BC}, respectively [91], [92]. Cao *et al*. compared the effect on P recovery when rape straw-derived biochar was produced through co-pyrolysing with a $CaCO_3$-rich biomass (eggshells) and $CaCO_3$ impregnation of the feedstock [93]. The biochar samples were reported to perform very similarly, with approximately equal equilibrium times and maximum adsorption capacities. The surface areas of pristine biochar, $CaCO_3$-doped biochar, and eggshell co-pyrolysed biochar were reported as 336, 32, and 181 m^2/g, respectively, suggesting that co-pyrolysis may block less of the biochar's pore structure compared to chemical impregnation; however, this appeared to have an insignificant effect on adsorption capacity in the presented case. There is limited work available in the literature optimising the ratio of carbon source biomass to calcium source biomass during co-pyrolysis; however, early studies agree that P removal capacity increases with higher ratios of calcium source biomass [94],[95].

Similarly, little work has been done studying the effect of Ca content on calcium oxide/carbonate decorated biochars. Wang *et al*. observed an increase in P adsorption with rising biochar:$Ca(OH)_2$ ratios; ratios of 1:0.25, 1:0.5, 1:1, 1:2 were tested, with 1:2 showing the highest adsorption capacity of 314.2 mg_P/g_{BC} [96]. The increase in phosphate sorption was credited to the enhanced interaction between PO_4^{3-} ions and $Ca(OH)_2$ on the biochar surface, forming $Ca_5(PO_4)_3OH$ crystals. However, a study comparing the effect of adding different quantities of CaO (15-65 wt%) during ball milling of corn straw biochar found that a loading of 50 wt% CaO produced biochar with the highest adsorption capacity (329 mg_P/g_{BC}), as overly high CaO proportions led to detrimental pore blockage [97].

Since temperature significantly influences the porous structure of biochar, it is likely that pyrolysis temperature also affects optimal Ca loading rates; however, no literature containing a systematic analysis of synergistic effects could be found.

When biochar has been decorated with $Ca(OH)_{2,}$ contrasting results on the effects of pyrolysis temperature have been reported. Zeng *et al*. compared the aqueous P adsorption capacity of wood-based biochar functionalised with $Ca(OH)_2$ produced at 100, 300, and 500 °C and reported P adsorption to decrease (range 109.55-138.70 mg_P/g_{BC}) with increasing pyrolysis temperature, which was thought to be due to the partial conversion of $Ca(OH)_2$ to less reactive $CaCO_3$ caused by higher pyrolysis temperatures [98]. However, Liu *et al*. reportedly observed that the P adsorption capacity of $Ca(OH)_2$ decorated straw biochar (97.4-197 mg_P/g_{BC}) increased with increasing pyrolysis temperatures within the range of 600-800°C due to an increase in CaO content and specific surface area [99]. Electrostatic attraction and surface precipitation are the key mechanisms seen for P adsorption on Cvatea-functionalised biochars. As seen in *Table 2.2* below, values reported for maximum aqueous P removal capacities of Ca-functionalised biochars are similar to those for Mg-functionalised biochars discussed above.

Table 2.2:Maximum aqueous P adsorption capacities of Ca-biochars with various functionalisation's.

Feedstock	**Modifying Agent**	**Surface Area (m^2/g)**	**Pore Volume (cm^3/g)**	**Ca content (wt%)**	**Max Adsorption Capacity (mg_P/g_{BC})**	**Ref.**
Tobacco straw	Co-pyrolysis: Oyster shell	7	0.03	11.6	88.6	[92]
Rape straw	$CaCO_3$	32	0.02	-	100.0	[93]
Rape straw	Co-pyrolysis: eggshells	181	0.09		103.3	[93]
Ramie biomass	$CaCl_2$	15	0.06	22.4	105.4	[100]
Sewage sludge	Co-pyrolysis: eggshells	35	0.08	-	107.0	[95]
Peanut Shells	Co-pyrolysis: eggshells	261	0.40	-	130.6	[101]
Wood	$Ca(OH)_2$	120	-	48.1	138.7	[98]
Sheep Manure	Co-pyrolysis: oyster shells	5	0.02	7.7	146.3	[94]
Sewage sludge	$CaCl_2$	-	-	18.6	153.9	[102]
Peanut shell	Co-pyrolysis: oyster shell	127	0.37	-	168.2	[91]
Black liquor	$Ca(OH)_2$	29	0.11	31.0	197.0	[99]
Flour	$Ca(OH)_2$	-	-	-	314.2	[96]
Corn straw	CaO	-	-	-	329.0	[97]

Calcium is an essential macronutrient for plant growth. Calcium is essential for cell wall and membrane stability; it also acts as a messenger in the growth of plants roots and shoots as well as fertilisation and stress management [103]. As

a basic metal it can be used to aid the remediation of acidic soils and is common in liming materials [104], [105]. Calcium is an inexpensive non-toxic element which is widely available, making it an appropriate choice for biochar modification [56].

2.2.1.5 Other Metals

Other metals such as copper, manganese, and zinc have also been used to improve the adsorption capacity of biochar. However, these metals tend to have lower adsorption capacity than those aforementioned. One study, comparing sewage sludge-derived biochar, showed Ca-modified biochar to have the highest performance in phosphate batch sorption experiments, followed by Mg, Al, Fe, and Cu in turn [102]. Similar results were seen when comparing the phosphate sorption capacity of metals for the modification of rhizofiltration biomass-derived biochar, where Fe performed the best, followed by Cu, Zn, and Mn [106].

Zinc, copper, and manganese are essential macro nutrients for plants. However, all can become highly toxic for plants at high concentrations, with copper toxicity a common side effect of industrial agriculture and manganese toxicity particularly common in acidic soils [118], [107]. While zinc, critical for healthy plant development, may be a beneficial additive to biochar used for soil amendment, Zn-modified biochars do not compare with the aqueous P-recovery success of those modified with other essential plant nutrients such as magnesium and calcium.

2.2.2 Magnetic Biochar- Iron and Nano Zero Valence Iron

Magnetic biochar can be produced through the precipitation of iron oxides onto the biochar surface, and allow for the use of magnets to ease the separation of biochar from solution [108]. The presence of iron oxides on the surface of biochar is known to increase its pH_{pzc}, resulting in enhanced sorption capacities [109]. Zhang *et al*. compared the phosphate adsorption of biochars treated with magnetite, ferrihydrite, goethite, and hematite. The trend in reported phosphate adsorption showed no correlation with the surface area or Fe content of the

biochars; however, it could be seen to reflect the trend in reported pH_{pzc} [110]. The addition of iron oxides often reduces the surface area of biochar; however, multiple studies have reported the adsorption of phosphate on iron oxide-modified biochar to be more than double that of pristine biochar [111], [112]. Despite improving the P adsorption capacity of biochar, generally iron oxide modified biochars still have a relatively modest P adsorption capacity, ranging from 2.81 to 51.6 mg_P/g_{BC}, compared to biochar treated with other metals [113], [114], [115].

Nano zero-valent iron (nZVI) is frequently employed in remediation processes owing to its low redox potential, which enables it to function as an effective electron donor for a variety of common pollutants [116]. Biochar can be loaded with nZVI to create magnetic modified biochar. Adsorption capacities of nZVI modified biochars, with values reported in the literature ranging from 3.96 to 95.2 mg_P/g_{BC}, are often higher than those of iron oxide modified biochars-likely due to the high reactivity of nZVI [117], [118], [119], [120].

While iron is safe to use in soil in small quantities, high concentrations of iron may poison soils, with the likelihood increasing in acidic soils. Recently, nZVI has been shown to age considerably in soil due to the presence of iron-reducing and oxidising bacteria [121].

2.2.3 Layered Double Hydroxide Biochar

LDHs are high surface area materials, with large anion sorption capacities, produced by alternating positively charged layers of divalent and trivalent metal hydroxides with negatively charged anions [122]. LDHs have the general formula $[M^{2+}_{(1-a)}\ M^{3+}(OH)_2]^{a+}[A^{n-}]_{a/n}.mH_2O$ where M^{2+} and M^{3+} represent divalent and trivalent cations respectively, A^{n-} is the anion, and a is the ratio $M^{3+}/(M^{2+} + M^{3+})$ [123].

Decorating biochar with LDHs has been reported to increase both the pH_{pzc} and surface area of biochar. This can be seen in Li et al's work, where decorating biochar with Mg/Al-LDH reportedly increased surface area and pH_{pzc}, increasing the maximum Langmuir adsorption capacity of pristine biochar from 3 to

81.83 mg_P/g_{BC} at pH 3 [123]. It has been reported that increased quantities of LDHs in LDH-biochar composites can block biochar pores and reduce surface area; despite this, various studies show LDH-biochar composites to display increasing phosphate adsorption with increasing quantity of LDH in composite [124], [125], [126]. Studies comparing pure LDHs to LDH-biochar composites report the pure LDH to have higher phosphate adsorption capacities; however, these studies generally consider adsorption on a weight of adsorbent basis, when considering adsorption on a weight of LDH basis, biochar composites outperform pure LDH, indicating synergistic effects [124], [126]. There are many potential combinations of metal cations for use in LDHs biochar composites. Mg/Al based composites have been shown to have enhanced maximum phosphate adsorption capacities over various other combinations such as Mg/Fe, Ni/Fe, and Zn/Al [124], [127]. Adsorption of phosphate by Mg/Al LDH-biochar is the result of interactions between LDH on the biochar surface and phosphate ions, with interactions governed by surface complexation and electrostatic attraction. Biochar feedstock has also been shown to affect the phosphate adsorption of these composites [128].

Whilst LDH-biochar composites are promising for aqueous phosphate recovery, most maximum adsorption capacities reported are relatively modest. Maximum adsorption capacities of Mg/Al LDH-biochar composites were 13, 39, 48, 50, and 56 mg_P/g_{BC} for feedstocks of tobacco stalk, rice husk, date palm, wheat straw, and bamboo, respectively [129], [130], [131], [132], [133]. These maximum adsorption capacities typically occur at low pH (2-4), much lower than that of eutrophic water systems. Furthermore, despite an acidic pH optimal for phosphate removal, some work has shown LDH to have low stability, with destruction of the LDH structure at acidic conditions or during phosphate adsorption [134].

2.2.4 Summary

Higher P-adsorption capacities are reported in the literature for Mg/Ca decorated biochars than Al, La, Mn, Cu, or Zn decorated biochars, Mg/Ca decorated

biochars also have a lower potential to become toxic in soil. Salts $MgCl_2$ and $CaCl_2$ are cheap and widely available making their use for biochar functionalisation suitable for large scale. Mg and Ca are essential plant macronutrients, as such the use of Mg/Ca decorated biochars in soil systems may be favourable. Magnetic biochars have been reported to enhance aqueous P recovery compared to pristine biochars, however maximum adsorption capacities reported are lower than those reported for Mg/Ca decorated biochars. Phosphorous is also known to experience a large degree of fixation with iron in soils, reducing the bioavailability of P and reducing the suitability of metallic biochar for circular use in soil systems. Biochars decorated with LDHs have been reported to demonstrate an improved P adsorption capacity compared to pristine biochar, however once again adsorption capacities reported are lower than those reported for Mg/Ca decorated biochars. Furthermore, some studies have reported LDHs on the biochar surface to demonstrate low stability in aqueous environments, particularly at low pH.

Across different metal modifiers, electrostatic attraction, complexation, ligand exchange, and surface precipitation are key adsorption mechanisms for P recovery. Among various types of functionalised biochars, Mg/Ca nano-composite biochar stands out for its consistently high P recovery and suitability for soil systems. The 2^+ charge of Mg and Ca promotes precipitation with HPO_4^{2-} [53]. However, an understanding of optimal functionalisation conditions remains lacking.

There is no consensus in the literature on how increasing pyrolysis temperature and loading of functionalisation agent affect the phosphate adsorption capacity of biochar. This may be explained by optimal functionalisation involving balancing the amount of functionalising agent with the risk of blocking biochar's porous structure—essentially balancing the effects of functionalisation on both chemical and physical properties. To optimise the functionalisation process, it is crucial to consider functionalising agent impregnation rate and pyrolysis temperature together, and to examine any synergistic effects that may exist. A

better understanding of these interactions could clarify conflicting results reported in different studies. Moreover, since various chemical functionalisation agents influence the physical properties of biochar differently, comparisons should be conducted at each metal salts optimal loading rate and pyrolysis temperature. To the author's knowledge, this has not yet been explored in the existing literature.

2.3 Nanocomposite Ca/Mg Biochar Production Methods

There are various methods available by which to produce Ca/Mg nanocomposite biochar as illustrated in *Figure 2.2*.

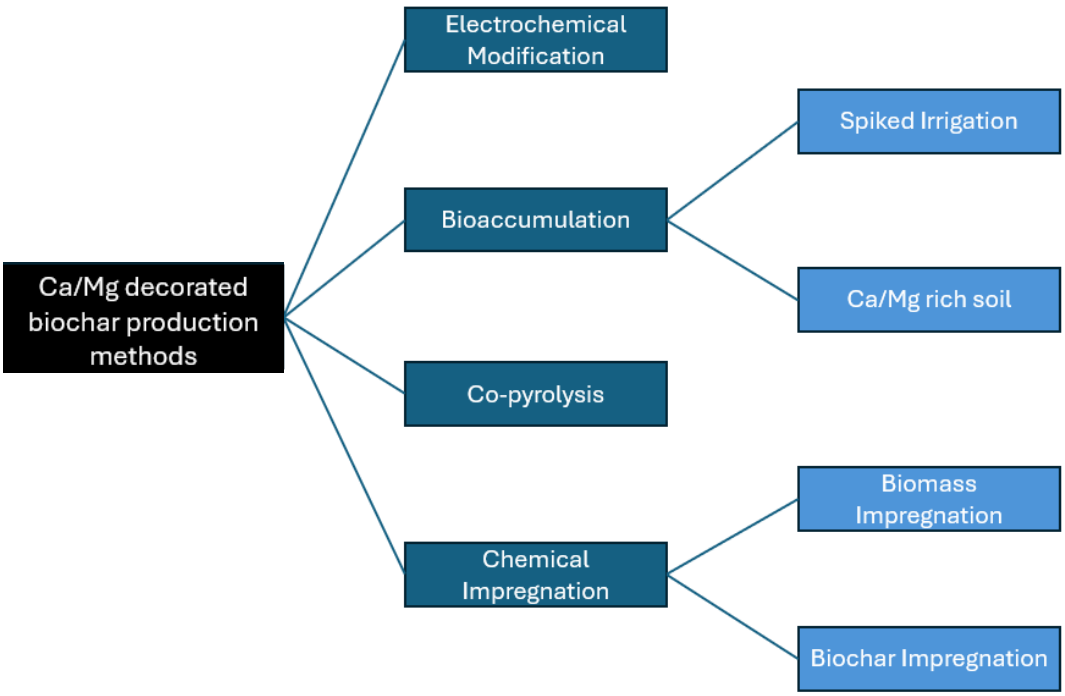

Figure 2.2: Tree diagram showing methods available for Ca/Mg nanocomposite biochar production.

2.3.1 Electrochemical Modification

Electrochemical modification involves passing an appropriate current through a solution containing biomass and an electrolyte to facilitate electrodeposition of the desired metal onto biomass prior to pyrolysis [135]. Electrode material and

salt used in the electrolyte solution are selected to include desired modifiers (e.g., an Al electrode and $MgCl_2$ solution to produce Al/Mg-biochar). Relatively few studies have been conducted on electrochemical modification; however, those available show high P removal. An excellent Langmuir-Freundlich (Sips) maximum adsorption capacity of 620 mg_P/g_{BC} was obtained from marine microalgae-derived Mg-modified biochar using electrochemical modification [136]. Similar methods have also been used to create a Ca-modified biochar, derived from marine microalgae, with a maximum adsorption capacity of 68.7 mg_P/g_{BC} [137].

2.3.2 Bioaccumulation

Bioaccumulation involves growing biomass rich in specific nutrients, which can be achieved through irrigation of crops using water spiked with metals or growing plants in soil enriched with a particular metal. Bioaccumulation has been used to produce Mg-enriched tomatoes and Ca-enriched tomatoes, with resulting biochars successfully removing approximately 89% and 65% of phosphate, respectively, during batch adsorption experiments [138]. Compared to other functionalisation methods, bioaccumulation is less reliable for obtaining reproducible results. It may be a valuable way to utilise soil that is overly rich in a specific compound, which would otherwise go unused; however, the scalability of this method is limited. Moreover, producing biomass specifically for use as a biochar feedstock is less environmentally beneficial than utilising existing waste.

2.3.3 Co-pyrolysis

Co-pyrolysis involves mixing biomass with a material naturally rich in the desired metal additive and pyrolysing these materials together. Eggshells and peanut shells are commonly used alongside other biomass as Ca sources, as discussed above in *Section 2.2.1.4*. Materials such as dolomite, phosphogypsum and antibiotic fermentation residues have been used as metal sources in co-pyrolysis to produce biochars rich in Mg, Ca, and Fe with adsorption capacities ranging from 102-207 mg_P/g_{BC} [139], [140], [141]. Co-pyrolysis is a suitable way of utilising multiple waste sources at once.

2.3.4 Chemical Impregnation

Chemical impregnation is the most commonly reported method of biochar functionalisation in the literature, likely due to its simplicity. Various studies have been conducted using impregnation of biomass (pre-pyrolysis impregnation) and impregnation of biochar (post-pyrolysis impregnation). However, studies directly comparing the effects of pre- and post-pyrolysis modification are scarce. One study compared the phosphate sorption capacity of five feedstocks (peanut shells, mung bean shells, rice husk, corn cob, and cotton stalk) when impregnated with $MgCl_2$ pre-pyrolysis and post-pyrolysis [142]. For all feedstocks tested, batch sorption experiments showed that pre-pyrolysis impregnated samples had a higher adsorption capacity; differences in adsorption performance between the pre- and post-modified biochars were insignificant at 300 °C but increased by a factor of ~4.5-10 at 450 °C, depending on the feedstock. The difference in adsorption performance was even greater at 600 °C, with phosphate uptake in pre-pyrolysis-modified biochars increasing by a factor of ~13-19 compared to their post-pyrolysis-modified counterparts. The use of metal-chloride salts has been hypothesised to increase porosity when used pre-pyrolysis compared to post-pyrolysis due to the release of hydrochloric acid during char formation, causing cracking within the forming biochar [79].

Compared to pre-pyrolysis functionalisation, post-pyrolysis functionalisation allows for greater control over biochar's surface chemistry and avoids thermal degradation of chemical agents used. However, post-pyrolysis functionalisation does not allow for the formation of pores around metal particles. The single study available on pre vs post pyrolysis functionalisation of biochar use the same metal chloride salt before and after pyrolysis, despite metal chloride rich feedstock often producing metal oxides/carbonate rich biochar during thermal degradation [78], [143], [144]. There are currently no papers to the best of our knowledge in the literature comparing pre-pyrolysis impregnation of feedstock with a metal chloride and post-pyrolysis impregnation of biochar with the desired metal

oxide/carbonate. Further studies directly comparing pre- and post-pyrolysis impregnation are needed.

2.3.5 Summary

There are various methods for producing Mg/Ca-rich biochar, with chemical impregnation being the most frequently used in the literature. Typically, biomass is impregnated with a metal chloride, while biochar is often impregnated with a metal oxide or carbonate. Pre- and post-pyrolysis impregnation have different effects on the physicochemical properties of biochar. Despite this, no work in the literature currently compares the impregnation of biomass with a precursor metal chloride to the impregnation of biochar with the metal oxide or carbonate derived from the thermal treatment of that chloride salt.

2.4 Functionalised Biochar for Eutrophication Control

The total phosphorus in waterbodies comprises particulate phosphorus, polyphosphates, organic phosphorus, and soluble reactive phosphorus (mainly consisting of orthophosphate, the direct contributor to eutrophication)[145]. Eutrophication is the detrimental surplus of plant nutrients in water, primarily inorganic forms of phosphorus and nitrogen, associated with low dissolved oxygen levels and algal blooms on the waterbody surface [146].In the UK, current policy and practice for eutrophication control focuses predominantly on prevention—reducing nutrient inputs to eutrophication-sensitive waterbodies [147], [148]. While this approach is essential for long-term recovery of eutrophic waterbodies, current control measures have yielded little ecological benefit, failing to address many of the issues associated with legacy P release from waterbed sediments [148]. Legacy P is described as pools of P present in waterbed sediments from historical P pollution where P is capable of being rereleased into a waterbody, these P-pools can sustain the release of P to waterbodies for timescales from years to centuries [149], [150]. As such, the use of biochar for direct remediation of eutrophic water bodies should be considered alongside its use in preventing eutrophication by recovering P from key pollution

sources. However, before biochar can be used for eutrophication control, a deeper understanding of the effect of environmentally relevant conditions on biochar's aqueous P-removal is necessary.

2.4.1 Effects of pH

An understanding of the effect of pH on biochars aqueous P recovery, as well as biochars resistance to pH fluctuations, is essential for its use in eutrophication control. The uptake of CO_2 by algae and cyanobacteria often causes an increase in the pH of eutrophic water compared to non-eutrophic water [54], [151]. Most eutrophic water bodies are slightly alkaline with pH values typically ranging from 7-9; however, in shallow hypertrophic lakes pH may rise as high as 11 [55], [152]. Furthermore, eutrophic water bodies often show a fluctuation of pH throughout the day[153] . Moreover, as pH also affects biochars' surface characteristics and the form of aqueous phosphate ions, it could have significant effects on biochars' P recovery. The protonation of hydroxyl and carboxylate groups on the biochar's surface at low pH may increase the number of favourable adsorption sites available for P adsorption. When the pH of a solution is below the biochar's pH_{pzc}, the electrostatic attraction between the biochar and P is enhanced [49], [56].

MgO-decorated biochars have reportedly demonstrated decreased phosphate adsorption with increased pH [58]. Both magnetic $MgFe_2O_4$ -decorated biochar and non-magnetic MgO-decorated biochar (pH_{pzc} 8.5 and >10, respectively) have displayed reduced P adsorption with increasing pH, particularly over pH 7[80], [154]. Phosphate adsorption was ~5 times higher at pH 3 than 11 for $MgFe_2O_4$ decorated biochar and 2 times higher for MgO-decorated biochar, with the significant drop off in adsorption seen between pH 7 and 9 likely due to the change of primary phosphate species from $H_2PO_4^-$ to HPO_4^{2-}. MgO and FeO groups present on the discussed chars' surface protonate to form $MgOH^+$ and $FeOH^+$ at low pH, reacting well with $H_2PO_4^{-1}$. Electrostatic repulsion will be increased with the simultaneous increase in negative charge of phosphate ions alongside deprotonation of biochar's surface groups as pH approaches and passes pH_{pzc}. Furthermore, as pH rises, additional OH- groups may compete with

phosphate for the positively charged sites still present. It is possible that the magnetic biochar is more heavily affected by pH increase due to possessing more surface groups to deprotonate. Despite various studies examining the effects of pH on biochar, many of these studies still carry out adsorption isotherms at optimal pH. Whilst this gives an accurate indication of a biochar's maximum adsorption capacity, these pH values are outside the range typical of eutrophic and waste waters— artificially inflating biochar's adsorption capacity in applications from eutrophication control.

Various studies have reported P adsorption to increase by a factor of ~2-23 between pH 2 and pH 12 for Ca-decorated biochars [94], [99], [100], [155]. There is often a significant increase in P uptake at neutral to high pH, likely due to an increasing proportion of P in the form HPO_4^{2-} . This would facilitate surface precipitation between Ca^{2+} ions and HPO_4^{2-} ions (the primary adsorption mechanism commonly proposed in Ca-decorated biochar). An exception to this trend has been reported by Ai *et al*. who produced Ca-biochar by mixing CaO particles with biochar at 15, 30, and 50 % wt/wt denoted BMCa15, BMCa30, and BMCa50, respectively [97]. BMCa15 (pHpzc=8.1) and BMCa30 (pHpzc=8.5) biochars showed a decrease in P adsorption between pH 2-9, with a substantial drop off above pH 7. However, adsorption by BMCa50 (pHpzc>11) was unaffected by pH. Increasing Ca content increased biochar's resistance to pH, likely due to an increase in pH_{pzc}, indicating that electrostatic interaction between aqueous P and biochar has a significant effect on adsorption.

2.4.2 Aqueous P Concentration

Eutrophic water conditions vary significantly from those used in the literature when testing biochars' P-recovery. The Scottish Environmental Protection Agency (SEPA) considers water with a P concentration of 0.035-0.1 mgP/L eutrophic, and concentrations above >0.1 mgP/L hypertrophic [156]. In England, phosphorus pollution to river water bodies is attributed to be 60-70 % from sewage treatment works, 25 % from agriculture, and 7 % from diffuse urban sources [148]. Concentrations of municipal wastewater treated in sewage works typically vary

between 4-12 mgP/L orthophosphate, with concentrations of farmyard drains ranging from 0.1-1.5 mgP/L total phosphate [157], [158], [159], [160], [161].

Most studies consider biochars aqueous P-removal at moderate to high P concentrations in the range of 10-1000 mgP/L. While these concentration ranges provide insight into biochars performance in some waste streams, such as sewage works, low concentration studies reflective of P concentrations associated with eutrophic water or agricultural diffuse pollution are lacking. The European Union limits the effluent of wastewater treatment plants to 1-2 mgP/L, depending on the sensitivity of the receiving water body to potential eutrophication [162]. Investigation into biochars' aqueous P-removal at low concentrations (such as 1-2 mgP/L) is necessary to understand biochars' suitability for polishing of current effluents to further enhance eutrophication prevention [145].

Adsorption studies carried out in simple P solutions at low concentrations are extremely limited, with no clear conclusion from the few available. When varying the initial concentration of phosphate solution from 0.8-43 mgP/L the adsorption efficiency of Fe-decorated biochar produced from Acorus calamus L, Canna indica L, and Thalia dealbata Fraser, was shown to decrease from 95.2-32.9 %, 98.4-39.8 %, and 91.5-32.5 % respectively [163]. This reduction was attributed to a decrease in available adsorption sites at increased P concentration. However, Cai *et al*. found P adsorption of MgO-decorated biochar in simulated wastewaters to increase with rising initial P concentration [80].

2.4.3 Coexisting Ions

Work present in the literature primarily focuses on the adsorption of P by biochar in simple phosphate salt solutions. The presence of other ions in eutrophic and wastewater systems may compete or interfere with the removal of phosphate, and organic matter may block the biochar's porous structure [164]. The presence of coexisting anions may also create an anionic environment surrounding active sites on the biochar surface, reducing electrostatic attraction between biochar

and target ions [165], [166]. It is therefore essential to study biochars performance in complex solutions.

Coexisting anions likely present in eutrophic waters and wastewaters include CO_3^{2-}, SO_4^{2-}, HCO_3^-, NO_3^- and Cl^-. Due to a similar ionic radius, SO_4^{2-} (0.230 nm) and PO_4^{3-} (0.238nm) compete for the same adsorption sites [167]. One study found SO_4^{2-} to be the only tested anion (Cl^-, NO_3^-, and SO_4^{2-}) to have any significant effect on phosphate adsorption upon MgO-impregnated biochar [79]. However, it has also been reported for co-existing ions (NO_3^-, CO_3^{2-}, SO_4^{2-}, CO^{3-}, Cl^-) to have a negligible reduction on phosphate sorption on MgAl-modified biochar [168]. Tao *et al*. found that resistance to the influence of Cl^- and SO_4^{2-} on Fe/Mg-decorated biochars P adsorption capacity to increase with rising Mg content and pH_{pzc} [169]. Very few studies have examined the effects of biochar's characteristics on its vulnerability to coexisting ions.

It is worth noting that interference caused by coexisting anions is not always unfavourable. The presence of SO_4^{2-}, NO_3^-, and Cl^- were reported to cause a slight decrease in phosphate sorption on $CaCO_3$-decorated sheep manure-derived biochar, whilst CO_3^{2-} and HCO_3^- were shown to increase phosphate adsorption [94]. Phosphate adsorption was reportedly increased 4.28 % in the presence of CO_3^{2-} and 1.31 % in the presence of HCO_3^-, which was hypothesised to be due to the increased solution pH (~9) caused by the weakly acidic ions. However, results have varied between different studies. One study using CaO_2-decorated biochar reported that when sufficient HCO_3^- was used to increase solution pH to 10, phosphate sorption decreased by 6.2 %, due to increased presence of OH^- converting HCO_3^- to CO_3^{-}, which subsequently formed precipitates with Ca in competition with P [170]. Similar results were reported by Liu *et al*. [99].

Whilst there has been some work on the effects of coexisting anions on biochars' aqueous phosphate removal, these studies are relatively few. Furthermore, there is a lack of consensus between different studies on the effects of specific ions on phosphate removal. Coexisting ions have been tested in simple solutions;

however, there is a lack of studies examining the combined effect of these ions. Additionally, there is a lack of consideration of the potential impact of cations present in water on biochars' P removal. Cations present have the potential to either facilitate adsorption (by assisting in the formation of precipitates on the biochar's surface) or hinder P adsorption by promoting the adsorption of other species. Future studies should focus on conducting research with a range of coexisting ions across environmentally relevant pH levels. Moreover, investigation into the effect of these ions in real eutrophic water is still required.

2.4.4 Real Water Systems

There is a significant need for further research on the efficiency of biochars in phosphate removal in real water systems. Ai *et al*. tested the phosphate adsorption of Ca-biochar in different types of water matrices. When phosphate was added to deionised water, tap water, river water and lake water, maximum adsorption capacities of 329, 321, 313, and 302 mgP/gBC were achieved, respectively [97]. Varying results were attributed to differences in anions and organic matter present in the different types of water bodies interfering with P recovery. Pap *et al*. demonstrated the ability of Fe/Al-sewage-sludge-derived biochar to effectively recover P from real wastewater in dynamic column tests [171]. Fixed bed columns of biochar successfully reduced the P concentration of wastewater (initial P concentration of 1.2-1.4 mgP/L) to below 0.1 mgP/L, with P adsorption efficiency increasing with increasing empty bed contact time. Little work has been carried out utilising Mg/Ca-decorated biochars. MgO-decorated biochar produced from Phragmites australis successfully reduced the total phosphorus (TP) concentration of a eutrophic lake from 0.152 to 0.002 mgP/L [172]. Whilst initial results presented in the literature are promising, there is a significant need for an increase in studies focusing on treated wastewater, particularly with a greater diversity of waterbodies tested.

2.4.5 P-Removal Mechanism

Functionalised biochar samples rich in Ca or Mg have been reported to adsorb phosphate through surface precipitation, electrostatic attraction, and ligand

exchange [84], [91], [100], [143], [170], [173]. While surface precipitation is often regarded as the primary adsorption mechanism for Ca and Mg rich biochars, no work in the literature considers any potential contributions to P-removal from bulk precipitation.

Leaching of metals from metal-rich biochars, including samples chemically functionalised with Mg or Ca compounds, has been reported in the literature [174], [175], [176]. As such, it is feasible that free Ca^{2+} or Mg^{2+} ions leached from functionalised biochar to the solution could react with aqueous phosphates via bulk precipitation. Bulk precipitation between metal ions present in solution and aqueous phosphate is a common process, with chemical precipitation with metal (Fe, Al, Na, and Ca) based salts commonly used to reduce the P-concentration of urban and commercial wastewaters [160], [161], [177]. Despite this, an investigation into the extent to which bulk precipitation may be involved in aqueous P-removal by biochar is, to the best of our knowledge, absent in the literature. Furthermore, there is a lack of understanding in the literature regarding what are the governing parameters that determine whether precipitation occurs in bulk or at the biochar's surface.

2.4.6 Summary

Eutrophic water can exist at a range of pH levels that vary over time; however, it is most commonly slightly alkaline, with pH between 7 and 9. Studying the effects of pH on P-adsorption not only examines the resistance of biochar to environmental changes but also provides key insights into adsorption mechanisms. While some research has investigated the effect of pH variation on Mg/Ca decorated-biochar, there is a need for more studies that perform adsorption modelling at typical eutrophic pH levels. Most current research tests P-recovery at initial P concentrations significantly higher than those found in eutrophic waters, wastewater discharges, and agricultural diffuse streams, with the effects of decreasing concentrations on biochar's P-recovery unclear. Similarly, inconsistent results have been reported regarding the impact of coexisting anions on Mg/Ca decorated-biochar P-removal, and there is limited

understanding of how cations and organic matter influence this process. To fully understand biochar's potential for use in eutrophic and wastewater systems, it is crucial that further research focuses on P-removal under conditions that reflect real water systems— specifically, low P concentrations, relevant pH ranges, and the presence of coexisting ions. After advancing research in more environmentally relevant simulated wastewater, emphasis should then shift toward studying biochar performance in real and diverse water matrices. Additionally, the potential role of bulk precipitation in biochar's aqueous P-removal is unclear, the potential of this P-removal pathway should be further investigated.

2.5 Biochar as a Soil Amendment

Biochar has been well established as a useful soil amendment capable of carbon sequestration. Biochar's benefits for soil are wide and varied, including: improving plant growth and yield [178]; improving soil fertility and water retention [179], [180]; remediating and immobilising pollutants [181], [182]; and providing nutrients [183].

2.5.1 Biochar as a Fertiliser Replacement

Recently, work has been carried out on investigating the use of P-rich biochar as a slow-release fertiliser, providing essential nutrients for plants in a less harmful way than conventional chemical fertilisers [184], [185], [186]. Under current nutrient management systems, chemical fertilisers are important to ensure plants have sufficient nutrients for growth. Fertilisers contain three main macronutrients plants need for growth— nitrogen, phosphorus, and potassium— as well as smaller quantities of micronutrients. Since 2021, 97 % of agricultural land in the UK has utilised artificial fertilisers [187]. Despite extremely widespread use, the efficiency of these fertilisers is low, with 40-70 % of nitrogen, 80-90 % of phosphorus, and 50-70 % of potassium lost to the environment. Biochar's ability to improve water holding capacity and alter the soil structure of

bacterial communities allows it to reduce the decomposition and therefore leaching of P and other nutrients [188].

2.5.2 Phosphorus Availability in Soil

Phosphorus-based fertilisers are often required to compensate for P fixation in soil [189]. Plants take up nutrient-containing water from the soil via their roots. Plant roots take up P in the form of orthophosphate (primarily $H_2PO_4^-$ and secondly as HPO_4^{2-}), with soils high in P having a more favourable concentration gradient. The mobility of phosphate and other ions is significantly reduced in heterogeneous soil systems compared to homogeneous water systems, with the diffusion coefficient of $H_2PO_4^-$ reducing from $0.9x10^{-9}$ m^2s^{-1} in water to values with magnitudes in the range of 10^{-12} to 10^{-15} m^2s^{-1} in soil [190]. The more strongly bound P is to soil, the less available it is for uptake by plant roots. The availability of P for uptake by plants depends on the form of P and which of the four inorganic pools (illustrated in *Figure 2.3*) it belongs to [191]. When P is in the soil solution (pool 1), it is immediately available to plants. The P in the second pool is adsorbed on the surface sites of soil and considered to be in equilibrium with the soil solution and readily extractable. The third pool consists of P absorbed within the soil matrix or strongly bonded to the soil. Whilst not immediately available, this P can become accessible to the plant over time. Finally, the fourth pool consists of P that will take a significant amount of time (often years) to become available to the plant. This P is either within inaccessible sites within the soil matrix, mineral or precipitated P, or very strongly bound to components within the soil. The vast majority of P in chemical fertilisers (75-85%) is in the form of pools 2,3, and 4 and is not immediately available to plants [177], [192].

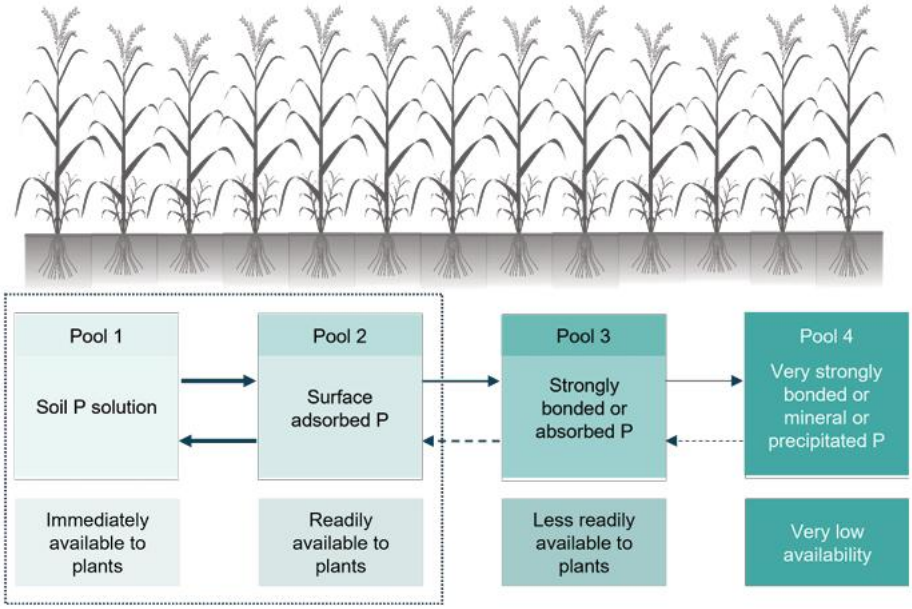

Figure 2.3: Diagram illustrating the plant availability of different forms of inorganic P in soil[191]

It is important to consider the availability of P in biochar. Lab-scale studies have proven the ability of nutrient-rich biochar for slow PO_4^{3-} release [193]. However, the bioavailability of P in spent biochar used for phosphate recovery from water is still not well understood. The availability of P from biochar may be affected by the soil itself. Fixation of P with other minerals to form precipitates is highly influenced by soil pH and the presence of iron, aluminium, and calcium, as illustrated by *Figure 2.4* [192]. Soil with neutral pH has the highest phosphorus availability.

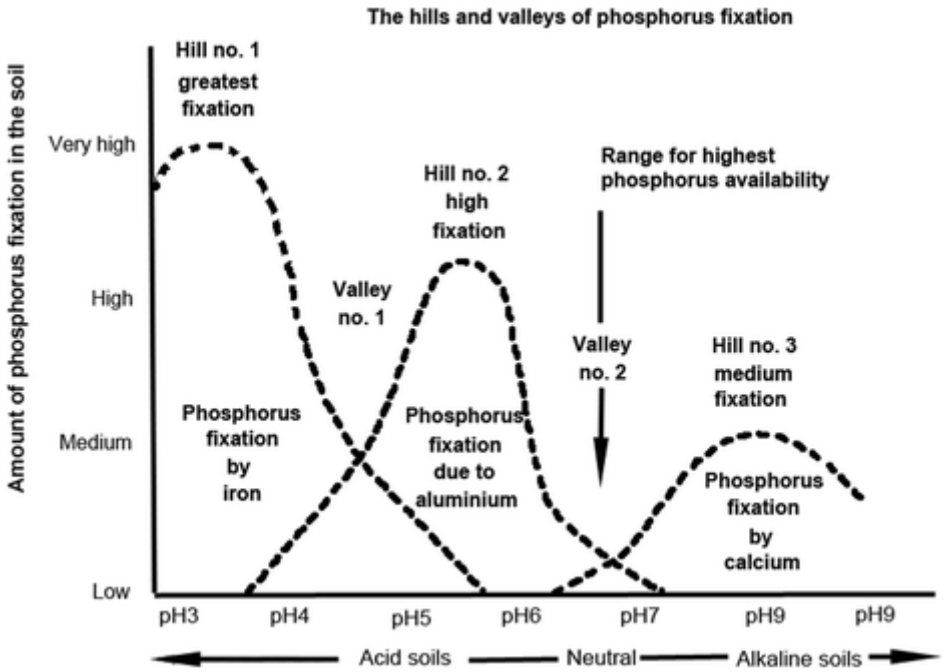

Figure 2.4: Effect of soil pH on P fixation with iron, aluminium, and calcium.[192]

2.5.3 Use of Mg/Ca Spent/ P-Charged Biochar

Whilst many studies which utilise biochar for P recovery state its suitability for use as a fertiliser replacement, relatively little research has been conducted to prove this. When Mehlich-3 bioavailable P testing (a common method of determining soil's bioavailable P content) was carried out on P-loaded $Mg(OH)_2$-decorated biochar, the bioavailability of P was shown to be high [194]. Post P-adsorption MgO decorated-biochar prepared at 400, 500, and 600 °C had bioavailable P contents of 82.5, 92.7, and 89.2 % respectively. However, Yao *et al*. reported only 19 % of P adsorbed by their Mg-decorated biochar to be bioavailable [173]. Despite a relatively small proportion of P in a bioavailable form, pot trials carried out over 13 days showed plants treated with P-laded biochar had improved seed germination and leaf growth of grass compared to control experiments. P-loaded $CaCO_3$ decorated-biochar was shown to increase both the fresh weight and dry weight of Spinacia grown for 15 days [91]. Increasing the content of $CaCO_3$ decorated-biochar did not have a significant effect on the weight of seedlings; however, when increasing biochar application from 0.25-0.5 wt%, more leaves could be seen to be present. Germination rate

was increased by 16.7 and 36.7 % compared to the control scenario for biochar application rates of 0.25 and 0.5 wt%, respectively. When P-laden CaO-decorated biochars P-loss and P-bioavailability were tested, the solubility of P in water was found to decrease with increasing Ca content; however, the availability of P was seen to increase [97]. Stem length and weight of plants were also seen to increase with increasing Ca content of P-laden Ca-biochar, after 14-day pot trials, reflecting trends in P adsorption. Improved plant growth using P-rich biochar over traditional chemical fertilisers has been reported. The treatment of soil with P-enriched MgO-decorated biochar has been shown to increase plant height and yield during pot trials of corn compared to both control samples and samples using chemical fertilisers after 31 days [195]. Similar results have been seen when using spent Mg-modified biochar enriched with phosphate from water sorption [196].

2.5.4 Summary

P-charged spent biochar has the potential for use in soil as a fertiliser replacement. Soil characteristics, such as soil pH and the presence of other nutrients, highly influence the availability of P in soil. Initial research into the use of P-laded Mg/Ca-decorated biochar is promising; however, relatively few studies have been carried out, with many critical research gaps still present. There is a lack of analysis on the effect of biochar's characteristics on P uptake by plants and the impact of chemically functionalised biochar on the soil system. The limited pot trials that have been carried out do not test for the leaching of compounds used to functionalise biochar into the soil system. Pot trials have been carried out over short time periods up to a month; however, there is a lack of research carrying out pot trials over a longer period spanning different life stages of the plant to examine the biochar's effect on overall plant growth, not just initial growth rate. Studies on spent biochars' P release or impact on plant growth utilise high concentrations of P, much higher than those seen in many eutrophic or wastewater systems.

2.6 Research Gaps and Novelties

2.6.1 Research Gaps

Much work has been carried out on utilising functionalised biochar for aqueous P recovery, with Mg and Ca decorated biochar showing particular promise. To advance the current state of research, the following key research gaps should be addressed:

- Previous studies in the literature have examined various functionalisation agents and functionalisation methods for biochars. It has been well established that the production of biochar for phosphorus removal involves both pyrolysis and functionalisation; however, the most effective approach to producing functionalised biochar with high P-removal remains uncertain.
- Numerous studies suggest that P-recovery is significantly influenced by the loading rate of the functionalisation agent and the pyrolysis temperature. However, the literature contains many conflicting reports regarding the precise effects of these conditions on the physicochemical properties of biochars and subsequent P-recovery. Additionally, there is a lack of research into the potential synergistic effects between chemical loading rates and pyrolysis temperatures.
- Leaching of metal cations from chemically functionalised biochars has been reported in the literature, including the leaching of metals traditionally used to remediate high levels of P in wastewater treatment works. However, the potential role of bulk precipitation in P-removal between aqueous P and metal cations leached from biochar has not been examined.
- The suitability of functionalised biochar for use in the remediation of eutrophic water and wastewater systems is often stated; however, there remains a lack of evidence provided in the literature. There is a lack of

studies conducted in water systems that replicate conditions of eutrophic and waste waters.

- Further work on P-laden functionalised biochars effect on plant growth and soil systems is required to prove its potential for use in a circular approach.

2.6.2 Research Novelties

The above-mentioned research gaps have been addressed in this thesis by carrying out the following work:

- To better understand the optimal production route for the creation of functionalised biochar for P-recovery, the performance of two high-performing functionalisation agents ($CaCl_2$ and $MgCl_2$) are compared at various CLR and pyrolysis temperatures. Furthermore, a comparison is provided on the effects of biomass impregnation versus biochar impregnation on the resulting chars' physicochemical characteristics and subsequent P recovery. The effects of two different particle size control methods are also examined.
- A Design of Experiments (DoE) methodology is used to examine the presence of any synergistic effects of CLR and pyrolysis temperature on biochars' physicochemical characteristics and P-recovery.
- The mechanisms of aqueous P-removal by functionalised biochar are examined, with a detailed analysis of P-removal pathways that highlights the roles of bulk precipitation and adsorption, including the factors influencing the dominance of each mechanism.
- The P-recovery of biochar in simulated water representative of real water systems is tested by examining the effects of initial pH, low initial P-concentration, and coexisting ions on P-recovery. The performance of biochar in a dynamic column is also tested.

- Pot trials using spent P-charged biochar are conducted to provide longer-term plant growth studies than those currently available in literature and examine the effect of biochar on bioavailability of P in soil.

References

[1] K. P. Kumar and N. Remya, “Technoeconomic analysis of biofuel production from agricultural residues through pyrolysis,” *Green Approach to Alternative Fuel for a Sustainable Future*, pp. 463–469, Jan. 2023, doi: 10.1016/B978-0-12-824318-3.00001-1.

[2] M. S. Safdari *et al.*, “Characterization of pyrolysis products from fast pyrolysis of live and dead vegetation native to the Southern United States,” *Fuel*, vol. 229, pp. 151–166, Oct. 2018, doi: 10.1016/J.FUEL.2018.04.166.

[3] S. A. El-Sayed, T. M. Khass, and M. E. Mostafa, “Thermal degradation behaviour and chemical kinetic characteristics of biomass pyrolysis using TG/DTG/DTA techniques,” *Biomass Conversion and Biorefinery 2023 14:15*, vol. 14, no. 15, pp. 17779–17803, Feb. 2023, doi: 10.1007/S13399-023-03926-2.

[4] M. B. Pecha and M. Garcia-Perez, “Pyrolysis of lignocellulosic biomass: oil, char, and gas,” *Bioenergy: Biomass to Biofuels and Waste to Energy*, pp. 581–619, Jan. 2020, doi: 10.1016/B978-0-12-815497-7.00029-4.

[5] J. Cai and R. Liu, “Research on Water Evaporation in the Process of Biomass Pyrolysis,” *Energy and Fuels*, vol. 21, no. 6, pp. 3695–3697, Nov. 2007, doi: 10.1021/EF700442N.

[6] M. A. Saeed, G. E. Andrews, H. N. Phylaktou, and B. M. Gibbs, “Global kinetics of the rate of volatile release from biomasses in comparison to coal,” *Fuel*, vol. 181, pp. 347–357, Oct. 2016, doi: 10.1016/J.FUEL.2016.04.123.

[7] D. Chen *et al.*, “Insight into biomass pyrolysis mechanism based on cellulose, hemicellulose, and lignin: Evolution of volatiles and kinetics, elucidation of reaction pathways, and characterization of gas, biochar and bio-oil,” *Combust Flame*, vol. 242, p. 112142, Aug. 2022, doi: 10.1016/J.COMBUSTFLAME.2022.112142.

[8] Y. Zhu *et al.*, “Effects of volatile-char interaction on the product properties from municipal sludge pyrolysis,” *Fuel*, vol. 335, p. 126936, Mar. 2023, doi: 10.1016/J.FUEL.2022.126936.

[9] H. Yang, S. Kudo, S. Hazeyama, K. Norinaga, O. Mašek, and J. I. Hayashi, “Detailed Analysis of Residual Volatiles in Chars from the Pyrolysis of

Biomass and Lignite," *Energy and Fuels*, vol. 27, no. 6, pp. 3209–3223, Jun. 2013, doi: 10.1021/EF4001192.

[10] T. A. Saleh, "Adsorption technology and surface science," in *Interface Science and Technology*, vol. 34, Elsevier, 2022, pp. 39–64. doi: 10.1016/B978-0-12-849876-7.00006-3.

[11] L. Leng *et al.*, "An overview on engineering the surface area and porosity of biochar," *Science of the Total Environment*, vol. 763, Apr. 2021, doi: 10.1016/J.SCITOTENV.2020.144204.

[12] S. P. Singh Yadav *et al.*, "Biochar application: A sustainable approach to improve soil health," *J Agric Food Res*, vol. 11, p. 100498, Mar. 2023, doi: 10.1016/J.JAFR.2023.100498.

[13] F. Tesfaye *et al.*, "Could biochar amendment be a tool to improve soil availability and plant uptake of phosphorus? A meta-analysis of published experiments," *Environ Sci Pollut Res Int*, vol. 28, no. 26, p. 34108, Jul. 2021, doi: 10.1007/S11356-021-14119-7.

[14] C. Strangfeld, P. Wiehle, and S. M. Munsch, "About the dominance of mesopores in physisorption in amorphous materials," *Molecules*, vol. 26, no. 23, Dec. 2021, doi: 10.3390/molecules26237190.

[15] P. Suresh Kumar, L. Korving, K. J. Keesman, M. C. M. van Loosdrecht, and G. J. Witkamp, "Effect of pore size distribution and particle size of porous metal oxides on phosphate adsorption capacity and kinetics," *Chemical Engineering Journal*, vol. 358, pp. 160–169, Feb. 2019, doi: 10.1016/J.CEJ.2018.09.202.

[16] L. Xue *et al.*, "High efficiency and selectivity of MgFe-LDH modified wheat-straw biochar in the removal of nitrate from aqueous solutions," *J Taiwan Inst Chem Eng*, vol. 63, pp. 312–317, Jun. 2016, doi: 10.1016/J.JTICE.2016.03.021.

[17] W. Chesworth, "Water holding capacity," in *Enciclopedia of Soil Science*, Springer, Dordrecht, 2008, pp. 822–822. doi: 10.1007/978-1-4020-3995-9_627.

[18] E. Cristiano, Y. J. Hu, M. Siegfried, D. Kaplan, and H. Nitsche, "A comparison of point of zero charge measurement methodology," *Clays Clay Miner*, vol. 59, no. 2, pp. 107–115, Apr. 2011, doi: 10.1346/CCMN.2011.0590201/METRICS.

[19] L. Ghodszad, A. Reyhanitabar, M. R. Maghsoodi, B. Asgari Lajayer, and S. X. Chang, “Biochar affects the fate of phosphorus in soil and water: A critical review,” Nov. 01, 2021, *Elsevier Ltd*. doi: 10.1016/j.chemosphere.2021.131176.

[20] M. Zhang *et al.*, “Evaluating biochar and its modifications for the removal of ammonium, nitrate, and phosphate in water,” *Water Res*, vol. 186, p. 116303, Nov. 2020, doi: 10.1016/J.WATRES.2020.116303.

[21] M. Fan, C. Li, Y. Shao, S. Zhang, M. Gholizadeh, and X. Hu, “Pyrolysis of cellulose: Correlation of hydrophilicity with evolution of functionality of biochar,” *Science of The Total Environment*, vol. 825, p. 153959, Jun. 2022, doi: 10.1016/J.SCITOTENV.2022.153959.

[22] P. R. Yaashikaa, P. S. Kumar, S. Varjani, and A. Saravanan, “A critical review on the biochar production techniques, characterization, stability and applications for circular bioeconomy,” *Biotechnology Reports*, vol. 28, p. e00570, Dec. 2020, doi: 10.1016/J.BTRE.2020.E00570.

[23] X. Zhang, “Essential scientific mapping of the value chain of thermochemically converted second-generation bio-fuels,” *Green Chemistry*, vol. 18, no. 19, pp. 5086–5117, Sep. 2016, doi: 10.1039/C6GC02335E.

[24] B. Ercan, K. Alper, S. Ucar, and S. Karagoz, “Comparative studies of hydrochars and biochars produced from lignocellulosic biomass via hydrothermal carbonization, torrefaction and pyrolysis,” *Journal of the Energy Institute*, vol. 109, p. 101298, Aug. 2023, doi: 10.1016/J.JOEI.2023.101298.

[25] F. Amalina, A. S. A. Razak, S. Krishnan, H. Sulaiman, A. W. Zularisam, and M. Nasrullah, “Biochar production techniques utilizing biomass waste-derived materials and environmental applications – A review,” *Journal of Hazardous Materials Advances*, vol. 7, p. 100134, Aug. 2022, doi: 10.1016/J.HAZADV.2022.100134.

[26] A. Tomczyk, Z. Sokołowska, and P. Boguta, “Biochar physicochemical properties: pyrolysis temperature and feedstock kind effects,” *Rev Environ Sci Biotechnol*, vol. 19, no. 1, pp. 191–215, Mar. 2020, doi: 10.1007/S11157-020-09523-3/TABLES/3.

[27] W. Barszcz, M. Łożyńska, and J. Molenda, “Impact of pyrolysis process conditions on the structure of biochar obtained from apple waste,” *Sci*

Rep, vol. 14, no. 1, p. 10501, Dec. 2024, doi: 10.1038/S41598-024-61394-8.

[28] P. Zhang, H. Sun, L. Yu, and T. Sun, "Adsorption and catalytic hydrolysis of carbaryl and atrazine on pig manure-derived biochars: Impact of structural properties of biochars," *J Hazard Mater*, vol. 244–245, pp. 217–224, Jan. 2013, doi: 10.1016/J.JHAZMAT.2012.11.046.

[29] M. Keiluweit, P. S. Nico, M. Johnson, and M. Kleber, "Dynamic molecular structure of plant biomass-derived black carbon (biochar)," *Environ Sci Technol*, vol. 44, no. 4, pp. 1247–1253, 2010, doi: 10.1021/ES9031419/SUPPL_FILE/ES9031419_SI_001.PDF.

[30] M. Zhang *et al.*, "Evaluating biochar and its modifications for the removal of ammonium, nitrate, and phosphate in water," *Water Res*, vol. 186, p. 116303, Nov. 2020, doi: 10.1016/J.WATRES.2020.116303.

[31] L. Zhou *et al.*, "Phosphorus and nitrogen adsorption capacities of biochars derived from feedstocks at different pyrolysis temperatures," *Water (Switzerland)*, vol. 11, no. 8, 2019, doi: 10.3390/w11081559.

[32] Y. Zhao, H. Yang, S. Xia, and Z. Wu, "Removal of ammonia nitrogen, nitrate, and phosphate from aqueous solution using biochar derived from Thalia dealbata Fraser: effect of carbonization temperature," *Environmental Science and Pollution Research*, pp. 1–17, Mar. 2022, doi: 10.1007/S11356-022-19870-Z/TABLES/14.

[33] K. Yadav and S. Jagadevan, "Influence of Process Parameters on Synthesis of Biochar by Pyrolysis of Biomass: An Alternative Source of Energy," *Recent Advances in Pyrolysis*, Jan. 2020, doi: 10.5772/INTECHOPEN.88204.

[34] H. Haykiri-Acma, S. Yaman, and S. Kucukbayrak, "Effect of heating rate on the pyrolysis yields of rapeseed," *Renew Energy*, vol. 31, no. 6, pp. 803–810, May 2006, doi: 10.1016/J.RENENE.2005.03.013.

[35] E. Cetin, B. Moghtaderi, R. Gupta, and T. F. Wall, "Influence of pyrolysis conditions on the structure and gasification reactivity of biomass chars," *Fuel*, vol. 83, no. 16, pp. 2139–2150, Nov. 2004, doi: 10.1016/J.FUEL.2004.05.008.

[36] D. Angin, "Effect of pyrolysis temperature and heating rate on biochar obtained from pyrolysis of safflower seed press cake," *Bioresour Technol*, vol. 128, pp. 593–597, Jan. 2013, doi: 10.1016/J.BIORTECH.2012.10.150.

[37] S. Yavari, A. Malakahmad, N. B. Sapari, and S. Yavari, “Sorption properties optimization of agricultural wastes-derived biochars using response surface methodology,” *Process Safety and Environmental Protection*, vol. 109, pp. 509–519, Jul. 2017, doi: 10.1016/J.PSEP.2017.05.002.

[38] R. S and B. P, “The potential of lignocellulosic biomass precursors for biochar production: Performance, mechanism and wastewater application—A review,” *Ind Crops Prod*, vol. 128, pp. 405–423, Feb. 2019, doi: 10.1016/J.INDCROP.2018.11.041.

[39] B. Zhao *et al.*, “Effect of pyrolysis temperature, heating rate, and residence time on rapeseed stem derived biochar,” *J Clean Prod*, vol. 174, pp. 977–987, Feb. 2018, doi: 10.1016/J.JCLEPRO.2017.11.013.

[40] M. Tripathi, J. N. Sahu, and P. Ganesan, “Effect of process parameters on production of biochar from biomass waste through pyrolysis: A review,” *Renewable and Sustainable Energy Reviews*, vol. 55, pp. 467–481, Mar. 2016, doi: 10.1016/J.RSER.2015.10.122.

[41] H. Zhang, R. Xiao, H. Huang, and G. Xiao, “Comparison of non-catalytic and catalytic fast pyrolysis of corncob in a fluidized bed reactor,” *Bioresour Technol*, vol. 100, no. 3, pp. 1428–1434, Feb. 2009, doi: 10.1016/J.BIORTECH.2008.08.031.

[42] M. Ertaş and M. Hakki Alma, “Pyrolysis of laurel (Laurus nobilis L.) extraction residues in a fixed-bed reactor: Characterization of bio-oil and bio-char,” *J Anal Appl Pyrolysis*, vol. 88, no. 1, pp. 22–29, May 2010, doi: 10.1016/J.JAAP.2010.02.006.

[43] A. C. Lua, F. Y. Lau, and J. Guo, “Influence of pyrolysis conditions on pore development of oil-palm-shell activated carbons,” *J Anal Appl Pyrolysis*, vol. 76, no. 1–2, pp. 96–102, Jun. 2006, doi: 10.1016/J.JAAP.2005.08.001.

[44] A. Al-Rumaihi, M. Shahbaz, G. Mckay, H. Mackey, and T. Al-Ansari, “A review of pyrolysis technologies and feedstock: A blending approach for plastic and biomass towards optimum biochar yield,” *Renewable and Sustainable Energy Reviews*, vol. 167, p. 112715, Oct. 2022, doi: 10.1016/J.RSER.2022.112715.

[45] M. Pahnila, A. Koskela, P. Sulasalmi, and T. Fabritius, “A Review of Pyrolysis Technologies and the Effect of Process Parameters on Biocarbon Properties,” *Energies 2023, Vol. 16, Page 6936*, vol. 16, no. 19, p. 6936, Oct. 2023, doi: 10.3390/EN16196936.

[46] P. A. Brownsort, “Biomass Pyrolysis Processes: Review of Scope, Control and Variability,” 2009.

[47] E. Cetin, R. Gupta, and B. Moghtaderi, “Effect of pyrolysis pressure and heating rate on radiata pine char structure and apparent gasification reactivity,” *Fuel*, vol. 84, no. 10, pp. 1328–1334, Jul. 2005, doi: 10.1016/J.FUEL.2004.07.016.

[48] F. Melligan, R. Auccaise, E. H. Novotny, J. J. Leahy, M. H. B. Hayes, and W. Kwapinski, “Pressurised pyrolysis of Miscanthus using a fixed bed reactor,” *Bioresour Technol*, vol. 102, no. 3, pp. 3466–3470, Feb. 2011, doi: 10.1016/J.BIORTECH.2010.10.129.

[49] X. Wang, Z. Guo, Z. Hu, and J. Zhang, “Recent advances in biochar application for water and wastewater treatment: a review,” *PeerJ*, vol. 8, p. e9164, May 2020, doi: 10.7717/PEERJ.9164.

[50] M. Z. Yameen, S. R. Naqvi, D. Juchelková, and M. N. A. Khan, “Harnessing the power of functionalized biochar: progress, challenges, and future perspectives in energy, water treatment, and environmental sustainability,” *Biochar 2024 6:1*, vol. 6, no. 1, pp. 25-, Mar. 2024, doi: 10.1007/S42773-024-00316-3.

[51] T. Vijay *et al.*, “Scotland’s Rural College Phosphorus adsorption by functionalized biochar Phosphorus adsorption by functionalized biochar: a review,” *Environ Chem Lett*, doi: 10.1007/s10311-022-01519-5.

[52] A. Fakhar, R. C. Canatoy, S. J. C. Galgo, M. Rafique, and R. Sarfraz, “Advancements in modified biochar production techniques and soil application: a critical review,” *Fuel*, vol. 400, p. 135745, Nov. 2025, doi: 10.1016/J.FUEL.2025.135745.

[53] M. L. Free, “Speciation and Phase Diagrams,” *Minerals, Metals and Materials Series*, pp. 69–88, 2022, doi: 10.1007/978-3-030-88087-3_3/FIGURES/9.

[54] J. A. Raven, C. J. Gobler, and P. J. Hansen, “Dynamic CO2 and pH levels in coastal, estuarine, and inland waters: Theoretical and observed effects on harmful algal blooms,” *Harmful Algae*, vol. 91, p. 101594, Jan. 2020, doi: 10.1016/J.HAL.2019.03.012.

[55] J. M. H. Verspagen, D. B. Van De Waal, J. F. Finke, P. M. Visser, E. Van Donk, and J. Huisman, “Rising CO2 Levels Will Intensify Phytoplankton Blooms

in Eutrophic and Hypertrophic Lakes," *PLoS One*, vol. 9, no. 8, p. e104325, Aug. 2014, doi: 10.1371/JOURNAL.PONE.0104325.

[56] I. W. Almanassra, G. Mckay, V. Kochkodan, M. Ali Atieh, and T. Al-Ansari, "A state of the art review on phosphate removal from water by biochars," *Chemical Engineering Journal*, vol. 409, p. 128211, Apr. 2021, doi: 10.1016/J.CEJ.2020.128211.

[57] Q. Yin, R. Wang, and Z. Zhao, "Application of Mg–Al-modified biochar for simultaneous removal of ammonium, nitrate, and phosphate from eutrophic water," *J Clean Prod*, vol. 176, pp. 230–240, Mar. 2018, doi: 10.1016/J.JCLEPRO.2017.12.117.

[58] R. Li *et al.*, "Recovery of phosphate from aqueous solution by magnesium oxide decorated magnetic biochar and its potential as phosphate-based fertilizer substitute," *Bioresour Technol*, vol. 215, pp. 209–214, Sep. 2016, doi: 10.1016/J.BIORTECH.2016.02.125.

[59] A. Nayak, B. Bhushan, V. Gupta, and S. Kotnala, "Fabrication of microwave assisted biogenic magnetite-biochar nanocomposite: A green adsorbent from jackfruit peel for removal and recovery of nutrients in water sample," *Journal of Industrial and Engineering Chemistry*, vol. 100, pp. 134–148, Aug. 2021, doi: 10.1016/J.JIEC.2021.05.028.

[60] T. Van Truong, Y. J. Kim, and D. J. Kim, "Study of biochar impregnated with Al recovered from water sludge for phosphate adsorption/desorption," *J Clean Prod*, vol. 383, p. 135507, Jan. 2023, doi: 10.1016/J.JCLEPRO.2022.135507.

[61] Q. Yin, H. Ren, R. Wang, and Z. Zhao, "Evaluation of nitrate and phosphate adsorption on Al-modified biochar: Influence of Al content," *Science of The Total Environment*, vol. 631–632, pp. 895–903, Aug. 2018, doi: 10.1016/J.SCITOTENV.2018.03.091.

[62] K. W. Jung, M. J. Hwang, T. U. Jeong, and K. H. Ahn, "A novel approach for preparation of modified-biochar derived from marine macroalgae: Dual purpose electro-modification for improvement of surface area and metal impregnation," *Bioresour Technol*, vol. 191, pp. 342–345, Sep. 2015, doi: 10.1016/J.BIORTECH.2015.05.052.

[63] K. W. Jung, T. U. Jeong, M. J. Hwang, K. Kim, and K. H. Ahn, "Phosphate adsorption ability of biochar/Mg–Al assembled nanocomposites prepared by aluminum-electrode based electro-assisted modification method with

MgCl2 as electrolyte," *Bioresour Technol*, vol. 198, pp. 603–610, Dec. 2015, doi: 10.1016/J.BIORTECH.2015.09.068.

[64] Y. Peng, Y. Sun, R. Sun, Y. Zhou, D. C. W. Tsang, and Q. Chen, "Optimizing the synthesis of Fe/Al (Hydr)oxides-Biochars to maximize phosphate removal via response surface model," *J Clean Prod*, vol. 237, p. 117770, Nov. 2019, doi: 10.1016/J.JCLEPRO.2019.117770.

[65] G. Peng *et al.*, "Synthesis of Mn/Al double oxygen biochar from dewatered sludge for enhancing phosphate removal," *J Clean Prod*, vol. 251, p. 119725, Apr. 2020, doi: 10.1016/J.JCLEPRO.2019.119725.

[66] E. Bojórquez-Quintal, C. Escalante-Magaña, I. Echevarría-Machado, and M. Martínez-Estévez, "Aluminum, a friend or foe of higher plants in acid soils," *Front Plant Sci*, vol. 8, p. 1767, Oct. 2017, doi: 10.3389/FPLS.2017.01767/BIBTEX.

[67] R. Shetty, C. S. N. Vidya, N. B. Prakash, A. Lux, and M. Vaculík, "Aluminum toxicity in plants and its possible mitigation in acid soils by biochar: A review," *Science of the Total Environment*, vol. 765, Apr. 2021, doi: 10.1016/J.SCITOTENV.2020.142744.

[68] Q. Tang *et al.*, "Preferable phosphate removal by nano-La(III) hydroxides modified mesoporous rice husk biochars: Role of the host pore structure and point of zero charge," *Science of The Total Environment*, vol. 662, pp. 511–520, Apr. 2019, doi: 10.1016/J.SCITOTENV.2019.01.159.

[69] Q. Xu *et al.*, "Novel lanthanum doped biochars derived from lignocellulosic wastes for efficient phosphate removal and regeneration," *Bioresour Technol*, vol. 289, p. 121600, Oct. 2019, doi: 10.1016/J.BIORTECH.2019.121600.

[70] Z. Jia, W. Zeng, H. Xu, S. Li, and Y. Peng, "Adsorption removal and reuse of phosphate from wastewater using a novel adsorbent of lanthanum-modified platanus biochar," *Process Safety and Environmental Protection*, vol. 140, pp. 221–232, Aug. 2020, doi: 10.1016/J.PSEP.2020.05.017.

[71] Z. Elkhlifi *et al.*, "Lanthanum hydroxide engineered sewage sludge biochar for efficient phosphate elimination: Mechanism interpretation using physical modelling," *Science of The Total Environment*, vol. 803, p. 149888, Jan. 2022, doi: 10.1016/J.SCITOTENV.2021.149888.

[72] I. Fastovets, A. Kotelnikova, O. Rogova, N. Sushkov, and P. Elena, “Effects of soil lanthanum on growth and elemental composition of plants,” *Geophysical Research Abstracts*, vol. 19, pp. 2017–305, 2017.

[73] E. Diatloff, F. W. Smith, and C. J. Asher, “Effects of Lanthanum and Cerium on the Growth and Mineral Nutrition of Corn and Mungbean,” *Ann Bot*, vol. 101, no. 7, p. 971, May 2008, doi: 10.1093/AOB/MCN021.

[74] A. García-Jiménez, F. C. Gómez-Merino, O. Tejeda-Sartorius, and L. I. Trejo-Téllez, “Lanthanum affects bell pepper seedling quality depending on the genotype and time of exposure by differentially modifying plant height, stem diameter and concentrations of chlorophylls, sugars, amino acids, and proteins,” *Front Plant Sci*, vol. 8, p. 308, Mar. 2017, doi: 10.3389/FPLS.2017.00308/BIBTEX.

[75] S. Von Tucher and U. Schmidhalter, “Lanthanum uptake from soil and nutrient solution and its effects on plant growth,” *Journal of Plant Nutrition and Soil Science*, vol. 168, no. 4, pp. 574–580, Aug. 2005, doi: 10.1002/JPLN.200520506.

[76] “Critical raw materials - Internal Market, Industry, Entrepreneurship and SMEs.” Accessed: Dec. 04, 2025. [Online]. Available: https://single-market-economy.ec.europa.eu/sectors/raw-materials/areas-specific-interest/critical-raw-materials_en

[77] Q. Yin, M. Liu, and H. Ren, “Removal of Ammonium and Phosphate from Water by Mg-modified Biochar: Influence of Mg pretreatment and Pyrolysis Temperature”.

[78] P. Wang, M. Zhi, G. Cui, Z. Chu, and S. Wang, “A comparative study on phosphate removal from water using Phragmites australis biochars loaded with different metal oxides,” 2021, doi: 10.1098/rsos.201789.

[79] R. Li *et al.*, “Simultaneous capture removal of phosphate, ammonium and organic substances by MgO impregnated biochar and its potential use in swine wastewater treatment,” *J Clean Prod*, vol. 147, pp. 96–107, Mar. 2017, doi: 10.1016/J.JCLEPRO.2017.01.069.

[80] G. Cai and Z. long Ye, “Concentration-dependent adsorption behaviors and mechanisms for ammonium and phosphate removal by optimized Mg-impregnated biochar,” *J Clean Prod*, vol. 349, p. 131453, May 2022, doi: 10.1016/J.JCLEPRO.2022.131453.

[81] S. Xu *et al.*, “Solvent-Free Synthesis of MgO-Modified Biochars for Phosphorus Removal from Wastewater,” *Int J Environ Res Public Health*, vol. 19, no. 13, p. 7770, Jul. 2022, doi: 10.3390/IJERPH19137770/S1.

[82] C. Fang, T. Zhang, P. Li, R. F. Jiang, and Y. C. Wang, “Application of Magnesium Modified Corn Biochar for Phosphorus Removal and Recovery from Swine Wastewater,” *Int J Environ Res Public Health*, vol. 11, no. 9, p. 9217, Sep. 2014, doi: 10.3390/IJERPH110909217.

[83] S. V. Novais, M. D. O. Zenero, J. Tronto, R. F. Conz, and C. E. P. Cerri, “Poultry manure and sugarcane straw biochars modified with MgCl2 for phosphorus adsorption,” *J Environ Manage*, vol. 214, pp. 36–44, May 2018, doi: 10.1016/J.JENVMAN.2018.02.088.

[84] M. Zhang, B. Gao, Y. Yao, Y. Xue, and M. Inyang, “Synthesis of porous MgO-biochar nanocomposites for removal of phosphate and nitrate from aqueous solutions,” *Chemical Engineering Journal*, vol. 210, pp. 26–32, Nov. 2012, doi: 10.1016/j.cej.2012.08.052.

[85] C. Y. Wang, Q. Wang, H. D. Zhou, X. Fang, Q. Zeng, and G. Zhu, “Adsorption of phosphate over a novel magnesium-loaded sludge-based biochar,” *PLoS One*, vol. 19, no. 4, p. e0301986, Apr. 2024, doi: 10.1371/JOURNAL.PONE.0301986.

[86] Y. H. Jiang *et al.*, “Characteristics of nitrogen and phosphorus adsorption by Mg-loaded biochar from different feedstocks,” *Bioresour Technol*, vol. 276, pp. 183–189, Mar. 2019, doi: 10.1016/J.BIORTECH.2018.12.079.

[87] C. Tan *et al.*, “Structurally improved MgO adsorbents derived from magnesium oxalate precursor for enhanced CO2 capture,” *Fuel*, vol. 278, p. 118379, Oct. 2020, doi: 10.1016/J.FUEL.2020.118379.

[88] H. N. Mcmurray, G. Williams, J. E. Board, B. Yan, and Y. Hou, “Effect of Soil Magnesium on Plants: a Review,” *IOP Conf Ser Earth Environ Sci*, vol. 170, no. 2, p. 022168, Jul. 2018, doi: 10.1088/1755-1315/170/2/022168.

[89] Z. Wang, M. U. Hassan, F. Nadeem, L. Wu, F. Zhang, and X. Li, “Magnesium Fertilization Improves Crop Yield in Most Production Systems: A Meta-Analysis,” *Front Plant Sci*, vol. 10, p. 1727, Jan. 2020, doi: 10.3389/FPLS.2019.01727/BIBTEX.

[90] A. Gransee and H. Führs, “Magnesium mobility in soils as a challenge for soil and plant analysis, magnesium fertilization and root uptake under

adverse growth conditions," *Plant Soil*, vol. 368, no. 1–2, pp. 5–21, Jul. 2013, doi: 10.1007/S11104-012-1567-Y/FIGURES/5.

[91] Y. Xu *et al.*, "A Novel Ca-Modified Biochar for Efficient Recovery of Phosphorus from Aqueous Solution and Its Application as a Phosphorus Biofertilizer," *Nanomaterials 2022, Vol. 12, Page 2755*, vol. 12, no. 16, p. 2755, Aug. 2022, doi: 10.3390/NANO12162755.

[92] M. Feng *et al.*, "Oyster Shell Modified Tobacco Straw Biochar: Efficient Phosphate Adsorption at Wide Range of pH Values," *International Journal of Environmental Research and Public Health 2022, Vol. 19, Page 7227*, vol. 19, no. 12, p. 7227, Jun. 2022, doi: 10.3390/IJERPH19127227.

[93] H. Cao *et al.*, "Characteristics and mechanisms of phosphorous adsorption by rape straw-derived biochar functionalized with calcium from eggshell," *Bioresour Technol*, vol. 318, p. 124063, Dec. 2020, doi: 10.1016/J.BIORTECH.2020.124063.

[94] Y. Feng *et al.*, "Adsorption of Phosphate in Aqueous Phase by Biochar Prepared from Sheep Manure and Modified by Oyster Shells," *ACS Omega*, vol. 6, no. 48, p. 33046, Dec. 2021, doi: 10.1021/ACSOMEGA.1C05191.

[95] J. Yang, M. Zhang, H. Wang, J. Xue, Q. Lv, and G. Pang, "Efficient recovery of phosphate from aqueous solution using biochar derived from co-pyrolysis of sewage sludge with eggshell," *J Environ Chem Eng*, vol. 9, no. 5, p. 105354, Oct. 2021, doi: 10.1016/J.JECE.2021.105354.

[96] S. Wang *et al.*, "Adsorption of phosphorus by calcium-flour biochar: Isotherm, kinetic and transformation studies," *Chemosphere*, vol. 195, pp. 666–672, Mar. 2018, doi: 10.1016/J.CHEMOSPHERE.2017.12.101.

[97] D. Ai, H. Ma, Y. Meng, T. Wei, and B. Wang, "Phosphorus recovery and reuse in water bodies with simple ball-milled Ca-loaded biochar," *Science of The Total Environment*, vol. 860, p. 160502, Feb. 2023, doi: 10.1016/J.SCITOTENV.2022.160502.

[98] S. Zeng and E. Kan, "Sustainable use of Ca(OH)2 modified biochar for phosphorus recovery and tetracycline removal from water," *Science of The Total Environment*, vol. 839, p. 156159, Sep. 2022, doi: 10.1016/J.SCITOTENV.2022.156159.

[99] X. Liu, F. Shen, R. L. Smith, and X. Qi, "Black liquor-derived calcium-activated biochar for recovery of phosphate from aqueous solutions,"

Bioresour Technol, vol. 294, p. 122198, Dec. 2019, doi: 10.1016/J.BIORTECH.2019.122198.

[100] S. B. Liu *et al.*, "Production of biochars from Ca impregnated ramie biomass (Boehmeria nivea (L.) Gaud.) and their phosphate removal potential," *RSC Adv*, vol. 6, no. 7, pp. 5871–5880, Jan. 2016, doi: 10.1039/C5RA22142K.

[101] X. Liu and J. Lv, "Efficient Phosphate Removal from Wastewater by Ca-Laden Biochar Composites Prepared from Eggshell and Peanut Shells: A Comparison of Methods," *Sustainability (Switzerland)*, vol. 15, no. 3, p. 1778, Feb. 2023, doi: 10.3390/SU15031778/S1.

[102] S. Saadat, E. Raei, and N. Talebbeydokhti, "Enhanced removal of phosphate from aqueous solutions using a modified sludge derived biochar: Comparative study of various modifying cations and RSM based optimization of pyrolysis parameters," *J Environ Manage*, vol. 225, pp. 75–83, Nov. 2018, doi: 10.1016/J.JENVMAN.2018.07.037.

[103] K. Thor, "Calcium—nutrient and messenger," *Front Plant Sci*, vol. 10, p. 440, Apr. 2019, doi: 10.3389/FPLS.2019.00440/BIBTEX.

[104] T.-W. Liu *et al.*, "Effects of calcium on seed germination, seedling growth and photosynthesis of six forest tree species under simulated acid rain," *Tree Physiol*, vol. 31, pp. 402–413, 2011, doi: 10.1093/treephys/tpr019.

[105] M. Á. Olego, M. J. Quiroga, C. Mendaña-Cuervo, J. Cara-Jiménez, R. López, and E. Garzón-Jimeno, "Long-Term Effects of Calcium-Based Liming Materials on Soil Fertility Sustainability and Rye Production as Soil Quality Indicators on a Typic Palexerult," *Processes 2021, Vol. 9, Page 1181*, vol. 9, no. 7, p. 1181, Jul. 2021, doi: 10.3390/PR9071181.

[106] A. Mosa, A. El-Ghamry, and M. Tolba, "Functionalized biochar derived from heavy metal rich feedstock: Phosphate recovery and reusing the exhausted biochar as an enriched soil amendment," *Chemosphere*, vol. 198, pp. 351–363, May 2018, doi: 10.1016/J.CHEMOSPHERE.2018.01.113.

[107] S. Alejandro, S. Höller, B. Meier, and E. Peiter, "Manganese in Plants: From Acquisition to Subcellular Allocation," *Front Plant Sci*, vol. 11, p. 300, Mar. 2020, doi: 10.3389/FPLS.2020.00300/BIBTEX.

[108] T. C. F. Silva, L. Vergütz, A. A. Pacheco, L. F. Melo, N. S. Renato, and L. C. A. Melo, "Characterization and application of magnetic biochar for the

removal of phosphorus from water," *An Acad Bras Cienc*, vol. 92, no. 3, pp. 1–13, 2020, doi: 10.1590/0001-3765202020190440.

[109] Z. Zhang, H. Yu, R. Zhu, X. Zhang, and L. Yan, "Phosphate adsorption performance and mechanisms by nanoporous biochar-iron oxides from aqueous solutions", doi: 10.1007/s11356-020-09166-5.

[110] Z. Zhang, H. Yu, R. Zhu, X. Zhang, and L. Yan, "Phosphate adsorption performance and mechanisms by nanoporous biochar–iron oxides from aqueous solutions," *Environmental Science and Pollution Research*, vol. 27, no. 22, pp. 28132–28145, Aug. 2020, doi: 10.1007/S11356-020-09166-5/FIGURES/7.

[111] Z. Ajmal, A. Muhmood, R. Dong, and S. Wu, "Probing the efficiency of magnetically modified biomass-derived biochar for effective phosphate removal," *J Environ Manage*, vol. 253, p. 109730, Jan. 2020, doi: 10.1016/J.JENVMAN.2019.109730.

[112] H. Zhou, Z. Jiang, and S. Wei, "A Novel Absorbent of Nano-Fe Loaded Biomass Char and Its Enhanced Adsorption Capacity for Phosphate in Water," *J Chem*, vol. 2013, no. 1, p. 649868, Jan. 2013, doi: 10.1155/2013/649868.

[113] Z. Zhu, C. P. Huang, Y. Zhu, W. Wei, and H. Qin, "A hierarchical porous adsorbent of nano-α-Fe2O3/Fe3O4 on bamboo biochar (HPA-Fe/C-B) for the removal of phosphate from water," *Journal of Water Process Engineering*, vol. 25, pp. 96–104, Oct. 2018, doi: 10.1016/J.JWPE.2018.05.010.

[114] J. Jack, T. M. Huggins, Y. Huang, Y. Fang, and Z. J. Ren, "Production of magnetic biochar from waste-derived fungal biomass for phosphorus removal and recovery," *J Clean Prod*, vol. 224, pp. 100–106, Jul. 2019, doi: 10.1016/J.JCLEPRO.2019.03.120.

[115] T. Zhang, H. Xu, H. Li, X. He, Y. Shi, and A. Kruse, "Microwave digestion-assisted HFO/biochar adsorption to recover phosphorus from swine manure," *Science of The Total Environment*, vol. 621, pp. 1512–1526, Apr. 2018, doi: 10.1016/J.SCITOTENV.2017.10.077.

[116] L. Zhu, L. Tong, N. Zhao, J. Li, and Y. Lv, "Coupling interaction between porous biochar and nano zero valent iron/nano α-hydroxyl iron oxide improves the remediation efficiency of cadmium in aqueous solution,"

Chemosphere, vol. 219, pp. 493–503, Mar. 2019, doi: 10.1016/J.CHEMOSPHERE.2018.12.013.

[117] X. Liu *et al.*, "Feasibility of nanoscale zerovalent iron-loaded sediment-based biochar (nZVI-SBC) for simultaneous removal of nitrate and phosphate: high selectivity toward dinitrogen and synergistic mechanism", doi: 10.1007/s11356-021-13322-w/Published.

[118] F. Ma, B. Zhao, J. Diao, Y. Jiang, and J. Zhang, "Mechanism of phosphate removal from aqueous solutions by biochar supported nanoscale zero-valent iron," *RSC Adv*, vol. 10, no. 64, pp. 39217–39225, Oct. 2020, doi: 10.1039/D0RA07391A.

[119] L. Ren *et al.*, "Recovery of phosphorus from eutrophic water using nano zero-valent iron-modified biochar and its utilization," *Chemosphere*, vol. 284, p. 131391, Dec. 2021, doi: 10.1016/J.CHEMOSPHERE.2021.131391.

[120] D. Ai, T. Wei, Y. Meng, X. Chen, and B. Wang, "Ball milling sulfur-doped nano zero-valent iron @biochar composite for the efficient removal of phosphorus from water: Performance and mechanisms," *Bioresour Technol*, vol. 357, p. 127316, Aug. 2022, doi: 10.1016/J.BIORTECH.2022.127316.

[121] S. Wu *et al.*, "Nano zero-valent iron aging interacts with the soil microbial community: a microcosm study," *Environ Sci Nano*, vol. 6, no. 4, pp. 1189–1206, Apr. 2019, doi: 10.1039/C8EN01328D.

[122] S. Mallakpour and E. Khadem, "Polymer layered double hydroxide hybrid nanocomposites," *Layered Double Hydroxide Polymer Nanocomposites*, pp. 531–564, Jan. 2020, doi: 10.1016/B978-0-08-101903-0.00013-1.

[123] R. Li *et al.*, "Enhancing phosphate adsorption by Mg/Al layered double hydroxide functionalized biochar with different Mg/Al ratios," *Science of The Total Environment*, vol. 559, pp. 121–129, Jul. 2016, doi: 10.1016/J.SCITOTENV.2016.03.151.

[124] S. Wan, S. Wang, Y. Li, and B. Gao, "Functionalizing biochar with Mg–Al and Mg–Fe layered double hydroxides for removal of phosphate from aqueous solutions," *Journal of Industrial and Engineering Chemistry*, vol. 47, pp. 246–253, Mar. 2017, doi: 10.1016/J.JIEC.2016.11.039.

[125] S. Y. Lee, J. W. Choi, K. G. Song, K. Choi, Y. J. Lee, and K. W. Jung, "Adsorption and mechanistic study for phosphate removal by rice husk-derived biochar functionalized with Mg/Al-calcined layered double

hydroxides via co-pyrolysis," *Compos B Eng*, vol. 176, p. 107209, Nov. 2019, doi: 10.1016/J.COMPOSITESB.2019.107209.

[126] Y. Azimzadeh, N. Najafi, A. Reyhanitabar, and S. Oustan, "Modeling of Phosphate Removal by Mg-Al Layered Double Hydroxide Functionalized Biochar and Hydrochar from Aqueous Solutions," *Iranian Journal of Chemistry & Chemical Engineering- International English Editiom*, vol. 40, no. 2, Nov. 2021, Accessed: Mar. 17, 2025. [Online]. Available: https://www.researchgate.net/publication/356210215_Modeling_of_Phosphate_Removal_by_Mg-Al_Layered_Double_Hydroxide_Functionalized_Biochar_and_Hydrochar_from_Aqueous_Solutions

[127] F. Yang, S. Zhang, Y. Sun, D. C. W. Tsang, K. Cheng, and Y. S. Ok, "Assembling biochar with various layered double hydroxides for enhancement of phosphorus recovery," *J Hazard Mater*, vol. 365, pp. 665–673, Mar. 2019, doi: 10.1016/J.JHAZMAT.2018.11.047.

[128] Z. Zhang, L. Yan, H. Yu, T. Yan, and X. Li, "Adsorption of phosphate from aqueous solution by vegetable biochar/layered double oxides: Fast removal and mechanistic studies," *Bioresour Technol*, vol. 284, pp. 65–71, Jul. 2019, doi: 10.1016/J.BIORTECH.2019.03.113.

[129] H. He, N. Zhang, N. Chen, Z. Lei, K. Shimizu, and Z. Zhang, "Efficient phosphate removal from wastewater by MgAl-LDHs modified hydrochar derived from tobacco stalk," *Bioresour Technol Rep*, vol. 8, p. 100348, Dec. 2019, doi: 10.1016/J.BITEB.2019.100348.

[130] S. Y. Lee, J. W. Choi, K. G. Song, K. Choi, Y. J. Lee, and K. W. Jung, "Adsorption and mechanistic study for phosphate removal by rice husk-derived biochar functionalized with Mg/Al-calcined layered double hydroxides via co-pyrolysis," *Compos B Eng*, vol. 176, p. 107209, Nov. 2019, doi: 10.1016/J.COMPOSITESB.2019.107209.

[131] O. Alagha, M. S. Manzar, M. Zubair, I. Anil, N. D. Mu'azu, and A. Qureshi, "Comparative Adsorptive Removal of Phosphate and Nitrate from Wastewater Using Biochar-MgAl LDH Nanocomposites: Coexisting Anions Effect and Mechanistic Studies," *Nanomaterials 2020, Vol. 10, Page 336*, vol. 10, no. 2, p. 336, Feb. 2020, doi: 10.3390/NANO10020336.

[132] Q. Zheng *et al.*, "High adsorption capacity of Mg–Al-modified biochar for phosphate and its potential for phosphate interception in soil,"

Chemosphere, vol. 259, p. 127469, Nov. 2020, doi: 10.1016/J.CHEMOSPHERE.2020.127469.

[133] S. Wan, S. Wang, Y. Li, and B. Gao, "Functionalizing biochar with Mg–Al and Mg–Fe layered double hydroxides for removal of phosphate from aqueous solutions," *Journal of Industrial and Engineering Chemistry*, vol. 47, pp. 246–253, Mar. 2017, doi: 10.1016/J.JIEC.2016.11.039.

[134] D. Pattappan, S. Kapoor, S. S. Islam, and Y. T. Lai, "Layered Double Hydroxides for Regulating Phosphate in Water to Achieve Long-Term Nutritional Management," *ACS Omega*, vol. 8, no. 28, pp. 24727–24749, Jul. 2023, doi: 10.1021/ACSOMEGA.3C02576/ASSET/IMAGES/LARGE/AO3C02576_0012.JPEG.

[135] G. J. Jiao *et al.*, "Recent advances and challenges on removal and recycling of phosphate from wastewater using biomass-derived adsorbents," *Chemosphere*, vol. 278, p. 130377, Sep. 2021, doi: 10.1016/J.CHEMOSPHERE.2021.130377.

[136] K. W. Jung and K. H. Ahn, "Fabrication of porosity-enhanced MgO/biochar for removal of phosphate from aqueous solution: Application of a novel combined electrochemical modification method," *Bioresour Technol*, vol. 200, pp. 1029–1032, Jan. 2016, doi: 10.1016/J.BIORTECH.2015.10.008.

[137] K. W. Jung, T. U. Jeong, J. W. Choi, K. H. Ahn, and S. H. Lee, "Adsorption of phosphate from aqueous solution using electrochemically modified biochar calcium-alginate beads: Batch and fixed-bed column performance," *Bioresour Technol*, vol. 244, pp. 23–32, Nov. 2017, doi: 10.1016/J.BIORTECH.2017.07.133.

[138] Y. Yao *et al.*, "Engineered carbon (biochar) prepared by direct pyrolysis of Mg-accumulated tomato tissues: Characterization and phosphate removal potential," *Bioresour Technol*, vol. 138, pp. 8–13, Jun. 2013, doi: 10.1016/J.BIORTECH.2013.03.057.

[139] R. Li *et al.*, "Recovery of phosphate and dissolved organic matter from aqueous solution using a novel CaO-MgO hybrid carbon composite and its feasibility in phosphorus recycling," *Science of The Total Environment*, vol. 642, pp. 526–536, Nov. 2018, doi: 10.1016/J.SCITOTENV.2018.06.092.

[140] B. Wang *et al.*, “Phosphogypsum as a novel modifier for distillers grains biochar removal of phosphate from water,” *Chemosphere*, vol. 238, p. 124684, Jan. 2020, doi: 10.1016/J.CHEMOSPHERE.2019.124684.

[141] M. Zhang *et al.*, “Pyrolysis of Ca/Fe-rich antibiotic fermentation residues into biochars for efficient phosphate removal/recovery from wastewater: Turning hazardous waste to phosphorous fertilizer,” *Science of the Total Environment*, vol. 869, Apr. 2023, doi: 10.1016/j.scitotenv.2023.161732.

[142] P. Yu, Y. Xue, F. Gao, Z. Liu, X. Cheng, and K. Yang, “Phosphorus Removal from Aqueous Solution by Pre- or Post-Modified Biochars Derived from Agricultural Residues”, doi: 10.1007/s11270-016-3066-x.

[143] F. Pan *et al.*, “Phosphorus adsorption by calcium chloride-modified buckwheat hulls biochar and the potential application as a fertilizer,” *J Clean Prod*, vol. 444, p. 141233, Mar. 2024, doi: 10.1016/J.JCLEPRO.2024.141233.

[144] R. Xiao *et al.*, “Biochar produced from mineral salt-impregnated chicken manure: Fertility properties and potential for carbon sequestration,” *Waste Management*, vol. 78, pp. 802–810, Aug. 2018, doi: 10.1016/J.WASMAN.2018.06.047.

[145] “Tertiary Phosphorus Removal,” 2019. Accessed: Sep. 14, 2025. [Online]. Available: www.waterrf.org

[146] M. Devlin and J. Brodie, “Nutrients and Eutrophication,” in *Marine Pollution- Monitoring, Management and Mitigation*, Springer, Cham, 2023, pp. 75–100. doi: 10.1007/978-3-031-10127-4_4.

[147] “Nutrient pollution: reducing the impact on protected sites - GOV.UK.” Accessed: Sep. 14, 2025. [Online]. Available: https://www.gov.uk/government/publications/nutrient-pollution-reducing-the-impact-on-protected-sites/nutrient-pollution-reducing-the-impact-on-protected-sites

[148] “Phosphorus-challenges-for-the-water-environment.odt,” Dec. 2022. Accessed: Sep. 09, 2025. [Online]. Available: https://view.officeapps.live.com/op/view.aspx?src=https%3A%2F%2Fassets.publishing.service.gov.uk%2Fmedia%2F64b50abe0ea2cb001315e366%2FPhosphorus-challenges-for-the-water-environment.odt&wdOrigin=BROWSELINK

[149] A. L. Shober *et al.*, “Toward a transdisciplinary and unifying definition of legacy phosphorus,” *J Environ Qual*, vol. 54, no. 4, pp. 882–892, Jul. 2025, doi: 10.1002/JEQ2.20659.

[150] D. W. O’Connell *et al.*, “Changes in Sedimentary Phosphorus Burial Following Artificial Eutrophication of Lake 227, Experimental Lakes Area, Ontario, Canada,” *J Geophys Res Biogeosci*, vol. 125, no. 8, p. e2020JG005713, Aug. 2020, doi: 10.1029/2020JG005713.

[151] X. Ji, J. M. H. Verspagen, M. Stomp, and J. Huisman, “Competition between cyanobacteria and green algae at low versus elevated CO2: who will win, and why?,” *J Exp Bot*, vol. 68, no. 14, p. 3815, Jun. 2017, doi: 10.1093/JXB/ERX027.

[152] L. Carvalho *et al.*, “Sustaining recreational quality of European lakes: Minimizing the health risks from algal blooms through phosphorus control,” *Journal of Applied Ecology*, vol. 50, no. 2, pp. 315–323, Apr. 2013, doi: 10.1111/1365-2664.12059;SUBPAGE:STRING:FULL.

[153] R. B. Wallace, H. Baumann, J. S. Grear, R. C. Aller, and C. J. Gobler, “Coastal ocean acidification: The other eutrophication problem,” *Estuar Coast Shelf Sci*, vol. 148, pp. 1–13, Jul. 2014, doi: 10.1016/J.ECSS.2014.05.027.

[154] K. W. Jung, S. Lee, and Y. J. Lee, “Synthesis of novel magnesium ferrite (MgFe2O4)/biochar magnetic composites and its adsorption behavior for phosphate in aqueous solutions,” *Bioresour Technol*, vol. 245, pp. 751–759, Dec. 2017, doi: 10.1016/J.BIORTECH.2017.09.035.

[155] Y. Xu *et al.*, “A Novel Ca-Modified Biochar for Efficient Recovery of Phosphorus from Aqueous Solution and Its Application as a Phosphorus Biofertilizer,” *Nanomaterials 2022, Vol. 12, Page 2755*, vol. 12, no. 16, p. 2755, Aug. 2022, doi: 10.3390/NANO12162755.

[156] Scottish Environmental Protection Agency (SEPA), “Annex E: Classification for Scotland’s Standing Waters.” Accessed: Jul. 21, 2025. [Online]. Available: https://www.sepa.org.uk/media/38358/loch-water-quality-classification-scheme.pdf

[157] G. Heckrath, P. C. Brookes, P. R. Poulton, and K. W. T. Goulding, “Phosphorus Leaching from Soils Containing Different Phosphorus Concentrations in the Broadbalk Experiment,” *J Environ Qual*, vol. 24, no.

5, pp. 904–910, Sep. 1995, doi: 10.2134/JEQ1995.00472425002400050018X.

[158] J. Cloy *et al.*, “A state of knowledge overview of identified pathways of diffuse pollutants to the water environment,” 2021.

[159] S. Harrison, C. McAree, W. Mulville, and T. Sullivan, “The problem of agricultural ‘diffuse’ pollution: Getting to the point,” *Science of The Total Environment*, vol. 677, pp. 700–717, Aug. 2019, doi: 10.1016/J.SCITOTENV.2019.04.169.

[160] S. A. Parsons and J. A. Smith, “Phosphorus Removal and Recovery from Municipal Wastewaters,” *Elements*, vol. 4, pp. 109–112, Apr. 2008, Accessed: Sep. 08, 2025. [Online]. Available: https://www.ceas3.uc.edu/ret/archive/2018/ret/docs/readings/Project%201/Phosphorus%20removal%20and%20recovery%20from%20municipal%20wastewaters.pdf

[161] “Preparing for phosphorus removal in AMP 7 - AquaEnviro.” Accessed: Sep. 08, 2025. [Online]. Available: https://aquaenviro.co.uk/preparing-for-phosphorus-removal-in-amp-7/

[162] EUW Directive -Off. J. Eur.Communities, “Council Directive of 21. May 1991 concerning urban waste water treatment (91/271/EEC),” 1991. Accessed: May 22, 2025. [Online]. Available: https://scholar.google.com/scholar?q=EU%2C%20Council%20Directive%2091%2F271%2FEEC%2C%20%E2%80%9CUrban%20Waste%20Water%20Treatment%20(OJ%20L%20135%2C%2030.5.1991).

[163] H. Xin *et al.*, “Potentials of emergent plant residue derived biochar to be alternative carbon-based phosphorus fertilizer by Fe(II)/Fe(III) magnetic modification,” *Biochar*, vol. 6, no. 1, pp. 1–14, Dec. 2024, doi: 10.1007/S42773-024-00300-X/METRICS.

[164] S. Kumari, Y. Dong, and S. I. Safferman, “Phosphorus adsorption and recovery from waste streams using biochar: review of mechanisms, modifications, and agricultural applications,” vol. 15, p. 162, 2025, doi: 10.1007/s13201-025-02523-0.

[165] M. Rashid, N. T. Price, M. Á. Gracia Pinilla, and K. E. O’Shea, “Effective removal of phosphate from aqueous solution using humic acid coated magnetite nanoparticles,” *Water Res*, vol. 123, pp. 353–360, Oct. 2017, doi: 10.1016/J.WATRES.2017.06.085.

[166] L. Dai *et al.*, “Engineered hydrochar composites for phosphorus removal/recovery: Lanthanum doped hydrochar prepared by hydrothermal carbonization of lanthanum pretreated rice straw,” 2014, doi: 10.1016/j.biortech.2014.03.086.

[167] R. Li *et al.*, “Enhancing phosphate adsorption by Mg/Al layered double hydroxide functionalized biochar with different Mg/Al ratios,” *Science of The Total Environment*, vol. 559, pp. 121–129, Jul. 2016, doi: 10.1016/J.SCITOTENV.2016.03.151.

[168] O. Alagha, M. Saood Manzar, M. Zubair, I. Anil, N. Dalhat Mu’azu, and A. Qureshi, “Comparative Adsorptive Removal of Phosphate and Nitrate from Wastewater Using Biochar-MgAl LDH Nanocomposites: Coexisting Anions Effect and Mechanistic Studies”, doi: 10.3390/nano10020336.

[169] X. Tao, T. Huang, and B. Lv, “Synthesis of Fe/Mg-Biochar Nanocomposites for Phosphate Removal,” *Materials 2020, Vol. 13, Page 816*, vol. 13, no. 4, p. 816, Feb. 2020, doi: 10.3390/MA13040816.

[170] X. Li *et al.*, “Enhanced phosphate removal from aqueous solution using resourceable nano-CaO2/BC composite: Behaviors and mechanisms,” *Science of the Total Environment*, vol. 709, Mar. 2020, doi: 10.1016/J.SCITOTENV.2019.136123.

[171] S. Pap, C. Karmann, T. Thompson, R. McConnell, T. Kennedy, and M. A. Taggart, “Insights into phosphate removal and recovery from wastewater using biosolids biochar: Pyrolysis optimisation, mechanistic and column studies,” *Journal of Water Process Engineering*, vol. 75, p. 107954, Jun. 2025, doi: 10.1016/J.JWPE.2025.107954.

[172] Y. P. Gong, Z. Y. Ni, Z. Z. Xiong, L. H. Cheng, and X. H. Xu, “Phosphate and ammonium adsorption of the modified biochar based on Phragmites australis after phytoremediation,” *Environmental Science and Pollution Research*, vol. 24, no. 9, pp. 8326–8335, Mar. 2017, doi: 10.1007/S11356-017-8499-2/FIGURES/6.

[173] Y. Yao, B. Gao, J. Chen, and L. Yang, “Engineered biochar reclaiming phosphate from aqueous solutions: Mechanisms and potential application as a slow-release fertilizer,” *Environ Sci Technol*, vol. 47, no. 15, pp. 8700–8708, Aug. 2013, doi: 10.1021/ES4012977/SUPPL_FILE/ES4012977_SI_001.PDF.

[174] Y. Zheng, A. R. Zimmerman, and B. Gao, “Comparative investigation of characteristics and phosphate removal by engineered biochars with different loadings of magnesium, aluminum, or iron,” *Science of The Total Environment*, vol. 747, p. 141277, Dec. 2020, doi: 10.1016/J.SCITOTENV.2020.141277.

[175] H. Samaraweera *et al.*, “Pyrolyzed Ca-impregnated lignite for aqueous phosphate removal: Batch and column studies,” *J Environ Chem Eng*, vol. 9, no. 5, p. 106077, Oct. 2021, doi: 10.1016/J.JECE.2021.106077.

[176] X. Zhang, X. Yuan, X. Yang, H. Zhang, and L. Han, “Environmental leaching of biochar: a full factorial analysis of composition and redundancy,” *Biomass Convers Biorefin*, vol. 15, no. 13, pp. 19993–20007, Jul. 2025, doi: 10.1007/S13399-024-06464-7/FIGURES/5.

[177] M. Preisner and M. Smol, “Investigating phosphorus loads removed by chemical and biological methods in municipal wastewater treatment plants in Poland,” *J Environ Manage*, vol. 322, p. 116058, Nov. 2022, doi: 10.1016/J.JENVMAN.2022.116058.

[178] T. Abbas *et al.*, “Biochar application increased the growth and yield and reduced cadmium in drought stressed wheat grown in an aged contaminated soil,” *Ecotoxicol Environ Saf*, vol. 148, pp. 825–833, Feb. 2018, doi: 10.1016/J.ECOENV.2017.11.063.

[179] F. Razzaghi, P. B. Obour, and E. Arthur, “Does biochar improve soil water retention? A systematic review and meta-analysis,” *Geoderma*, vol. 361, p. 114055, Mar. 2020, doi: 10.1016/J.GEODERMA.2019.114055.

[180] J. Lehmann, M. C. Rillig, J. Thies, C. A. Masiello, W. C. Hockaday, and D. Crowley, “Biochar effects on soil biota – A review,” *Soil Biol Biochem*, vol. 43, no. 9, pp. 1812–1836, Sep. 2011, doi: 10.1016/J.SOILBIO.2011.04.022.

[181] M. A. Rao, G. Di Rauso Simeone, R. Scelza, and P. Conte, “Biochar based remediation of water and soil contaminated by phenanthrene and pentachlorophenol,” *Chemosphere*, vol. 186, pp. 193–201, Nov. 2017, doi: 10.1016/J.CHEMOSPHERE.2017.07.125.

[182] M. Uchimiya, S. C. Chang, and K. T. Klasson, “Screening biochars for heavy metal retention in soil: Role of oxygen functional groups,” *J Hazard Mater*, vol. 190, no. 1–3, pp. 432–441, Jun. 2011, doi: 10.1016/J.JHAZMAT.2011.03.063.

[183] M. Z. Hossain *et al.*, “Biochar and its importance on nutrient dynamics in soil and plant,” *Biochar 2020 2:4*, vol. 2, no. 4, pp. 379–420, Sep. 2020, doi: 10.1007/S42773-020-00065-Z.

[184] D. Rosa *et al.*, “Functionalized biochar from waste as a slow-release nutrient source: Application on tomato plants,” *Heliyon*, vol. 10, no. 8, p. e29455, Apr. 2024, doi: 10.1016/J.HELIYON.2024.E29455.

[185] C. Wang *et al.*, “Biochar-based slow-release of fertilizers for sustainable agriculture: A mini review,” *Environmental Science and Ecotechnology*, vol. 10, p. 100167, Apr. 2022, doi: 10.1016/J.ESE.2022.100167.

[186] J. F. Lustosa Filho, J. S. da S. Carneiro, C. F. Barbosa, K. P. de Lima, A. do A. Leite, and L. C. A. Melo, “Aging of biochar-based fertilizers in soil: Effects on phosphorus pools and availability to Urochloa brizantha grass,” *Science of The Total Environment*, vol. 709, p. 136028, Mar. 2020, doi: 10.1016/J.SCITOTENV.2019.136028.

[187] S. Barnett and J. Wentworth, “The future of fertiliser use,” Jan. 2024. doi: 10.58248/PN710.

[188] Y. Dai, W. Wang, L. Lu, L. Yan, and D. Yu, “Utilization of biochar for the removal of nitrogen and phosphorus,” *J Clean Prod*, vol. 257, p. 120573, Jun. 2020, doi: 10.1016/J.JCLEPRO.2020.120573.

[189] J. Shen *et al.*, “Phosphorus Dynamics: From Soil to Plant,” *Plant Physiol*, vol. 156, no. 3, p. 997, 2011, doi: 10.1104/PP.111.175232.

[190] J. K. Syers, A. E. Johnston, and D. Curtin, “Efficiency of soil and fertilizer phosphorus use: Reconciling changing concepts of soil phosphorus behaviour with agronomic information,” Rome, 2008.

[191] W. J. Brownlie, M. A. Sutton, K. V Heal, D. S. Reasy, and B. M. Spears, “Our Phosphorus Future Towards global phosphorus sustainability With support from the Natural Environment Research Council, The United Nations Environment Programme, The Global Environment Facility, through the International Nitrogen Management System project and the European Sustainable Phosphorus Platform,” Edinburgh, 2022. doi: 10.13140/RG.2.2.17834.08645.

[192] N. J. Barrow, “The effects of pH on phosphate uptake from the soil,” *Plant Soil*, vol. 410, no. 1–2, pp. 401–410, Jan. 2017, doi: 10.1007/S11104-016-3008-9/FIGURES/10.

[193] W. Gwenzi, T. J. Nyambishi, N. Chaukura, and N. Mapope, “Synthesis and nutrient release patterns of a biochar-based N–P–K slow-release fertilizer,” *International Journal of Environmental Science and Technology*, vol. 15, no. 2, pp. 405–414, Feb. 2018, doi: 10.1007/s13762-017-1399-7.

[194] D. Jiang, B. Chu, Y. Amano, and M. Machida, “Removal and recovery of phosphate from water by Mg-laden biochar: Batch and column studies,” *Colloids Surf A Physicochem Eng Asp*, vol. 558, pp. 429–437, Dec. 2018, doi: 10.1016/J.COLSURFA.2018.09.016.

[195] B. Arwenyo, J. J. Varco, A. Dygert, and T. Mlsna, “Phosphorus availability from magnesium-modified P-enriched Douglas fir biochar as a controlled release fertilizer,” *Soil Use Manag*, vol. 38, no. 1, pp. 691–702, Jan. 2022, doi: 10.1111/SUM.12751.

[196] Q. He, X. Li, and Y. Ren, “Analysis of the simultaneous adsorption mechanism of ammonium and phosphate on magnesium-modified biochar and the slow release effect of fertiliser,” *Biochar 2022 4:1*, vol. 4, no. 1, pp. 1–16, Apr. 2022, doi: 10.1007/S42773-022-00150-5.

3 Methodology

This chapter outlines the experimental methods employed by the research carried out in this thesis, as illustrated in *Figure 3.1*. The material selection used is first justified, the experimental methodology is then detailed, and finally, the theory of operating principles of the methods used is provided.

Work in this thesis can be categorised into three different sections: production of biochar, characterisation of biochar, and nutrient determination in water, soil, or biomass. *Figure 3.1* illustrates the experimental techniques used in each section of this thesis. Biochar was produced via pyrolysis of softwood woodchips, with chemical impregnation of these woodchips carried out to produce functionalised biochar. A range of both surface and bulk analysis techniques were employed to determine the biochars' physicochemical properties. Spectroscopy and chromatography were used to measure the concentrations of specific nutrients in water, soil, and biomass.

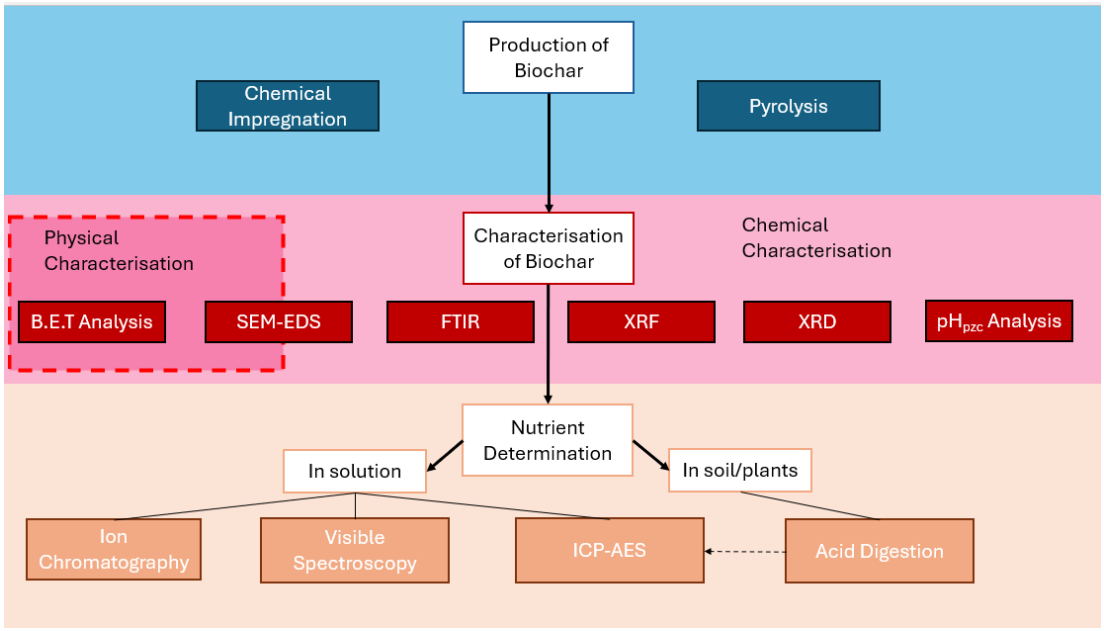

Figure 3.1:Illustration of experimental techniques used in various sections of this work.

3.1 Materials

The following chemicals and reagents were of analytical grade and purchased from FisherScientific UK: $CaCl_2$ powder, $MgCl_2$ powder, KH_2PO_4 powder, Na_2CO_3

powder, $NaNO_3$ powder, K_2SO_4 powder, 0.1M NaOH solution, and 0.1M HCl solution. Vanadate Molybdate reagent for phosphate determination was of analytical grade and purchased from Merck UK. Deionized water was taken from in lab deionized water tank.

3.1.1 Biochar Feedstock Selection

Choosing the right biomass is crucial for producing biochar that is effective in both water remediation and soil amendment. Demolition wood waste and commercial/industrial waste wood are among the UK's most abundant non-virgin feedstocks, with the reportedly second highest carbon abatement potential (1.15 tCO_2/odt), behind forestry residue chips (1.24 tCO_2/odt) [1], [2] . A meta-analysis review, comparing wood-based feedstocks with plant-based, grass-based, and manure/biosolid-based options, found that wood-based feedstocks produced biochar with the highest specific surface area, anion exchange capacity, and pore volume [3]. Wood was selected as the feedstock for biochar production due to the aforementioned advantages, softwood was chosen in this work specifically due to its high availability and high carbon abatement potential, as well as its lower internal heat transfer resistance compared to hardwood [2], [4].

Softwood woodchips were donated from Sustainable Thinking Scotland (STS) C.I.C. (Kinneil Estate, Bo'ness, Scotland), obtained from a tree on the estate. A non-disclosure agreement with STS, designed to protect patenting potential, prevents the disclosure of further feedstock details. Wood was taken from all parts of the tree, and woodchips were of varying sizes.

3.1.2 Selection of Functionalisation Agent

Section 2.3 has summarised potential functionalisation agents for biochar for aqueous P-recovery and highlights that biochars decorated with calcium (Ca) oxides/carbonates and magnesium (Mg) oxide show improved aqueous phosphate adsorption compared to other functionalisation agents reported in the literature, with Ca/Mg biochar also suitable for use in soil systems. In this thesis, different forms of Ca/Mg were utilised depending on whether

impregnation occurred before or after pyrolysis, referred to as pre-pyrolysis impregnation and post-pyrolysis impregnation, respectively. During pre-pyrolysis impregnation, $MgCl_2$ and $CaCl_2$ were used due to the well-established success of impregnating feedstock with metal chlorides to produce biochars with a metal oxide or carbonate-rich surface. Post-pyrolysis impregnation focussed on the creation of Ca-rich biochars due to experimental work (Section 4.3.4) conducted in this thesis demonstrating Ca rich biochar to have a higher aqueous P-removal across a wide range of initial P concentrations than Mg-rich biochar. As such, $CaCO_3$ and $Ca(OH)_2$ were used to create post pyrolysis impregnated biochar decorated with the same crystalline groups as those reported in the literature for biochar produced via pre-pyrolysis impregnation with $CaCl_2$.

3.2 Experimental Methods

In this work, both functionalised and non-functionalised biochar were produced from softwood woodchips, characterised, and used for either applications in aqueous P-recovery or soil amendment. A summary of methods used can be seen in *Figure 3.2*.

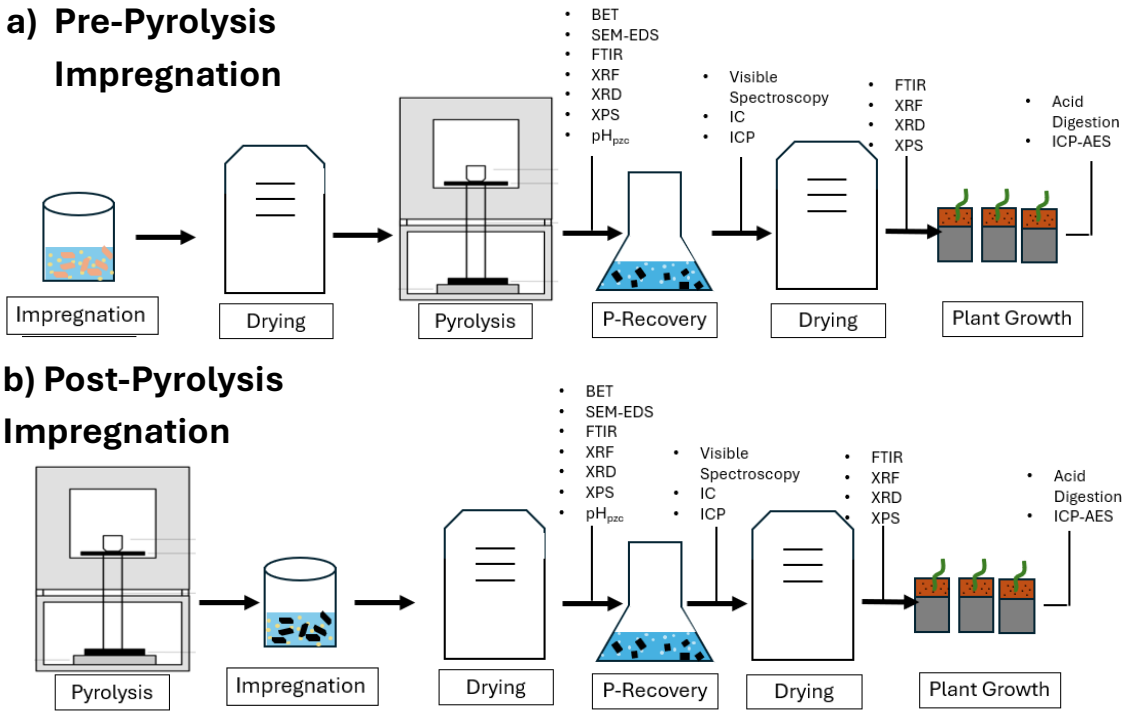

Figure 3.2: Schematic of process a) pre-pyrolysis impregnation and b) post-pyrolysis impregnation, showing where in the process experimental techniques are used.

Functionalised biochar was created via either impregnation of softwood (pre-pyrolysis impregnation) with $CaCl_2$ or $MgCl_2$ at various chemical loading ratios (CLR), or impregnation of biochar (post-pyrolysis impregnation) with $CaCO_3$ or CaOH. Softwood was pyrolysed in an N_2 environment at various pyrolysis temperatures to produce biochar.

Various methods were used to characterise biochars' physicochemical properties to provide a comprehensive overview of biochar's characteristics. Physical characteristics were determined using BET analysis to assess porosity and surface area. SEM further examined the physical features of biochar, allowing the morphology of the biochars to be observed. Several chemical analysis techniques were employed, including EDS, FTIR, XRF, XRD and XPS. Conducting XRF on samples provides elemental analysis of biochar; combined with EDS, it is possible to examine the types and quantities of elements present in biochar and their dispersion on the char surface. Analysis with FTIR offers evidence of functional groups present, helping to determine the types of

compounds, which is further complemented by XRD, used to identify crystal structures in biochar, and XPS. The point of zero charge is useful for understanding the effect of solutions on biochar's net charge, a key factor in adsorption.

Batch adsorption experiments were conducted in this work using a mixture of simple phosphate solutions and solutions containing other common anions and cations. Adsorption experiments were performed at various temperatures, pH levels, and biochar dosage rates. Dynamic adsorption experiments were also carried out through small-scale rapid column testing. The suitability of biochar samples as soil amendments was evaluated during pot trials, where plant growth and soil characteristics (pH, moisture content, and bioavailable P) were monitored.

3.2.1 Chemical Impregnation

3.2.1.1 Pre-Pyrolysis Impregnation

Pre-pyrolysis chemical impregnation was carried out by immersing softwood in a solution of chemical functionalisation agent, either $MgCl_2$ or $CaCl_2$, and DI water. Powder of the functionalisation agent was weighed and placed in a beaker. The mass of functionalisation agent used varied with CLR (ratio of mass of functionalisation agent powder to softwood feedstock). CLR's ranging from 1-2 were used to cover the range of common CLR's used in literature [5], [6], [7], [8], [9], [10], [11], [12]. The powder of functionalisation agent was then slowly poured into a beaker containing 200 mL of deionised water while the solution was continuously stirred. A 35 g softwood sample was then fully immersed in the modifying solution and left to impregnate for 2 or 24 h, depending on the experiment being carried out. During impregnation experiments, the solution was shaken on a mechanical shaker at 450 rpm. A water volume of 200 mL was chosen through trial and error to identify the minimum amount of water needed to completely dissolve the maximum amount of functionalisation agent and fully submerge the wood sample. After impregnation, wood was removed from the

functionalisation solution and rinsed with deionised water. The impregnated wood was then placed in an oven at 100 °C for 24 hours to dry and drive off moisture.

Pyrolysis temperatures used (see Section 3.2.2 below) are expected to influence the decomposition of $CaCl_2$ during pyrolysis and the strength of its binding to biochar. Decomposition of $CaCl_2$ during pyrolysis is expected to begin at temperatures of 400 °C and above with melting above the melting point of $CaCl_2$ of 775 °C [13], [14],[15],[16]. Calcium from $CaCl_2$ may adhere to the biochar surface through several mechanisms, ranging from weak physical entrapment of crystalline $CaCl_2$ within pores, to stronger interactions such as electrostatic attraction to oxygenated surface groups and, most strongly, chemical binding via conversion into insoluble minerals (e.g., $CaCO_3$ or $Ca(OH)_2$) or mechanical incorporation after molten-salt infiltration at high temperatures [17], [18], [19].

3.2.1.2 Post-Pyrolysis Impregnation

Wood samples were washed by rinsing samples with deionised water over a 0.5mm sieve to remove any dust and dirt present. The samples were then placed in an oven at 100 °C for 24 h to dry the wood and drive off moisture.

Similar to the pre-pyrolysis impregnation, post-pyrolysis impregnation was carried out by immersing biochar in a solution of functionalisation agent and DI water. Two different post-pyrolysis functionalisation agents were tested, $CaCO_3$ and $Ca(OH)_2$. Powder of the functionalisation agent with a CLR of 1.5 (ratio of mass of functionalisation agent to biochar) was weighed and placed in a beaker. The powder of functionalisation agent was then slowly poured into a beaker containing 200 mL of deionised water, while the solution was continuously stirred. The biochar sample was then fully immersed in the modifying solution and left to impregnate for 2 h. During impregnation, the solution was shaken on a mechanical shaker at 450 rpm. After impregnation, biochar was removed from the functionalisation solution and rinsed with deionised water. The impregnated biochar was then placed in an oven at 100 °C for 24 h to dry.

Post-pyrolysis impregnation was conducted without thermal or mechanical activation to maintain energy efficiency and avoid reheating the biochar, making the process more sustainable and cost-effective. However, it should be noted that post-pyrolysis impregnation without heat or mechanical activation leaves $CaCO_3$ and $Ca(OH)_2$ loosely attached to the biochar surface, limiting bonding, reactivity, and long-term stability.

3.2.2 Pyrolysis

Pyrolysis was carried out in a 10L Thermoconcept KLS 10/12/WS muffle furnace (20 cm x 20 cm, 10 cm (internal dimensions)), shown in *Figure 3.3*. Softwood feedstock was weighed and placed in 4 separate semi-circular ceramic crucibles (truncated cone shape, lower base 3.5 cm, height 4 cm, upper base 6 cm), the crucibles were then covered with lids and placed in the muffle furnace for pyrolysis. A 250 mL/min flow of nitrogen gas to the furnace was then turned on and maintained for 40 minutes to create an inert atmosphere. In the experiments carried out in *Chapter 4*, after the inert atmosphere was created, the nitrogen flow was reduced to 150 mL/min; in the experiment carried out in Chapters 5-7, the nitrogen flow was left at 250 mL/min. In early experiments (DoE 1) a flow rate of 150 mL/min was used as moderate flow rates are recommended to help create favourable porosity in biochar; however, during experimental work it was discovered the muffle furnace did not have as tight an air seal as desired, as such carrier gas flow rate was increased to help compensate for this (DoE2). The heating rate was set to 10 °C/min, the hold time was set to 60 min, and the pyrolysis temperature was varied depending on the specific experiment being carried out. To carry out optimisation of pyrolysis temperature and chemical loading rate, Design of Experiments (DoE), detailed in *Section 3.3.1* below, was used to employ multivariate analysis. Pyrolysis temperatures of 500-700 °C were selected for initial biochar production experiments to identify the optimal temperature for producing biochar with high porosity and surface area before the softwoods' inflection point [20]. Pyrolysis temperatures chosen in subsequent biochar production were based on results of previous experiments.

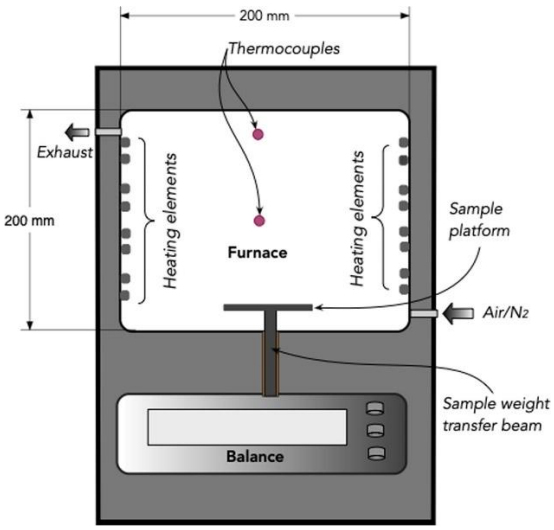

Figure 3.3:Schematic of Thermoconcept KLS 10/12/WS Muffle Furnace used in this work [21] .

Once pyrolysis was completed and the furnace had cooled down to under 300 °C, the nitrogen flow was then turned off, and the apparatus was left overnight to cool to room temperature. The crucibles were removed from the furnace, and the biochar samples were weighed. Yield was calculated using *Equation 3.1*. Biochar samples were then sealed in an airtight bag and labelled.

$$Yield\ (\%) = \frac{Biochar\ produced\ (g)}{Wood\ placed\ furnace\ (g)} \times 100 \qquad (3.1)$$

3.2.3 Pore Structure Characterisation

A Micrometrics ASAP 2420 Surface Area and Porosity Analyser (Limit of Detection (LoD) = 0.00001 mmHg) was used to determine surface area, pore volume, and pore size distribution of biochar samples.

Data collection consisted of 2 stages: degas and analysis. During degassing, approximately 0.5 g of biochar was added to a glass test tube with a bulb at the bottom, ensuring that all the biochar was entirely within the bulb space. The tube was connected to the degas port and covered with a heating jacket fitted with a thermocouple. The sample tube was then placed under vacuum, and the jacket

was heated to 200 °C at a rate of 5 °C/min for 2 h. Once degas was complete, the sample was allowed to cool to room temperature and backfilled with nitrogen. The sample was then reweighed to account for any volatile losses, and a filler rod was inserted into the sample tube to reduce excess volume. A thermal jacket was placed on the neck of the sample tube, and the tube was attached to the analysis port. During analysis, the tube was held in an insulated Dewar and immersed in liquid nitrogen at -196 °C. Isotherm data was collected by Micrometrics software and subsequently used for further data analysis. Surface area characterisation was carried out using the BET method, Barret, Joyner, and Halenda (BJH) analysis was used to determine mesopore size distributions of biochars, and micropore analysis was carried out utilising the t-plot method. Further detail of methods used for data analysis are given below in *Section 3.3.2*.

3.2.4 SEM-EDS Analysis

A JEOL JSM-IT100 InTouchScope microscope with a 3 nm spatial resolution was used to conduct SEM-EDS analysis. High vacuum conditions were used to prevent electrons from being scattered or absorbed by air; as such, double-sided carbon adhesive tape was used to secure biochar samples on aluminium stubs. SEM images were captured at 95 x magnification (200µm) and 550 x magnification (20µm) using a working distance of 13 mm, voltage acceleration of 20kV, and beam current of 50. Note, the beam current has arbitrary units and varies from 0-99. EDS analysis was carried out at 550 x magnification (20µm) using a voltage acceleration of 20 kV and a beam current of 65.

3.2.5 FTIR Analysis

FTIR analysis was carried out using an ABB IR Instrument MB 3000 series (LoD 0.06 cm^{-1}) using Attenuated Total Reflectance (ATR) for analysis. A small quantity of biochar (approximately 0.1 g) was placed on the sampling surface, and 32 scans were taken in transmission mode at a resolution of 4 cm^{-1} between the wavenumbers 400-4000 cm^{-1}. A new air reference was taken twice a day when using the machine, and detector gain was set at 80 %.

3.2.6 XRF Analysis

XRF analysis was carried out Shimadzu XRF EDX-8100P (LoD=0.001 wt%). An X-ray intensity check was performed daily when using the machine with a calibration material. A sample pot was filled with biochar so that there was an even covering over the entire face of the pot with no gaps. The sample pot was then covered with polyethylene film to secure the biochar in place. The Navi software was used to apply correction factors for organic samples. Note this correction assumes anything the XRF is not able to measure belongs to atomic number 12 and lighter. Two scans were taken in series, the first at 40 kV and the second at 15 kV.

3.2.7 XRD Analysis

XRD analysis was carried out on DoE 1 samples (*Chapter 4*) using a Bruker D8 Advance machine with the following settings: 50 kV/40 mA, Cu K_{α} radiation. The sample was prepared for data collection by lightly triturating the dry powder in an agate mortar and pestle to improve particle homogeneity and minimise any preferred orientation. Samples were then loaded into a 1 mm OD borosilicate glass capillary before being loaded into a rotating goniometer head and aligned. The samples were then measured at ambient temperature ~22°C. Samples were scanned in a 2θ range of 10-80 ° for $MgCl_2$ impregnated biochars and 10-70 ° for $CaCl_2$ impregnated biochars. Peaks were assigned using Diffrac.Eva software.

XRD DoE2 samples (*Chapters 5-7*) were carried out on a Rigaku MiniFlex600-C machine with the following settings: 40kV/10mA, Cu K_{α} radiation. The sample was prepared by crushing with a mortar and pestle before loading the biochar onto a 0.5 mm glass plate. Samples were scanned in a 2θ range of 10-80°. Peaks were assigned using MindGenuis software.

Note: analysis was carried out on different instruments between the analysis of DoE1 samples and DoE2 samples due to the departmental acquisition of the Rigaku XRD at this time. Prior to the acquisition of the Rigaku XRD, analysis was

carried out at cost by CMAC, University of Strathclyde Technology Innovation Centre.

3.2.8 XPS Analysis

X-ray Photoelectron Spectroscopy (XPS) was carried out externally by the analytical chemistry facilities in the School of Chemistry, University of Glasgow using a Kratos AXIS Supra+ machine. A wide survey scan was used for initial element identification followed by high resolution C1s, O1s, Ca2p, Cl2p, and P2p scans used to examine the chemical states and bonding environments of specific elements. An Al Kα X-ray source was used with an X-ray power of 225 W, step size of 1 eV, and dwell time of 100ms used for the survey scan and an X-ray power of 375W, step size of 0.1eV, and dwell time of 397ms used for C1s, O1s, Ca2p, Cl2p, and P2p scans.

3.2.9 Point of Zero Charge

The point of zero charge (pH_{pzc}) of biochar samples was determined using the salt addition method[22]. In brief, five solutions of 0.1M $NaNO_3$ were made at various pHs: 3, 5, 7, 9, and 11. To adjust pH 0.1 M NaOH and 0.1M HCl were used. Biochar (25 mg) was added to 15 mL of $NaNO_3$ solution and shaken at 450 rpm for 24 h. After 24 h, solutions were filtered, and the pH of the solution was measured. The change in pH (ΔpH) was plotted against the initial pH (pHi) value for each solution. When the initial solution pH is lower than pH_{pzc}, protons are adsorbed onto the biochar surface and the solution pH is decreased, resulting in a negative ΔpH [22]. When pHi is higher than pH_{pzc}, protons are released from the biochar surface to the solution, resulting in a positive ΔpH. The point at which ΔpH=0 is the pH_{pzc}, this was calculated from the graph of pHi vs ΔpH using linear interpolation.

3.2.10 Batch Adsorption Experiments

All biochar screening, isotherm, kinetic, and ideal dosage experiments were carried out in batch. Batch phosphate adsorption experiments were conducted to evaluate the adsorption potential of various biochar samples. Phosphate

stock solutions of concentrations 10 mgP/L, 20 mgP/L, and 300 mgP/L were prepared by dissolving the necessary quantities of monobasic potassium phosphate for the desired concentrations in deionised water. Batch experiments were shaken on a mechanical shaker at 450 rpm for the entire duration of the batch experiments. Experiments were carried out in 50 mL solutions with biochar mass used dependent on dosage rate being tested. Experimental set up can be seen in *Figure 3.4*.

Figure 3.4:Batch adsorption experimental set up.

For all adsorption experiments, the post-adsorption solution was filtered using general-use cellulosic filter paper from Fisher Scientific to remove biochar from the solution. Phosphate concentration in the filtrate was measured according to the American standard method APHA method 4500-P (visible spectroscopy) for experiments with initial phosphate concentrations higher than 1 mgP/L. For experiments where initial phosphate concentrations were lower than 1 mgP/L ion chromatography was used. The difference in phosphate concentration before and after batch adsorption was assumed to be entirely due to the removal of phosphate by biochar.

All adsorption kinetic and isotherm models were fitted to adsorption data using non-linear fitting in Origin software.

3.2.11 Adsorption- Rapid Small Scale Column Tests

Rapid small-scale column tests (RSSCTs) were conducted to evaluate the performance of biochar in a fixed-bed configuration. RSSCTs were performed using a column with a 15 cm bed length (approximately 1g of biochar) and an 8 mm internal diameter (ID). Biochar particles were flakes of approximately 1-2 mm, and the flow rate of P solution was 5 mL/min. The phosphate solution entered the column from the top and exited the column through the bottom. Glass wool and glass beads were used to fix biochar's position inside the column. Glass wool and glass beads were placed both above and below the bed length of biochar ensuring the entire column length was filled. The experimental set-up can be seen in *Figure 3.5*.

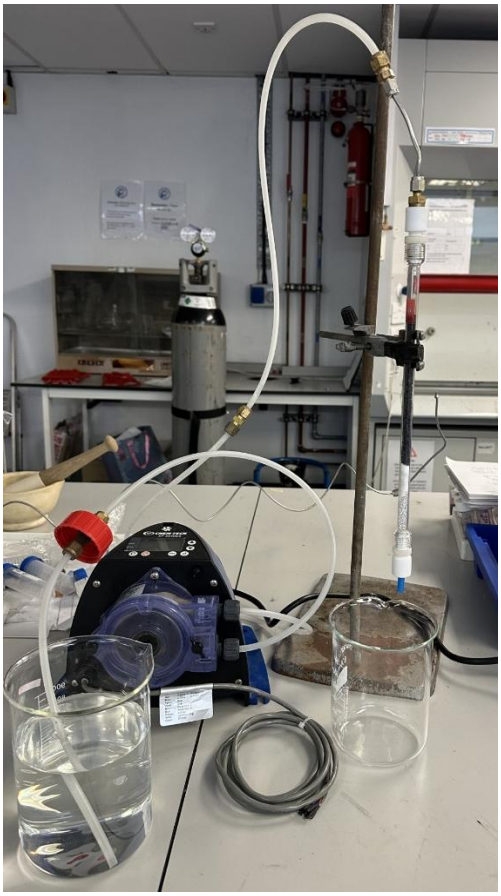

Figure 3.5: Experimental set up of rapid small scale column testing.

3.2.12 Phosphate Detection Methods

3.2.12.1 Visible Spectroscopy

A ThermoSpectronic Heλos β spectrophotometer (LoD=0.001 absorbance) was used at a wavelength of 470 nm to determine the phosphate concentration of solutions, following the APHA Method 4500-P [23]. The American standard method was used due to the British standard method's lack of suitability for the tested concentration ranges and the common use of this method in literature. Whilst the method is no longer the current British standard, it was previously BS 2690-105:1983. In short, phosphate solutions were diluted (based on initial concentration) to below 20 mgP/L, 35 mL of post adsorption solution was added to a beaker along with 5 mL of DI and 10 mL of molybdate-vanadate solution and the solution was allowed to sit for 10 min, before measurement, to ensure full colour evolution. The resulting solution was yellow with intensity of colour proportional to phosphate concentration. A calibration curve was created (*Appendix A1*) using solutions of known concentration: 0, 4, 8, 12, 16, and 20 mgP/L.

3.2.12.2 Ion Chromatography

A 850 Metrohm Professional IC-AnCat-MCS (LoD= 0.0001mgP/L) was used to carry out ion chromatography according to BS EN 10304-1:2009 [24]. Solutions were syringed through a 0.45 µm filter prior to use in the IC. The machine was recalibrated each time using solutions of 0.1, 1, 3, 5, 10mgP/L, and two quality control tests were carried out using solutions of known concentration.

3.2.13 Determination of Coexisting Ions

Determination of chlorine, nitrate, carbonate, and sulphate for competing ion experiments were carried out using ion chromatography as described above in *Section 3.2.12.2*.

3.2.14 Pot Trials

Two rounds of pot trials growing different types of beans were carried out. Beans were planted by placing one seed in a plastic flowerpot 9 cm H x 9 cm D filled with one of the soil treatments below, with five replicates of each scenario:

1. Soil
2. Soil + washed biochar
3. Soil + P-laden biochar
4. Soil + P-laden biochar + P-precipitate

Washed biochar was obtained by mixing Ca-biochar with deionised water, adjusted to pHi=8 using 0.1M NaOH, for 24 h. P-precipitate biochar was obtained by mixing Ca-biochar with 250 mgP/L monobasic potassium phosphate solution (pHi=8), for 24 h, resulting in a biochar containing adsorbed P and coated in precipitated $CaHPO_4.2H_2O$. P-laden biochar was obtained by thoroughly rinsing P-precipitate biochar with DI water to remove the $CaHPO_4.2H_2O$ coating. Biochar samples were dried in an oven for 24 hours after treatment before being mixed with soil. Biochar was added to soil at an application rate of 1 wt% to mirror application rates commonly used in the literature [25], [26], [27], [28]. Beans were obtained from a commercial garden centre (sourced: B&Q, brand: Thompson & Morgan). For each scenario, biochar and soil were thoroughly mixed using a layering and turning technique and a coning and quartering technique was used to divide biochar and soil mixtures between 5 pots. Plants were given 15-30 mL of deionised water 3 times a week.

Round 1 of pot trials was carried out planting French beans (cobra) in commercially available topsoil sieved to < 2mm. Pot trials were carried out in August-October in a temperature-controlled (20°C) growing room under a controlled light regime (15 h day, 9 h night) and harvested after 56 days. Unfortunately, the controlled light regime in this room failed, resulting in the plants receiving 24 h of light each day subsequently killing the plants; as such trials had to be repeated.

Round 2 of pot trials was conducted by taking the 5 pots from each treatment scenario in Round 1, removing any plant matter, mixing the contents, and redistributing them among 5 fresh plant pots. Runner beans (scarlet emperor) were planted, and plants were harvested 65 days after seeds were sown. Plants were grown in natural light on a south-facing window sil from the last week of March to the final week of May.

3.2.15 Soil Analysis

All soil characterisation was carried out both before and after pot trials for each pot.

3.2.15.1 Soil pH

Following BS ISO 10390:2005, approximately 5 g of soil was added to 25 mL of DI water and shaken for 1 h using an orbital shaker [29]. Soil mixtures were then left to stand for 2 h. Solution pH was then taken using a Fisher Scientific pH meter calibrated with three standard pH buffer solutions: pH 4, 7, and 10.

3.2.15.2 Moisture and Organic Matter Content

Approximately 1 g of soil was weighed, placed in a crucible of known weight, and dried at 110 °C for 24 h. The crucible was then removed from the oven and placed in a desiccator, cooled to room temperature, and reweighed. Moisture content was calculated using *Equation 3.2*.

$$\%MC = \frac{(m_{initial} - m_{oven\ dried}) \times 100}{m_{intial}} \tag{3.2}$$

The crucible containing dry soil was then placed in a muffle furnace and the temperature increased to 550 °C at a ramp rate of 10 °C/min, where it was held for 8 h. The crucible was then allowed to come to room temperature inside the furnace and weighed. The organic matter content was calculated using *Equation 3.3*.

$$\%OM = \frac{\left(m_{oven\ dried} - m_{post\ combustion}\right) \times 100}{m_{oven\ dried}} \quad (3.3)$$

3.2.15.3 Bioavailable Phosphorus Determination

The Olsen method was used to determine the bioavailable P in the soil and soil/biochar mixtures [30]. In short, 5 g of soil was immersed in a 100 mL solution of 0.05 M $NaHCO_3$ adjusted to pH 8.5 using 0.1 M NaOH. Mixtures were then shaken on a mechanical shaker at 450 rpm for 30 minutes. Hydroxide and bicarbonate ions competitively undergo ion exchange with phosphate. Once bioavailable P has been extracted, the soil was filtered out of solution using general use cellulosic Fisher Scientific filter paper. Extracted P concentration was measured by inductively coupled plasma atomic emission spectroscopy (ICP-AES) by the trace analysis facility in the Department of Civil and Environmental Engineering, University of Strathclyde.

3.2.16 Plant Analysis

Germination time, stem length, fresh weight (FW), dry weight (DW), plant P, and plant Ca concentration were used to compare plant growth performance of various pots. Germination time was defined as the number of days required for the first shoot to emerge through the soil. Stem length was measured using a ruler. Leaves and stems of plants were weighed to obtain FW, the plant was then dried at 70 °C for 72 h to obtain DW. The P and Ca content of plants was determined using acid digestion, and analysis of the extraction solution was carried out using ICP-AES. Both acid digestion and ICP-AES were carried out by the trace analysis facility in the Department of Civil and Environmental Engineering, University of Strathclyde.

3.3 Background Theory of Techniques Used

3.3.1 Design of Experiments

DoE is a statistical approach to experimental design which allows for the simultaneous varying of experimental variables to give a superior coverage of experimental space in fewer experiments than using a traditional vary one factor. DoE is based on three key principles: randomisation, replication, and blocking[31]. DoE can be used for various design types[32]:

- ***Comparison*** *tests* use t-tests, F-tests, or z-tests to choose between alternatives.
- ***Screening*** *tests* use factorial design to select key factors affecting response variables.
- ***Transfer function*** *tests* study the relationship between a specified output variable and relevant input variables.
- ***System Optimisation*** allows for the optimisation of system variables to achieve the desired output.
- ***Robust design*** aims to reduce system variation without eliminating the root cause.

It has been well established in previous work carried out in the literature that key factors affecting aqueous phosphate adsorption of biochar chemically impregnated with metal chloride salts are CLR and pyrolysis temperature (see *Section 2.2.3*). A DoE methodology was used in this work to carry out system optimisation of these variables utilising response surface methodology.

3.3.1.1 Response Surface Methodology

Response surface methodology (RSM) was first developed to improve manufacturing processes in the chemical industry and utilises polynomial regression modelling to optimize response variables affected by the value of process factors[33]. The response surface is created by plotting the mean response as a function of the factor levels being optimised. The response surface will have $N_{factors}$+1 dimensions. A factor can be defined as an independent

variable capable of affecting the response variable, levels are discrete possible values of a factor.

3.3.1.2 Central Composite Design

Central Composite Designs (CCD) are the most commonly used type of second order design[33]. There are three types of CCD shown in *Figure 3.6*: circumscribed central composite design (CCC), inscribed central composite design (CCI), and face-centred central composite design (FCC). The CCD utilises factorial design with two levels (coded as -1 and +1), central points (coded as 0), and axial points (which represent the extreme values of each factor and allow for the calculation of curvature in a response surface) [34], [35]. The distance between central points and axial points is denoted as ±α.

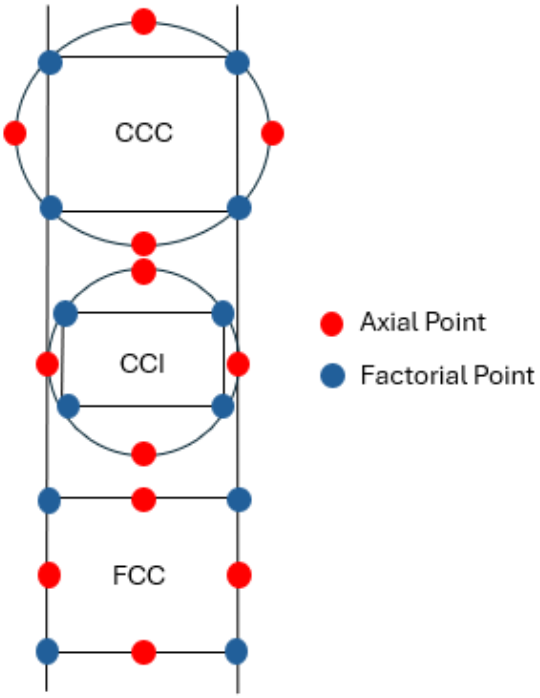

Figure 3.6:Schematic illustrating different types of central composite design: circumscribed central composite (CCC), inscribed central composite (CCI), and face centred central composite (FCC). Diagram reproduced from [34].

In CCC models, each factor has five levels with axial points used to test extreme high and low levels, outside of factorial design, for all factors. In CCI models, each factor has five levels, and axial points are taken as the limits of the factors

analysed. FCC models have three levels for each factor, with α=1 placing axial points on factorial points [34], [35].

RSM fits a polynomial function to the plotted response surface, estimating coefficients to do so. Variability in the estimate of these coefficients is a key indicator in the quality of a DoE design. This is often taken into account during experimental design by considering the rotatability of a design. A design is rotatable when prediction error is the same for all points located equal distance from the centre point. A design is orthogonal when all independent variables are uncorrelated to each other. *Figure 3.7* above shows prediction variance for different types of two-factor designs [36]. Orthogonal design is more accurate than rotatable at the centre of the experimental map, whereas rotatable design has higher accuracy at map edges, with designs that are rotatable and orthogonal balancing the two. Choice of design plan dictates the value of alpha, with *Table 3.1* below showing alpha for different plans for a two-factor design[36].

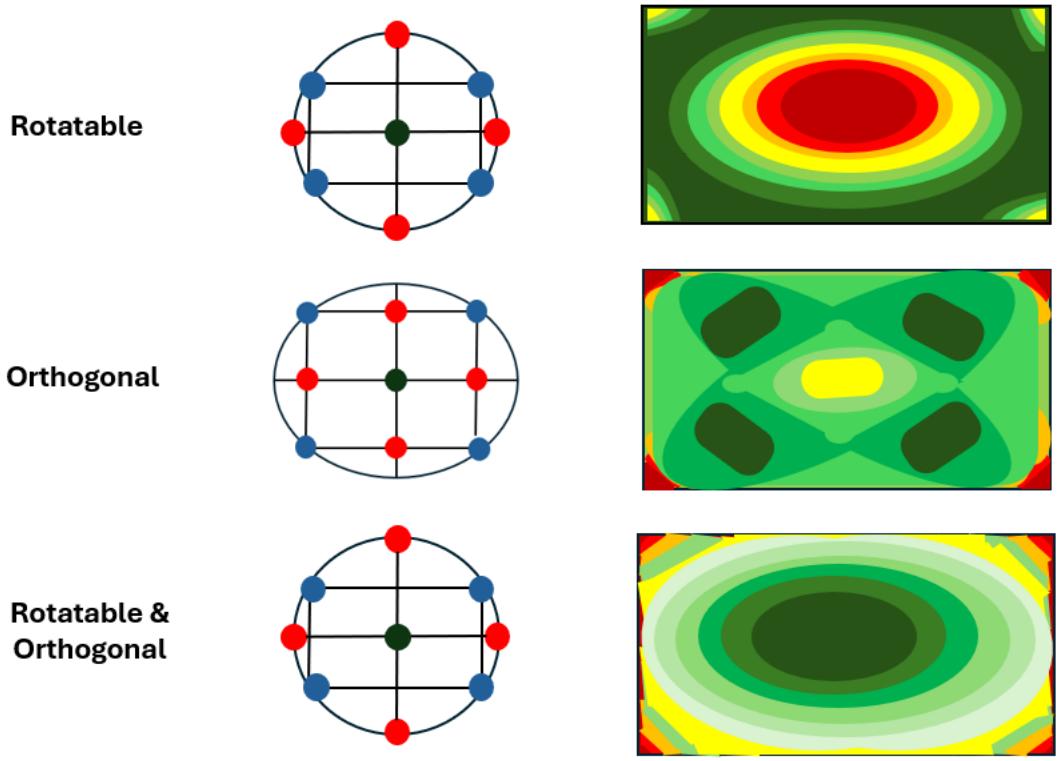

Figure 3.7:Schematic illustrating the difference in prediction error between rotatable, orthogonal, and rotatable & orthogonal designs. Reproduced from [36].

Table 3.1: Parameters of rotatable, orthogonal, and rotatable & orthogonal designs.

Design Plan	α	No. Centre Points
Rotatable	1.41 or 0.7071 (CCI)	1
Orthogonal	0.5	1
Rotatable & Orthogonal	1.41 or 0.7071 (CCI)	8

3.3.1.3 Analysis of Variance (ANOVA)

ANOVA is a statistical tool commonly used to analyse data collected for response surface analysis. ANOVA tests for the difference between the population means of three or more groups to test if a statistically significant difference exists between them[37]. ANOVA compares variance estimates due to random error with variance estimates due to random error plus a treatment effect [38]. ANOVA can also test for interaction effects between factors, regardless of whether those

factors are found to influence the response variable independently. In the context of this work, carrying out a two-factor ANOVA allows for the determination of the influence of functionalisation parameters (temperature and CLR) on any selected response yield (biochar surface area, phosphate adsorption, etc).

3.3.2 Adsorption

Adsorption is the adhesion of molecules in a fluid phase onto the surface of a solid [39]. The component being adsorbed is termed the adsorbate, and the solid on which surface adsorption occurs is termed the adsorbent. Adsorption can occur via either physisorption or chemisorption [39], [40]. During physisorption bonding between the adsorbate and adsorbent occurs via electrostatic interaction. Physisorption is a fast, non-specific process that can form mono- or multi-layers. Any desorbed species will remain unchanged in its original form. Chemisorption involves the formation of chemical bonds via the transfer of electrons. Chemisorption is slower than physisorption, involves a larger enthalpy change, is highly specific, and can only form a monolayer on the adsorbent; any desorbed species may be different from the original adsorbate.

Adsorbent materials are often classified based on their porosity. Porosity is a term used to describe pores (cavities in a solid material) and their distribution in an adsorbent. IUPAC classifies porosity in the following way[41]:

Micropores width < 2nm

Mesopores width = 2-50nm

Macropores width > 50nm

Micropores can be further divided into 3 categories:

Ultramicropores width <0.5nm

Micropores width =0.5-1.4nm

Supermicropores width = 1.4-2.0 nm

The wider the pore the greater the number of molecules required to fill the opening. Pore geometry may also affect adsorption. Pore geometries are commonly split into 4 shapes (cylinder, slit, cone, and inkbottle) in literature as shown below in *Figure 3.8* [42].

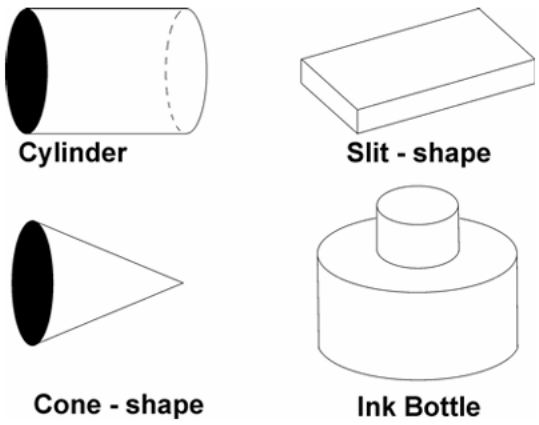

Figure 3.8: Schematic of pore geometries [79]

3.3.2.1 Gas Characterisation

The Brunauer-Emmet-Teller (BET) method is the most widely used technique for analysis of an adsorbents surface area and porosity [43], [44]. At constant temperature, the adsorbent is immersed in inert gas (most commonly N_2 or CO_2) with the relative pressure increased from vacuum until saturation of the adsorbent. The adsorption is followed by a desorption stage where the pressure is decreased and gas molecules are recovered from the adsorbent.

Calculation of Surface Area Using BET Methodology and Rouquerol Corrections

The BET isotherm is an extension of the Langmuir isotherm, which accounts for multilayer adsorption. The BET isotherm is based on the following assumptions [45]:

1. The adsorbent surface consists of energetically homogeneous binding sites with a constant enthalpy of adsorption.
2. There is no adsorbate-adsorbate interactions between neighbouring molecules.
3. Multilayer formation is unlimited.

4. Adsorption energy in multilayers is equal to the enthalpy of liquefaction.
5. The final adsorbed layer in in equilibrium with the surrounding bulk fluid.

The BET equation can be seen in *Equation 3.4*:

$$\frac{\frac{p}{p^0}}{n\left(1-\frac{p}{p^0}\right)} = \frac{1}{n_m c} + \frac{c-1}{n_m}\left(\frac{p}{p^0}\right) \tag{3.4}$$

Where $\frac{p}{p^0}$ is the dimensionless relative pressure, n is the quantity of gas adsorbed in mol/g at $\frac{p}{p^0}$, n_m is the monolayer capacity of the adsorbent in mol/g, and c is the dimensionless BET constant. A plot of the linear section of $\frac{\frac{p}{p^0}}{n\left(1-\frac{p}{p^0}\right)}$ vs $\frac{p}{p^0}$ allows for the calculation of n_m and c from the gradient and y-intercept of the slope, respectively. Despite its frequent use, the BET method is widely documented to be inherently erroneous in determining the surface area of microporous materials [46]. A key issue is that the selection of the linear region of the isotherm can be subjective due to plots often containing various regions that appear linear [47]. Two approaches are available to address this subjectivity. The first potential solution is the use of a 'standard' relative pressure region (0.05-0.3). However, despite the proposed range being generally suitable for mesoporous materials, it often does not replicate the true linear region of micropore-containing materials [48]. The second solution, utilised in this work, is the use of additional criteria for an objective choice of a single linear region proposed by Rouquerol. The linear region can be selected using Rouquerol corrections by adhering to the following criteria [48]:

1. A linear region may only be selected if $n\left(1-\frac{p}{p^0}\right)$ is increasing with $\frac{p}{p^0}$.
2. A linear region may only be selected if that region yields a positive y-intercept to result in a valid value of c.
3. The selected $\frac{p}{p^0}$ range should include the value which corresponds to n_m.

Pore Size Distribution- BJH Methodology

The most popular method for the determination of pore volume and pore size distribution of mesoporous and microporous adsorbents is the Barret, Joyner, and Halenda (BJH) method [49]. However, the BJH method is not suitable for the determination of micropores with an associated error of 20% when pores are less than 5 nm [50]. Pores with diameter smaller than 10nm can also be underestimated. The BJH method makes the following assumptions[51]:

1. All pores are cylindrical.
2. Adsorbate molecules are physiosorbed to pore walls and capillary volume is filled with condensate at equilibrium.
3. Pores are fully saturated at the highest $\frac{p}{p^0}$.

The BJH method is based on the theory of pores, which consists of three sections, as shown in *Figure 3.9*: the pore walls, the pore core, and an adsorbed layer on the pore walls. The pore core describes the volume of liquid/condensate which fills the pore and evaporates once the critical pressure is reached for a pore of that radius. The adsorbed layer is a layer of adsorbate which remains adhered to the pore walls when evaporation initially occurs in the core. The adsorbed layer, which will gradually reduce as pressure is reduced, until it is entirely removed and the pore is left empty. [51]

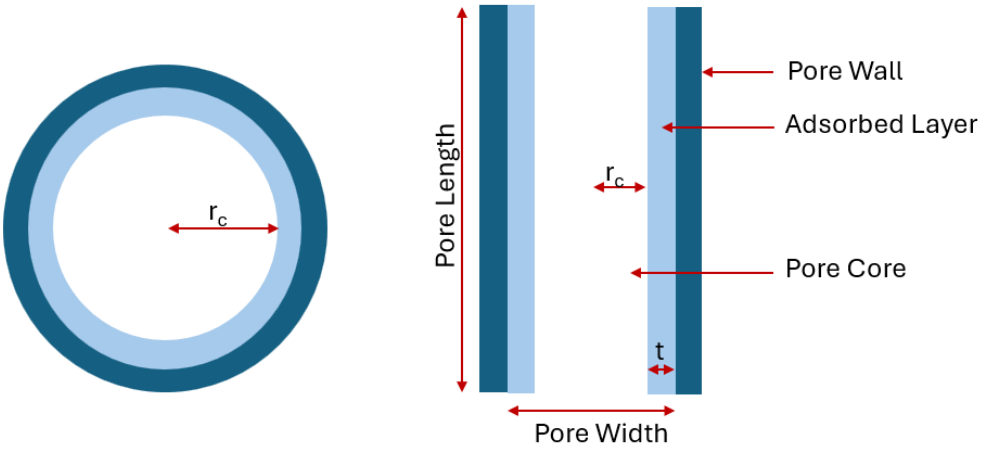

Figure 3.9:Diagram showing sections of pores.

The BJH method utilises the Kelvin Equation (*Equation 3.5* below) to estimate pore size by calculating the Kelvin core radius at various pressure intervals in given desorption isotherm data[49].

$$ln\left(\frac{p}{p_0}\right) = \frac{2\gamma V_m}{r_c RT} \tag{3.5}$$

Where γ is the surface tension at the liquid-vapour interface (N/m), V_m is liquid molar volume (m^3/mol), r_c is meniscus radius (m), R is the universal gas constant (8.3145 J/(mol.K)), and T is temperature (K). Rearrangement allows the equation to be solved for meniscus radius. Pore radius can be calculated by adding the thickness of adsorbent remaining on the pore wall to the meniscus radius. Thickness of adsorbate on the pore wall is dependent on adsorbent-adsorbate interactions and will vary depending on the surface chemistry of the adsorbate material. Various empirical formulas are available to calculate adsorbate layer thickness. The carbon black empirical formula (*Equation 3.6* below) [52] is used as an appropriate approximation for thickness (t) of adsorbate on biochar (Å).

$$t = 2.98 + 6.45\left(\frac{p}{p_0}\right) + 0.88\left(\frac{p}{p_0}\right)^2 \tag{3.6}$$

3.3.2.2 Liquid Adsorption Isotherms

Adsorption behaviour can be described using various adsorption isotherms. Isotherms used in this work include Langmuir, Freundlich, and Sips.

The Langmuir isotherm, given in *Equation 3.7* is based on three major assumptions[53]:

1. All adsorption sites are energetically homogeneous.
2. There is no adsorbate-adsorbate interaction between neighbouring molecules.
3. Adsorption is limited to one molecule per active site, with saturation occurring at monolayer coverage.

$$q_e = \frac{k_l q_m Ce}{(1 + k_l C_e)} \tag{3.7}$$

The Langmuir equation can be seen above, where q_e is the amount adsorbed (mg/g_{BC}), q_m is the theoretical maximum adsorption capacity (mg/g_{BC}), Ce is equilibrium concentration (mg/L), and k_l is the Langmuir constant (L/mg).

If a data set fits the Langmuir model well R_L, the dimensionless separation factor, can be used to determine favourability of adsorption as shown in *Equation 3.8*, where C_0 is the initial adsorbate concentration (mg/L) [54]. Adsorption is considered favourable if 0< R_L<1, if R_L>1 adsorption is considered unfavourable. If R_L=1 the system is linear and if R_L=0 adsorption is irreversible.

$$R_L = \frac{1}{1 + k_l C_0} \tag{3.8}$$

The Freundlich isotherm, *Equation 3.9*, is an empirical formula capable of describing multilayer adsorption on heterogeneous sites [54], [55]. The Freundlich equilibrium constant is represented by k_f((mg$^{(n-1)/n}$.L$^{1/n}$)/g), and n denotes the heterogeneity factor. This isotherm can not be used to determine a maximum adsorption capacity as it does not predict limited surface coverage.

$$q_e = k_f C_e^{\frac{1}{n}} \tag{3.9}$$

The Sips model, shown in *Equation 3.10*, is an empirical equation which combines the Langmuir and Freundlich isotherms [54], [55]. At low adsorbate concentrations, the model reduces to the Freundlich isotherm; however, it exhibits a monolayer capacity, similar to the Langmuir isotherm, at high concentrations. The sips equilibrium constant is given by k_s ((L/mg)$^{-ns}$). The Sips isotherm can be used to describe homo or hetro-geneous systems with level of heterogeneity reflected by the value of the dimensionless parameter n_s. When n_s=1, the model simplifies to the Langmuir equation; as such, values close to one represent uniform binding sites. When the value of is n_s<1 the adsorption is heterogeneous with the model tending towards the Freundlich isotherm as n_s tends towards 0.

$$q_e = \frac{q_m (k_s C_e)^{n_s}}{(1 + (k_s C_e)^{n_s})} \tag{3.10}$$

3.3.2.3 Liquid Adsorption Kinetics

Adsorption occurs in four stages, where the slowest step is considered the rate-controlling step [55], [56]:

1. The transport of adsorbate from the bulk liquid to liquid film present at the adsorbent surface (bulk diffusion).
2. Diffusion of the adsorbate through the thin liquid layer at the absorbent surface (film diffusion).
3. Internal diffusion into the internal pore structure of the adsorbent (intraparticle diffusion).
4. Equilibrium of adsorption/desorption of adsorbate onto the surface active sites (surface reaction).

The rate of adsorption may be governed by one or a combination of the above steps. The rate-determining step may change throughout the adsorption process.

The pseudo first order (PFO), pseudo second order (PSO), Elovich, and intraparticle diffusion kinetic models (*Equations 3.11-3.14*) were used to determine the adsorption mechanisms of phosphate onto biochars in this work.

$$q_t = q_e(1 - e^{-k_1 t}) \tag{3.11}$$

$$q_t = \frac{k_2 q_e^2 t}{1 + k_2 q_e t} \tag{3.12}$$

$$q_t = \frac{1}{\beta} ln(\alpha\beta t + 1) \tag{3.13}$$

$$q_t = k_{ip} t^{1/2} + c_i \tag{3.14}$$

Where q_t is the amount adsorbed (mg_P/g) at time t (min); q_e is the amount adsorbed (mg_P/g) at equilibrium; k_1 (min^{-1}), k_2 (g/mg min), k_{ip}(mg/g.$min^{0.5}$) are the PFO, PSO, and intraparticle diffusion rate constants respectively; α (mg/g) and β (mg/g) are the Elovich adsorption and desorption rate constants, respectively; and c_i (mg_P/g) is a constant representing the boundary layer thickness.

The PFO model assumes a first-order equation with the rate-controlling mechanism to be diffusion of adsorbate to the adsorbent surface [56]. The PSO model assumes the rate of adsorption to be proportional to the number of available surface sites on the adsorbent [57]. The Elovich model assumes a heterogeneous adsorbent surface in which decrease in adsorption rate is exponentially related to increase in quantity of adsorbate adsorbed. When applying the intraparticle diffusion model, the plot of q_t vs $t^{1/2}$ gives a linear function. If this function passes through the origin, intraparticle diffusion can be said to control the adsorption process. Often this is not the case and multiple linear sections are present, representing different stages of adsorption.

3.3.3 Rapid Small Scale Column Testing

Rapid small-scale column tests (RSSCT) were carried out to test the performance of biochar in a fixed bed configuration, as shown in *Figure 3.10*. During RSSCTs test water is pumped into a small column filled with adsorbent[58]. RSSCTs were

developed to provide a scaled-down version of pilot testing, with minimal time and economic demands, capable of performing equally to a small-scale system. The ability to test proportionally large water quantities with a small quantity of adsorbent was particularly advantageous for this work. In theory, RSSCTs scale down mass transfer phenomena and hydrodynamic characteristics of pilot-scale columns, enabling them to produce breakthrough curves with profiles matching those of their pilot-scale equivalent [59]. Effective simulation of pilot-scale mass transfer relies on the following assumptions[59]:

1. There is no backwashing.
2. Scaling is based on dispersed flow and adherence to the pore-surface diffusion model is followed.
3. Internal mass transfer is the rate limiting factor of adsorption and the adsorbent has a microporous nature.
4. Pore size distribution of adsorbent is independent of particle size.
5. All adsorbent particles have equal adsorption properties.

Process variables for RSSCTs are: Empty bed contact time (EBCT), bed length and diameter, water flow rate, hydraulic loading rate (HLR), water throughput volume, adsorbent operation time, adsorbent usage rate[58], [59].

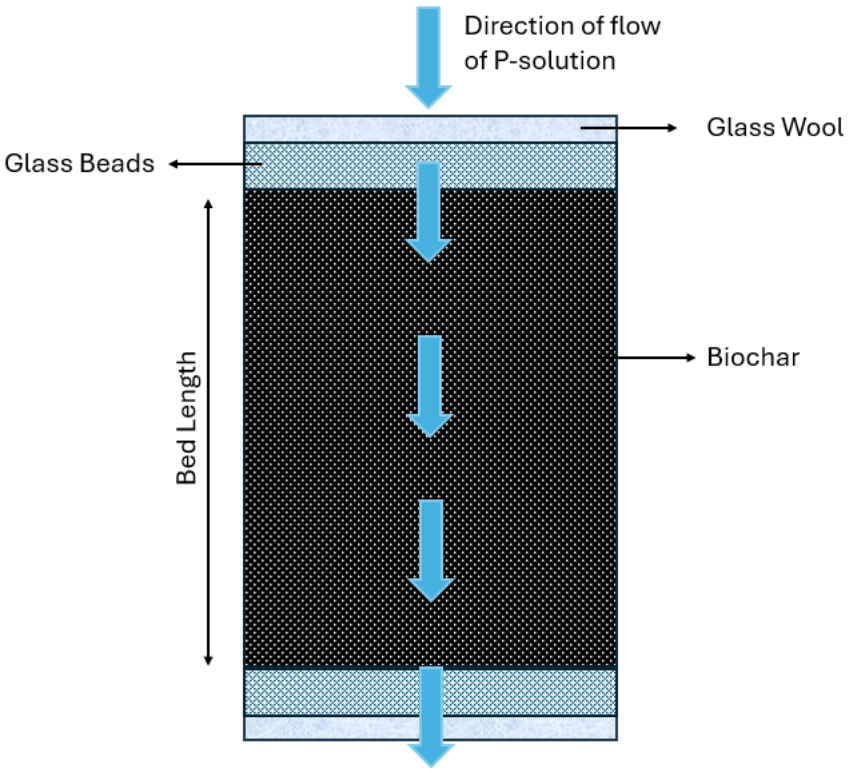

Figure 3.10:Schematic of RSSCT set-up.

3.3.4 Physicochemical Characterisation Techniques

3.3.4.1 SEM-EDS

Scanning electron microscope (SEM) is a common method for analysing the morphology of solids. SEM operates by irradiating a sample with an electron beam, as the beam hits the surface of the sample backscattered electrons, secondary electrons, and X-rays are released [60]. Various detectors are used to capture the signal from the released electrons and photons allowing an image to be created.

SEM instruments often include an Energy dispersive spectroscopy (EDS) system to characterise the surface chemically. During EDS, the energy of X-rays emitted during SEM are measured [60]. The energies released can be used to determine the elements present and their concentrations. EDS can detect elements with concentrations higher than 1 wt% [61]. The detection limits of EDS can decrease with the roughness of the surface.

3.3.4.2 FTIR Analysis

Infrared (IR) spectroscopy is a non-destructive bulk analysis technique which can be used to determine the chemical functional groups present in a sample. When IR radiation is passed through a material, atomic vibrations within its molecules (vibrational and rotational motions) are excited at specific frequencies [62].

The most common type of IR spectroscopy is Fourier transform infrared (FTIR) spectroscopy which possess a high signal to noise ratio. In FTIR, radiation emitted from an IR source is split into two beams, one beam is reflected off a stationary mirror and the other off a movable mirror [62], [63]. When the beams recombine after reflection, an interference pattern is produced. The recombined beam passes through the analysis sample which absorbs some of the light. The light passed through the sample is measured by a detector and converted to an electrical signal called an interferogram. The interferogram then undergoes Fourier transformations to create a spectrum of transmittance/absorbance against wavenumber. Wavenumber can be calculated from *Equation 3.15*. As wavenumber is dependent on both bond strength and mass, FTIR allows for differentiation of different bond types between the same pair of elements. FTIR spectra were analysed via comparison to known spectra available in the literature.

$$v = \sqrt{\frac{bond\ strength}{mass}} \tag{3.15}$$

3.3.4.3 XRF

X-Ray Fluorescence (XRF) Spectroscopy involves the emission of fluorescent/secondary X-rays from a sample bombarded with high energy x-rays or gamma rays when excited core level electrons undergo radiative decay back to their respective ground states[64], [65]. As the fluorescent x-rays emitted are characteristic of the energy levels of the atomic species they were emitted from they act as a spectroscopic fingerprint [65]. XRF is a non-destructive bulk

analysis technique [66]. XRF had an improved detection limit compared to EDS, making it more suitable for the detection of trace elements [61].

3.3.4.4 XRD

X-ray Diffraction (XRD) can be used to determine the presence of crystalline compounds on a material as well as their size. This technique works by firing X-rays at a material, crystals present on the material will diffract these X-rays in a pattern which is dependent on the size, position, and arrangement of constituents of the crystal [67]. The scattered photons which result from the contact of a crystal with the x-rays create a characteristic diffraction pattern which can act as a fingerprint.

3.3.4.5 XPS

X-ray Photoelectron Spectroscopy (XPS) was carried out externally by the analytical chemistry facilities in the School of Chemistry, University of Glasgow. XPS can be used to identify and determine the quantity of surface elements [68]. This technique works by bombarding the surface of a material with X-rays resulting in the ejection of valence and core electrons, the kinetic energy of these electrons is measured by a spectrometer and used to determine their binding energies [69]. The resulting spectrum of binding energy vs number of emitted electrons can be compared to characteristic spectra for different elements to identify elements and their chemical environment.

3.3.5 Phosphate Determination

3.3.5.1 Visible Spectroscopy

Visible spectroscopy operates within the visible region of the electromagnetic spectrum (350-800 nm) and measures the absorbance of light at specific wavelengths. When a beam of light of a specific wavelength is passed through a material, some of the light is absorbed as ground state electrons within the material transition to excited state [62]. Absorbance of molecules is wavelength-specific, allowing for qualitative analysis. According to Beer-Lambert law (Equation 3.16), the concentration of a solute is proportional to its absorbance, allowing for quantitative analysis.

$$A = abc \tag{3.16}$$

Where A is absorbance, a is wave-length dependant absorption, b is path length, and c is concentration.

3.3.5.2 Ion Chromatography

Ion chromatography allows for the separation of ions based upon interactions with a stationary phase (resin) and a mobile phase (eluent)[70]. More specifically, the type of chromatography used in this work is ion exchange chromatography. Ions in eluent move through the ion exchange column at differing speeds, dependent on their affinity for the resin in the column. The affinity of ions for the resin varies with charge and size [71]. The stronger the affinity for the resin, the slower ions move through the column [72]. As ions exit the column, the conductivity of eluent is measured to produce a chromatograph plotting conductivity vs. time. The time it takes for different ions to move through the column is known, allowing for the identification of ions present, with the strength of conductivity enabling the quantification of these ions.

3.3.5.3 Inductively Coupled Plasma Atomic Emission Spectroscopy

Inductively Coupled Plasma Atomic Emission Spectroscopy (ICP-AES) analysis was carried out by the trace analysis facility in the Department of Civil and Environmental Engineering, University of Strathclyde. During ICP-AES, inductively coupled plasma is used to excite sample atoms, which emit electromagnetic radiation, at element characteristic wavelengths, when returning to their ground state [73]. Emitted light is directed into a spectrometer, which separates it into its component wavelengths [74]. A detector is used to determine light intensity at each wavelength, with intensity directly proportional to the concentration of the corresponding element.

3.3.5.4 Bioavailable Phosphorus in Soil

Bioavailable phosphorous can be determined using various techniques. P-determination technique is usually picked based on soil pH as this is usually indicative of the form of bioavailable phosphate [75]. In this work, the P-

determination method was selected based on the likely forms of P considering biochar functionalisation. The Olsen method was chosen due to its suitability for the determination of bioavailable P in the forms of Ca-P, Mg-P, and Al-P, making it appropriate for the determination of P in biochar treated soil [75].

3.3.6 Statistics

3.3.6.1 Calculation of Errors

Where experiments were repeated and an average value reported, all errors reported in tables and as error bars on graphs are standard errors unless specified otherwise. Standard errors were calculated using *Equation 3.17*, where σ is the sample standard deviation. Standard errors were not reported for metrics of plant growth during pot trials and were instead replaced with standard deviation. This is due to a lack of physical meaning when fitting standard errors to the repetition of a plant growth experiment, where the addition of standard error would incorrectly imply that each plant should be the same and deviation is due to error, rather than natural variation.

$$SE = \frac{\sigma}{Number\ of\ samples} \tag{3.17}$$

3.3.6.2 Calculation of Model Fit

When measuring the accuracy of fit of a mathematical model to data, R^2 (coefficient of determination) and adjusted R^2 were used. *Equation 3.18* shows how R^2 is calculated where SSE is the sum of squared error, and SST is the sum of squared total.

$$R^2 = 1 - \frac{SSE}{SST} \tag{3.18}$$

R^2 is a measure of how well variation of a dependent variable is explained by independent variables in a regression model. R^2 assumes that all independent variables affect the result of the model; as such, R^2 can artificially increase with the addition of extra model parameters, even when extra parameters are not

statistically significant, due to chance correlation over enhancement of how a model reflects data. Adjusted R^2 adjusts for the number of parameters, only increasing if an additional variable truly increases model fit. Adjusted R^2, calculated using *Equation 3.19*, is useful for comparing models with different numbers of parameters, such as comparing the Sips isotherm to Freundlich or Langmuir isotherms.

$$Adjusted\ R^2 = 1 - \left(\frac{(1 - R^2)(No\ obeservations - 1)}{(No\ observations - No\ independent\ variables - 1)}\right) \quad (3.19)$$

When fitting models for adsorption kinetics and isotherms reduced χ^2 was also used to measure the statistical fit of models to experimental data obtained. Reduced χ^2 is a statistical measure that quantifies the difference between observed data and expected model values which has been normalised, similar to adjusted R^2, to account for the degrees of freedom in the fitted model. Reduced χ^2 values close to 1 indicates the model adequately explains the data relative to the measurement uncertainties, values much greater than 1 suggest underfitting (or underestimated errors), and values much less than 1 suggest overfitting (or overestimated errors).

During DoE analysis, predicted R^2 was also considered. Using predicted R^2 helps ensure that a model not only fits data well but is also capable of making accurate predictions. StatEase360 was used to analyse DoE data; the software calculates predicted R^2 by going through each data point and removing the point, calculating the regression equation and evaluating how well the missing observation can be predicted. A predicted R^2 significantly lower than R^2 may indicate a regression model has been overfitted and an artificially high R^2 has been achieved due to chance fitting of random noise.

3.3.6.3 Diagnostic Plots

Four types of diagnostic plot are used in this thesis to detect outlier data points during DoE analysis: normal plot, residuals vs predicted, and predicted vs actual, and a difference in fits (DFFITS) plot.

A normal plot shows how well data fits a standard normal distribution; an almost straight line suggests data adheres to a normal curve [76]. Some deviation from a straight line is expected. A residual vs predicted plot helps visualise if any outliers are present, and whether the error is relatively even throughout the data range for the fitted model [76]. Randomly distributed residuals forming a horizontal band around 0, with no one point standing out, indicate a good model fit with no outliers. Both normal plots and residual vs predicted plots use studentized residuals to identify outlier data points, these are a type of standardised residual used to. Studentised residuals are calculated by removing the i^{th} data point from data set, refitting the regression model, and calculating the difference in predicted y(i) at point (A(i), B(i)) with and without the i^{th} observation, then dividing this difference by the residuals estimated standard deviation [77].

The predicted vs actual plot shows the response values predicted by the model for a set of conditions versus the actual experimental data obtained for those conditions, where the straight-line y=x shows perfect agreement between experimental data and the model [76]. A DFFITS analysis is used to assess the influence of individual data points. DFFITS measures the number of standard deviations by which the predicted value of an observation changes if that observation is removed; a data point with high influence is not necessarily problematic if there is confidence in its accuracy [78].

References

[1] S. Shackley, J. Hammond, J. Gaunt, and R. Ibarrola, “The feasibility and costs of biochar deployment in the UK,” *https://doi.org/10.4155/cmt.11.22*, vol. 2, no. 3, pp. 335–356, Jun. 2014, doi: 10.4155/CMT.11.22.

[2] S. Ahmed, J. Hammond, R. Ibarrola, S. Shackley, and S. Haszeldine, “The potential role of biochar in combating climate change in Scotland: an analysis of feedstocks, life cycle assessment and spatial dimensions,” *http://dx.doi.org/10.1080/09640568.2011.608890*, vol. 55, no. 4, pp. 487–505, May 2012, doi: 10.1080/09640568.2011.608890.

[3] J. A. Ippolito *et al.*, “Feedstock choice, pyrolysis temperature and type influence biochar characteristics: a comprehensive meta-data analysis review,” vol. 1, pp. 421–438, 123AD, doi: 10.1007/s42773-020-00067-x.

[4] M. U. Jamal, “Design of Experiments Optimisation of Scottish Wood Biochars for Water Remediation targeting selected Persistent Organic Pollutants,” The University of Strathclyde, Glasgow, 2023.

[5] Q. Yin, M. Liu, and H. Ren, “Removal of Ammonium and Phosphate from Water by Mg-modified Biochar: Influence of Mg pretreatment and Pyrolysis Temperature”.

[6] R. Chanda *et al.*, “Functionalized biochar from vegetable waste for phosphorus removal from aqueous solution and its potential use as a slow-release fertilizer,” *Cleaner Materials*, vol. 15, p. 100287, Mar. 2025, doi: 10.1016/J.CLEMA.2024.100287.

[7] G. Cai and Z. long Ye, “Concentration-dependent adsorption behaviors and mechanisms for ammonium and phosphate removal by optimized Mg-impregnated biochar,” *J Clean Prod*, vol. 349, p. 131453, May 2022, doi: 10.1016/J.JCLEPRO.2022.131453.

[8] S. Xu *et al.*, “Solvent-Free Synthesis of MgO-Modified Biochars for Phosphorus Removal from Wastewater,” *Int J Environ Res Public Health*, vol. 19, no. 13, p. 7770, Jul. 2022, doi: 10.3390/IJERPH19137770/S1.

[9] S. V. Novais, M. D. O. Zenero, J. Tronto, R. F. Conz, and C. E. P. Cerri, “Poultry manure and sugarcane straw biochars modified with MgCl2 for phosphorus adsorption,” *J Environ Manage*, vol. 214, pp. 36–44, May 2018, doi: 10.1016/J.JENVMAN.2018.02.088.

[10] S. Wang *et al.*, “Adsorption of phosphorus by calcium-flour biochar: Isotherm, kinetic and transformation studies,” *Chemosphere*, vol. 195, pp. 666–672, Mar. 2018, doi: 10.1016/J.CHEMOSPHERE.2017.12.101.

[11] S. Zeng and E. Kan, “Sustainable use of Ca(OH)2 modified biochar for phosphorus recovery and tetracycline removal from water,” *Science of The Total Environment*, vol. 839, p. 156159, Sep. 2022, doi: 10.1016/J.SCITOTENV.2022.156159.

[12] X. Liu, F. Shen, R. L. Smith, and X. Qi, “Black liquor-derived calcium-activated biochar for recovery of phosphate from aqueous solutions,” *Bioresour Technol*, vol. 294, p. 122198, Dec. 2019, doi: 10.1016/J.BIORTECH.2019.122198.

[13] C. Liu *et al.*, “Silica-assisted pyro-hydrolysis of CaCl2 waste for the recovery of hydrochloric acid (HCl): Reaction pathways with the evolution of Ca(OH)Cl intermediate by experimental investigation and DFT modelling,” *J Hazard Mater*, vol. 439, p. 129620, Oct. 2022, doi: 10.1016/J.JHAZMAT.2022.129620.

[14] Y. Zhao, L. Wen, Y. Zhang, J. Wang, and Z. Yang, “Study on the pyro-hydrolysis of CaCl2 with steam and CO2 by experiments and DFT calculation,” *Colloids Surf A Physicochem Eng Asp*, vol. 683, p. 133075, Feb. 2024, doi: 10.1016/J.COLSURFA.2023.133075.

[15] N. Sophonrat *et al.*, “Ex Situ Catalytic Pyrolysis of a Mixture of Polyvinyl Chloride and Cellulose Using Calcium Oxide for HCl Adsorption and Catalytic Reforming of the Pyrolysis Products,” *Ind Eng Chem Res*, vol. 58, no. 31, pp. 13960–13970, Aug. 2019, doi: 10.1021/ACS.IECR.9B02299/ASSET/IMAGES/MEDIUM/IE-2019-02299M_M004.GIF.

[16] W. M. Haynes, Ed., “CRC Handbook of Chemistry and Physics,” in *CRC Handbook of Chemistry and Physics*, CRC Press, 2014, pp. 4–54. doi: 10.1201/B17118.

[17] M. Ali, F. Mahmood, C. F. Magoua Mbeugang, J. Tang, X. Xie, and B. Li, “Molten chloride salt pyrolysis of biomass: Effects of temperature and mass ratio of molten salt to biomass,” *Energy*, vol. 316, Feb. 2025, doi: 10.1016/j.energy.2025.134634.

[18] F. Shao *et al.*, “An attempt to enhance the adsorption capacity of biochar for organic pollutants - Characteristics of CaCl2 biochar under multiple

design conditions," *Science of The Total Environment*, vol. 854, p. 158675, Jan. 2023, doi: 10.1016/J.SCITOTENV.2022.158675.

[19] M. Fan *et al.*, "Activation of biochar by CO2 produced from the same pyrolysis process and captured in situ by CaO," *Chemical Communications*, vol. 61, no. 3, pp. 484–487, Jan. 2025, doi: 10.1039/D4CC04931D.

[20] L. Leng *et al.*, "An overview on engineering the surface area and porosity of biochar," *Science of the Total Environment*, vol. 763, Apr. 2021, doi: 10.1016/J.SCITOTENV.2020.144204.

[21] W. Cao, J. Li, L. Lin, and X. Zhang, "Release of potassium in association with structural evolution during biomass combustion," *Fuel*, vol. 287, p. 119524, Mar. 2021, doi: 10.1016/J.FUEL.2020.119524.

[22] E. Cristiano, Y. J. Hu, M. Siegfried, D. Kaplan, and H. Nitsche, "A comparison of point of zero charge measurement methodology," *Clays Clay Miner*, vol. 59, no. 2, pp. 107–115, Apr. 2011, doi: 10.1346/CCMN.2011.0590201/METRICS.

[23] American Public Health Association, "APHA Method 4500-P," in *Standard Methods for the Examination of Water and Wastewater*, 18th ed., A. E. Greenberg, L. S. Clesceri, A. D. Eaton, and M. A. H. Franson, Eds., Washington, DC: American Public Health Association, 1992, ch. 4, pp. 108–117.

[24] "Water quality. Determination of dissolved anions by liquid chromatography of ions," BSI British Standards, London, Jan. 1997. doi: 10.3403/00903800.

[25] F. Wali *et al.*, "Effect of Consecutive Application of Phosphorus-Enriched Biochar with Different Levels of P on Growth Performance of Maize for Two Successive Growing Seasons," *Sustainability 2022, Vol. 14, Page 1987*, vol. 14, no. 4, p. 1987, Feb. 2022, doi: 10.3390/SU14041987.

[26] C. Yu, "Recovery of NH4+-N and PO43--P from urine using sludge-derived biochar as a fertilizer: Performance and mechanism," *RSC Adv*, vol. 12, no. 7, pp. 4224–4233, Feb. 2022, doi: 10.1039/D1RA08558A.

[27] X. Chen, L. Liu, Q. Yang, H. Xu, G. Shen, and Q. Chen, "Optimizing Biochar Application Rates to Improve Soil Properties and Crop Growth in Saline–Alkali Soil," *Sustainability (Switzerland)* , vol. 16, no. 6, p. 2523, Mar. 2024, doi: 10.3390/SU16062523/S1.

[28] J. Liu, Z. Chen, S. Wu, H. Sun, J. Xing, and Z. Zhang, “Interaction of Biochar Addition and Nitrogen Fertilizers on Wheat Production and Nutrient Status in Soil Profiles,” *Plants*, vol. 13, no. 5, p. 614, Mar. 2024, doi: 10.3390/PLANTS13050614.

[29] “BS ISO 10390:2005 Soil quality. Determination of pH,” BSI British Standards, London, Feb. 1995. doi: 10.3403/00427777.

[30] “Standard operating procedure for soil available phosphorus - Olsen method,” Romw, 2021. Accessed: Aug. 16, 2025. [Online]. Available: http://www.wipo.int/amc/en/mediation/rules

[31] “Knovel - Design and Analysis of Experiments (8th Edition).” Accessed: May 08, 2024. [Online]. Available: https://app-knovel-com.proxy.lib.strath.ac.uk/kn/resources/kpDAEE0013/toc

[32] B. Durakovic, “Design of experiments application, concepts, examples: State of the art,” *Periodicals of Engineering and Natural Sciences*, vol. 5, no. 3, pp. 421–439, Dec. 2017, doi: 10.21533/pen.v5i3.145.

[33] A. Dean, D. Voss, and D. Draguljić, “Springer Texts in Statistics Design and Analysis of Experiments Second Edition.” [Online]. Available: http://www.springer.com/series/417

[34] S. S. Ranade and P. Thiagarajan, “Selection of a design for response surface,” *IOP Conf Ser Mater Sci Eng*, vol. 263, no. 2, Dec. 2017, doi: 10.1088/1757-899X/263/2/022043.

[35] S. Bhattacharya and S. Bhattacharya, “Central Composite Design for Response Surface Methodology and Its Application in Pharmacy,” *Response Surface Methodology in Engineering Science*, Jan. 2021, doi: 10.5772/INTECHOPEN.95835.

[36] B. Ait-Amir, P. Pougnet, and A. El Hami, “Meta-Model Development,” *Embedded Mechatronic Systems 2: Analysis of Failures, Modeling, Simulation and Optimization*, pp. 157–187, Jan. 2020, doi: 10.1016/B978-1-78548-190-1.50006-2.

[37] G. P. Jones, C. Stambaugh, N. Stambaugh, and K. E. Huber, “Analysis of variance,” *Translational Radiation Oncology*, pp. 171–177, Jan. 2023, doi: 10.1016/B978-0-323-88423-5.00041-8.

[38] B. M. King, “Analysis of Variance,” *International Encyclopedia of Education, Third Edition*, pp. 32–36, Jan. 2010, doi: 10.1016/B978-0-08-044894-7.01306-3.

[39] T. A. Saleh, “Adsorption technology and surface science,” in *Interface Science and Technology*, vol. 34, Elsevier, 2022, pp. 39–64. doi: 10.1016/B978-0-12-849876-7.00006-3.

[40] M. Atif, H. Z. Haider, R. Bongiovanni, M. Fayyaz, T. Razzaq, and S. Gul, “Physisorption and chemisorption trends in surface modification of carbon black,” *Surfaces and Interfaces*, vol. 31, p. 102080, Jul. 2022, doi: 10.1016/J.SURFIN.2022.102080.

[41] K. S. W. Sing *et al.*, “Reporting physisorption data for gas/solid systems with special reference to the determination of surface area and porosity (Recommendations 1984),” *Pure and Applied Chemistry*, vol. 57, no. 4, pp. 603–619, Jan. 1985, doi: 10.1351/PAC198557040603.

[42] B. D. Zdravkov, J. J. Čermák, M. Šefara, and J. Janků, “Pore classification in the characterization of porous materials: A perspective,” *Central European Journal of Chemistry*, vol. 5, no. 2, pp. 385–395, Jun. 2007, doi: 10.2478/S11532-007-0017-9/MACHINEREADABLECITATION/RIS.

[43] M. Jaroniec, M. Kruk, and A. Sayari, “Adsorption methods for characterization of surface and structural properties of mesoporous molecular sieves,” *Stud Surf Sci Catal*, vol. 117, pp. 325–332, Jan. 1998, doi: 10.1016/S0167-2991(98)81008-2.

[44] J. Zou *et al.*, “A preliminary study on assessing the Brunauer-Emmett-Teller analysis for disordered carbonaceous materials,” *Microporous and Mesoporous Materials*, vol. 327, p. 111411, Nov. 2021, doi: 10.1016/J.MICROMESO.2021.111411.

[45] S. Brunauer, P. H. Emmett, and E. Teller, “Adsorption of Gases in Multimolecular Layers,” *J Am Chem Soc*, vol. 60, no. 2, pp. 309–319, Feb. 1938, doi: 10.1021/JA01269A023.

[46] F. Ambroz *et al.*, “Evaluation of the BET Theory for the Characterization of Meso and Microporous MOFs,” *Small Methods*, vol. 2, no. 11, p. 1800173, Nov. 2018, doi: 10.1002/SMTD.201800173.

[47] J. Zou *et al.*, “A preliminary study on assessing the Brunauer-Emmett-Teller analysis for disordered carbonaceous materials,” *Microporous and Mesoporous Materials*, vol. 327, p. 111411, Nov. 2021, doi: 10.1016/J.MICROMESO.2021.111411.

[48] J. Rouquerol, P. Llewellyn, and F. Rouquerol, “Is the BET equation applicable to microporous adsorbents?,” *Stud Surf Sci Catal*, vol. 160, pp. 49–56, 2007, doi: 10.1016/s0167-2991(07)80008-5.

[49] K. S. W. Sing, F. Rouquerol, J. Rouquerol, and P. Llewellyn, “Assessment of Mesoporosity,” *Adsorption by Powders and Porous Solids: Principles, Methodology and Applications: Second Edition*, pp. 269–302, Jan. 2014, doi: 10.1016/B978-0-08-097035-6.00008-5.

[50] S. Fu *et al.*, “Accurate characterization of full pore size distribution of tight sandstones by low-temperature nitrogen gas adsorption and high-pressure mercury intrusion combination method,” *Energy Sci Eng*, vol. 9, no. 1, pp. 80–100, Jan. 2021, doi: 10.1002/ESE3.817.

[51] E. P. Barrett, L. G. Joyner, P. P. Halenda Vol, R. -RnAtn Apj, and R. A. Vn-Rn Atn Ac, “The Determination of Pore Volume and Area Distributions in Porous Substances. I. Computations from Nitrogen Isotherms,” *J Am Chem Soc*, vol. 73, no. 1, pp. 373–380, Jan. 1951, doi: 10.1021/JA01145A126.

[52] ASTM International, “Standard Test Method for Carbon Black-Total and External Surface Area by Nitrogen Adsorption 1”, doi: 10.1520/D6556-14.

[53] H. Swenson and N. P. Stadie, “Langmuir’s Theory of Adsorption: A Centennial Review,” *Langmuir*, vol. 35, no. 16, pp. 5409–5426, Apr. 2019, doi: 10.1021/ACS.LANGMUIR.9B00154/SUPPL_FILE/LA9B00154_SI_001.PDF.

[54] S. Kalam, S. A. Abu-Khamsin, M. S. Kamal, and S. Patil, “Surfactant Adsorption Isotherms: A Review,” *ACS Omega*, vol. 6, no. 48, pp. 32342–32348, Dec. 2021, doi: 10.1021/ACSOMEGA.1C04661/ASSET/IMAGES/MEDIUM/AO1C04661_M047.GIF.

[55] S. Azizian and S. Eris, “Adsorption isotherms and kinetics,” *Interface Science and Technology*, vol. 33, pp. 445–509, Jan. 2021, doi: 10.1016/B978-0-12-818805-7.00011-4.

[56] A. M. Muliwa, O. A. Oyewo, and A. Maity, “Recent progress on the removal of aqueous mercury by carbon-based adsorbents: A review,” *Inorg Chem Commun*, vol. 156, p. 111207, Oct. 2023, doi: 10.1016/J.INOCHE.2023.111207.

[57] G. W. Kajjumba *et al.*, “Modelling of Adsorption Kinetic Processes—Errors, Theory and Application,” *Advanced Sorption Process Applications*, Nov. 2018, doi: 10.5772/INTECHOPEN.80495.

[58] A. Kólová and L. Stejskalová, “A review article of Rapid Small-Scale Column Tests.”

[59] M. Poddar, A. N. Brijesh Nair, and A. B. Mahindrakar, “A Review on the Use of Rapid Small Scale Column Test (RSSCT) on Predicting Adsorption of Various Contaminants.” [Online]. Available: www.Iosrjournals.Org

[60] J. I. Goldstein, D. E. Newbury, J. R. Michael, N. W. M. Ritchie, J. H. J. Scott, and D. C. Joy, *Scanning electron microscopy and x-ray microanalysis*, Fourth. Springer New York, 2017. doi: 10.1007/978-1-4939-6676-9/COVER.

[61] S. Nasrazadani and S. Hassani, “Modern analytical techniques in failure analysis of aerospace, chemical, and oil and gas industries,” *Handbook of Materials Failure Analysis with Case Studies from the Oil and Gas Industry*, pp. 39–54, Jan. 2016, doi: 10.1016/B978-0-08-100117-2.00010-8.

[62] M. Omidi *et al.*, “Characterization of biomaterials,” *Biomaterials for Oral and Dental Tissue Engineering*, pp. 97–115, Jan. 2017, doi: 10.1016/B978-0-08-100961-1.00007-4.

[63] I. Fleming and D. Williams, “Spectroscopic Methods in Organic Chemistry, Seventh Edition,” *Spectroscopic Methods in Organic Chemistry, Seventh Edition*, pp. 1–432, Jan. 2020, doi: 10.1007/978-3-030-18252-6.

[64] C. M. Sayes and A. B. Santamaria, “Toxicological Issues to Consider When Evaluating the Safety of Consumer Products Containing Nanomaterials,” *Nanotechnology Environmental Health and Safety: Risks, Regulation, and Management: Second Edition*, pp. 77–115, Jun. 2014, doi: 10.1016/B978-1-4557-3188-6.00005-0.

[65] A. H. Simon, “Sputter Processing,” *Handbook of Thin Film Deposition: Techniques, Processes, and Technologies: Third Edition*, pp. 55–88, Jan. 2012, doi: 10.1016/B978-1-4377-7873-1.00004-8.

[66] H. Ardebili, J. Zhang, and M. G. Pecht, “Defect and failure analysis techniques for encapsulated microelectronics,” *Encapsulation*

Technologies for Electronic Applications, pp. 317–373, Jan. 2019, doi: 10.1016/B978-0-12-811978-5.00008-0.

[67] T. Tamiri and S. Zitrin, "Explosives: Analysis," *Encyclopedia of Forensic Sciences: Second Edition*, pp. 64–84, Jan. 2013, doi: 10.1016/B978-0-12-382165-2.00083-0.

[68] "University of Glasgow - Schools - School of Chemistry - Analytical Services - XPS." Accessed: Sep. 18, 2025. [Online]. Available: https://www.gla.ac.uk/schools/chemistry/analyticalservices/xps/

[69] F. A. Stevie and C. L. Donley, "Introduction to x-ray photoelectron spectroscopy ," *J. Vac. Sci. Technol. A*, vol. 38, p. 63204, 2020, doi: 10.1116/6.0000412.

[70] "Exploring the Principle of Ion Exchange Chromatography and Its Applications | Technology Networks." Accessed: May 13, 2024. [Online]. Available: https://www.technologynetworks.com/analysis/articles/exploring-the-principle-of-ion-exchange-chromatography-and-its-applications-357491

[71] D. Li and S. Liu, "Drinking Water Detection," *Water Quality Monitoring and Management*, pp. 251–267, Jan. 2019, doi: 10.1016/B978-0-12-811330-1.00010-7.

[72] C. Chagué-Goff and H. K. Y. Wong, "14.23 Wet Chemical Methods (pH, Electrical Conductivity, Ion-Selective Electrodes, Colorimetric Analysis, Ion Chromatography, Flame Atomic Absorption Spectrometry, Inductively Coupled Plasma-Atomic Emission Spectroscopy, and Quadrupole Inductively Coupled Plasma-Mass Spectrometry)," *Treatise on Geomorphology: Volume 1-14*, vol. 1–14, pp. 274–281, Jan. 2013, doi: 10.1016/B978-0-12-374739-6.00391-2.

[73] V. Kadam and A. Lakshmanan, "Microscopy and spectroscopy of wool fiber," in *Wool Fiber Reinforced Polymer Composites*, Woodhead Publishing, 2022, pp. 33–48. doi: 10.1016/B978-0-12-824056-4.00005-4.

[74] M. K. Singh and A. Singh, "Inductively coupled plasma–atomic emission spectrometry," in *Characterization of Polymers and Fibres*, Elsevier, 2022, pp. 421–434. doi: 10.1016/B978-0-12-823986-5.00007-5.

[75] D. J. Wanke, J. Heichel, S. Zikeli, T. Müller, and T. E. Hartmann, "Comparison of soil phosphorus extraction methods regarding their suitability for organic farming systems," *Journal of Plant Nutrition and Soil*

Science, vol. 186, no. 5, pp. 599–608, Oct. 2023, doi: 10.1002/JPLN.202300129.

[76] "Stat-Ease » v23.1 » General Sequence of Analysis » Diagnostics » Diagnostics Plots." Accessed: Sep. 22, 2025. [Online]. Available: https://www.statease.com/docs/v23.1/contents/analysis/diagnostics/diagnostics-plots/

[77] "9.4 - Studentized Residuals | STAT 462." Accessed: Sep. 13, 2025. [Online]. Available: https://online.stat.psu.edu/stat462/node/247/

[78] "9.5 - Identifying Influential Data Points | STAT 462." Accessed: Sep. 16, 2025. [Online]. Available: https://online.stat.psu.edu/stat462/node/173/

[79] J. Čejka and S. Mintova, "Perspectives of micro/mesoporous composites in catalysis," *Catal Rev Sci Eng*, vol. 49, no. 4, pp. 457–509, Oct. 2007, doi: 10.1080/01614940701583240;PAGE:STRING:ARTICLE/CHAPTER.

4 Optimising the Biochar Functionalisation Process for Aqueous P-Recovery

4.1 Introduction

To utilise biochar for nutrient recovery it is necessary to determine its capacity in multiple cycles, which firstly requires the biochar to be optimised for recovery of the target nutrient. In this study, it is therefore, necessary to determine optimal production conditions of the biochar with a response of phosphorous recovery, and its subsequent capacity on reuse. Previous work published in the literature has focused on comparison of different functionalisation agents and functionalisation methods for such biochars; and the process of producing biochar for phosphorous removal herein involves both pyrolysis and functionalisation, however the optimal route is unclear [1], [2], [3]. This chapter will address three key factors in the optimisation of functionalised biochar preparation process.

The first factor focusses on functionalisation agents. Whilst many papers compare the performance of different metals for the functionalisation of biochar, they are typically compared at set functionalisation conditions, which may be more optimal for one metal over another, potentially failing to identify the optimal conditions overall [4], [5], [6], [7]. In this work, the performance of two promising metal based functionalisation agents, magnesium (Mg) and calcium (Ca), will be compared at their optimal chemical loading ratio (CLR) and as a function of pyrolysis temperature.

Previous work has also been undertaken to determine the favourable particle size of biochar for adsorption applications, with many studies regulating the particle size of the feedstock or controlling the particle size of the final decorated biochar [4], [8], [9], [10], [11]. However, no work has been carried out comparing particle size control before and after pyrolysis. Hence, the variation in surface chemistry

of functionalised biochar produced via two different methods of particle size control— wood grinding vs biochar grinding— is examined.

Finally, chemical impregnation of biomass or biochar is by far the most common method of functionalisation used in the literature [2], [12], [13]. Typically, biomass is impregnated with a metal chloride whereas biochar is impregnated with a metal oxide/carbonate. Currently, no work in the literature compares the impregnation of biomass with a precursor metal chloride salt to the impregnation of biochar with the metal oxide/carbonate derived from thermal treatment of said chloride salt. This work will compare the P-recovery performance of biochar produced from pre-pyrolysis $CaCl_2$ impregnated feedstock, post pyrolysis $Ca(OH)_2$ decorated biochar, and post pyrolysis $CaCO_3$ decorated biochar.

4.2 Method and Nomenclature

Functionalised biochar was produced according to the procedure detailed in *Section 3.2.1*, where softwood wood chips were gently stirred in either $MgCl_2$ or $CaCl_2$ solution for 2 h at the chemical loading ratio (CLR) given in *Table 4.2*, dried in an oven at 100 °C for 24 h, pyrolyzed at pyrolysis temperatures in *Table 4.2*, and resulting char ground to particle sizes of 0.5-1 mm.

Samples were named using a system of two identifiers. Firstly, a component related to the functionalisation method: for those involving a functionalisation agent, the initial letters in the prefix to T (temperature) indicate the functionalisation agent used, while the numbers within this prefix indicate the CLR of the functionalisation agent used to modify the wood feedstock from which the biochar was prepared. Note that non-functionalised samples are denoted NA in the prefix. Secondly, the number in the suffix to T is the temperature used for pyrolysis. For example, the notation Mg-1.5-T500 would represent a magnesium decorated biochar with a mass ratio of 1:1.5 wood to $MgCl_2$ powder pyrolyzed at 500 °C, while NA600 would be a non-functionalised biochar obtained via pyrolysis at 600 °C.

4.3 Comparison of Mg-rich and Ca-rich biochar

The phosphate adsorption performance of biochars produced using two different functionalisation agents were compared, alongside non-functionalised biochar. As discussed in *Section 2.2.3,* pyrolysis temperature and CLR are key process parameters that affect the adsorption performance of chemically functionalised biochar. Optimisation of these conditions was carried out for both functionalisation agents to compare performance at their respective optimal functionalisation conditions. CLR's ranging from 1-2 were used, covering the range commonly used in the literature [14], [15], [16], [17], [18], [19], [20], [21]. Pyrolysis temperatures ranging from 500-700 °C were selected, based on optimal temperatures for favourable physical characteristics of wood-based feedstocks in previous studies [22]. To carry out optimisation of pyrolysis temperature and CLR, an orthogonal central composite design was used to carry out multivariate analysis, with coded values reported in *Table 4.1*.

Table 4.1: Functionalisation parameters and their coded values for central composite design to produce biochars synthesised in this study

Variables (factors)	**Units**	**Variables (α=0.5)**				
		Low (-1)	Mid (0)	High (1)	-α	+α
Temperature (A)	°C	500	600	700	550	650
CLR (B)	Wt:wt	1	0	2	1.25	1.75

Table 4.2: Pyrolysis temperatures and functionalisation agent chemical loading ratios (CLR) used in the experimental design to produce biochars synthesised in this study, selected using Design of Experiments statistical design

Non-Modified									
Temperature (°C)	500			600			700		
CLR (Wt:wt)	0			0			0		
Mg-Modified									
Temperature (°C)	500	550	550	600	600	600	650	650	700
CLR (Wt:wt)	1.5	1.25	1.75	1	1.5	2	1.25	1.75	1.5
Ca-modified									
Temperature (°C)	500	550	550	600	600	600	650	650	700
CLR (Wt:wt)	1.5	1.25	1.75	1	1.5	2	1.25	1.75	1.5

4.3.1 Chemical Characterisation

XRD was used to confirm the presence of nanocrystals on the biochar surface from the transformation of functionalisation agents during pyrolysis, as such analysis was carried out on biochar samples only. *Figure 4.1a* shows the XRD spectrum obtained for a wood treated with $MgCl_2$ to form a biochar with MgO crystals on the surface, whilst a wood sample treated with $CaCl_2$ produced a biochar with $CaCO_3$ (calcite) on its surface (*Figure 4.1b)*. *Figure 4.1c* shows the XRD spectrum obtained for a non-functionalised biochar produced at a pyrolysis temperature of 600 °C. This biochar also shows $CaCO_3$ crystals on the surface, despite a lack of any chemical agent in the synthesis process, suggesting the presence of calcium in the feedstock itself. Peaks for calcite are more intense in the calcium treated biochar (*Figure 4.1b*) than the non-functionalised biochar (*Figure 4.1c*), possibly due to a greater number of crystals present in the calcium treated biochar. The presence of MgO and $CaCO_3$ on the biochar surface was further confirmed by FTIR results shown in *Figure 4.2*. The broad peak centring at 3348 cm^{-1} is attributed to convoluted O-H bonds in the biochar/woodchips [23].

Biochar produced from magnesium treated wood exhibits a peak at 553 cm^{-1}, characteristic of Mg-O vibrations [24]. The peak at 1416 cm^{-1}, present on the spectra of Ca-1.75-T650 and NA600 biochar, can be ascribed to the asymmetric stretching of the C-O bond of carbonated calcium oxide particles, with the peak at 871cm^{-1} characteristic of out-of-plane bending of the C-O bond in calcite [25], [26], [27]. Wood chips also show the presence of a P-O bond at 1025 cm^{-1} [28], and various peaks characteristic of cellulose (1315 cm^{-1}), and lignin (1215,1230,1270,1740 cm^{-1}) as well as peaks common to both (1371,1420,1460, 1647 cm^{-1}) can be seen on the spectra for woodchips between 1700-1180 cm^{-1} [29], [30] . The presence of phosphate from the feedstock can be seen to remain in the spectra of non-functionalised biochar, however no distinct peak can be seen in the functionalised samples. The absence of peaks representing cellulose and lignin on the spectra of the biochar samples indicate these components of woodchips to be successfully broken-down during pyrolysis.

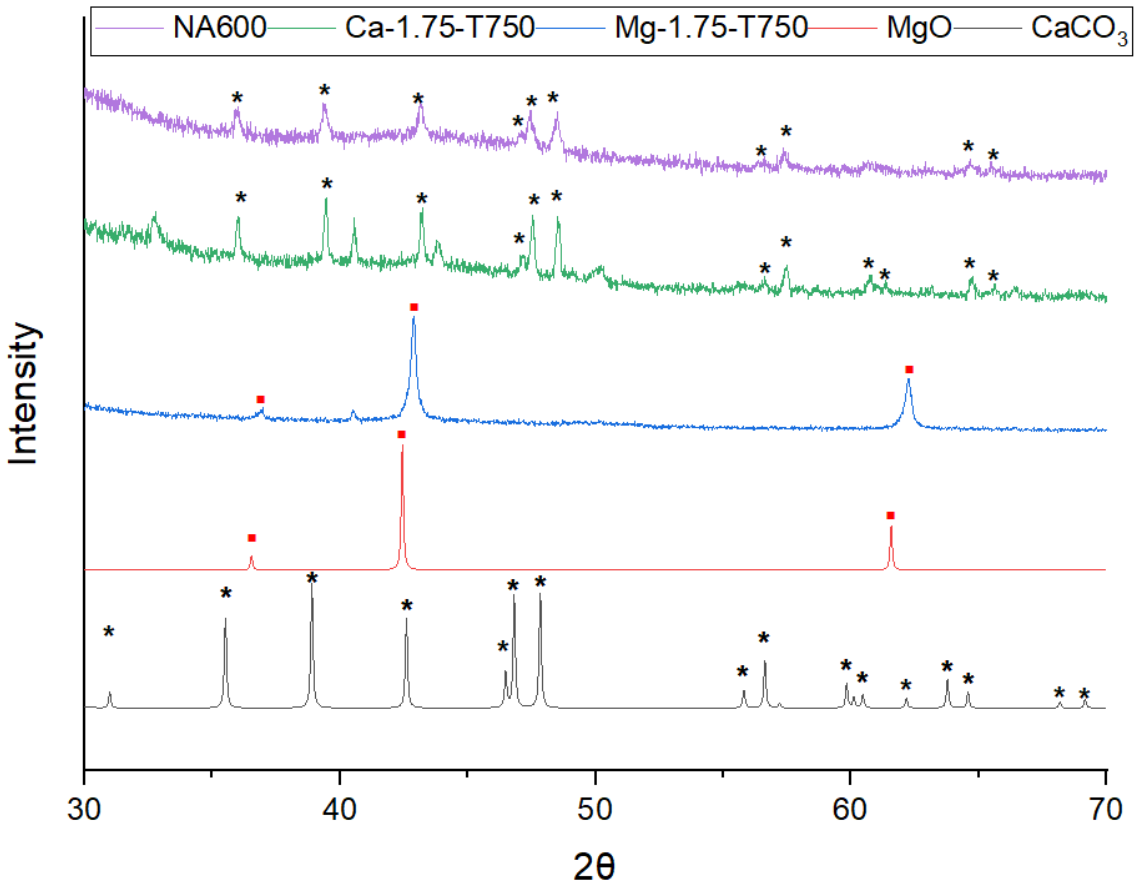

Figure 4.1: XRD pattern of NA600 (purple), Ca-1.75-T650 (green), and Mg-1.75-T650 (blue0 biochar samples synthesised in this work with XRD patterns of pure $CaCO_3$ (black) and MgO (red).

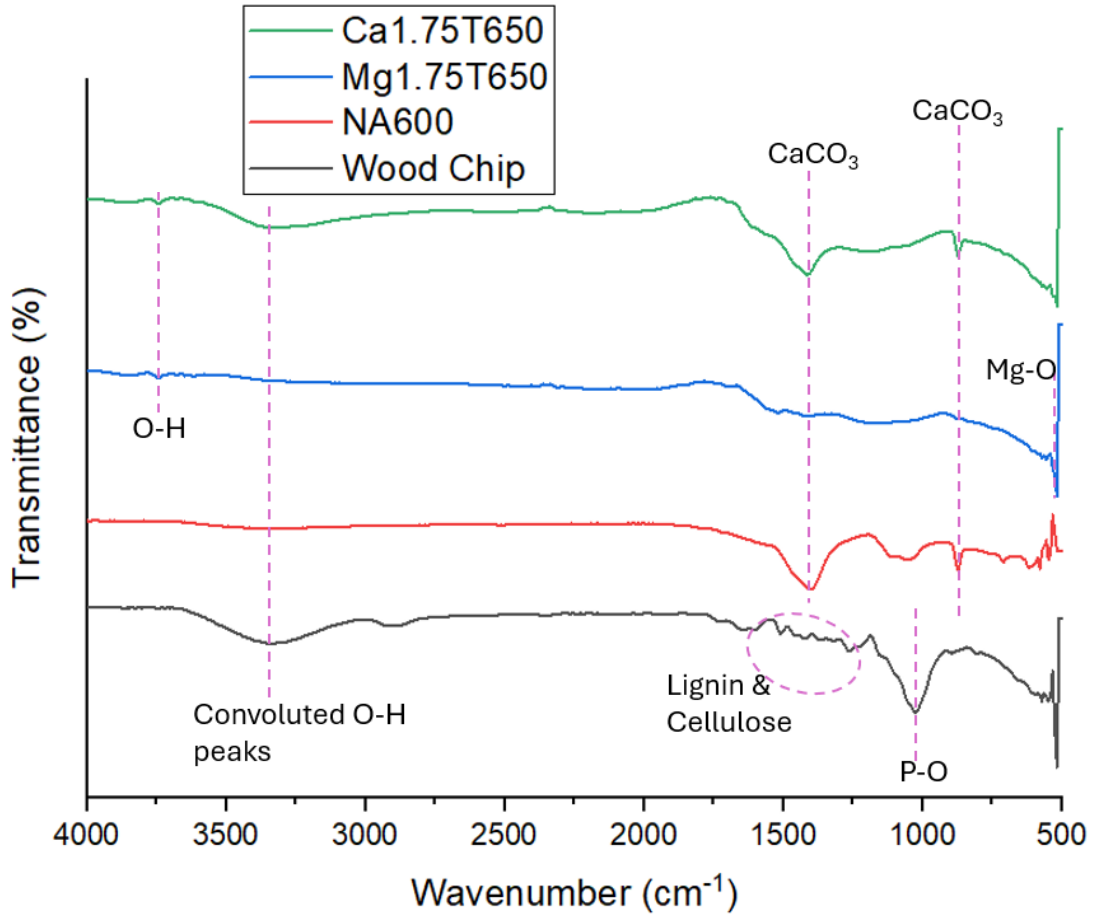

Figure 4.2: FTIR spectra of wood chips(black), NA600 biochar (red), Mg-1.75-T650 biochar (blue), and Ca-1.75-T650 biochar (green) synthesised in this work.

4.3.2 Physical Characterisation

Table 4.3 shows the yields and physical properties of the various biochars synthesised within this study. For functionalised biochar yield was based on the total mass of chemically impregnated softwood (mass of softwood plus metal chloride salt absorbed by the woodchips) entering the furnace. The yields for non-functionalised biochars ranged from 17.7 to 31.3 %, for Mg-decorated char from 30.3 to 38.5 %, and for Ca-decorated char from 29.2 to 40.5 %. As expected, due to increased thermal degradation and volatilisation of organic material, yield decreased with increasing pyrolysis temperature. Biochars produced from chemically impregnated feedstock exhibited notably higher yields than those

produced from non-impregnated feedstock, this can be attributed both to the mass of Mg and Ca based mineral compounds (MgO, $MgCl_2$, $CaCO_3$, and $CaCl_2$) in the functionalised biochar and the potential of $MgCl_2$ and $CaCl_2$ to promote char formation and suppress volatile release [31]. During pyrolysis Ca^{2+} and Mg^{2+} can act as Lewis acid catalysts, catalysing dehydration and cross-linking reactions, supporting the formation of thermally stable carbonaceous structures and reducing the release of volatiles[32], [33]. Generally, there is a mild decrease in yield with increasing CLR, and the formation of pore blocking heavy tars has been known to be reduced by the presence of metals during pyrolysis. It is possible that the presence of magnesium and calcium reduced the formation of tars within the biochars, in turn, decreasing the yield [34], [35]. During pyrolysis dehydration and depolymerisation reactions directly compete. When dehydration reactions dominate due to being catalysed in the presence of a Lewis acid (Ca^{2+} and Mg^{2+}) fewer volatiles capable of producing tars are produced, with cracking of volatiles which are present into smaller molecules also catalysed by the presence of Ca^{2+} and Mg^{2+}(primarily through interactions with oxygen containing functional groups), resulting in fewer heavy tars condensing inside pores. The proportion of external surface area increased with increasing pyrolysis temperature. Non-functionalised biochar samples exhibited higher surface area than those of Mg-biochars, which were higher again than the Ca-chars. One reason for this could be due to the presence of metal oxide/carbonate crystals sitting on the external char surface, blocking pores and, subsequently, reducing the surface area. The Ca-char surfaces are decorated with $CaCO_3$, whereas Mg-chars show a distribution of MgO on their surfaces (as seen in *Section 4.3.1* above). The notable reduction in surface area between the Mg and Ca biochars may be due to larger crystals present on the surface of the Ca-chars, blocking more of the porosity of the char.

*Table 4.3: Yields and physical characteristics of biochar samples synthesised in this study.**

Biochar Sample	Yield (%)	Surface Area (m^2/g)	External Surface Area (m^2/g)	Pore Volume (cm^3/g)	Average pore size (nm)
NA500	31.3	345	45	0.05	9
NA600	24.8	389	85	0.19	5
NA700	17.7	563	183	0.31	3
Mg-1.5-T500	38.5	360	29	0.06	4
Mg-1.25-T550	37.4	327	65	0.13	3
Mg-1.75T550	35.8	355	51	0.09	4
Mg-1-T600	35.4	399	60	0.14	4
Mg-1.5-T600	33.9	357	68	0.14	3
Mg-2-T600	34.9	427	62	0.19	4
Mg-1.25-T650	32.1	431	64	0.15	3
Mg-1.75-T650	31.4	315	57	0.19	4
Mg-1.5-T700	30.3	431	183	0.31	3
Ca-1.5-T500	40.5	21	2	0.02	10
Ca-1.25-T550	36.7	112	17	0.05	10
Ca-1.75-T550	37.8	43	5	0.03	5
Ca-1-T600	39.8	146	55	0.09	3
Ca-1.5-T600	36.0	209	51	0.10	6
Ca-2-T600	33.1	281	88	0.15	2
Ca-1.25-T650	33.6	250	84	0.15	3
Ca-1.75-T650	31.4	159	77	0.13	4
Ca-1.5-T700	29.2	206	101	0.17	4

*Analytical errors for the calculation of total & external surface area, respectively, were 0.1-1.7 m^2/g & 0.1-1.9 m^2/g for Ca-biochars, 1.3-2.1 m^2/g & 1.7-3.6 m^2/g for Mg-biochars, and 1.9-2.7 m^2/g & 3.6-4.6 m^2/g for NA-biochars.

4.2.2.1 Regression Analysis

Regression analysis (ANOVA) was carried out on data obtained from the synthesis and characterisation of Mg and Ca decorated biochars, with temperature and CLR used as variables and all physical characteristics given in *Table 4.3* used as responses. Stat Ease 360 software was used to fit all data to linear, two-factor interaction (2FI), quadratic, and cubic models. For both Mg and Ca decorated biochars, yield was the only response to show good predicted R^2 values (>0.7) for any tested models, fitting the linear model best. The linear

relationships for yield of Mg and Ca decorated biochars with pyrolysis temperature (A) and CLR (B) are shown in *Equations 4.1 & 4.2*, respectively, with summary statistics given in *Table 4.4*.

$$Yield = 34.41 - 4.35A - 0.55B \quad (4.1)$$

$$Yield = 35.34 - 5.35A - 2.42B \quad (4.2)$$

*Table 4.4: Summary statistics for linear fits of yields obtained for Mg and Ca-decorated biochars synthesised in this study. **

Chemical Agent	Mean	Std. Dev	C.V. %	Adj. R^2	Predicted R^2	Adequate Precision	ANOVA model p-value
$MgCl_2$	34.41	0.67	1.95	0.94	0.89	22.49	< 0.0001
$CaCl_2$	35.34	1.46	4.12	0.85	0.74	12.72	0.0013

*Std. Dev is the standard deviation, C.V. is the coefficient of variance, and Adj. R^2 is Adjusted R^2.

The coefficient of variation (C.V.) is a measure of the reproducibility of data, calculated by taking a ratio of the standard deviation of a data set to the mean. A model is generally considered to be reproducible if C.V. is less than 10%. Adequate precision is used by StatEase360 software as a measure of the signal to noise ratio in a dataset, with values above 4 being desirable. The low C.V. values and high adequate precision values show the data to be reproducible with a favourable signal to noise ratio. For both *Equations 4.1 & 4.*2, adjusted and predicted R^2 are in good agreement (less than 0.2 difference) and low p-values show the models to be statistically significant within a 99% confidence interval.

4.3.3 Phosphate Removal Screening

Screening experiments were carried out in duplicate to determine the effects of CLR and pyrolysis temperature on the P-removal potential of the synthesised biochars. Batch phosphate adsorption experiments were carried out at 20 mg_P/L solutions at a 2 g/L dosage rate for a residence time of 2 h. As shown in *Figures 4.3 & 4.4*, a wide range of phosphate removals were observed. The non-functionalised biochars (*Figure 4.4*) not only failed to remove phosphate but

phosphate was leached from the char into solution. In contrast, all biochars produced from chemically impregnated feedstock (*Figure 4.3*) successfully removed phosphate. Phosphate recovery was significantly improved for biochars produced using pyrolysis temperatures above 550 °C; for both Mg-decorated and Ca-decorated biochar samples, this is likely due to an increase in metal oxide/carbonate crystals on the biochar surface as a result of the release of more volatile species during synthesis, promoting adsorption of phosphate [9], [21], [36]. Despite lower surface areas obtained for the functionalised chars, these samples exhibit a greater quantity of favourable sorption sites on the surface. For both functionalisation agents, the production conditions that resulted in optimal phosphate removal were a CLR of 1.75 and a pyrolysis temperature of 650 °C. Overall, the optimal Mg-biochar sample demonstrated a higher level of phosphate recovery than the optimal Ca-decorated biochar sample; however, the functionalisation agent demonstrating the highest P-removal varied for different CLR and pyrolysis temperatures. This demonstrates the importance of comparing different functionalisation agents at individual optimal functionalisation conditions.

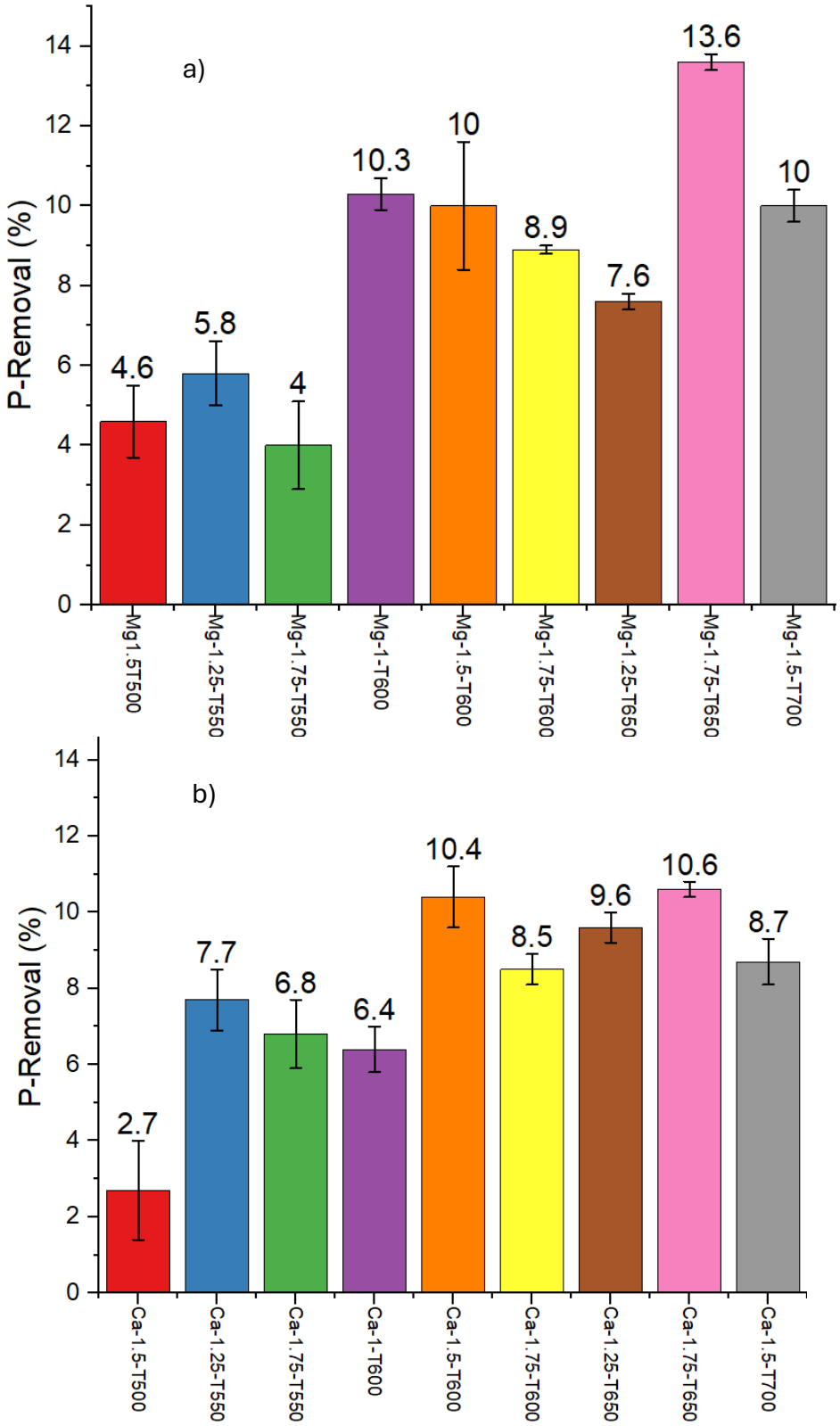

Figure 4.3: Phosphate removal by a) Mg-biochar samples and b) Ca-biochar samples synthesised in this study (batch system, 2 h residence time, 50 mL of 20 mg_P/L phosphate solution, 2g/L biochar dosage, 25 °C, pH~4.5 (unmodified)). Error bars are standard error. Experiments were carried out in duplicate.

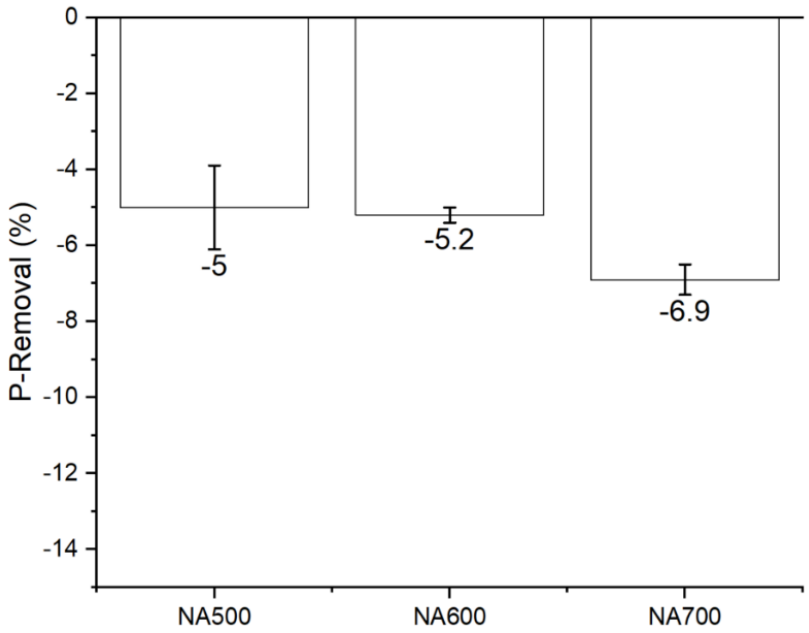

Figure 4.4:Phosphate removal by non-functionalised biochar samples synthesised in this study (batch system, 2 h residence time, 50 mL of 20 mg_P/L phosphate solution, 2g/L biochar dosage,25 °C, pH~4.5 (unmodified)). Error bars are standard error. Experiments were carried out in duplicate.

4.2.3.1 Regression Analysis

Regression analysis was carried out on Mg and Ca decorated biochars, with temperature and CLR used as variables and phosphate removal used as a response. Linear, 2FI, quadratic, and cubic models were fitted to data obtained for both types of functionalised biochar. However, only for Ca-biochar did phosphate removal data fit any of the models with good R^2 values (>0.7). The quadratic relationship between phosphate adsorption, pyrolysis temperature and CLR is given in *Equation 4.3*, with the summary of statistical quantities presented in *Table 4.5*.

$$P - Removal = 10.57 + 2.95A + 0.7167B + 1.9AB - 4.82A^2 - 3.07B^2 \quad (4.3)$$

*Table 4.5: Summary statistics for quadratic fits of 2 h batch phosphate removal for Ca-biochars synthesised in this study (50 mL of 20 mg_P/L phosphate solution, 2g/L biochar dosage, 25 °C, pH~4.5 (unmodified)).**

Chemical Agent	Mean	Std. Dev	C.V. %	Adj. R^2	Predicted R^2	Adequate Precision
$CaCl_2$	7.93	0.50	6.28	0.96	0.82	19.94

*Std. Dev is the standard deviation, C.V. is the coefficient of variance, and Adj. R^2 is Adjusted R^2.

The low C.V. and high adequate precision, shown in *Table 4.5*, indicate that the data for P-removal by Ca-biochar are reproducible with a high signal-to-noise ratio. Values of adjusted and predicted R^2 are high and in relatively good agreement, suggesting the model is a reliable representation of the data. Results obtained from ANOVA analysis are presented below in *Table 4.6*. P-values of the individual factors show A, A^2, and B^2 to be significant model terms. The term AB is shown to have a p-value of 0.1525, suggesting the interaction between pyrolysis temperature and CLR is statistically insignificant, within a 95% confidence interval, with respect to P-removal. Despite this, when this term was removed from the model both adjusted and predicted R^2 decreased, and so the term was retained in *Equation 4.3*. The F-values presented in *Table 4.6* indicate pyrolysis temperature to be the most influential factor with respect to P-removal, while the interaction between temperature and CLR is the least influential.

*Table 4.6: ANOVA results for 2 h batch aqueous phosphate removal of Ca-biochars synthesised in this study (50 mL of 20 mg_P/L phosphate solution, 2g/L biochar dosage, 25 °C, pH~4.5 (unmodified)). *Statistically insignificant*

Source	F-value	p-value
Model	*38.07*	*0.0065*
A-Temperature	105.25	0.0020
B-CLR	6.21	0.0883*
AB	3.64	0.1525*
A^2	75.08	0.0032
B^2	30.50	0.0117

It was unexpected for the DoE modelling to provide a good fit for the data obtained for the Ca-biochars but not for the Mg-biochars. For both

functionalisation agents, when considering the data presented in *Figure 4.3*, the optimal CLR for P-removal appears to increase with increasing pyrolysis temperature. The Mg-biochars show a significant increase in P-removal for chars obtained for pyrolysis temperatures above 550 °C. Additionally, kinetic factors may skew the results. The phosphate removal screening experiments were run for short residence times, as such they were unlikely to have reached equilibrium, with the potential, given that each system is likely to have a different equilibration time, that some experiments managed to reach closer to this state than others. Furthermore, as can be seen in *Figure 4.3* several adsorption experiments exhibited a relatively high associated standard error, which may also have masked any potential trends present. It is likely that a conflation of the aforementioned causes have masked potential relationships between pyrolysis temperature and CLR with true P-removal potential. *Figure 4.5* shows a 3D plot of the relationship of aqueous P-removal of Ca-biochars as a function of pyrolysis temperature and CLR. The plot shows an increase in P-removal with increasing temperature and CLR up to an inflection point of A = 650 °C and B = 1.75. An orthogonal design, where error is reduced in the centre of the experimental map, was used when carrying out this DoE. *Figure 4.5* illustrates optimal conditions to be closer to the edges of the experimental map; indicating further optimisation may be achieved through repeated DoE analysis starting at higher temperatures and CLR, or with a design that is rotatable as well as orthogonal.

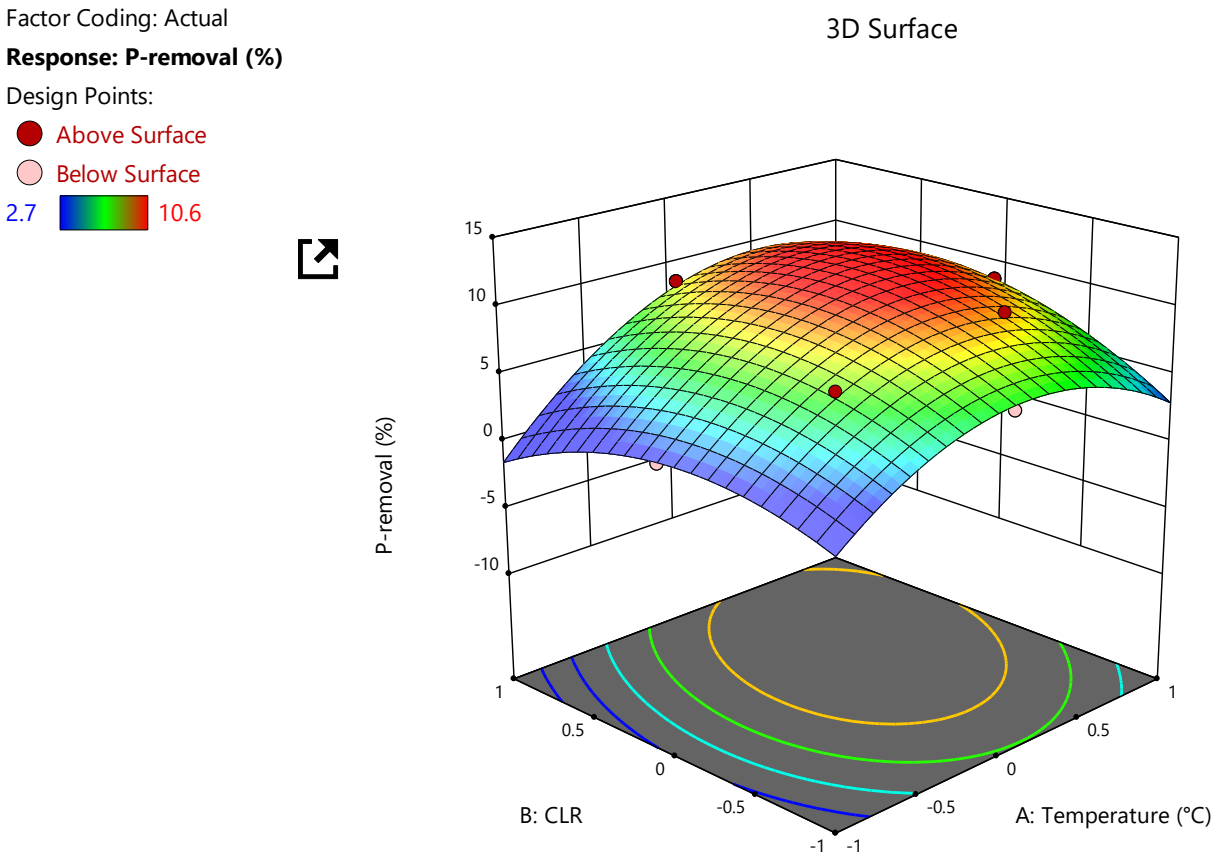

Figure 4.5: 3D contour plot showing interactions of 2 h batch aqueous phosphate removal with pyrolysis temperature and CLR for Ca-biochars synthesised in this study. Coded values are used with CLR ranging from -1 (1) to 1(2) and pyrolysis temperature ranging from -1 (500 °C) to 1 (700 °C). Experimental conditions: 50 mL of 20 mg_P/L phosphate solution, 2g/L biochar dosage, 25 °C, pH~4.5 (unmodified)

4.3.4 Further Adsorption Analysis- Kinetics and Isotherms

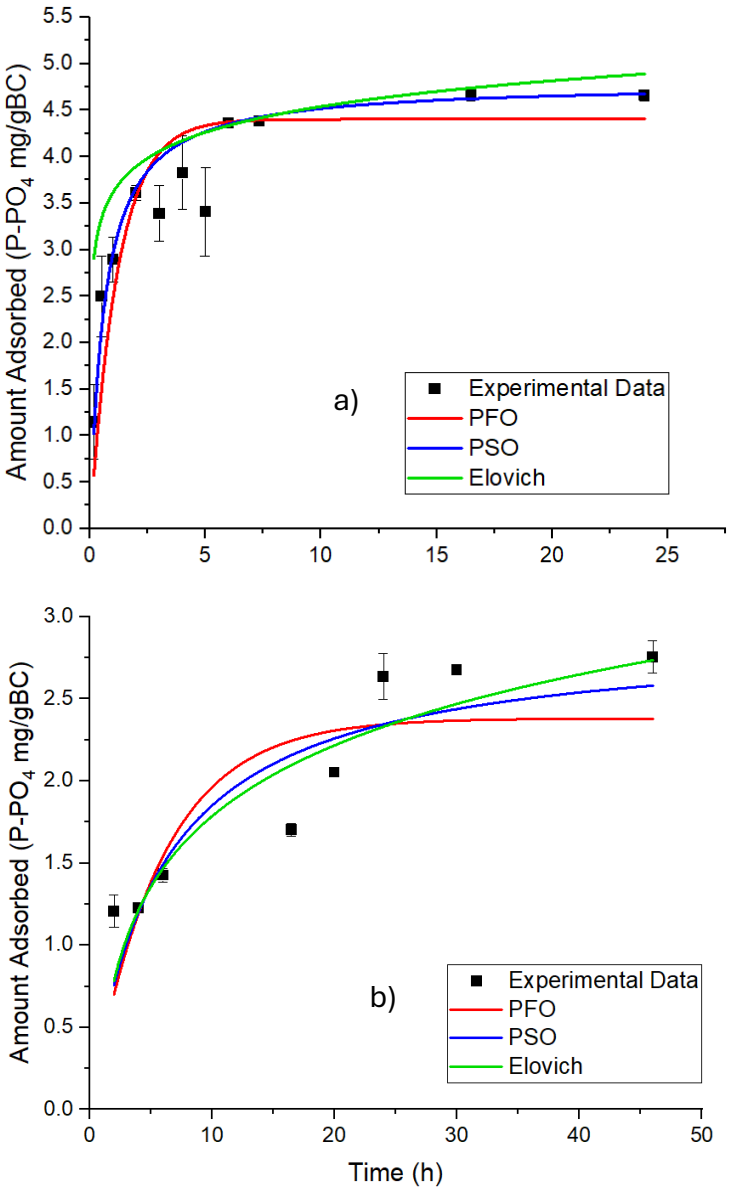

Figure 4.6: Time dependant adsorption of phosphate on a) Mg-1.75-T650 biochar and b) Ca-1.75-T650 biochar with kinetic model fittings: pseudo-first-order (PFO) (red), pseudo-second-order (PSO) (blue), and Elovich model (green).Experimental conditions: 50 mL of 20 mg_P/L phosphate solution, 2g/L biochar dosage, 25 °C, pH~4.5 (unmodified). Error bars are given for all data points, where error bars are not visible this is because error bars are smaller than the symbol size.

Samples Mg-1.75-T650 and Ca-1.75-T650 were chosen for further investigation due to demonstrating the highest P-removal during screening experiments presented in *Figure 4.3*, as such their adsorption kinetics and isotherms were

examined. Batch kinetic experiments were carried out in duplicate using 0.1 g of biochar in 50 mL of 20 mg_P/L phosphate solution. Pseudo-first-order, pseudo-second-order, and Elovich models were fitted to the data obtained for each biochar sample, as shown in *Figure 4.6a&b* with the parameters obtained from the fits given in *Table 4.7*. The pseudo-second-order model provided the best fit of the data obtained for sample Mg-1.75-T650 (adjusted R^2=0.94 and reduced χ^2=1.76). Sample Ca-1.75-T650 exhibited poor fits across all models, with extremely high reduced χ^2 values (>50). The Mg-char removed ~ 47% of the phosphate in solution in an equilibration time of 16.5 h, while the Ca-char removed ~ 28% of phosphate in an equilibration time of 24 h. P-removal experiments demonstrated relatively large error bars for several experimental data points, likely due to low P-removal, resulting in usually small errors being proportionally large. Error bars were considered when fitting models by using instrumental error weighting. Instrumental weighting involves assigning weight to data points based on the reciprocal of the squared error, so that data points with smaller error values are given more importance.

Although several kinetic models produced relatively high R^2 values, the corresponding reduced χ^2 values were often large, indicating that the models captured the overall trend but did not statistically fit the data within expected error margins. This discrepancy suggests systematic deviations between experimental data and model assumptions; this is likely due to P-removal occurring not only through adsorption but also through bulk precipitation as discussed further in *Chapter 6 (Section 6.4.3.2)* of this work.

Table 4.7: Kinetic model parameters and correlation coefficients obtained for phosphate adsorption on selected biochars synthesised in this study. Experimental conditions: 50 mL of 20 mg_P/L phosphate solution, 2g/L biochar dosage, 25 °C, pH~4.5 (unmodified).

	Mg-1.75-T650				
	Parameter 1	**Parameter 2**	**R^2**	**Adjusted R^2**	**Reduced χ^2**
Pseudo-first-order	q_e=4.40	k_1=0.83	0.789	0.766	6.53
Pseudo-second-order	q_e=4.80	k_2=0.34	0.943	0.937	1.76
Elovich	α=2.52	β=3430	0.708	0.676	6.31
	Ca-1.75-T650				
	Parameter 1	**Parameter 2**	**R^2**	**Adjusted R^2**	**Reduced χ^2**
Pseudo-first-order	q_e=2.38	k_1=0.17	0.870	0.848	110.61
Pseudo-second-order	q_e=2.90	k_2=0.06	0.917	0.903	70.84
Elovich	α=1.61	β=1.09	0.940	0.930	50.63

The Langmuir, Freundlich, and Sips adsorption models were used to describe the adsorption performance of samples Mg-1.75-T650 and Ca-1.75-T650, as shown in *Figure 4.7*. Although some models achieved high R^2=0.94 values, the reduced χ^2 values varied dramatically, indicating that statistical fit quality differed substantially among models. For sample Mg-1.75-T650, the Sips isotherms fitted the experimental data the best (adjusted R^2=0.90 and reduced χ^2=0.42). Sample Ca-1.75-T650 was also best described by the Sips model (adjusted R^2=0.85 and reduced χ^2=9.09), suggesting that both biochars possess heterogeneous surfaces. Sample Ca-1.75-T650 displayed extremely high reduced χ^2 values for Langmuir and Freundlich models (>29,000), despite moderate R^2 values. When fitting Langmuir and Freundlich models, instrumental weighting was used, however, when fitting the Sips model the Origin software used for fitting

suggested removing weightings to help with convergence. It is possible that instrumental weighting may have artificially increased R^2 values for the Langmuir and Freundlich models during fitting.

As can be seen from the data presented in *Table 4.8*, the Sips maximum adsorption capacity was 15.6 mg_P/g_{BC} and 78.0 mg_P/g_{BC} for samples Mg-1.75-T650 and Ca-1.75-T650, respectively. The Ca-biochar achieved a moderately high theoretical maximum adsorption capacity compared to reported values for metal-doped biochars; however, this value is still relatively low compared to other Ca-doped chars compared in *Table 2.2, Section 2.2.3.4*. Sample Ca-1.75-T650 demonstrated a higher maximum sorption capacity than sample Mg-1.75-T650, despite the latter displaying both faster kinetics and higher equilibrium uptake for P-removal during kinetic studies at 20 mg_P/L. The adsorption capacity for P on sample Ca-1.75-T650 biochar varied from 28% at c_i = 20 mg_P/L to 21% at c_i = 200 mg_P/L, showing a greater resistance to initial concentration change than for sample Mg-1.75-T750, which ranged from 47% at c_i = 20 mg_P/L to only 9% at c_i = 200 mg_P/L.

Values obtained for the Sips theoretical maximum adsorption capacities are significantly higher than the highest experimental adsorption capacities demonstrated (8.8 mg_P/g_{BC} for sample Mg-1.75-T650 and 21.4 mg_P/g_{BC} for sample Ca-1.75-T650). The cause of large discrepancies between theoretical and experimental adsorption capacities, and poor model fits with extremely large χ^2 values, is likely due to models used assuming all P-removal is adsorption which occurs only on biochar surface sites while the actual process involves a combination of adsorption and bulk precipitation (explained further in Chapter 6). The Sips model incorporates surface heterogeneity and a variable site energy distribution with more curvature flexibility during model fitting than the Langmuir and Freundlich models explaining the substantially reduced χ^2 values. The comparatively better statistical fit of both kinetic and isotherm models for data obtained for sample Mg-1.75-T650 compared to sample Ca-1.75-T650 is likely due to a greater degree of bulk precipitation during P-removal in Ca-decorated

biochars compared to Mg-decorated biochars. This may also account for the greater resistance in percentage P-removal to changes in initial P concentration of sample Ca-1.75-T650 compared to Mg-1.75-T650.

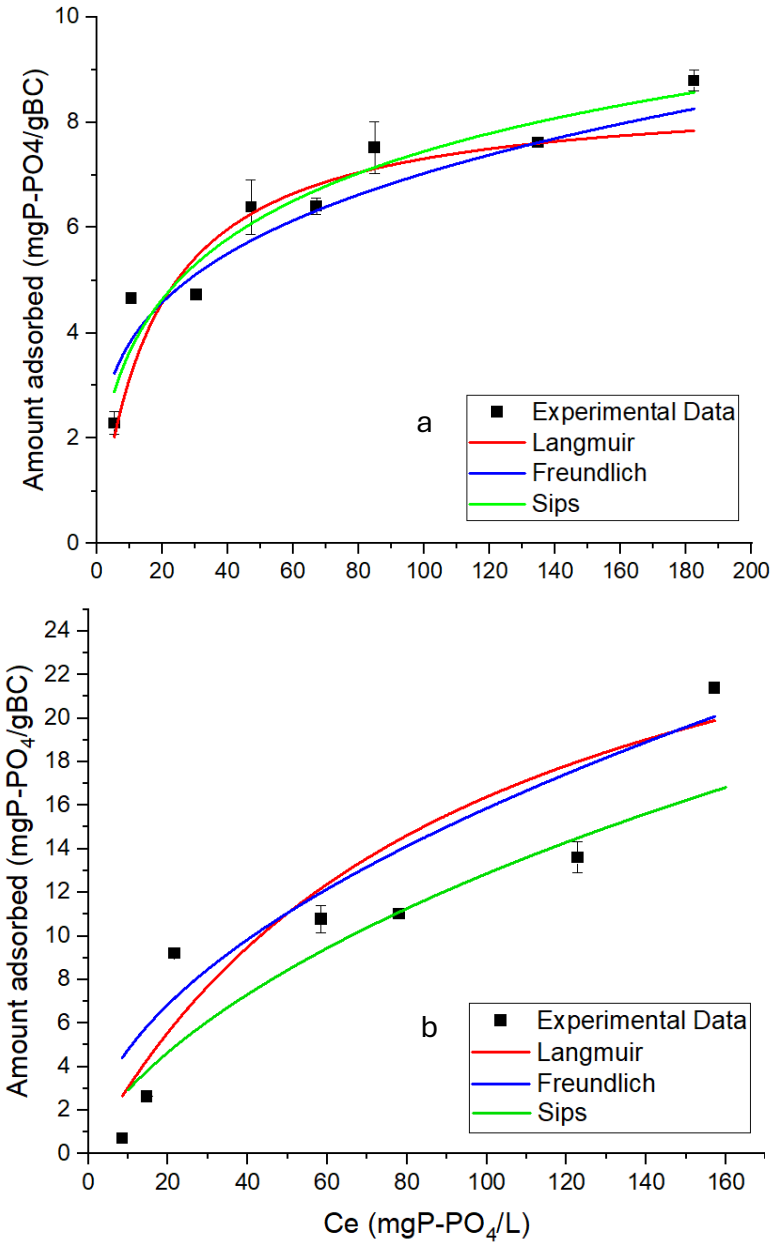

Figure 4.7: The equilibrium adsorption isotherms obtained for phosphate on a) Mg-1.75-T650 biochar and b) Ca-1.75-T650 biochar. Adsorption isotherm fittings: Langmuir (red), Freundlich (blue), Sips (green).Experimental conditions: 50 mL of phosphate solution (10-200 mg_P/L), 2g/L biochar dosage, 25 °C, pH~4.5 (unmodified), equilibriation time for Mg-biochar = 16.5 h and Ca-biochar= 24 h. Error bars are given for all data points, where error bars are not visible this is because error bars are smaller than the symbol size.

Table 4.8: Adsorption isotherm model parameters and correlation coefficients obtained for phosphate adsorption on selected biochars synthesised in this study.). Experimental conditions: 50 mL of phosphate solution (10-200 mg_P/L), 2g/L biochar dosage, 25 °C, pH~4.5 (unmodified), equilibriation time for Mg-biochar = 16.5 h and Ca-biochar= 24 h.

Mg-1.75-T650						
	q_m, experimental= 8.79					
	Parameter 1	**Parameter 2**	**Parameter 3**	**R^2**	**Adjusted R^2**	**Reduced χ^2**
Langmuir	q_m=8.59	k_l=0.06	-	0.880	0.861	157.28
Freundlich	1/n=2.06	k_f=0.27	-	0.961	0.954	51.65
Sips	q_m=15.6	k_s=0.008	n_s= 0.480	0.930	0.902	0.42
Ca-1.75-T650						
	q_m, experimental= 21.39					
	Parameter 1	**Parameter 2**	**Parameter 3**	**R^2**	**Adjusted R^2**	**Reduced χ^2**
Langmuir	q_m=31.8	k_l=0.01	-	0.723	0.668	48876.97
Freundlich	1/n=0.52	k_f=1.44	-	0.834	0.801	29253.41
Sips	q_m=78.0	k_s=0.001	n_s=0.704	0.915	0.852	9.09

In summary, chemical characterisation confirmed the successful production of functionalised biochars via feedstock impregnation. Adsorption screening experiments, reported in this section, illustrate the benefit of functionalised biochars for use as aqueous phase phosphate adsorbents. Both Mg-biochars and Ca-biochars exhibited identical optimal functionalisation conditions. However, adsorption screening experiments demonstrated that changes in CLR and pyrolysis temperature favour the two char types differently. This indicates the need to compare functionalisation agents at individual optimal conditions to understand the best combination of functionalisation conditions, instead of applying a one-size-fits-all approach. Considering the physical characteristics of the biochars, it is evident that, for chemically decorated chars, many factors

commonly used to indicate adsorption performance, such as pore volume and surface area, may not be an appropriate gauge of the potential of biochars in such applications. Data obtained for adsorption kinetics and isotherms revealed that, for both Mg- and Ca-biochars, adsorption occurred on a heterogeneous surface. Overall, despite slower kinetics for the Ca-decorated biochar, this sample was shown to have a higher phosphate removal potential than Mg-decorated biochar over a wide P-concentration range.

4.4 Feedstock vs biochar particle size control

To address the lack of clarity in the associated literature, the effects of controlling particle size at two different process stages were investigated. Based on the results reported earlier in the chapter (Figure 4.7 and Table 4.8), where Ca-biochars demonstrated a superior theoretical and experimental maximum adsorption capacity compared to Mg-biochar, the decision was taken to focus on Ca-decorated biochars for this and future sections of the experimental study. Although calcium decorated biochar (see *Section 4.3.4*) shows a reasonable theoretical maximum adsorption capacity, the system never achieved a high percentage removal of total aqueous phosphate in the system.

In the investigation into the effect of stage of particle size control, it was hypothesised that controlling the particle size of wood feedstock prior to functionalisation, instead of grinding the functionalised biochar, would result in increased phosphate adsorption by preventing any 'dilution' effect of functionalisation via disruption of the decorated biochar surface. Prior to grinding, the surface of decorated biochar is expected to be covered in a large number of $CaCO_3$ crystals on each (external) face of the biochar particle, when grinding the biochar the non-decorated internal structure of biochar is exposed and fewer $CaCO_3$ crystals would be expected on each biochar particle with a lower external surface coverage of favourable adsorption sites for phosphate as illustrated in *Figure 4.8*.

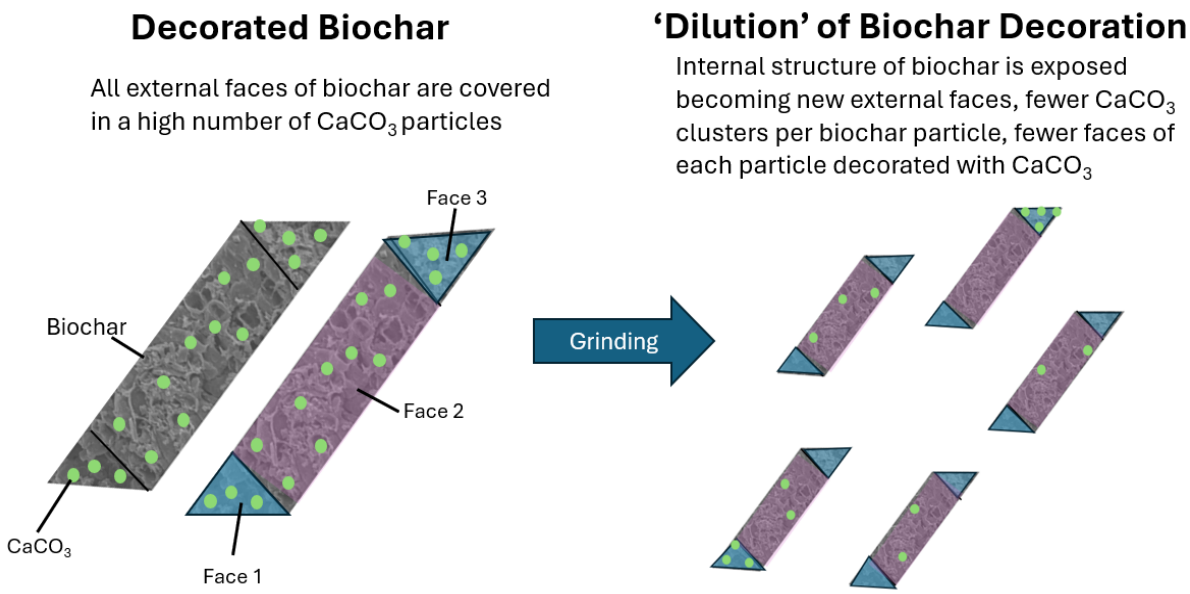

Figure 4.8: Illustration of 'dilution' effect of surface decoration after grinding a decorated biochar.

In the first scenario, softwood chips were ground to 1-2 mm flakes, before being gently stirred in a solution of $CaCl_2$ at a CLR of 1.5 for 2 h. The impregnated wood flakes were then dried in an oven for 24 h at 100 °C and pyrolysed at 650 °C. In scenario 2, as in *Section 5.3* above, wood chips of various sizes were gently stirred for 2 h in a $CaCl_2$ solution at a CLR of 1.5; impregnated wood chips were then dried in an oven for 24 h at 100 °C, pyrolysed at 650 °C, and finally ground to a particle size of 0.5-1 mm. Biochar particle sizes of 0.5-2 mm have been shown to be favourable for application in adsorption systems [38], [39]. Note that larger particle sizes were used for wood grinding (scenario 1) to allow for the reduction of particle size during pyrolysis.

4.4.1 Physical Characteristics

*Table 4.9: Physical characteristics of Ca-1.5-T650 biochar samples synthesised in this work using different particle size control methods: wood grinding and biochar grinding.**

Particle Size Control	Surface Area (m^2/g)	External Surface Area (m^2/g)	Pore Volume (cm^3/g)	Average pore size (nm)
Wood Grinding	388	76	0.12	3
Biochar Grinding	310	51	0.15	2

*Analytical errors for the calculation of surface area are 1.9 m^2/g and 1.2 m^2/g for wood grinding and biochar grinding, respectively. Analytical errors for the calculation of external surface area are 3.2 m^2/g and 2.9 m^2/g for wood grinding and biochar grinding, respectively.

Biochar samples obtained via different particle size methods appeared to exhibit similar physical characteristics displayed in *Table 4.9*. Results obtained from XRF (*Table 4.10*) indicate a higher uptake of functionalisation agent when wood grinding was used compared to biochar grinding. As such, increased specific surface area as a result of wood grinding is, at first, counterintuitive as the content of non-porous Ca-based mineral increases; however, may reflect the potential increase in carbonisation also indicated by XRF results (*Table 4.10*). Instead of a real-terms decrease in pore volume and pore size, for wood grinding compared to biochar grinding, it is assumed these decreased values are rather a reflection of pores being less accessible due to an increased number of Ca-based crystals blocking access to biochars porous structure during BET analysis.

4.4.2 Chemical Characterisation and Morphology

SEM-EDS was used to study the morphological structure and surface chemistry of biochars produced via both particle control scenarios. At x95 magnification (*Figures 4.9*a&c), the top flat surface of biochar produced using wood grinding is similar to that produced using biochar grinding. This structure is similar to SEM results obtained for wood and physically activated softwood biochar in other work, indicating it to be highly dependent on the parent material [40]. In both biochars produced in this work, the top surface comprises of long smooth

channels with relatively evenly distributed rows of pores. However, when wood grinding was used, the biochar can be seen to be covered in crystalline solid flakes. Whilst these flakes are still present on the image of the selected sample where biochar grinding was used, there are fewer present and flakes appear less clustered – this is particularly noticeable at x550 magnification.

EDS mapping, shown in *Figures 4.10 & 4.11*, shows flakes to be areas of high calcium concentration. It is possible the difference in distribution of these flakes is due to a combination of the effects of wood grinding, which increases $CaCl_2$ uptake during feedstock impregnation, and a lack of disruption of the decorated surface. EDS mapping images show calcium to be well distributed over both biochar samples, with the flakes shown to not only be areas of high calcium content, but also high carbon and oxygen content, indicating that these flakes could potentially be clusters of $CaCO_3$ crystals.

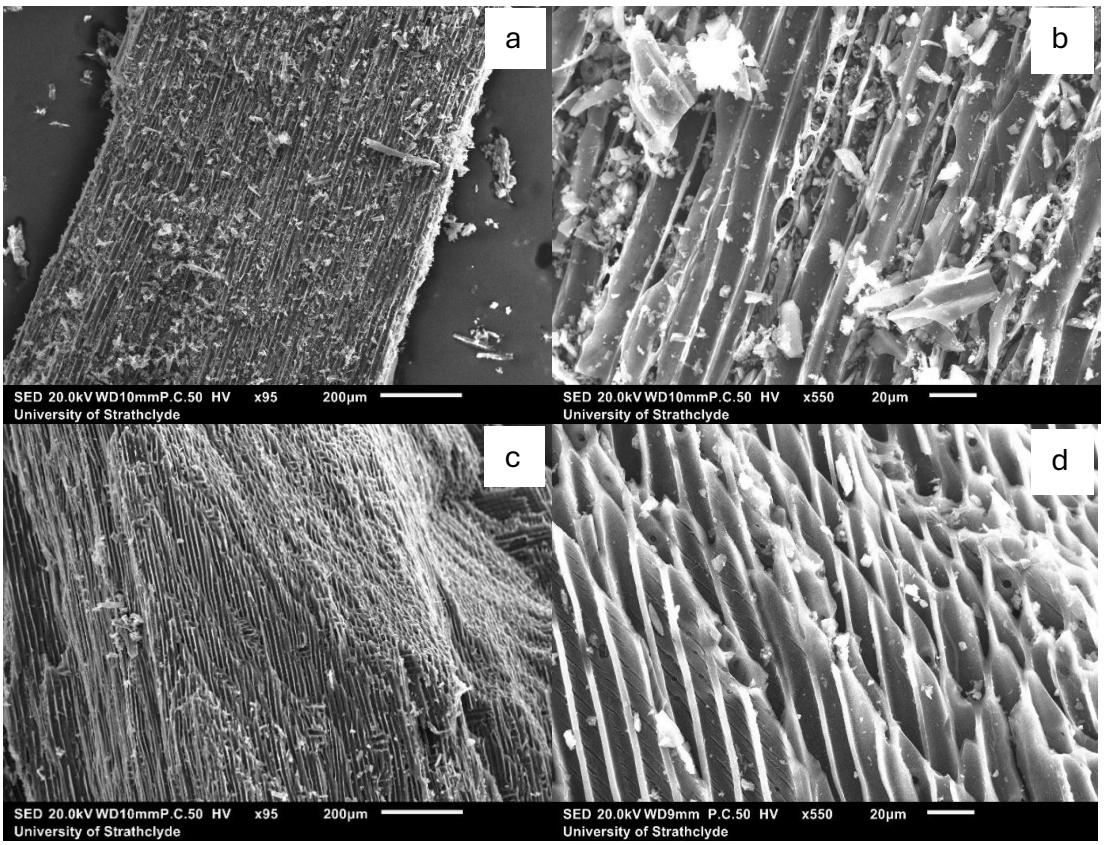

Figure 4.9:SEM images for Ca-1.5-T650 biochar synthesised in this work using wood grinding at a) x95 and b) x550 magnification; and Ca-1.5-T650 biochar synthesised in this work using biochar grinding at c) x95 and d) x550 magnification.

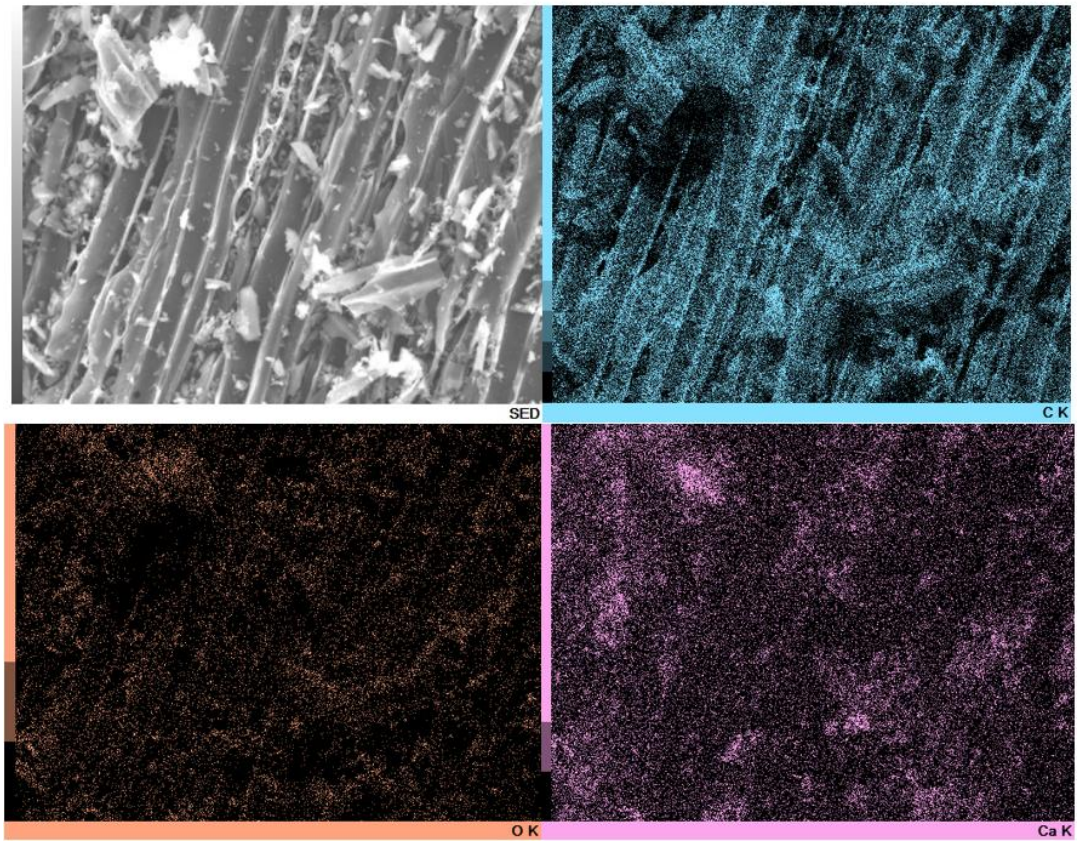

Figure 4.10: SEM-EDS mapping of Ca-1.5-T650 synthesised in this work using wood grinding as a particle size control method showing distribution of C(blue), O (orange), and Ca (purple).

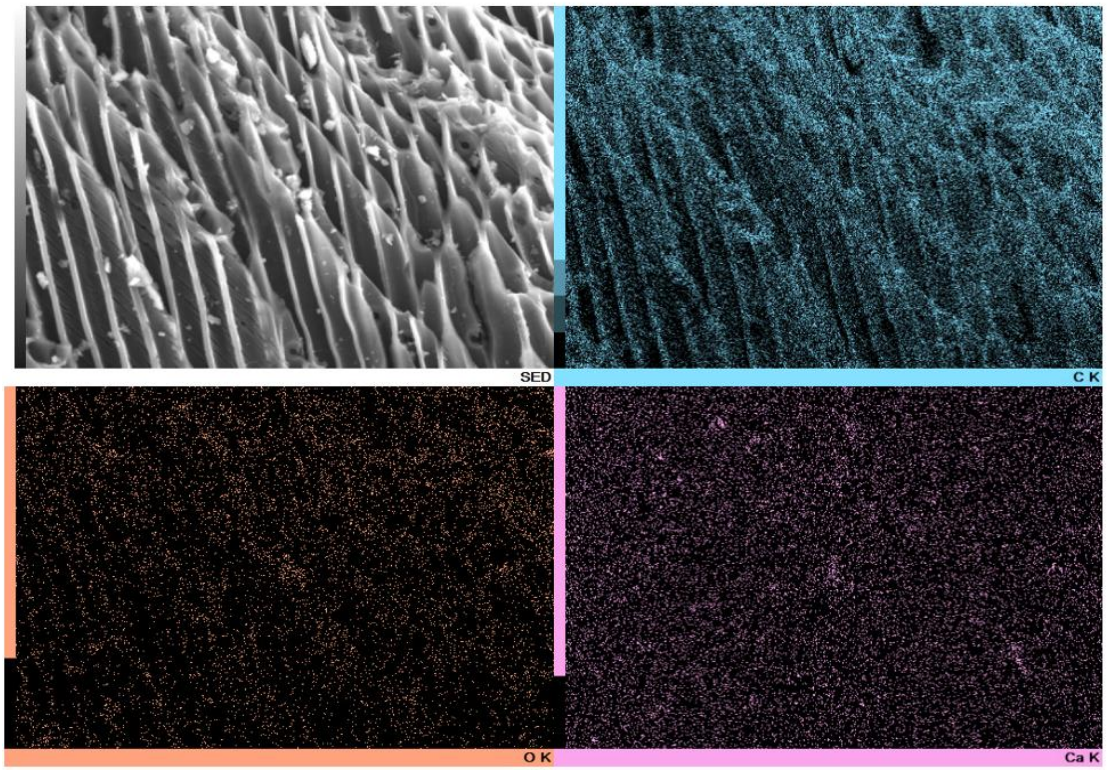

Figure 4.11:SEM-EDS mapping of Ca-1.5-T650 biochar synthesised in this work using biochar grinding as the particle size control method showing distribution of C(blue), O (orange), and Ca (purple).

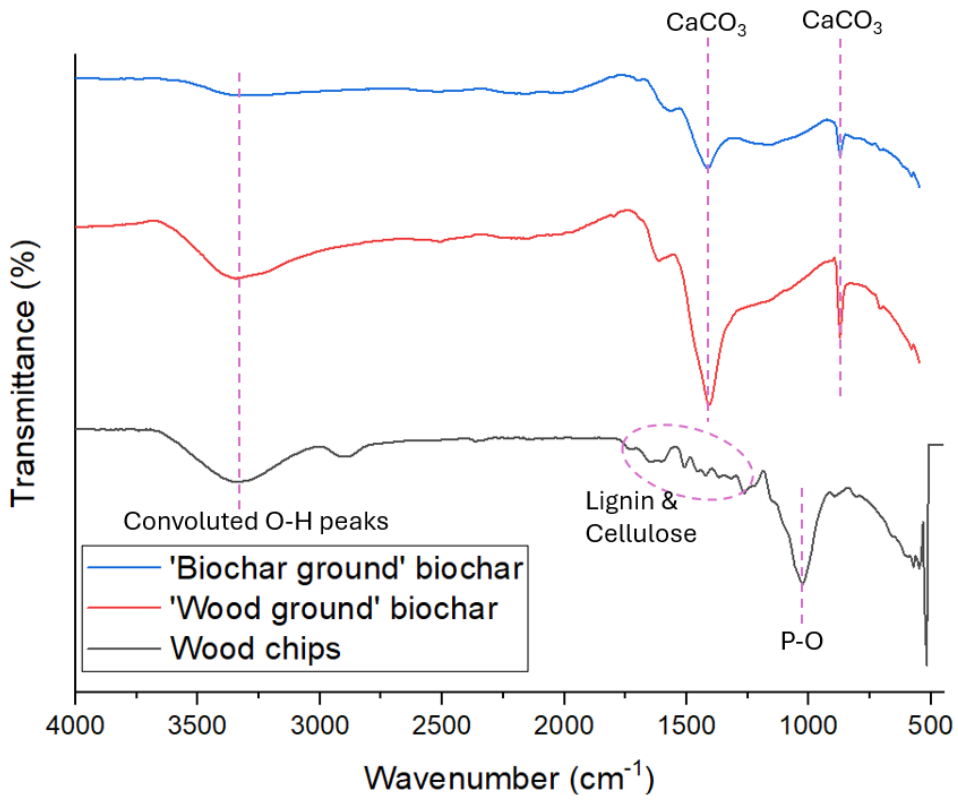

Figure 4.12:FTIR spectra of wood chips (black); Ca-1.5-T650 biochar, where particle size of softwood feedstock was controlled prior to impregnation (wood ground biochar) (red) ; Ca-1.5-T650 biochar, where particle size of decorated biochar was controlled after production (biochar ground biochar) (blue).

FTIR spectra, shown in *Figure 4.12*, for biochar produced via wood grinding and the sample produced via biochar grinding. The spectra indicate the presence of $CaCO_3$ on the surface of the biochars produced using both particle size control methods, with peaks characteristic of asymmetric stretching of the C-O bond of carbonated calcium oxide particles seen at 1410 cm^{-1}, and peaks characteristic of out-of-plane bending of the C-O bond in calcite at 870 cm^{-1} [25], [26], [27]. The most significant difference between the spectra is in the hydrogen bond region. Broad peaks seen between 3700-3000 cm^{-1} in the wood chips and wood ground biochar spectra are representative of various convoluted O-H bonds, very closely resembling spectra for wood in other work, however this peak is significantly reduced for biochar ground char [29]. The broad peaks showing convoluted O-H bonds can result from highly hydrogen bonded polymer O-H networks in the

native wood, or from the presence of various metal associated OH species. It is possible the greater presence of the broad convoluted O-H peak in wood ground biochar compared to biochar ground samples is due to wood grinding enhancing $CaCl_2$ uptake (see *Table 4.10*) increasing the number of metal associated OH species. Once again, the absence of peaks representing cellulose and lignin on the spectra of the biochar samples indicates these components of woodchips to be successfully broken down during pyrolysis.

Table 4.10 shows the data obtained from XRF analysis of biochars produced via both particle size control methods. The percentage weight of lightweight elements was calculated during XRF analysis by PCEDX-Navi software using a correction that assumes all unidentified mass belongs to elements with atomic numbers 12 or lighter; in the case of biochar, this is most likely a mixture of C, H, N, O, and small amounts of lightweight minerals, such as Na and Mg. Mass attributed to lightweight elements is assumed to be predominantly organic in character.

Table 4.10 shows both samples to exhibit a higher mass of calcium than chlorine, suggesting calcium to be present in forms other than $CaCl_2$, in agreement with the results obtained from FTIR analysis. Wood grinding was noted to increase both the calcium and chlorine contents of the biochar; as XRF is a bulk analysis method, this suggests a higher uptake of functionalisation agent, by the softwood, when soaking small wood flakes in the $CaCl_2$ solution, compared to soaking woodchips of varying size. This is likely due to the reduction in particle size of the wood prior to impregnation, increasing the contact area of the softwood with the $CaCl_2$ solution. Whilst the mass of chlorine in the biochar only increased by a factor of 2.2, the mass of calcium increased by a factor of 4.4. A potential reason for the disproportionately high increase in calcium content observed for the sample produced via wood grinding compared to that from biochar grinding could be an increase in the proportion of $CaCl_2$ in the impregnated feedstock forming calcium carbonates/oxides during pyrolysis. An increased number of $CaCO_3$ crystals would explain the larger peaks seen in the

FTIR spectrum when particle size is controlled via wood grinding, compared to biochar grinding. The data presented in *Table 4.10* show that trace metals are present in a higher proportion (by weight), which may indicate a higher degree of carbonisation during pyrolysis via wood grinding compared to biochar grinding.

Table 4.10: XRF results obtained for Ca-1.5-T650 biochar samples synthesised in this work using different particle size control methods: wood grinding and biochar grinding.

	'Wood ground' biochar	**'Biochar ground' biochar**
Calcium (wt%)	18.4	4.2
Chlorine (wt%)	6.0	2.7
Lightweight Elements (wt%)	73.6	92.8
Trace Metals (wt%)	2	0.3

4.4.3 Adsorption

Table 4.11 shows data obtained for aqueous phosphate removal, at residence times of 2 h and 24 h, for biochar samples produced via different particle size control methods. Batch adsorption experiments were carried out in duplicate using 50 mL of 20 mg_P/L solutions with a biochar dosage of 2 g/L.

Table 4.11: Phosphate removal by Ca-1.5-T650 biochar samples synthesised via wood grinding and biochar griding (batch system, 2 h and 24 h residence time, 50 mL of 20 mg_P/L phosphate solution, 2g/L biochar dosage, 25 °C, pH~4.5 (unmodified)). Error given is standard error. Experiments were carried out in duplicate.

Particle Size Control	**Batch phosphate sorption in 2 h (%)**	**Batch phosphate sorption in 24 h (%)**
Wood Grinding	8.2 +/- 0.4	21.3 +/- 1.0
Biochar Grinding	3.7 +/- 0.2	15.6 +/- 0.4

The biochar sample produced using wood grinding was shown to exhibit a significantly higher initial uptake of phosphate after 2 h, removing twice the amount removed by the sample produced using biochar grinding. After 24 h, the

biochar sample produced using wood grinding demonstrated notably higher phosphate removal than the sample produced from biochar grinding. It is suggested that the increased quantity of Ca in the wood ground char (*Table 4.10*) was highly influential in improving the associated P-recovery, by contributing to an enhanced number of sites available for adsorption, as compared to the biochar ground sample. Findings presented in *Table 4.11* support the earlier stated hypothesis: controlling the particle size of wood feedstock prior to impregnation, instead of grinding post-synthesis decorated biochar, results in increased phosphate recovery.

In summary, aqueous P-recovery by biochar was enhanced when particle size was controlled via wood grinding compared to biochar grinding. However, considering all of the physicochemical characterisation data obtained for these samples, particularly XRF data and SEM-EDS analysis, the improvement in adsorption performance can not only be attributed to a lack of disruption of the decorated biochar surface, but is also likely to be from enhanced uptake of $CaCl_2$ during feedstock impregnation and formation of $CaCO_3$ during pyrolysis.

4.5 Comparison of Pre-Pyrolysis and Post-Pyrolysis Biochar Impregnation

A research gap exists in the understanding of how pre- and post-pyrolysis impregnation influences the physicochemical properties of biochar and its efficiency in aqueous P recovery. Addressing this gap is essential for identifying the potential of biochar in the application of water treatment. Following on from the previous results in this chapter it was decided to focus on Ca-decorated biochars for this section of experimental study. During pyrolysis, $CaCl_2$ present on impregnated wood may react with pyrolysis vapours to form $CaCO_3$ or $Ca(OH)_2$ [41]. Functionalised biochar samples produced via three different impregnations are compared: pre-pyrolysis $CaCl_2$ impregnation of wood feedstock (Ca-1.5-T650), post-pyrolysis $Ca(OH)_2$ impregnation of biochar ($Ca(OH)_2$T650), and post-pyrolysis $CaCO_3$ impregnation of biochar ($CaCO_3$T650).

To produce pre-pyrolysis impregnated biochar, softwood wood chips were ground to 1-2 mm flakes, gently stirred in $CaCl_2$ solution for 2 h with a CLR of 1.5, dried in an oven at 100 °C for 24 h, and pyrolysed at 650 °C. To produce post-pyrolysis impregnated biochar softwood wood chips were ground to 1-2 mm flakes, pyrolysed at 650 °C, and the resulting char was gently stirred in either $CaCO_3$ or $Ca(OH)_2$ solution for 2 h at a CLR of 1.5. The post-pyrolysis impregnated biochars were then dried in an oven at 100 °C for 24 h. Unfortunately, $CaCO_3$T650 biochar did not appear to successfully impregnate and was not able to remove any phosphate from solution, for this reason the sample was omitted from chemical and morphological characterisation.

4.5.1 Physical Characteristics

BET data obtained, presented in *Table 4.12*, shows the $CaCO_3$T650 biochar sample to exhibit similar physical characteristics to those of the NA600 and NA700 biochar samples shown in *Table 4.3*. This is expected due to the unsuccessful impregnation of the $CaCO_3$T650 sample. Average pore size did not appear to vary between different functionalisation methods. Pore volume was significantly higher in biochar impregnated post-pyrolysis, with surface area also increasing. Considering the XRF data presented in *Table 4.13*, pore volume and surface area appear to decrease with increasing calcium content, likely due to an increase in non-porous mineral Ca-compounds present leading to proportionally lower area and volume per unit mass, as well as an increase in crystalline groups facilitating a higher degree of pore blocking of biochars carbon structure. Despite differences in total surface area all biochars had a similar proportion of external surface area.

Table 4.12: Physical characteristics of biochar synthesised in this work via pre pyrolysis impregnation (Ca-1.5-T650) and post pyrolysis impregnation ($CaCO_3$T650 and $Ca(OH)_2$T650)

Biochar Sample	Surface Area (m^2/g)	External Surface Area (m^2/g)	Pore Volume (cm^3/g)	Average pore size (nm)
Ca-1.5-T650	388	76	0.12	3
$CaCO_3$T650	490	97	0.26	3
$Ca(OH)_2$T650	459	79	0.23	3

*Analytical errors for the calculation of total & external surface area, respectively, were 1.4-2.4 m^2/g & 3.1-3.9 m^2/g.

4.5.2 Chemical Characterisation

SEM images of $Ca(OH)_2$T650 shown in *Figures 4.13a&b* are similar to that of Ca-1.5-T650 shown in *Figures 4.9a&b*, biochar samples comprise of long smooth channels characteristic of parent material with relatively evenly distributed rows of pores. Comparing images of Ca-1.5-T650 and $Ca(OH)_2$T650 samples at x550 magnification, crystal clusters on the surface of the $Ca(OH)_2$T650 sample selected appear smaller and more spherical. At x 550 magnification, shown in SEM-EDS mapping presented in *Figure 4.14*, the location of crystalline clusters to coincide with areas of high calcium and oxygen concentration, suggesting these crystals could be $Ca(OH)_2$.

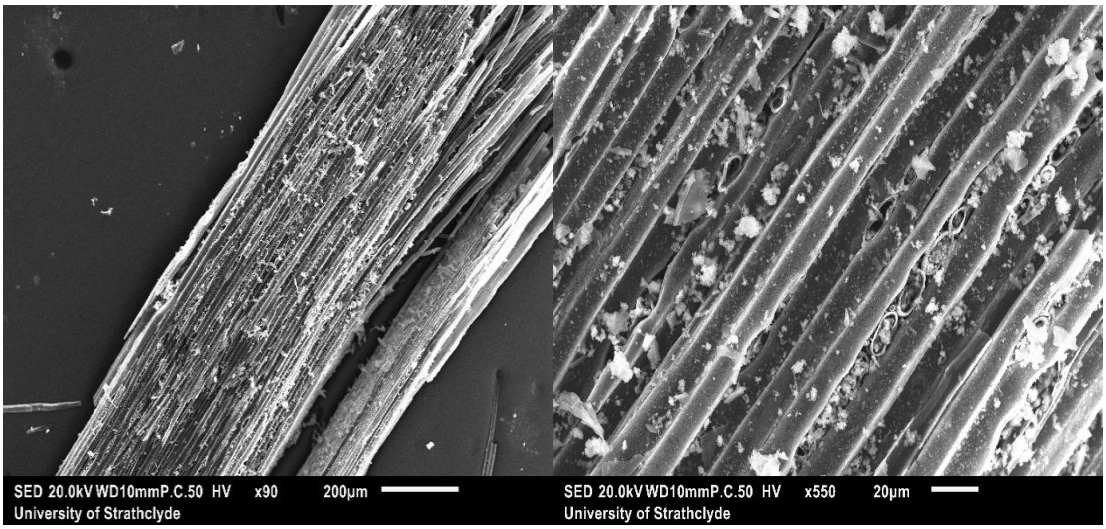

Figure 4.13: SEM imaging of $Ca(OH)_2$T650 biochar synthesised in this study at a) x90 and b) x550 magnification

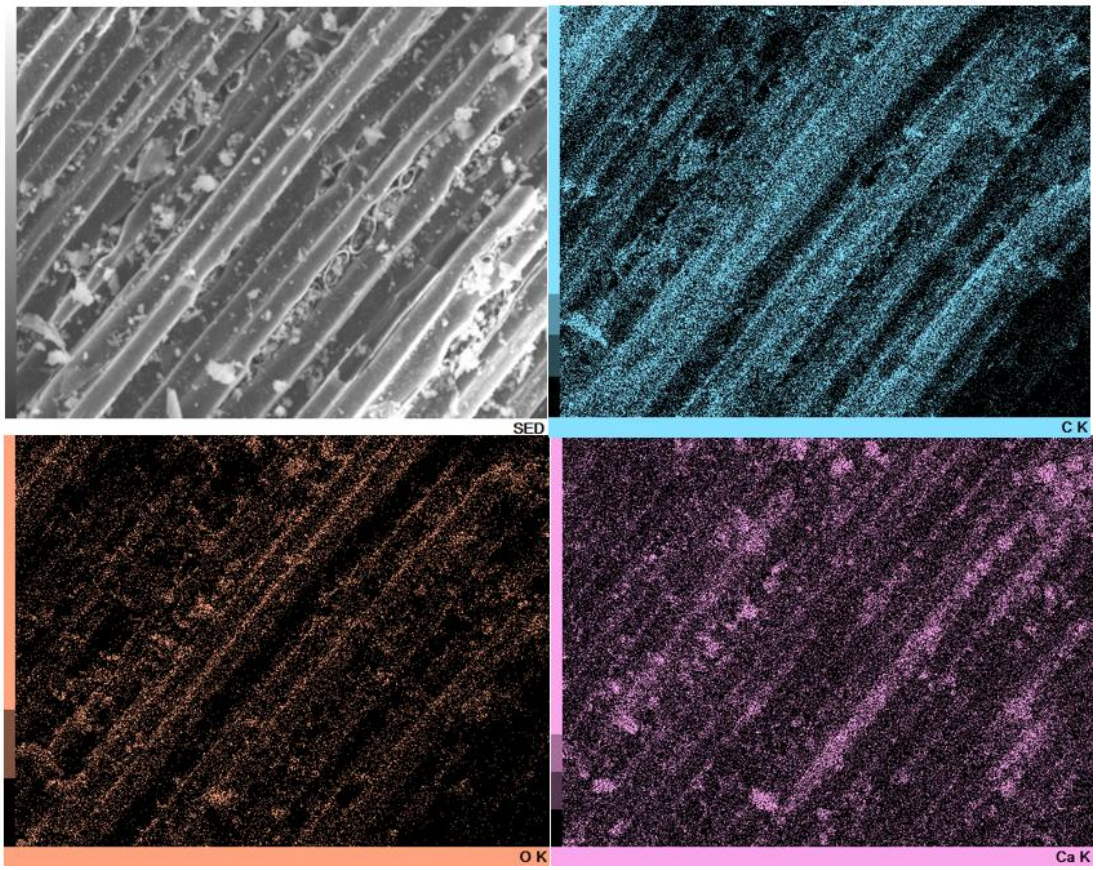

Figure 4.14: SEM-EDS mapping of $Ca(OH)_2$T650 biochar synthesised in this study at x550 magnification showing distribution of C(blue), O (orange), and Ca (purple).

FTIR spectra presented in *Figure 4.15* for Ca-1.5-T650 and $Ca(OH)_2$T650 biochar both provide evidence of $CaCO_3$ (asymmetric stretching of the C-O bond of at 1410 cm^{-1}, and peaks characteristic of out of plane bending of the C-O bond in calcite at 870 cm^{-1}), however peaks are much larger in the Ca-1.5-T650 spectrum, indicating a higher $CaCO_3$ content [25], [26], [27] [42].

The presence of $CaCO_3$ in non-functionalised biochar samples is discussed above (see *Section 4.3.1*), as such its presence in the $Ca(OH)_2$T650 sample was expected, despite impregnation with $Ca(OH)_2$ only. Spectra of the two biochar samples differ most in the hydrogen bond region, $Ca(OH)_2$T650 biochar shows clear peaks between 3590-3550 cm^{-1} indicative of hydrogen bonds with the sharp peak at 3640 cm^{-1} characteristic of O-H stretching in $Ca(OH)_2$ [43]. The broad peak seen between 3700-3000 cm^{-1} in the spectrum of Ca-1.5-T650 is representative of various convoluted O-H bonds [29]. Comparison of $CaCO_3$ and

$Ca(OH)_2$ post-pyrolysis impregnated chars would have been useful to examine the effect of the type of calcium crystal on phosphate uptake.

Characteristic peaks of C=O stretching (1740 cm^{-1}) and C-O stretching (1230 cm^{1}) in lignin are still present in the post-pyrolysis impregnated biochar sample but not the pre-pyrolysis impregnated sample, indicating the presence of $CaCl_2$ to help facilitate the breakdown of lignin during pyrolysis [29], [30].

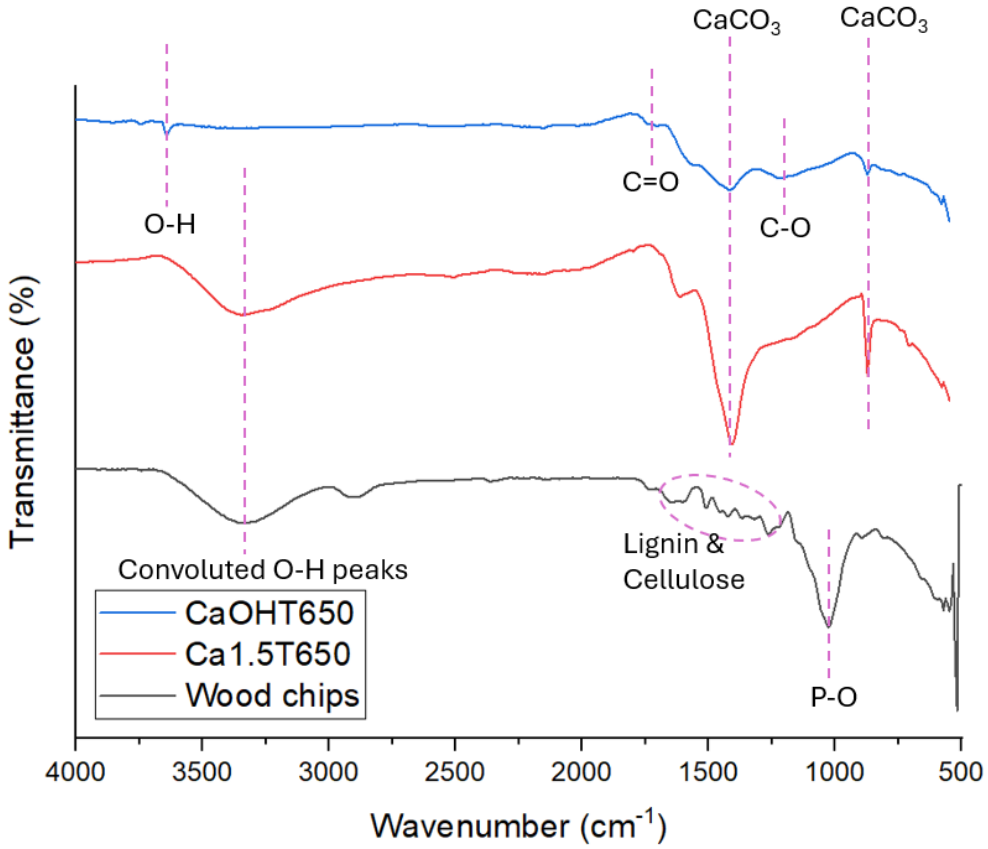

Figure 4.15: FTIR spectra of post-pyrolysis impregnated biochar: $Ca(OH)_2$T650 biochar (blue), pre-pyrolysis impregnated biochar: Ca-1.5-T650 (red), and wood chips feedstock (black).

XRF data obtained and presented in *Table 4.13* provides further evidence of Ca-1.5-T650 biochar sample's elevated $CaCO_3$ content, exhibiting almost twice the calcium content of $Ca(OH)_2$T650 biochar. Sample Ca-1.5-T650 displayed a proportionally low chlorine content compared to calcium, as such calcium must be present in forms other than $CaCl_2$. The increased calcium content of the Ca-1.5-T650 sample compared to the $Ca(OH)_2$T650 sample may be due to a more successful uptake of $CaCl_2$ by wood than $Ca(OH)_2$ by biochar. During

impregnation $CaCl_2$ or $Ca(OH)_2$ are dissolved in water to increase their mobility, it is probable the greater uptake of functionalisation agent is partly due to the significantly higher solubility of $CaCl_2$ than $Ca(OH)_2$ in water. However, this is also likely a significant consequence of pre-pyrolysis impregnated biochar undergoing thermal treatment via pyrolysis after impregnation (helping bind calcium groups to the biochar surface), whilst no thermal or mechanical treatment to provide energy was used during post-pyrolysis impregnation leaving $Ca(OH)_2$ loosely attached to the biochar surface.

Table 4.13: XRF results obtained for biochar samples synthesised in this work: pre-pyrolysis impregnated biochar (Ca-1.5-T650) and post-pyrolysis impregnated biochar($Ca(OH)_2$T650).

	Ca-1.5-T650	**$Ca(OH)_2$T650**
Calcium (wt%)	18.4	9.7
Chlorine (wt%)	6.0	-
Lightweight Elements (wt%)	73.6	88.9
Trace Metals (wt%)	2	1.4

4.5.3 Aqueous P-Removal

Table 4.14 shows data obtained for aqueous P-removal by biochar samples impregnated pre-pyrolysis and post-pyrolysis. Batch experiments were carried out in duplicate for 24 h in 20 mg_P/L solutions with a biochar dosage of 2 g/L.

Table 4.14: Phosphate removal by biochar samples synthesised in this study (batch system, 2 h residence time, 50 mL of 20 mg_P/L phosphate solution, 2g/L biochar dosage, 25 °C, pH~4.5 (unmodified)). Error given is standard error. Experiments were carried out in duplicate.

Biochar Sample	**Batch phosphate sorption (%)**
Ca-1.5-T650	21.3 +/- 1.0
$CaCO_3$T650	-3.1 +/- 1.0
$Ca(OH)_2$T650	9.5 +/- 0.1

Similar to non-functionalised biochar (*Figure 4.4)*, $CaCO_3$T650 did not appear to recover any phosphate, and instead leached out phosphate to the solution. It is suspected that the impregnation of biochar with $CaCO_3$ was partly unsuccessful due to the low solubility of $CaCO_3$ in water. During impregnation with $CaCO_3$ a slurry was formed, whereas $Ca(OH)_2$ and $CaCl_2$ successfully dissolved in solution; as water is used to increase mobility of functionalisation agents it is suspected that $CaCO_3$ never successfully bound to biochar. Furthermore, the thermal energy supplied during pyrolysis helps bind calcium groups to the biochar surface of the pre-pyrolysis impregnated sample through several mechanisms including physical entrapment of crystalline $CaCl_2$ during the formation of pores, electrostatic attraction to oxygenated surface groups, chemical binding via conversion into insoluble minerals (e.g., $CaCO_3$ or $Ca(OH)_2$), and mechanical incorporation after molten-salt infiltration at high temperatures [44], [45], [46]. No thermal or mechanical treatment to provide energy was used during post-pyrolysis impregnation, as such it is unsurprising that decoration of the biochar surface with $CaCO_3$ and $Ca(OH)_2$ was detrimentally affected. Post pyrolysis impregnation with $Ca(OH)_2$ was likely more successful than with $CaCO_3$ due to the more highly alkaline nature and higher solubility of $Ca(OH)_2$ increasing its reactivity with biochars surface (primarily oxygen containing functional groups) compared to $CaCO_3$.

Pre pyrolysis impregnation of woodchips with $CaCl_2$ was shown to increase P-recovery in 24 h batch experiments compared to post pyrolysis impregnation of biochar with $Ca(OH)_2$. However, comparison of biochar samples with the desired similarity in surface functional groups was not achieved due to unsuccessful post-pyrolysis impregnation with $CaCO_3$, the primary form of calcium present on pre pyrolysis impregnated biochars surface (as indicated by *Figure 4.15*).

P recovery was seen to increase with increasing Ca content (*Table 4.13*) despite a decrease in surface area and pore volume (*Table 4.12*) , indicating the extent of

P-recovery to be more dependent on the content of calcium carbonate/hydroxide present on biochars surface than biochars physical characteristics. Current results are not able to distinguish if the increase in P recovery from pre-pyrolysis impregnated biochar is due to increased calcium content or increased favourability of $CaCO_3$ compared to $Ca(OH)_2$ during adsorption. However both Ca content (*Table 4.13*) and 24 h batch P recovery demonstrated by Ca-1.5-T650 was approximately twice that of $Ca(OH)_2$T650 char, implying an increase in functionalisation agent uptake to result in a direct increase in phosphate removal.

4.6 Conclusions

The performance of two functionalisation agents ($CaCl_2$ and $MgCl_2$) were tested at various pyrolysis temperatures and CLRs with Ca-decorated biochar found to display a higher theoretical and experimental P-removal capacity than Mg-decorated biochar over a wide P concentration range. Biochar decorated with Ca was also shown to exhibit a higher degree of pore blocking the biochar decorated with Mg. DoE optimisation of functionalisation conditions found that Ca-biochars and Mg-biochars respond differently to variations in functionalisation conditions, highlighting the importance of using a range of functionalisation conditions when comparing different functionalising agents.

Pre-pyrolysis particle size control of softwood was found to both increase the uptake of $CaCl_2$ by softwood and increase the P-removal potential of biochar, in 24 h batch experiments, compared to post-pyrolysis particle size control. Pre-pyrolysis impregnation was more favourable than post-pyrolysis impregnation for the production of biochar for aqueous P recovery. The increased P recovery is attributed to increased uptake of $CaCl_2$ pre-pyrolysis, likely due to the reduced solubility of $Ca(OH)_2$ and $CaCO_3$ compared to $CaCl_2$ and limitations associated with the lack of thermal treatment after post-pyrolysis impregnation. Overall, the work in this chapter shows the importance of process optimisation for functionalised biochar production. When optimising Ca-decorated biochars production for high aqueous P recovery, process decisions which favoured

increased functionalisation agent uptake enhanced aqueous P removal. Optimal P recovery was achieved when impregnating particle-size-controlled wood flakes pre-pyrolysis with $CaCl_2$.

References

[1] I. W. Almanassra, G. Mckay, V. Kochkodan, M. Ali Atieh, and T. Al-Ansari, "A state of the art review on phosphate removal from water by biochars," *Chemical Engineering Journal*, vol. 409, p. 128211, Apr. 2021, doi: 10.1016/J.CEJ.2020.128211.

[2] T. Vijay *et al.*, "Scotland's Rural College Phosphorus adsorption by functionalized biochar Phosphorus adsorption by functionalized biochar: a review," *Environ Chem Lett*, doi: 10.1007/s10311-022-01519-5.

[3] S. Kumari, Y. Dong, and S. I. Safferman, "Phosphorus adsorption and recovery from waste streams using biochar: review of mechanisms, modifications, and agricultural applications," *Appl Water Sci*, vol. 15, no. 7, pp. 1–25, Jul. 2025, doi: 10.1007/S13201-025-02523-0/METRICS.

[4] F. Yang *et al.*, "Metal chloride-loaded biochar for phosphorus recovery: Noteworthy roles of inherent minerals in precursor," *Chemosphere*, vol. 266, p. 128991, Mar. 2021, doi: 10.1016/J.CHEMOSPHERE.2020.128991.

[5] R. Chanda *et al.*, "Functionalized biochar from vegetable waste for phosphorus removal from aqueous solution and its potential use as a slow-release fertilizer," *Cleaner Materials*, vol. 15, p. 100287, Mar. 2025, doi: 10.1016/J.CLEMA.2024.100287.

[6] A. Mosa, A. El-Ghamry, and M. Tolba, "Functionalized biochar derived from heavy metal rich feedstock: Phosphate recovery and reusing the exhausted biochar as an enriched soil amendment," *Chemosphere*, vol. 198, pp. 351–363, May 2018, doi: 10.1016/J.CHEMOSPHERE.2018.01.113.

[7] S. Saadat, E. Raei, and N. Talebbeydokhti, "Enhanced removal of phosphate from aqueous solutions using a modified sludge derived biochar: Comparative study of various modifying cations and RSM based optimization of pyrolysis parameters," *J Environ Manage*, vol. 225, pp. 75–83, Nov. 2018, doi: 10.1016/J.JENVMAN.2018.07.037.

[8] M. Chen, Y. Liu, J. Pan, Y. Jiang, X. Zou, and Y. Wang, "Low-cost Ca/Mg co-modified biochar for effective phosphorus recovery: Adsorption mechanisms, resourceful utilization, and life cycle assessment," *Chemical Engineering Journal*, vol. 502, p. 157993, Dec. 2024, doi: 10.1016/J.CEJ.2024.157993.

[9] M. Zhang, B. Gao, Y. Yao, Y. Xue, and M. Inyang, “Synthesis of porous MgO-biochar nanocomposites for removal of phosphate and nitrate from aqueous solutions,” *Chemical Engineering Journal*, vol. 210, pp. 26–32, Nov. 2012, doi: 10.1016/j.cej.2012.08.052.

[10] S. B. Liu *et al.*, “Production of biochars from Ca impregnated ramie biomass (Boehmeria nivea (L.) Gaud.) and their phosphate removal potential,” *RSC Adv*, vol. 6, no. 7, pp. 5871–5880, Jan. 2016, doi: 10.1039/C5RA22142K.

[11] D. Zhu *et al.*, “Synthesis and characterization of magnesium oxide nanoparticle-containing biochar composites for efficient phosphorus removal from aqueous solution,” *Chemosphere*, vol. 247, p. 125847, May 2020, doi: 10.1016/J.CHEMOSPHERE.2020.125847.

[12] X. Wang, Z. Guo, Z. Hu, and J. Zhang, “Recent advances in biochar application for water and wastewater treatment: a review,” *PeerJ*, vol. 8, p. e9164, May 2020, doi: 10.7717/PEERJ.9164.

[13] F. Pan *et al.*, “Biochar-enabled phosphorus recovery from aqueous: Advances, applications and challenges,” *Environ Res*, vol. 285, p. 122329, Nov. 2025, doi: 10.1016/J.ENVRES.2025.122329.

[14] Q. Yin, M. Liu, and H. Ren, “Removal of Ammonium and Phosphate from Water by Mg-modified Biochar: Influence of Mg pretreatment and Pyrolysis Temperature”.

[15] R. Chanda *et al.*, “Functionalized biochar from vegetable waste for phosphorus removal from aqueous solution and its potential use as a slow-release fertilizer,” *Cleaner Materials*, vol. 15, p. 100287, Mar. 2025, doi: 10.1016/J.CLEMA.2024.100287.

[16] G. Cai and Z. long Ye, “Concentration-dependent adsorption behaviors and mechanisms for ammonium and phosphate removal by optimized Mg-impregnated biochar,” *J Clean Prod*, vol. 349, p. 131453, May 2022, doi: 10.1016/J.JCLEPRO.2022.131453.

[17] S. Xu *et al.*, “Solvent-Free Synthesis of MgO-Modified Biochars for Phosphorus Removal from Wastewater,” *Int J Environ Res Public Health*, vol. 19, no. 13, p. 7770, Jul. 2022, doi: 10.3390/IJERPH19137770/S1.

[18] S. V. Novais, M. D. O. Zenero, J. Tronto, R. F. Conz, and C. E. P. Cerri, “Poultry manure and sugarcane straw biochars modified with MgCl2 for

phosphorus adsorption," *J Environ Manage*, vol. 214, pp. 36–44, May 2018, doi: 10.1016/J.JENVMAN.2018.02.088.

[19] S. Wang *et al.*, "Adsorption of phosphorus by calcium-flour biochar: Isotherm, kinetic and transformation studies," *Chemosphere*, vol. 195, pp. 666–672, Mar. 2018, doi: 10.1016/J.CHEMOSPHERE.2017.12.101.

[20] S. Zeng and E. Kan, "Sustainable use of Ca(OH)2 modified biochar for phosphorus recovery and tetracycline removal from water," *Science of The Total Environment*, vol. 839, p. 156159, Sep. 2022, doi: 10.1016/J.SCITOTENV.2022.156159.

[21] X. Liu, F. Shen, R. L. Smith, and X. Qi, "Black liquor-derived calcium-activated biochar for recovery of phosphate from aqueous solutions," *Bioresour Technol*, vol. 294, p. 122198, Dec. 2019, doi: 10.1016/J.BIORTECH.2019.122198.

[22] L. Leng *et al.*, "An overview on engineering the surface area and porosity of biochar," *Science of the Total Environment*, vol. 763, Apr. 2021, doi: 10.1016/J.SCITOTENV.2020.144204.

[23] A. B. D. Nandiyanto, R. Oktiani, and R. Ragadhita, "How to read and interpret ftir spectroscope of organic material," *Indonesian Journal of Science and Technology*, vol. 4, no. 1, pp. 97–118, 2019, doi: 10.17509/IJOST.V4I1.15806.

[24] M. Tlili *et al.*, "Synthesis and characterization of mgo thin films obtained by spray technique for optoelectronic applications," *Nanomaterials*, vol. 11, no. 11, p. 3076, Nov. 2021, doi: 10.3390/NANO11113076/S1.

[25] L. Habte, N. Shiferaw, D. Mulatu, T. Thenepalli, R. Chilakala, and J. W. Ahn, "Synthesis of nano-calcium oxide fromwaste eggshell by sol-gel method," *Sustainability (Switzerland)*, vol. 11, no. 11, Jun. 2019, doi: 10.3390/SU11113196.

[26] G. Bin Cai *et al.*, "1,3-Diamino-2-hydroxypropane-N,N,N',N'-tetraacetic acid stabilized amorphous calcium carbonate: Nucleation, transformation and crystal growth," *CrystEngComm*, vol. 12, no. 1, pp. 234–241, 2010, doi: 10.1039/B911426M.

[27] M. Ni and B. D. Ratner, "Differentiation of Calcium Carbonate Polymorphs by Surface Analysis Techniques – An XPS and TOF-SIMS study," *Surf Interface Anal*, vol. 40, no. 10, p. 1356, Oct. 2008, doi: 10.1002/SIA.2904.

[28] Y. Xu *et al.*, “A Novel Ca-Modified Biochar for Efficient Recovery of Phosphorus from Aqueous Solution and Its Application as a Phosphorus Biofertilizer,” *Nanomaterials 2022, Vol. 12, Page 2755*, vol. 12, no. 16, p. 2755, Aug. 2022, doi: 10.3390/NANO12162755.

[29] C. M. Popescu, M. C. Popescu, G. Singurel, C. Vasile, D. S. Argyropoulos, and S. Willfor, “Spectral characterization of eucalyptus wood,” *Appl Spectrosc*, vol. 61, no. 11, pp. 1168–1177, Nov. 2007, doi: 10.1366/000370207782597076.

[30] S. Cheng, A. Huang, S. Wang, and Q. Zhang, “Effect of different heat treatment temperatures on the chemical composition and structure of chinese fir wood,” *Bioresources*, vol. 11, no. 2, pp. 4006–4016, May 2016, doi: 10.15376/BIORES.11.2.4006-4016.

[31] O. Oginni *et al.*, “Phosphorus adsorption behaviors of MgO modified biochars derived from waste woody biomass resources,” *J Environ Chem Eng*, vol. 8, no. 2, p. 103723, Apr. 2020, doi: 10.1016/J.JECE.2020.103723.

[32] S. Li, C. Wang, Z. Luo, and X. Zhu, “Investigation on the Catalytic Behavior of Alkali Metals and Alkaline Earth Metals on the Biomass Pyrolysis Assisted with Real-Time Monitoring,” *Energy and Fuels*, vol. 34, no. 10, pp. 12654–12664, Oct. 2020, doi: 10.1021/ACS.ENERGYFUELS.0C01938.

[33] D. Liu, Y. Yu, J. I. Hayashi, B. Moghtaderi, and H. Wu, “Contribution of dehydration and depolymerization reactions during the fast pyrolysis of various salt-loaded celluloses at low temperatures,” *Fuel*, vol. 136, pp. 62–68, Nov. 2014, doi: 10.1016/J.FUEL.2014.07.025.

[34] S. Tuomi, N. Kaisalo, P. Simell, and E. Kurkela, “Effect of pressure on tar decomposition activity of different bed materials in biomass gasification conditions,” *Fuel*, vol. 158, pp. 293–305, Oct. 2015, doi: 10.1016/J.FUEL.2015.05.051.

[35] Y. hong Niu, Z. yang Chi, M. Li, J. zheng Du, and F. tao Han, “Advancements in biomass gasification and catalytic tar-cracking technologies,” *Materials Reports: Energy*, vol. 4, no. 4, p. 100295, Nov. 2024, doi: 10.1016/J.MATRE.2024.100295.

[36] C. Tan *et al.*, “Structurally improved MgO adsorbents derived from magnesium oxalate precursor for enhanced CO2 capture,” *Fuel*, vol. 278, p. 118379, Oct. 2020, doi: 10.1016/J.FUEL.2020.118379.

[37] R. L. Tseng and F. C. Wu, “Inferring the favorable adsorption level and the concurrent multi-stage process with the Freundlich constant,” *J Hazard Mater*, vol. 155, no. 1–2, pp. 277–287, Jun. 2008, doi: 10.1016/J.JHAZMAT.2007.11.061.

[38] J. I. Bautista Quispe, L. C. Campos, O. Mašek, and A. Bogush, “Optimisation of biochar filter for handwashing wastewater treatment and potential treated water reuse for handwashing,” *Journal of Water Process Engineering*, vol. 54, p. 104001, 2023, doi: 10.1016/j.jwpe.2023.104001.

[39] S. Nasrollahpour, R. Pulicharla, and S. K. Brar, “Functionalized biochar for the removal of poly- and perfluoroalkyl substances in aqueous media,” *iScience*, vol. 28, no. 3, p. 112113, Mar. 2025, doi: 10.1016/J.ISCI.2025.112113.

[40] M. U. Jamal, “Design of Experiments Optimisation of Scottish Wood Biochars for Water Remediation targeting selected Persistent Organic Pollutants,” The University of Strathclyde, Glasgow, 2023.

[41] Z. Wang, C. Zhang, and S. Li, “Study on the conversion of CaCl2 with H2O and CO2 for dechlorinating pyrolysis of municipal solid waste,” *Thermochim Acta*, vol. 717, p. 179362, Nov. 2022, doi: 10.1016/J.TCA.2022.179362.

[42] A. do A. Leite *et al.*, “Magnesium-enriched poultry manure enhances phosphorus bioavailability in biochars,” *Chemosphere*, vol. 331, p. 138759, Aug. 2023, doi: 10.1016/J.CHEMOSPHERE.2023.138759.

[43] D. Pokorná, P. Cuřínová, and J. Pola, “Calcium Hydroxide Effect in Degradation of Aqueous Naphthalene: Nucleophilic Substitution of Hydrogen at the C(sp2)–H Bond,” *Polycycl Aromat Compd*, vol. 41, no. 4, pp. 841–850, 2021, doi: 10.1080/10406638.2019.1624975.

[44] M. Ali, F. Mahmood, C. F. Magoua Mbeugang, J. Tang, X. Xie, and B. Li, “Molten chloride salt pyrolysis of biomass: Effects of temperature and mass ratio of molten salt to biomass,” *Energy*, vol. 316, Feb. 2025, doi: 10.1016/j.energy.2025.134634.

[45] F. Shao *et al.*, “An attempt to enhance the adsorption capacity of biochar for organic pollutants - Characteristics of CaCl2 biochar under multiple design conditions,” *Science of The Total Environment*, vol. 854, p. 158675, Jan. 2023, doi: 10.1016/J.SCITOTENV.2022.158675.

[46] M. Fan *et al.*, “Activation of biochar by CO2 produced from the same pyrolysis process and captured in situ by CaO,” *Chemical Communications*, vol. 61, no. 3, pp. 484–487, Jan. 2025, doi: 10.1039/D4CC04931D.

5 Maximising the P-Removal: Synergistic Effects of Chemical Loading Rate and Pyrolysis Temperature

5.1 Introduction

The physical characteristics of biochar, such as surface area and pore volume, are commonly used to indicate its effectiveness as an adsorbent. Metal-impregnated biochars have been shown to be useful for the adsorption of aqueous phosphate, with reports of increased impregnation improving P-recovery despite often reducing biochars' surface area [1], [2], [3], [4]. This is potentially due to an increased number of favourable surface sites, even with a reduction in the total number of surface sites available for adsorption. However, over-blocking of the pores within the structure of a biochar could prevent internal diffusion and limit its adsorption capacity. As such, the concept that optimal functionalisation of biochars may depend on achieving the best balance of quantity of functionalisation agent and potential blocking of porous structure should be considered. Temperature is a key influencing factor in developing porosity within biochars [5]. The effects of chemical impregnation, and more specifically chemical loading ratio (CLR) (the mass ratio of functionalisation agent: feedstock), on biochars physical properties is unclear, with contradicting reports given in the literature [1], [4], [6], [7]. Furthermore, an understanding of synergistic effects between pyrolysis temperature and chemical loading ratio (CLR) is missing entirely.

This chapter aims to fill the aforementioned knowledge gap in the literature by examining the singular and synergistic effects of pyrolysis temperature and CLR on the properties of biochars, using a Design of Experiments (DoE) inscribed central composite experimental design to optimise the conditions of synthesis.

5.2 Methodology

Based on results obtained within *Chapter 4*, which showed optimal production of Ca-decorated biochar for aqueous P-removal to occur via pre-pyrolysis

impregnation of particle size-controlled feedstock, the functionalised biochar used in this chapter was produced using wood flakes (1-2 mm) impregnated with $CaCl_2$ prior to pyrolysis. The results presented here allow for examination of the effects of pyrolysis temperature and CLR on the physicochemical characteristics of biochars and their aqueous P-removal.

To produce Ca-decorated biochar, chips of softwood were ground to flakes of 1-2 mm; with the flakes subsequently gently stirred for 24 h in a solution of $CaCl_2$ (CLRs given in *Table 5.1*), dried, and pyrolysed at pre-determined pyrolysis temperatures (*Table 5.1*). Based on the results presented in *Section 4.2*, it was decided to extend the temperature range to 600-900 °C in the DoE, and limit CLR to the upper range previously tested (i.e. 1.5-2). Furthermore, based on the results presented in *Section 4.3*, an orthogonal and rotatable design was chosen, with coded values used for the DoE analysis shown in *Table 5.2*. Note that, in order to create a rotatable design, a biochar was produced at the midpoint (0,0) conditions eight times, and each of these midpoint biochars was analysed to account for error within data when fitting models during regression analysis.

Table 5.1:Pyrolysis temperature and functionalisation agent CLRs used in experimental design, selected using Design of Experiments statistical design.

	Ca-modified								
Temperature (°C)	600	644	644	750	750	750	856	856	900
CLR (wt:wt)	1.75	1.57	1.93	1.5	1.75	2	1.57	1.93	1.75

Table 5.2: Functionalisation parameters and their coded values for inscribed central composite experimental design used in this work.

Variables (factors)	**Units**	**Variables (α=0.7071)**				
		Low (-1)	Mid (0)	High (1)	-α	+α
Temperature (A)	°C	600	700	900	644	856
CLR (B)	Wt:wt	1.5	1.75	2	1.57	1.93

5.3 Physical Characteristics

Table 5.3 shows the yield and physical characteristics of the biochar samples obtained using the design outlined in *Table 5.2*. The yield increased with increasing CLR and decreased with increased temperature. Increasing CLR increases the mass of mineral compounds in the wood feedstock and resulting biochar and increased temperature increases devolatilization of biomass during pyrolysis, as such these results were expected. Yields shown in *Table 5.3* are very high compared to typical values reported in the literature (~16-40 %), this is likely due to the ability of $CaCl_2$ to promote char formation and suppress volatile release by acting as Lewis acid catalysts, catalysing dehydration and cross-linking reactions, supporting the formation of thermally stable carbonaceous structures and reducing the release of volatiles [8], [9],[10], [11], [12]. Yields in *Table 5.3* are also notably higher than those reported in *Chapter 4* (29.2-40.5 %), likely due to an increase in uptake of $CaCl_2$ by softwood when wood chips were ground to 1-2 mm wood flakes prior to feedstock impregnation.

As the pyrolysis temperature increased, both surface area and pore volume decreased, while the proportion of total surface area present externally increased. This is potentially due to the increased blockage of pores by calcium-based crystals, with higher pyrolysis temperatures resulting in greater formation and agglomeration of these crystals. However, reduced surface area and pore volume are likely to be at least partly a consequence of the collapsing and merging of pores at higher temperatures [5]. The surface area decreased with increasing CLR, indicating that pore blockage contributes towards low surface area values for these samples.

*Table 5.3: Yield and physical characteristics of biochar samples synthesised in this work. Where values are presented as x ± y, x represents the average value and y represents the standard error (n=8).**

Biochar Sample	Yield (%)	Surface Area (m^2/g)	External Surface Area (m^2/g)	Pore Volume (cm^3/g)	Average pore size (nm)
Ca-1.75-T600	54.1	166	42	0.13	7
Ca-1.57-T644	49.7	184	60	0.13	5
Ca-1.93-T644	55.4	130	34	0.11	8
Ca-1.5-T750	45.8	151	60	0.12	5
Ca-1.75-T750	43.7 ± 0.8	157 ± 5	58 ± 2	0.12 ± 0.003	4 ± 0.1
Ca-2-T750	49.0	121	40	0.12	7
Ca-1.57-T856	48.1	113	51	0.12	6
Ca-1.93-T856	49.6	78	33	0.10	8
Ca-1.75-T900	48.5	83	43	0.10	7

* Analytical error associated with the calculation of surface area and external surface area ranged from 0.6 to 0.9 m^2/g and from 0.5 to 2 m^2/g, respectively.

There is no clear correlation between the average pore size presented in *Table 5.3* and either pyrolysis temperature or CLR. However, as shown in *Figure 5.1*, the pore size distribution appears to be affected by CLR, with an increase in CLR causing an increase in mesopore size and volume. All chars show a prominent, sharp peak between 2-4 nm, indicating a significant volume of small mesopores; this peak decreases with increasing CLR. As the CLR increases, the volume of larger pores (broad peaks, ~7-23 nm) can be seen to increase, and the distribution of these pores shifts slightly to the right, towards larger pore sizes. An exception to this is sample Ca-1.93-T856, and the difference is notable when compared to sample Ca-1.57-T856. While the pore size distribution of the sample with the higher CLR still shifts right towards larger pore size, the volume of pores in this region of the graph does not increase with increasing CLR. An increase in the mesopore volume of a biochar is favourable for aqueous pollutant removal[13], [14]. However, the observed apparent increase in mesopore volume with CLR may not accurately reflect broader pores in biochar's carbon skeleton but instead reflect increased blocking of smaller pores by Ca crystals.

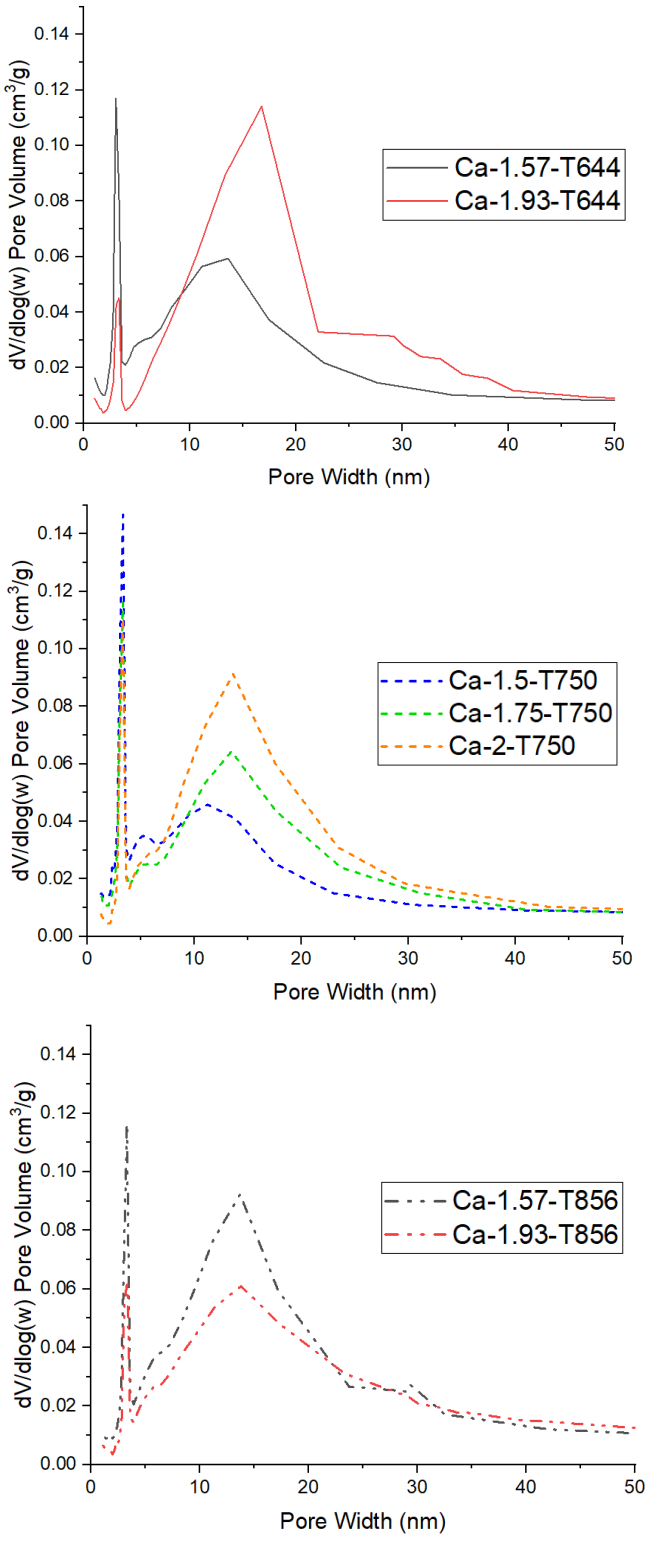

Figure 5.1:BJH plots for biochar samples synthesised in this work.

5.3.1 Regression Analysis

Regression analysis was carried out using the coded values provided in *Table 5.2*, with pyrolysis temperature as factor A and CLR as factor B. The yield and all physical characteristics listed in *Table 5.3* were used as response variables. Stat Ease 360 software was used to fit all data to linear, two-factor interaction (2FI), quadratic, and cubic models. Quadratic models presented the best fit for all response variables and are discussed further in this section. Yield, surface area, and average pore size all fit quadratic models with good predicted R^2 values (>0.7) with models given in *Equations 5.1, 5.2, and 5.3,* respectively.

$$Yield = 43.68 - 2.71A + 2.07B - 2.1AB + 8.3A^2 + 4.4B^2 \quad (5.1)$$

$$Surface\ Area = 156.87 - 42.49A - 23.23B + 9.5AB - 34.38A^2 - 22.88B^2 \quad (5.2)$$

$$Average\ Pore\ Size = 4.38 + 0.1768A + 1.38B - 0.5AB + 2.75A^2 + 1.75B^2 \quad (5.3)$$

Summary statistics for the models (*Equations 5.1, 5.2, and 5.3)* are presented in *Table 5.4*. The coefficient of variation (C.V.) is a measure of the reproducibility of data, calculated by taking a ratio of the standard deviation of a data set to the mean. A model is generally considered to be reproducible if C.V. is less than 10%. Adequate precision is used by StatEase360 software as a measure of the signal to noise ratio in a dataset, with values above 4 being desirable. All responses show C.V. values of less than 10% and adequate precision values above 4, showing the data to be reproducible with a favourable signal-to-noise ratio for model fitting. The adjusted and predicted R^2 values are in good agreement (difference <0.2) for all three response models.

5.4: Summary statistics for quadratic fits of yield, surface area, and average pore size for biochar samples synthesised in this work.

Response	Mean	Std. Dev	C.V. %	Adjusted R^2	Predicted R^2	Adequate Precision
Yield	46.85	1.96	4.19	0.78	0.71	9.15
Surface Area	142.56	12.05	8.45	0.85	0.74	13.48
Average Pore Size	5.5	0.52	9.47	0.87	0.74	10.51

5.3.2.1 Diagnostic plots

Description of the diagnostic plots used in *Figures 5.2-5.4* (normal plot, residual vs precited plot, and predicted vs actual plot) including how they can be used to identify outliers in a data set is provided in *Section 3.3.6.3*.

Diagnostic plots for yield indicate that the data points have relatively good normality. The residual vs predicted plot (*Figure 5.2b*) shows some large errors around a predicted value of 44; these values are all midpoint repeats, indicating the data to be less replicable than initially hoped, potentially due to softwood flakes not always taking up the same amount of $CaCl_2$ at the same CLR. Despite this, the studentised residuals remain within reasonable limits (within the red lines). Besides the midpoint repeats, residuals are relatively evenly distributed in a horizontal band around 0, with no fanning out of the data. Considering the normal and residual plots together (*Figures 5.2a&b*), the model fits the data relatively well, and no transforms are required. Overall, the predicted vs actual plot (*Figure 5.2c)* shows relatively good agreement between *Equation 5.1* and the experimental data, with points randomly distributed around the straight line.

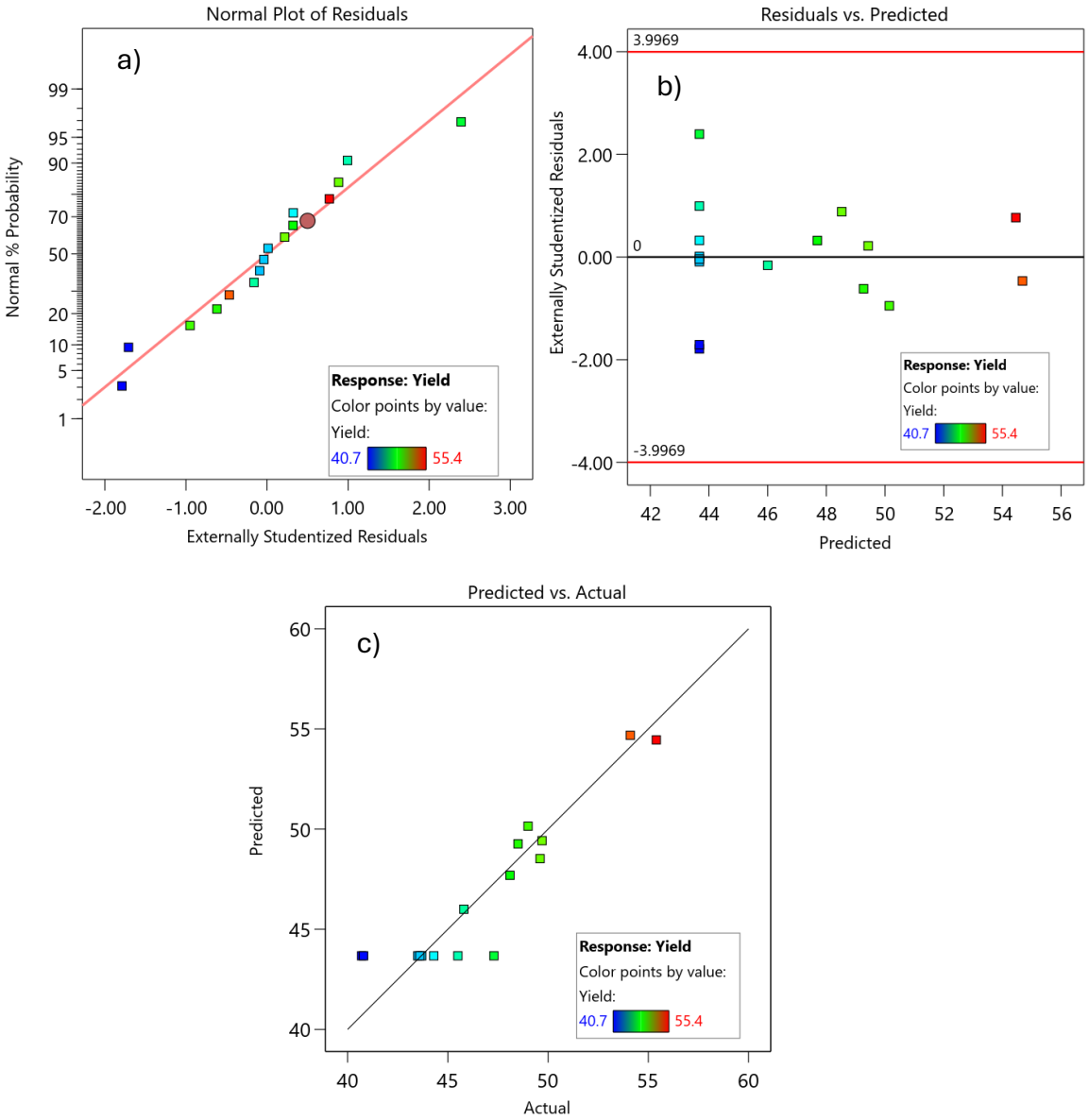

Figure 5.2:Diagnostic plots for yield: a) normal plot, b) residuals vs predicted, and c) predicted value vs actual value.

The normal plot for surface area, shown in *Figure 5.3a*, highlights one clear outlier (run 16, circled in red), while the rest of the data can be seen to adhere to a normal distribution. The residual vs predicted (*Figure 5.3b*) plot shows roughly even distribution of studentised residuals around 0, with the exception of the data point circled in red, run 16. Whilst data from run 16 is just shy of the cut-off value (indicated by red lines in *Figure 5.3b*) for an acceptable studentised residual, its difference from other data points suggests this value should still be omitted. The

predicted vs. actual plot shows that the data fits the model well, better than would be indicated by the R^2 values, suggesting that the outlier data point (run 16) is skewing these values. Omitting this data point and refitting the quadratic model from this analysis gives the model presented in *Equation 5.4* with adjusted and predicted R^2 values of 0.94 and 0.82, respectively. Compared to *Equation 5.2,* R^2 values have been significantly increased despite half the model terms remaining unchanged and only a small change to the rest.

$$Surface\ Area = 160.86 - 42.49A - 23.23B + 9.5AB - 38.36A^2 - 26.86B^2 \quad (5.4)$$

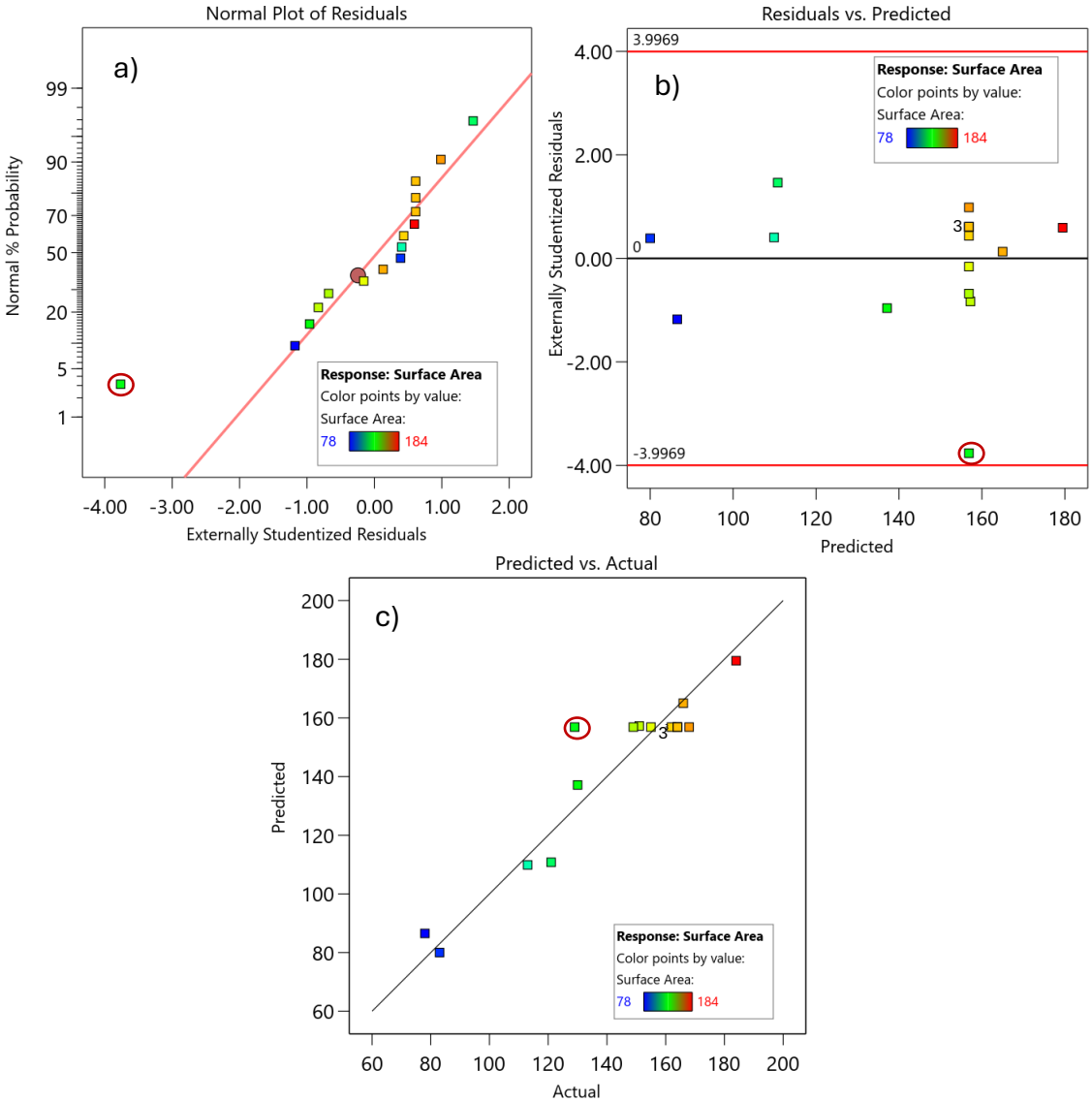

Figure 5.3: Diagnostic plots for surface area: a) normal plot, b) residuals vs predicted, and c) predicted value vs actual value. Data point circled in red is run 16, an outlier.

Diagnostic plots for average pore size are shown below in *Figure 5.4*. The normal plot (*Figure 5.4a*) indicates that the data adheres to a normal distribution, with the two vertical bands of data points belonging to the midpoint repeats. The residual vs predicted plot (*Figure 5.4b*) shows well-balanced random error with no outliers, as does the actual vs predicted plot. It is worth noting that the data presented in the actual vs predicted plot (*Figure 5.4c*) appears bunched, with even spaces between data points; however, this is due to the fact that pore size is considered to the nearest whole nm, resulting in discretised data intervals.

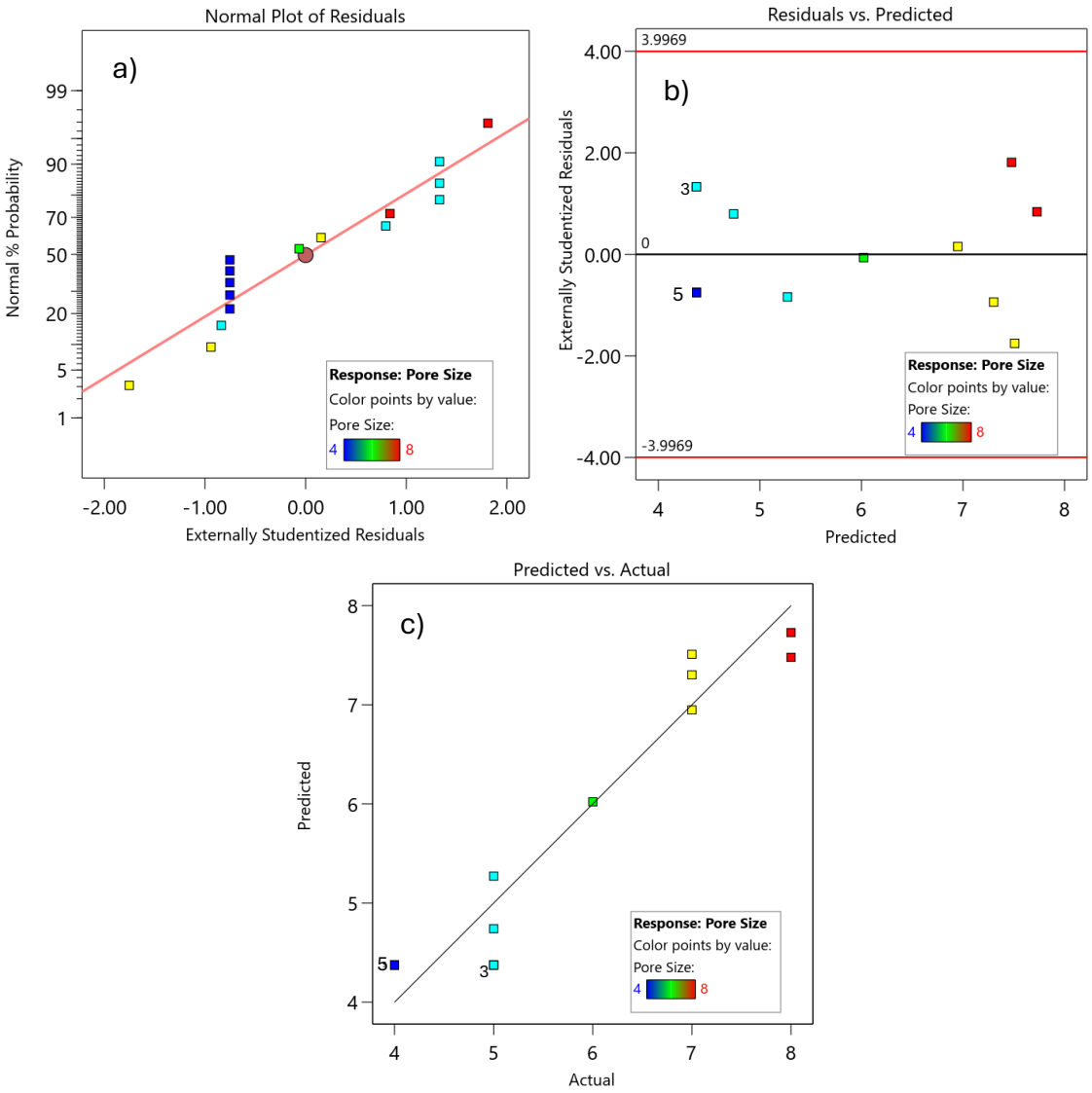

Figure 5.4:Diagnostic plots for average pore size: a) normal plot, b) residuals vs predicted, and c) predicted value vs actual value.

5.3.2.2 Model Reduction

When carrying out ANOVA analysis for yield, surface area, and average pore size, not all model terms were found to be statistically significant within a 95 % confidence interval. To refine models, model reduction was carried out to test the effect on adjusted and predicted R^2 values.

*Table 5.5: ANOVA results for yield before and after model reduction, *non-significant.*

Source	F-value	p-value	Adjusted R^2	Predicted R^2
		Original Model		
Model	11.79	0.0006	***0.7824***	***0.7107***
A-Temperature (°C)	7.60	0.0202		
B-CLR (wt:wt)	4.45	0.0610*		
AB	1.14	0.3102*		
A^2	35.70	0.0001		
B^2	10.03	0.0100		
		Reduced Model		
Model	14.26	0.0002	***0.7796***	***0.7074***
A-Temperature (°C)	7.50	0.0192		
B-CLR (wt:wt)	4.40	0.0599*		
A^2	35.25	< 0.0001		
B^2	9.91	0.0093		

As shown in *Table 5.5*, the original fitted model demonstrated an F-value of 11.79, implying that the model is statistically significant, with only a 0.06% chance that an F-value as large as that calculated could occur due to noise. Significant model terms are A, A^2, and B^2, with A^2 the most influential. The higher influence of temperature, than CLR, on yield is expected; while $CaCl_2$ is seen to promote char formation effect on the softwood feedstock during pyrolysis, the strong influence of temperature on yield is widely discussed in the literature [12], [15]. The interaction term AB was the least influential on the model and was also shown to be statistically insignificant at a 95% confidence level. This suggests that while both temperature and CLR individually affect yield, synergistic effects on yield are not present. When the interaction term AB was removed from the model the adjusted and predicted R^2 values decreased slightly (note that within the recalculation, despite being statistically insignificant, B was retained to

maintain hierarchy). As such, the original model (*Equation 5.1*) was retained and used to create *Figure 5.5* below. The contour plot in *Figure 5.5* shows that optimal yield occurs at low temperature and high CLR. Despite a statistically insignificant interaction term, the contour plot does show that the limited impact of temperature on yield decreases slightly with increasing CLR.

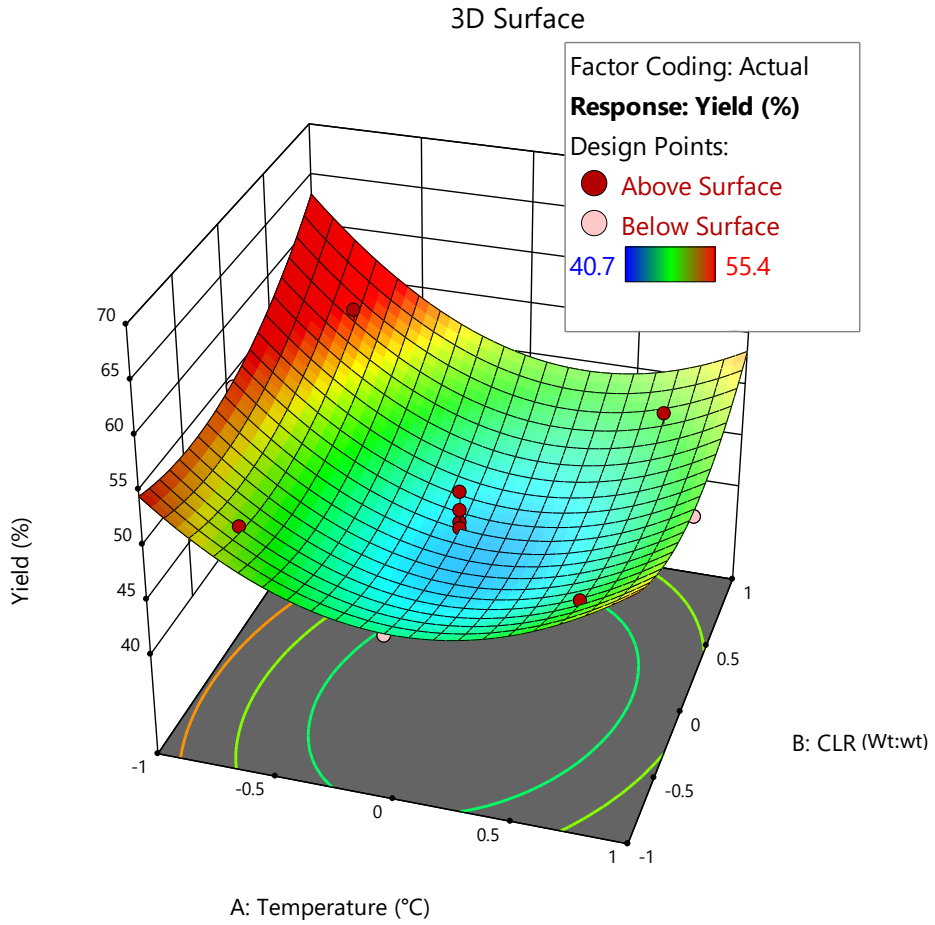

Figure 5.5:3D contour plot showing interactions of pyrolysis temperature and CLR on yield of Ca-biochar. Coded values are used with CLR ranging from -1 (1.5) to 1(2) and pyrolysis temperature ranging from -1 (600 °C) to 1 (900 °C).

*Table 5.6:ANOVA results for surface area before and after model reduction, *non-significant.*

Source	F-value	p-value	Adjusted R^2	Predicted R^2
Original Model- outlier removed				
Model	43.32	< 0.0001	***0.9379***	***0.8208***
A-Temperature (°C)	115.27	< 0.0001		
B-CLR (wt:wt)	34.46	0.0002		
AB	1.44	0.2607*		
A^2	45.34	< 0.0001		
B^2	22.23	0.0011		
Reduced Model				
Model	51.53	< 0.0001	***0.9352***	***0.8539***
A-Temperature (°C)	110.40	< 0.0001		
B-CLR (wt:wt)	33.00	0.0002		
A^2	43.43	< 0.0001		
B^2	21.29	0.0010		

Table 5.6 shows that all of the model terms for surface area are statistically significant, except the interaction term AB. When reducing the model and removing this interaction term, the predicted R^2 is increased. An F-value of 51.52 indicates that the model is significant, with only a 0.01% chance that this F-value could occur due to noise. Model terms A and A^2 have higher F-values than B and B^2, showing that temperature is more influential than CLR (within the chosen design space) on the surface area of biochar. Once again, there appears to be no statistically significant synergistic effect of pyrolysis temperature and CLR on biochar surface area. The final reduced model for surface area is given in *Equation 5.5* below:

$$Surface\ Area = 160.86 - 42.49A - 23.23B - 38.36A^2 - 26.86B^2 \qquad (5.5)$$

Figure 5.6 shows the optimal surface area to occur at low temperature and low CLR. The contour plot effectively illustrates the greater effect that temperature has on surface area compared to CLR. It is unusual for surface area to decrease with increasing pyrolysis temperature; however, this is most likely a decrease in measurable surface area opposed to true surface area. As temperature increases a greater number of $CaCO_3$ crystals form on the surface of biochar (see Section 5.4.5 below), as such pores experience an increased level of pore

blocking. This blocking of pores of reduces the accessibility of N_2 particles to the internal biochar structure during BET analysis, artificially reducing the total surface area measured compared to true total surface area.

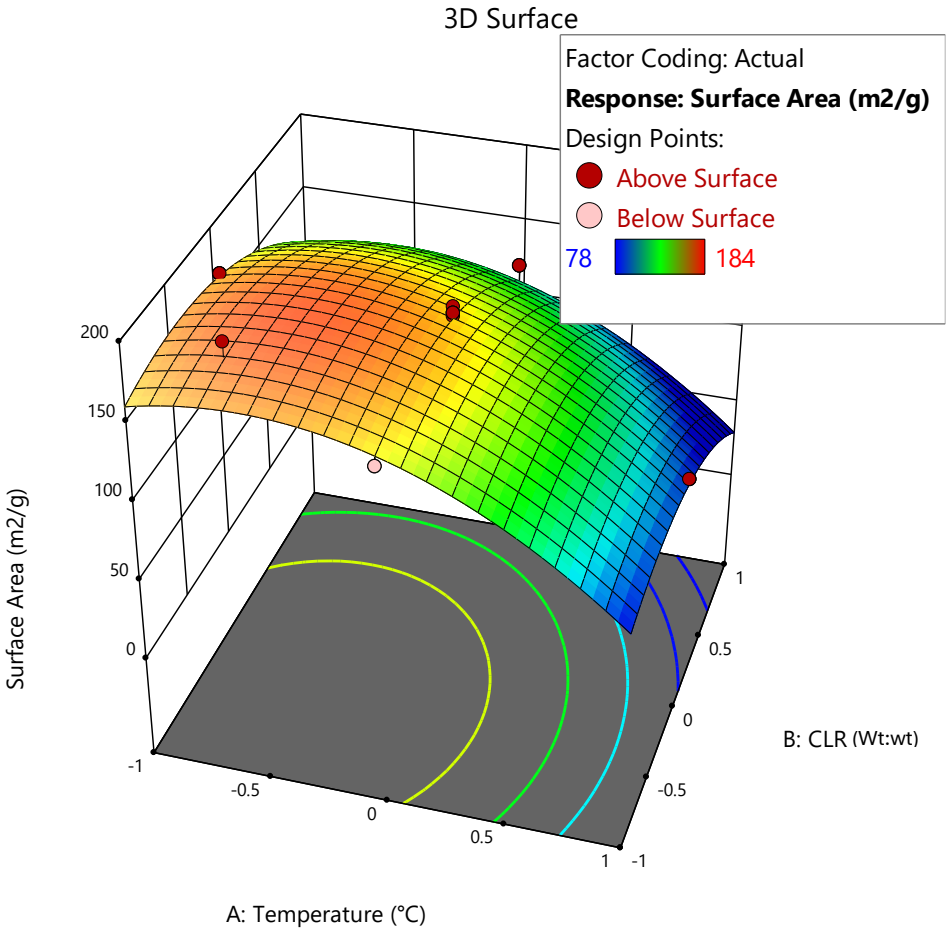

Figure 5.6:3D contour plot showing interactions of pyrolysis temperature and CLR on surface area of Ca-biochar. Coded values are used with CLR ranging from -1 (1.5) to 1(2) and pyrolysis temperature ranging from -1 (600 °C) to 1 (900 °C).

*Table 5.7: ANOVA results for average pore size before and after model reduction, *non-significant.*

Source	F-value	p-value	Adjusted R^2	Predicted R^2
Original Model				
Model	21.58	< 0.0001	***0.8728***	***0.7369***
A-Temperature (°C)	0.4605	0.5128*		
B-CLR (wt:wt)	28.22	0.0003		
AB	0.9210	0.3598*		
A^2	55.72	< 0.0001		
B^2	22.56	0.0008		
Reduced Model				
Model	26.93	< 0.0001	***0.8737***	***0.7766***
A-Temperature (°C)	0.4638	0.5099*		
B-CLR (wt:wt)	28.42	0.0002		
A^2	56.12	< 0.0001		
B^2	22.73	0.0006		

Displayed in *Table 5.7*, model terms B, A^2, and B^2 for average pore size were found to be statistically significant. The interaction term AB was found to be statistically insignificant, indicating no synergistic effects between pyrolysis temperature and CLR on the average pore size of biochar samples. The reduced model removed the term AB but retained A to maintain the model hierarchy. Reducing the model successfully increased the predicted R^2. The reduced model has a high F-value of 29.04, indicating the model is significant, with only a 0.01% chance of an F-value this high occurring due to noise. Despite temperature having the lowest F-value, the square of temperature is the most influential factor, followed by CLR. The final reduced model for average pore size is given in *Equation 5.6* below:

$$Average\ Pore\ Size = 4.38 + 0.1768A + 1.38B - 0.5AB + 2.75A^2 + 1.75B^2 \quad (5.6)$$

The contour plot in *Figure 5.7* highlights the dominance of CLR over temperature in influencing the average pore size of biochar. This increase in average pore size is due to the previously mentioned observation that increasing CLR increases the volume of larger pores.

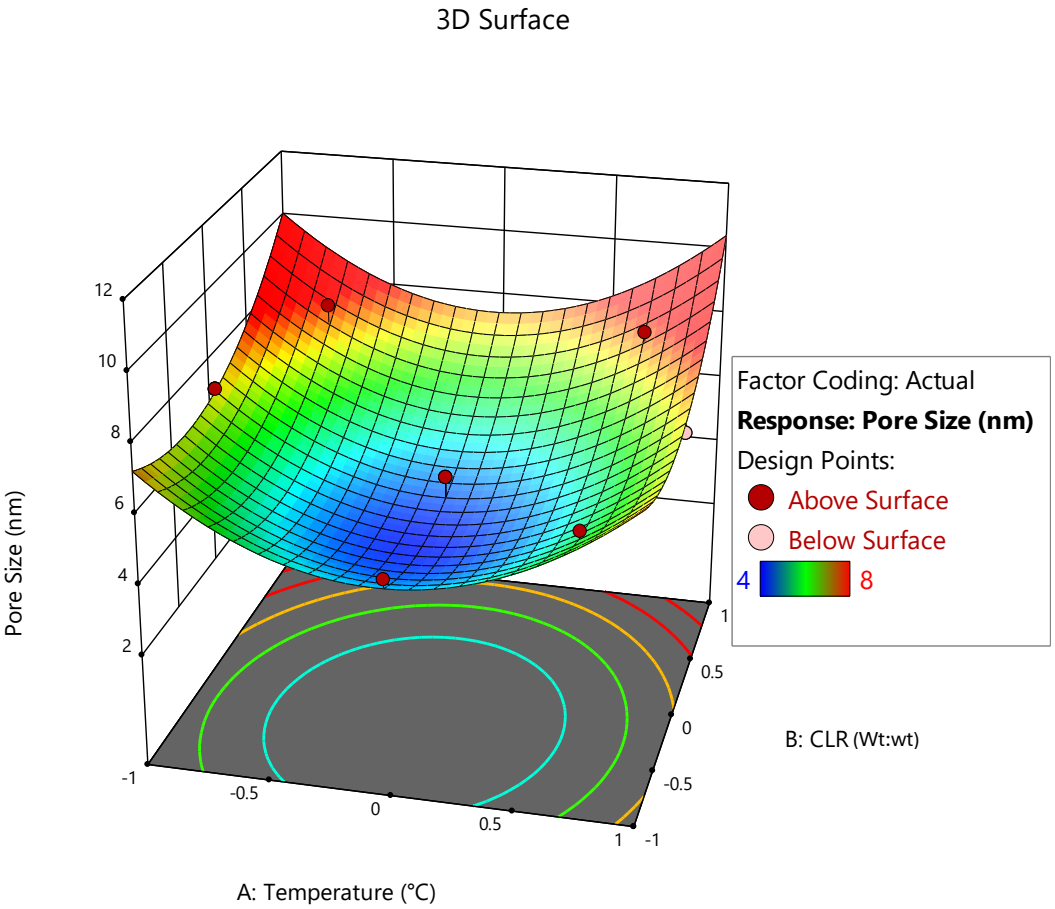

Figure 5.7:3D contour plot showing interactions of pyrolysis temperature and CLR on average pore size of Ca-biochar. Coded values are used with CLR ranging from -1 (1.5) to 1(2) and pyrolysis temperature ranging from -1 (600 ℃) to 1 (900 ℃).

5.4 Chemical Characteristics

5.4.1 FTIR Analysis

From *Figure 5.8*, it can be seen that all biochars produced similar spectra during FTIR analysis. Evidence of $CaCO_3$, present in the form of calcite, can be seen as a result of asymmetric stretching of the C-O bond at 1410 cm^{-1}, peaks characteristic of out-of-plane bending of the C-O bond in calcite at 870 cm^{-1} and C=O in carboxylate groups at 1613 cm^{-1} [16], [17], [18] [19]. In well-crystallised calcite the peak at 1410 cm^{-1} is sharp and intense compared to the peak at 870 cm^{-1}, as calcite or its environment becomes more poorly crystalline these peaks broaden and become more similar in intensity as increased disorder reduces vibrational coupling and symmetry. As pyrolysis temperature increases

peaks at 1410 cm^{-1} and 870 cm^{-1} can be seen to become sharper with intensity of the peak at 1410 cm^{-1} increasing relative to the peak at 870 cm^{-1}, indicating either $CaCO_3$ to become more crystalline or the surrounding biochar matrix to become less amorphous. No clear changes indicating increased crystallinity of $CaCO_3$ can be seen from the XRD patterns of the biochars (Appendix A.2), as such the difference in intensity and sharpness of calcite peaks are likely a reflection of biochars carbon structure becoming less amorphous with increasing pyrolysis temperature. The broad peak seen between 3700-3000 cm^{-1} is representative of various convoluted O-H bonds [20]. As pyrolysis temperature increases broad bands representative of O-H bonds shift to a lower wavenumber suggesting more strongly bonded OH groups.

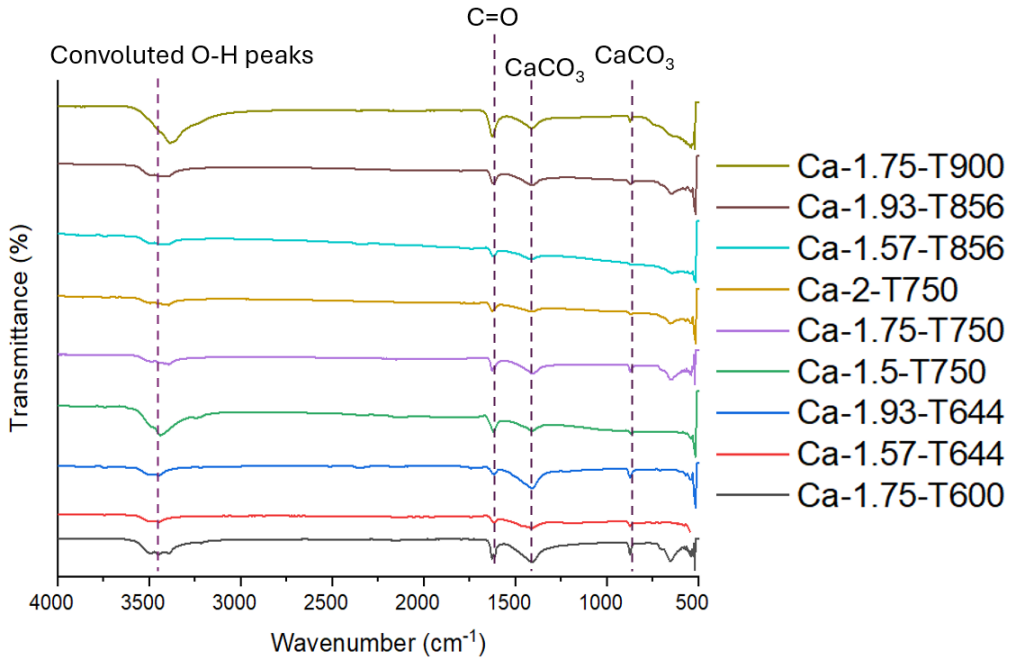

Figure 5.8:FTIR spectra of Ca-biochar produced at various pyrolysis temperatures and CLRs.

5.4.2 SEM-EDS Analysis

From the SEM images presented in *Figures 5.9 & 5.10,* at x 95 magnification, for the samples selected, exposure of the internal pore network to the outer surface appears to increase with increasing pyrolysis temperature. EDS mapping images, shown in *Figure 5.11*, show flakes to have high calcium content. The content of oxygen and carbon is increased in areas of large flakes where there are high levels

of calcium, suggesting these clusters to be $CaCO_3$. However, mapping also suggests areas of high calcium and carbon content, which lack high oxygen content, indicating that calcium is also present in other forms.

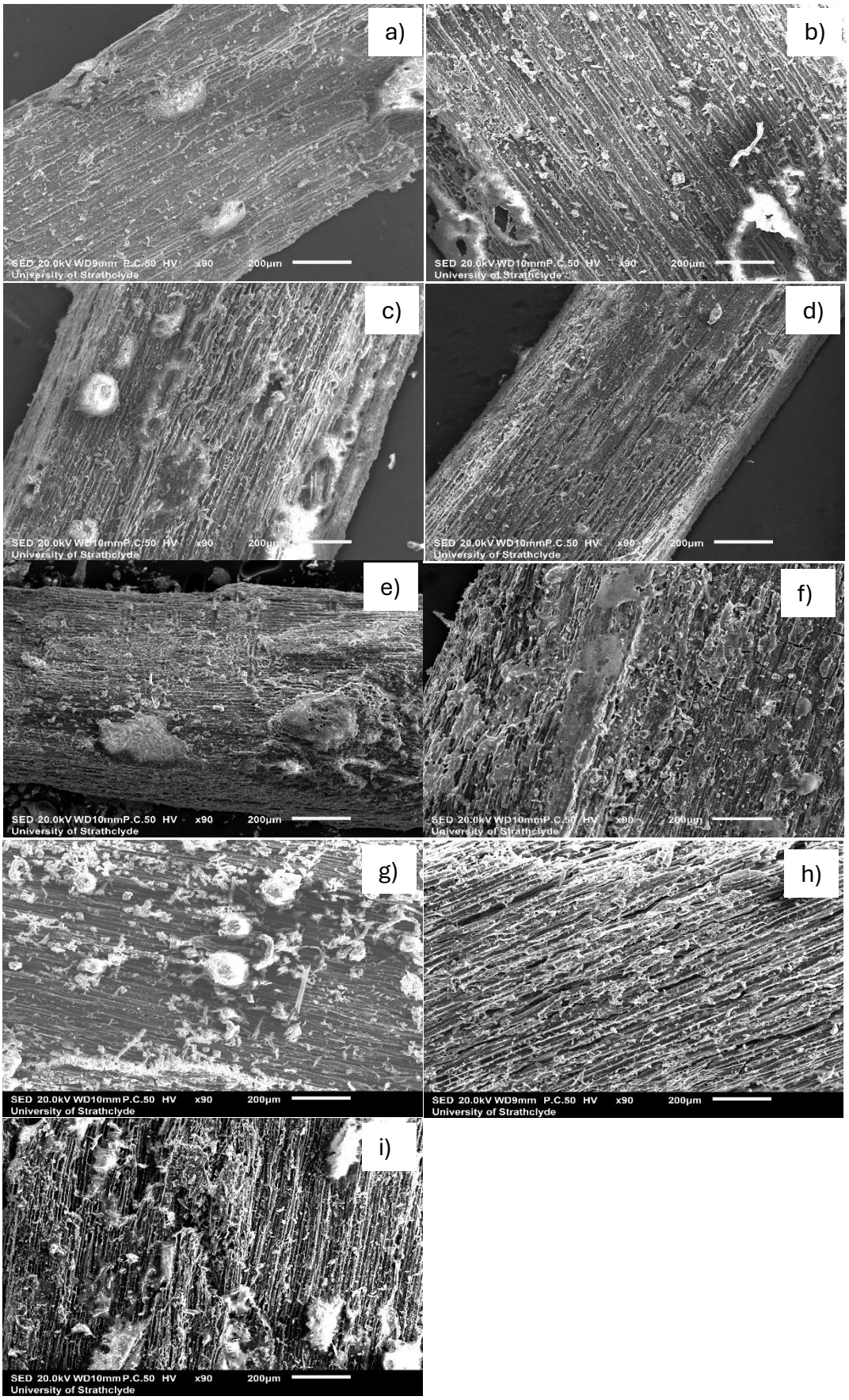

Figure 5.9:SEM images at x95 magnification of a) Ca-1.75-T600, b) Ca-1.57-T644, c) Ca-1.93-T644, d) Ca-1.5-T750, e) Ca-1.75-T750, f) Ca-2-T750, g) Ca-1.57-T856, h) Ca-1.93-T856, i) Ca-1.75-T900.

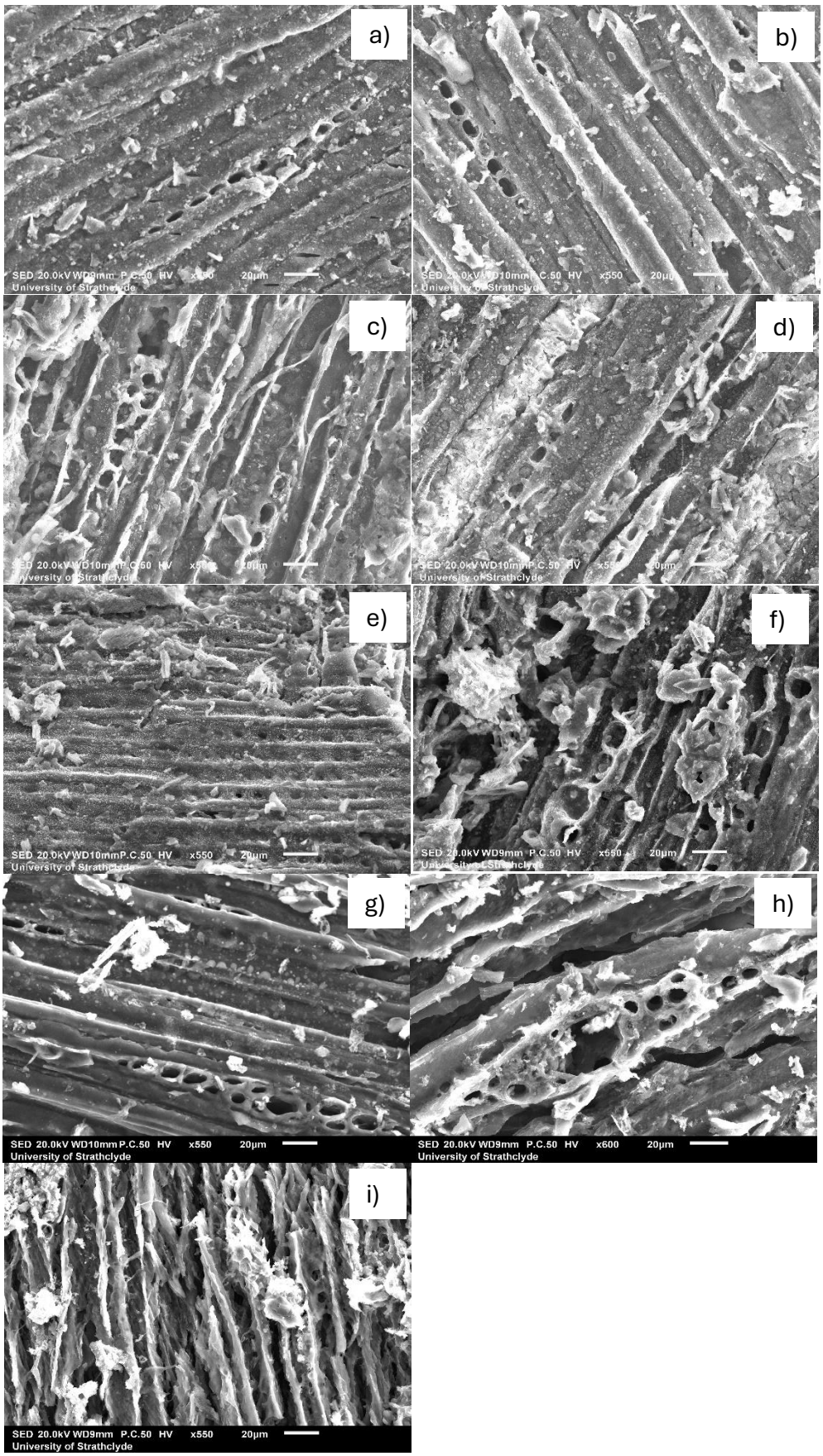

Figure 5.10:SEM images at x 550 magnification of a) Ca-1.75-T600, b) Ca-1.57-T644, c) Ca-1.93-T644, d) Ca-1.5-T750, e) Ca-1.75-T750, f) Ca-2-T750, g) Ca-1.57-T856, h) Ca-1.93-T856, i) Ca-1.75-T900.

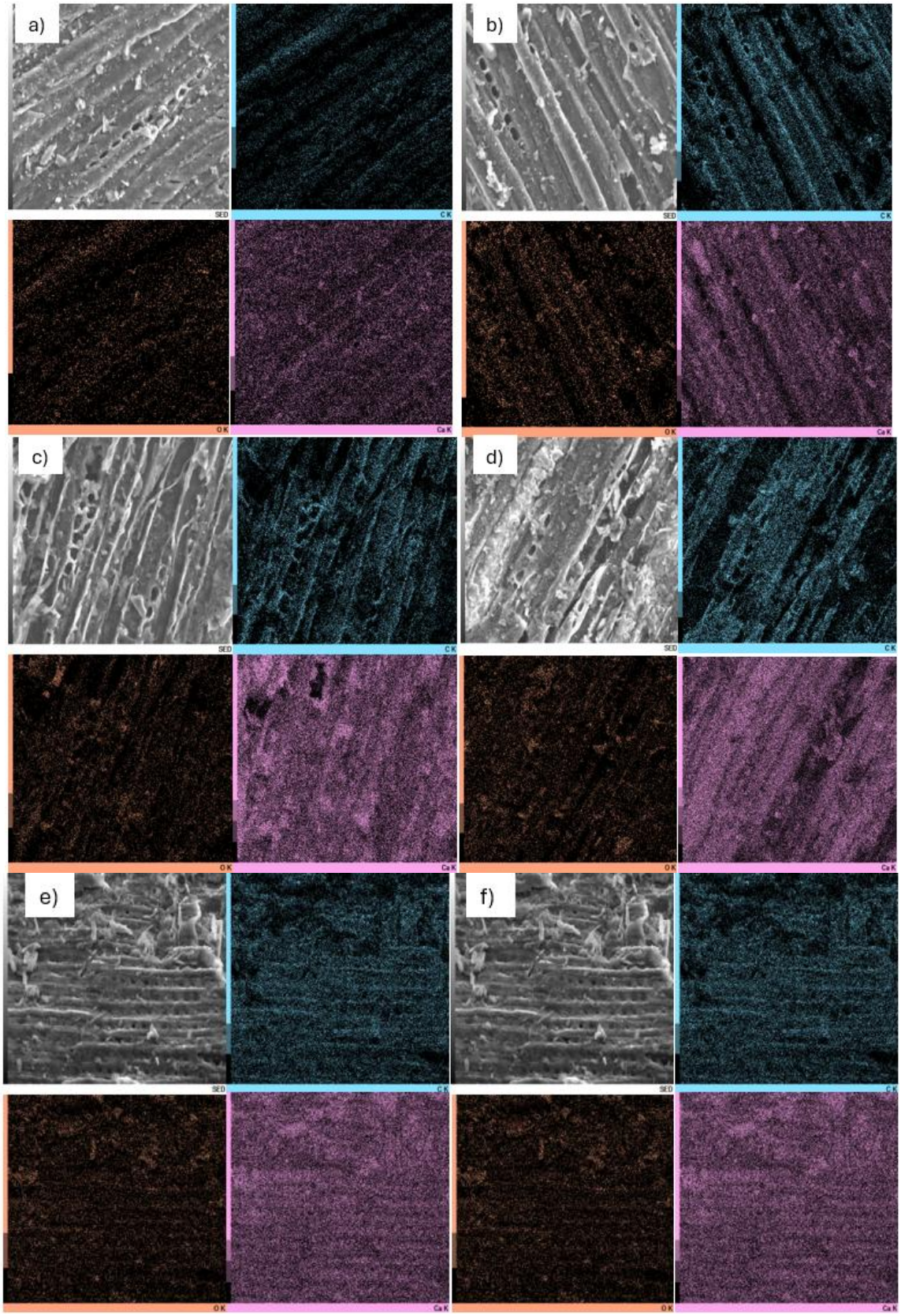
a)
b)
c)
d)
e)
f)

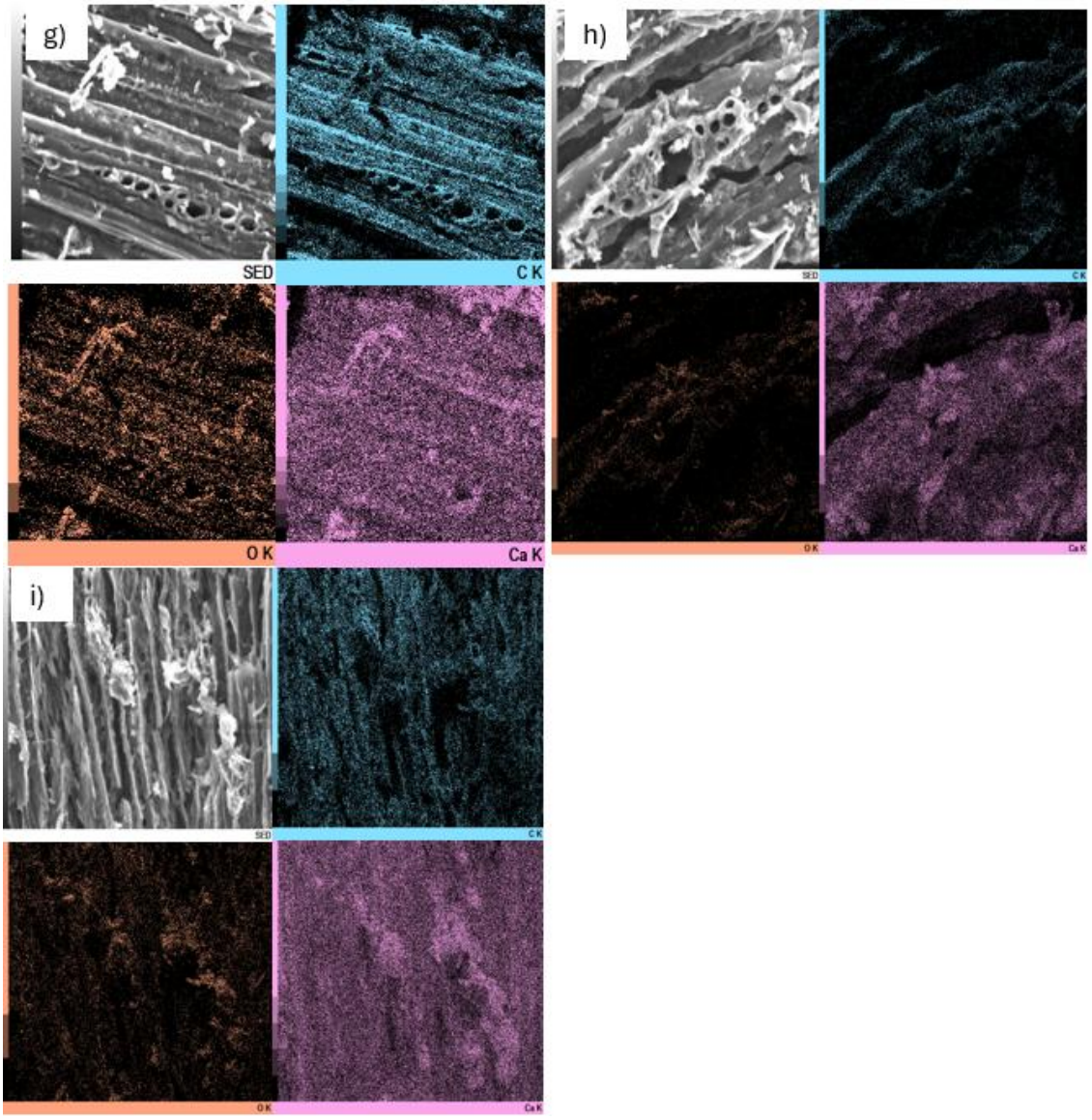

Figure 5.11:EDS mapping images at x 550 magnification of a) Ca-1.75-T600, b) Ca-1.57-T644, c) Ca-1.93-T644, d) Ca-1.5-T750, e) Ca-1.75-T750, f) Ca-2-T750, g) Ca-1.57-T856, h) Ca-1.93-T856, i) Ca-1.75-T900 showing dispersion of C (blue), O (orange), and Ca (purple).

5.4.3 Surface Charge

Values of pH_{pzc}, presented in *Table 5.8,* were similar for all biochars, with an average pH_{pzc} of 7.24. Despite pH_{pzc} appearing to mildly decrease with increasing pyrolysis temperature and CLR, the values presented in *Table 5.8* vary less than the inherent error associated with the measurement technique used (~0.1). Average pH_{pzc} was extremely similar to average pH_{pzc} (7.40) of non-functionalised biochar produced from the same feedstock physically activated with CO_2 [21]. This indicates that functionalisation had a minor effect on the pH_{pzc} of biochar.

Table 5.8: Point of zero charge of Ca-decorated biochar samples synthesised in this work.

	pH_{pzc}
Ca-1.75-T600	7.2
Ca-1.57-T644	7.3
Ca-1.93-T644	7.2
Ca-1.5-T750	7.3
Ca-1.75-T750	7.3
Ca-2-T750	7.2
Ca-1.57T-856	7.2
Ca-1.93-T856	7.2
Ca-1.75-T900	7.2

5.4.4 XRF Analysis

XRF results obtained for the samples synthesised in this work are presented in *Table 5.9*. XRF analysis almost exclusively showed biochar samples to contain higher levels of chlorine compared to calcium. The percentage weight of lightweight elements was calculated during XRF analysis by PCEDX-Navi software using a correction that assumes all unidentified mass belongs to elements with atomic numbers 12 or lighter; in the case of biochar, this is most likely a mixture of C, H, N, O, and small amounts of lightweight minerals, such as Na and Mg. Mass attributed to lightweight elements is assumed to be predominantly organic in character. As would be expected with increased decarbonisation, organic content decreases with increased pyrolysis temperature. The data presented in *Table 5.9* shows that the trace metals content remains almost consistent between biochar samples. There are no clear trends between chlorine content and either CLR or pyrolysis temperature. Similarly, no trend is observed between calcium content and CLR, which is somewhat counterintuitive; by contrast, calcium content is observed to increase with increasing temperature.

Considering the data in *Table 5.9*, it can be seen that the atomic ratio of chlorine to calcium decreases with increasing temperature at a constant CLR, and increases with increasing CLR at a constant temperature. A lower chlorine-to-calcium atomic ratio may indicate that calcium is present in more crystalline

forms, other than $CaCl_2$, which has a ratio of 2. This suggests that the proportion of $CaCl_2$ transforming into other calcium-based crystalline species decreases with increasing CLR and increases with increasing temperature. The transformation of $CaCl_2$-impregnated feedstock to $CaCO_3$ and CaOH-rich biochar has been reported in the literature[2], [6], [22]. It is possible the formation of $CaCO_3$ and CaOH during pyrolysis occurs from the interaction of $CaCl_2$ with pyrolysis vapours. Increasing CLR alone would only increase the formation of other calcium-based crystals if $CaCl_2$ were the limiting reactant. Assuming $CaCl_2$ to be present in excess on the biochar surface, an increase in temperature, resulting in a higher formation of pyrolysis gases, would be necessary to increase the proportion of $CaCl_2$ forming other calcium-based crystal species. The notable decrease in the chlorine-to-calcium ratio above 750 °C may also be explained by the melting of $CaCl_2$ above temperatures of 772 °C, producing solid calcium and chlorine gas [23].

Table 5.9: Results of bulk composition analysis using XRF for biochar samples synthesised in this work.

	Calcium (wt%)	**Chlorine (wt%)**	**Lightweight Elements (wt%)**	**Trace Metals (wt%)**	**Atomic Ratio (Cl:Ca)**
Woodchips	0.05	-	99.9	>0.1	-
Ca-1.75-T600	5.1	8.6	85.6	0.7	1.91
Ca-1.57-T644	4.6	6.8	87.9	0.7	1.67
Ca-1.93-T644	4.7	8.6	86.0	0.7	2.07
Ca-1.5-T750	5.4	7.7	86.2	0.7	1.61
Ca-1.75-T750 (average)	5.8± 0.3	8.5±0.3	85.0±0.6	0.7±0.01	1.66±0.01
Ca-2T-750	4.3	6.8	88.3	0.6	1.79
Ca-1.57-T856	8.6	9.7	80.1	1.6	1.28
Ca-1.93-T856	7.1	10.4	81.7	0.8	1.66
Ca-1.75-T900	8.6	8.4	82.3	0.7	1.10

*Expected atomic ratio of Cl:Ca in $CaCl_2$ =2

5.4.5 $CaCl_2$ Transformation During Pyrolysis

The main pyrolysis vapours released during pyrolysis of woody biomass include water, carbon monoxide, carbon dioxide, hydrogen, methane, ethane and other

light-weight hydrocarbons [24], [25], [26]. The reaction of $CaCl_2$ with pyrolysis vapours released during biomass pyrolysis is challenging to test and not well understood in the literature. However, previous work has been conducted on the thermal conversion of waste $CaCl_2$ in the presence of various gases to recover lime and HCl[27], [28], with the following reactions proposed [29]:

$$CaCl_2(s) + H_2O(g) \rightarrow Ca(OH)Cl(s) + HCl\,(g) \quad 410 - 740°C \qquad (R1)$$

$$CaCl_2(s) + H_2O(g) + CO_2(g) \rightarrow CaCO_3(s) + 2HCl\,(g) \quad < 640°C \qquad (R2)$$

$$CaCl_2(s) + 0.5O_2(g) \rightarrow CaO(s) + Cl_2(g) \quad 600 - 800°C \qquad (R3)$$

$$Ca(OH)Cl\,(s) + CO_2(g) \rightarrow CaCO_3(s) + HCl\,(g) \quad 410 - 640°C \qquad (R4)$$

$$Ca(OH)Cl\,(s) \rightarrow CaO(s) + HCl\,(g) \quad 640 - 740°C \qquad (R5)$$

Liu *et al*. tested the thermal degradation of $CaCl_2$ in the presence of H_2O, and found that the release of HCl gas increased linearly with increasing temperature between 400-900 °C [27]. The relative content of CaO to Ca(OH)Cl in the post-degradation residue was also found to increase with increasing temperature between 600-900 °C. Overall, the following reaction mechanism was proposed:

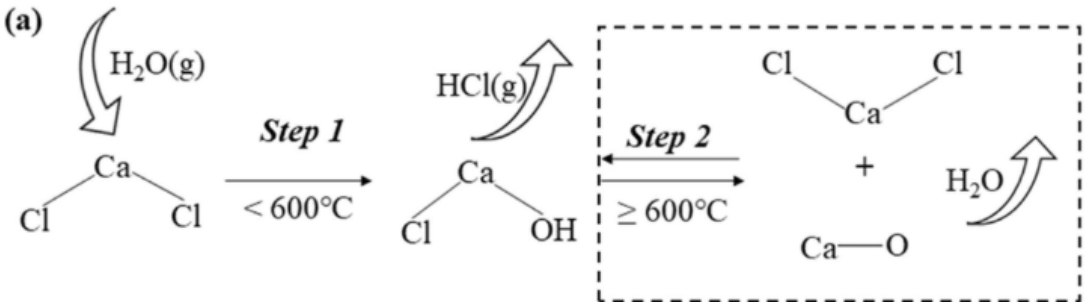

Figure 5.12: Reaction mechanism for the thermal degradation of $CaCl_2$ in the presence of H_2O as proposed by Liu et al[27].

Similarly, Zhao *et al*. tested the thermal decomposition of $CaCl_2$ in the presence of CO_2 [28]. The quantity of $CaCl_2.nH_2O$ (n = 2, 4) in the decomposition residue was seen to decrease with increasing temperature between 300-500 °C whilst

the quantity of $CaCO_3$ increased. Thermal degradation of wood between 600-900 °C in an inert N_2 atmosphere has been shown to produce pyrolysis gas mixtures with high CO_2 content in various studies[30], [31]. Whilst the presented reaction pathways are likely simplified compared to the processes occurring in a chemically complex carbonaceous material, such as biochar, they provide valuable insight into probable, similar thermal degradation pathways of $CaCl_2$ in the presence of pyrolysis gas.

An attempt was made to further investigate how the proportion of Ca in $CaCO_3$ and $CaCl_2$ changes with varying CLR and pyrolysis temperature through further characterisation. However, the chemically complex surface of the biochar samples made this problematic. An attempt was made to use XPS to calculate the proportion of Ca in $CaCO_3$ vs $CaCl_2$. This was unfortunately unsuccessful; Ca^{2+} peaks for $CaCO_3$, CaO, and $CaCl_2$ all fall within the same range, and thus it was not possible to distinguish the ligands to which Ca was bound. As mentioned above, FTIR did not show peaks distinct of $CaCl_2$, and EDS mapping on the surfaces of the biochar samples did not show any Cl at all, likely due to Cl being present in too small a quantity on the surface tested.

XRD patterns shown in *Figure 5.13* indicate the presence of calcium chloride tetrahydrate ($CaCl_2.4H_2O$) and calcite ($CaCO_3$) on the surface of biochars produced at 750 °C. All char samples produced similar diffraction patterns; thus, it was decided to display three at varying CLR with the diffraction patterns of the remaining char samples given in *Appendix A.2*. MindGenuis software was used to aid the matching process and select $CaCl_2.4H_2O$ and $CaCO_3$ peaks, for which example XRD patterns of pure samples are given for comparison in *Figure 5.13*. Diffraction patterns for biochar samples appear to be slightly shifted to the right on the x-axis, likely due to samples protruding further from the sample holder than expected, which may have also led to reduced peak intensity. The peaks for calcite within the biochar samples are clear and relatively sharp. Biochar samples are amorphous, making fitting of their backgrounds difficult and analysis of their XRD patterns challenging. It is acknowledged that, despite

calcium chloride being identified by the match software, if looking at any single biochar spectra the presence of $CaCl_2.4H_2O$ could not be determined confidently due to: a combination of disordered biochar background, a high number of similar intensity peaks in the $CaCl_2.4H_2O$ spectra, and low relative intensity of $CaCl_2.4H_2O$ peaks compared to $CaCO_3$. When considering only the diffraction pattern of Ca-1.5-T750, no characteristic peaks of $CaCl_2.4H_2O$ can be seen at all. However, when considering the diffraction patterns of all three samples, the key peaks for $CaCl_2.4H_2O$ can be seen to appear with increasing sharpness as CLR increases, making this identification more reasonable. The diffraction patterns of the tested biochars can also be seen to become increasingly disordered with increasing CLR, likely due to increased visibility of the smaller peaks given by $CaCl_2.4H_2O$.

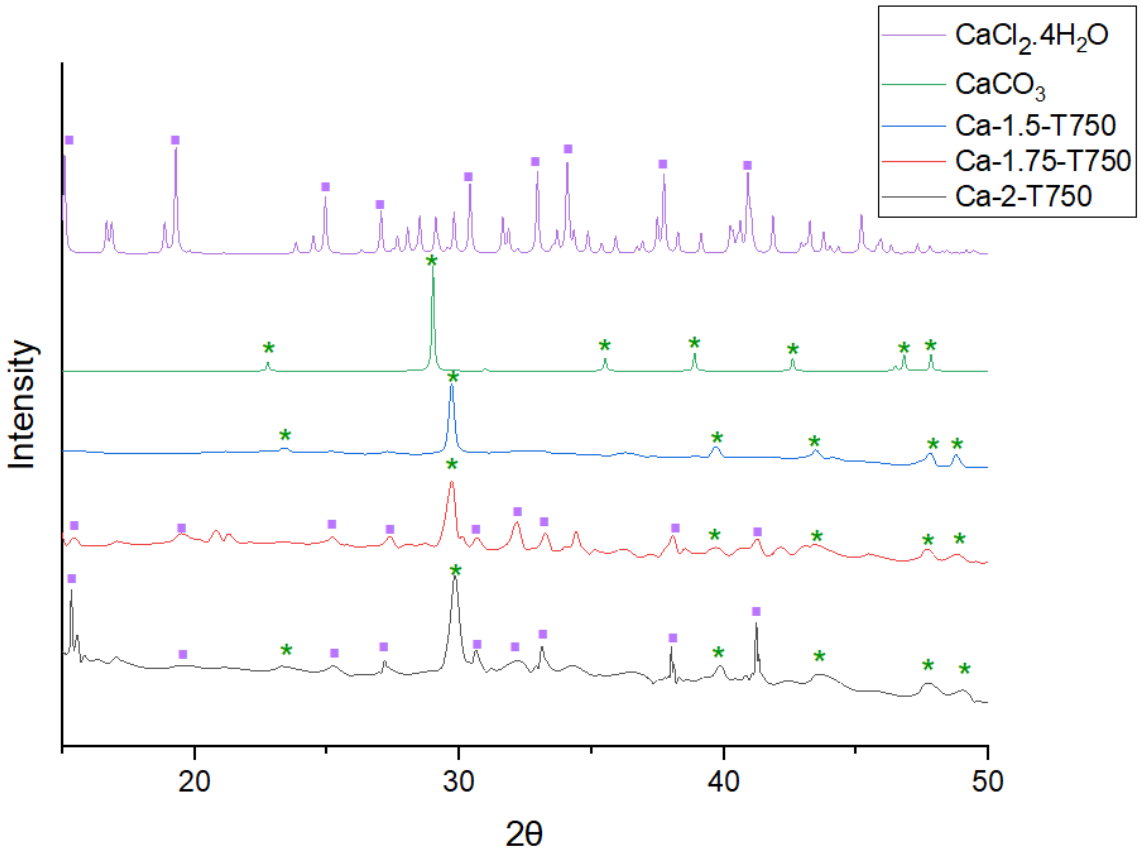

Figure 5.13: XRD pattern of Ca-1.5-T750 (blue), Ca-1.75-T750 (red), and Ca-2-T750 (black) biochar samples synthesised in this work with spectra of pure calcium chlorite (purple) and calcite (green).

5.4.5.1 Regression Analysis

To determine the relationship between pyrolysis temperature, CLR and the ratio of Cl:Ca, and to test its statistical significance, regression analysis was conducted. Regression analysis showed the ratio of Cl:Ca in the Ca-biochars to follow a linear relationship, given *in Equation 5.7*, with summary statistics given in *Table 5.10*.

$$Ratio\ Cl{:}Ca = 1.45 - 0.3015A + 0.1584B \tag{5.7}$$

*Table 5.10: Summary statistics for linear fit of Cl:Ca ratio (wt%) in Ca-biochars.**

Mean	**Std. Dev**	**C.V. %**	**Adjusted R^2**	**Predicted R^2**	**Adequate Precision**
1.45	0.08	5.43	0.83	0.70	19.15
ANOVA p-value					
Model	<0.0001				
A-Temperature (°C)	<0.0001				
B-CLR (wt:wt)	0.0014				

*Std. Dev is the standard deviation, C.V. is the coefficient of variance.

A C.V. value less than 10%, and adequate precision above 4, shows the data to be reproducible with a favourable signal-to-noise ratio for model fitting. The adjusted and predicted R^2 are in good agreement (difference <0.2). All model terms are statistically significant within a 95% confidence level. From *Equation 5.7*, the ratio of Cl:Ca can be seen to decrease with temperature and increase with CLR, as discussed above. Temperature is markedly more influential than CLR (approximately twice as much so), which is in agreement with the aforementioned hypothesis that $CaCl_2$ is present in excess and pyrolysis vapours are the rate-limiting reactant in the release of Cl from $CaCl_2$.

5.4.6 Summary

The presence of calcite on the surfaces of Ca-decorated biochar samples can be confirmed from FTIR, SEM-EDS, and XRD analysis. As shown by XRF analysis, the atomic ratio of Cl:Ca decreases away from that of $CaCl_2$ at constant CLR with increasing pyrolysis temperature, and increases towards the ratio of $CaCl_2$ at

constant pyrolysis temperature with increasing CLR. The relationship between mass ratio of Cl:Ca with pyrolysis temperature and CLR was found to be statistically significant. It is proposed that thermal degradation of $CaCl_2$ during biomass pyrolysis in an inert atmosphere follows reactions *R1, R2, & R4* reported above, with any remaining $CaCl_2$ absorbing water from the air post-pyrolysis, due to its highly hygroscopic nature.

While no quantitative chemical characterisation was capable of successfully confirming the proportion of Ca in $CaCO_3$ compared to $CaCl_2$ at different pyrolysis temperatures and CLRs; XRF and XRD results presented support for the proposed mechanism. Further experimental work to confirm or deny this mechanism may help in determining optimal functionalisation conditions based on the desired forms of Ca on the biochar surface.

5.5 Aqueous P-Recovery

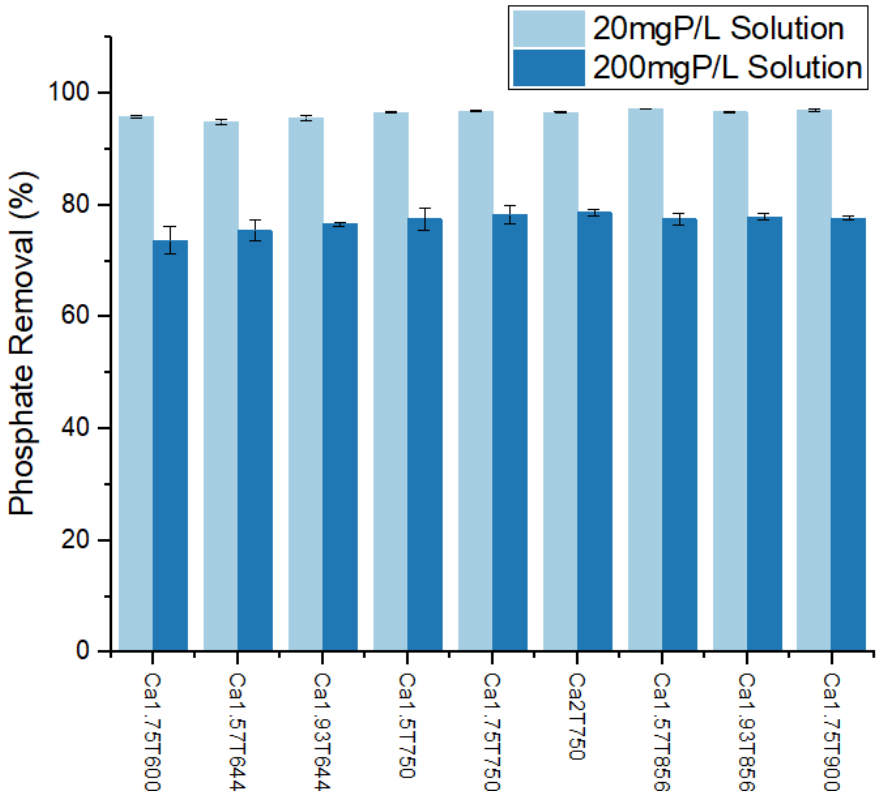

Figure 5.14: 24 h batch adsorption results of biochar samples synthesised in this work in 50mL of a 20 mg_P/L solution, biochar dosage of 2 g/L, 25°C, pH=8.

Figure 5.14 shows the results of 24 h batch phosphate removal tests carried out in duplicate at pH_i=8 for 20 mg_P/L and 200 mg_P/L solutions. Experiments were carried out at pH 8 to simulate the pH of eutrophic water, this pH is above the pH_{pzc} of the biochar samples, resulting in a negative net charge on the surface of the biochar samples. The data is also given in tabular form in *Table 5.11*. All biochars performed extremely well, removing up to 97% of phosphate from a 20 mg_P/L solution and up to 79% from a 200 mg_P/L solution. At 20 mg_P/L, removal was generally seen to increase slightly with increasing temperature and remained unchanged with increasing CLR. Due to marginally larger errors, the same cannot be said with confidence at 200 mg_P/L. With all biochars performing so well, it is challenging to identify any clear trends or best-performing chars. Regression analysis did not show P-removal to fit any of the tested models (linear, 2FI, quadratic, and cubic) due to the fact that removal capacities obtained were so similar across the range of biochars produced. Similarly, it was not possible to determine any correlation between biochar physicochemical properties and P-removal.

Table 5.11: 24h batch adsorption results of samples synthesised in this work in 50mL of a 20 mg_P/L solution, biochar dosage of 2 g/L, 25°C, pH=8.

	Phosphate sorption in 20mg_P/L solution (%)	**Phosphate sorption in 200mg_P/L solution (%)**
Ca-1.75-T600	95.8 ± 0.2	73.7 ± 2.5
Ca-1.57-T644	94.9 ± 0.4	75.4 ± 1.9
Ca-1.93-T644	95.6 ± 0.4	76.6 ± 0.4
Ca-1.5-T750	96.6 ± 0.2	77.5 ± 2
Ca-1.75-T750	96.8 ± 0.1	78.3 ± 1.7
Ca-2-T750	96.6 ± 0.2	78.7 ± 0.6
Ca-1.57-T856	97.2 ± 0.1	77.5 ± 1.0
Ca-1.93-T856	96.7 ± 0.1	77.9 ± 0.6
Ca-1.75-T900	97.0 ± 0.2	77.7 ± 0.4

5.6 Conclusions

Equations describing the relationships of pyrolysis temperature and CLR with four response variables (yield, surface area, average pore volume, and mass ratio of Cl:Ca) are presented. Temperature (A) was shown to be the most influential factor in terms of yield, surface area, and mass ratio of Ca:Cl of biochars, while A^2 was found to be the most influential factor on average pore size. Optimal conditions for high yield and average pore size were low temperature and high CLR, while optimal conditions for high surface area were low temperature and low CLR. No statistically significant interaction effects of pyrolysis temperature and CLR were present for any of the four response variables.

The presence of $CaCO_3$ on the surfaces of biochars was confirmed by FTIR, SEM-EDS, and XRD, with XRD also providing evidence of $CaCl_2.4H_2O$. It is proposed that $CaCl_2$ reacts with pyrolysis vapours (predominantly H_2O and CO_2) during pyrolysis to form $CaCO_3$, with excess $CaCl_2$ absorbing water from the atmosphere and forming $CaCl_2.4H_2O$.

All biochar samples demonstrated excellent phosphate removal, achieving up to 97% removal from a 20 mg_P/L solution and 79% from a 200 mg_P/L solution at a pH of 8. This is likely due to high uptake of $CaCl_2$ during impregnation and solution pH being favourable for precipitation reactions between Ca and phosphate. Due to the similarly high performance of all biochar samples, it was not possible to determine any correlation between the P-removal capacity of biochar samples and functionalisation conditions or physicochemical properties.

References

[1] Y.-K. Choi, H. M. Jang, E. Kan, A. R. Wallace, and W. Sun, “Adsorption of phosphate in water on a novel calcium hydroxide-coated dairy manure-derived biochar,” *Environmental Engineering Research*, vol. 3, no. 24, pp. 434–442, Oct. 2018, Accessed: Sep. 13, 2025. [Online]. Available: https://doi.org/10.4491/eer.2018.296

[2] F. Pan *et al.*, “Phosphorus adsorption by calcium chloride-modified buckwheat hulls biochar and the potential application as a fertilizer,” *J Clean Prod*, vol. 444, p. 141233, Mar. 2024, doi: 10.1016/J.JCLEPRO.2024.141233.

[3] R. Li *et al.*, “Simultaneous capture removal of phosphate, ammonium and organic substances by MgO impregnated biochar and its potential use in swine wastewater treatment,” *J Clean Prod*, vol. 147, pp. 96–107, Mar. 2017, doi: 10.1016/J.JCLEPRO.2017.01.069.

[4] Z. Ajmal, A. Muhmood, R. Dong, and S. Wu, “Probing the efficiency of magnetically modified biomass-derived biochar for effective phosphate removal,” *J Environ Manage*, vol. 253, p. 109730, Jan. 2020, doi: 10.1016/J.JENVMAN.2019.109730.

[5] L. Leng *et al.*, “An overview on engineering the surface area and porosity of biochar,” *Science of the Total Environment*, vol. 763, Apr. 2021, doi: 10.1016/J.SCITOTENV.2020.144204.

[6] P. Wang, M. Zhi, G. Cui, Z. Chu, and S. Wang, “A comparative study on phosphate removal from water using Phragmites australis biochars loaded with different metal oxides,” 2021, doi: 10.1098/rsos.201789.

[7] S. B. Liu *et al.*, “Production of biochars from Ca impregnated ramie biomass (Boehmeria nivea (L.) Gaud.) and their phosphate removal potential,” *RSC Adv*, vol. 6, no. 7, pp. 5871–5880, Jan. 2016, doi: 10.1039/C5RA22142K.

[8] K. Yadav, S. Jagadevan, K. Yadav, and S. Jagadevan, “Influence of Process Parameters on Synthesis of Biochar by Pyrolysis of Biomass: An Alternative Source of Energy,” *Recent Advances in Pyrolysis*, Jul. 2019, doi: 10.5772/INTECHOPEN.88204.

[9] A. Altıkat, M. H. Alma, A. Altıkat, M. E. Bilgili, and S. Altıkat, “A Comprehensive Study of Biochar Yield and Quality Concerning Pyrolysis

Conditions: A Multifaceted Approach," *Sustainability 2024, Vol. 16, Page 937*, vol. 16, no. 2, p. 937, Jan. 2024, doi: 10.3390/SU16020937.

[10] E. S. Khater, A. Bahnasawy, R. Hamouda, A. Sabahy, W. Abbas, and O. M. Morsy, "Biochar production under different pyrolysis temperatures with different types of agricultural wastes," *Sci Rep*, vol. 14, no. 1, p. 2625, Dec. 2024, doi: 10.1038/S41598-024-52336-5.

[11] C. Strangfeld, P. Wiehle, and S. M. Munsch, "About the dominance of mesopores in physisorption in amorphous materials," *Molecules*, vol. 26, no. 23, Dec. 2021, doi: 10.3390/molecules26237190.

[12] P. Suresh Kumar, L. Korving, K. J. Keesman, M. C. M. van Loosdrecht, and G. J. Witkamp, "Effect of pore size distribution and particle size of porous metal oxides on phosphate adsorption capacity and kinetics," *Chemical Engineering Journal*, vol. 358, pp. 160–169, Feb. 2019, doi: 10.1016/J.CEJ.2018.09.202.

[13] "9.4 - Studentized Residuals | STAT 462." Accessed: Sep. 13, 2025. [Online]. Available: https://online.stat.psu.edu/stat462/node/247/

[14] X. Zhang, P. Zhang, X. Yuan, Y. Li, and L. Han, "Effect of pyrolysis temperature and correlation analysis on the yield and physicochemical properties of crop residue biochar," *Bioresour Technol*, vol. 296, p. 122318, Jan. 2020, doi: 10.1016/J.BIORTECH.2019.122318.

[15] L. Habte, N. Shiferaw, D. Mulatu, T. Thenepalli, R. Chilakala, and J. W. Ahn, "Synthesis of nano-calcium oxide fromwaste eggshell by sol-gel method," *Sustainability (Switzerland)*, vol. 11, no. 11, Jun. 2019, doi: 10.3390/SU11113196.

[16] G. Bin Cai *et al.*, "1,3-Diamino-2-hydroxypropane-N,N,N',N'-tetraacetic acid stabilized amorphous calcium carbonate: Nucleation, transformation and crystal growth," *CrystEngComm*, vol. 12, no. 1, pp. 234–241, 2010, doi: 10.1039/B911426M.

[17] M. Ni and B. D. Ratner, "Differentiation of Calcium Carbonate Polymorphs by Surface Analysis Techniques – An XPS and TOF-SIMS study," *Surf Interface Anal*, vol. 40, no. 10, p. 1356, Oct. 2008, doi: 10.1002/SIA.2904.

[18] A. Ojstršek and S. Gorgieva, "Cellulose Nanofibrils-Reinforced Pectin Membranes for the Adsorption of Cationic Dyes from a Model Solution," *Polymers (Basel)*, vol. 16, no. 6, Mar. 2024, doi: 10.3390/POLYM16060724.

[19] C. M. Popescu, M. C. Popescu, G. Singurel, C. Vasile, D. S. Argyropoulos, and S. Willfor, “Spectral characterization of eucalyptus wood,” *Appl Spectrosc*, vol. 61, no. 11, pp. 1168–1177, Nov. 2007, doi: 10.1366/000370207782597076.

[20] M. U. Jamal, “Design of Experiments Optimisation of Scottish Wood Biochars for Water Remediation targeting selected Persistent Organic Pollutants,” The University of Strathclyde, Glasgow, 2023.

[21] R. Xiao *et al.*, “Biochar produced from mineral salt-impregnated chicken manure: Fertility properties and potential for carbon sequestration,” *Waste Management*, vol. 78, pp. 802–810, Aug. 2018, doi: 10.1016/J.WASMAN.2018.06.047.

[22] R. C. Ropp, “Group 17 (H, F, Cl, Br, I) Alkaline Earth Compounds,” in *Encyclopedia of the Alkaline Earth Compounds*, Elsevier, 2013, pp. 25–104. doi: 10.1016/B978-0-444-59550-8.00002-8.

[23] M. M. Ramirez-Corredores, “Pathways and Mechanisms of Fast Pyrolysis: Impact on Catalyst Research,” *The Role of Catalysis for the Sustainable Production of Bio-Fuels and Bio-Chemicals*, pp. 161–216, Jan. 2013, doi: 10.1016/B978-0-444-56330-9.00006-1.

[24] C. Di Blasi, “Combustion and gasification rates of lignocellulosic chars,” *Prog Energy Combust Sci*, vol. 35, no. 2, pp. 121–140, Apr. 2009, doi: 10.1016/J.PECS.2008.08.001.

[25] J. Lee, A. K. Sarmah, and E. E. Kwon, “Production and Formation of Biochar,” *Biochar from Biomass and Waste: Fundamentals and Applications*, pp. 3–18, Jan. 2019, doi: 10.1016/B978-0-12-811729-3.00001-7.

[26] C. Liu *et al.*, “Silica-assisted pyro-hydrolysis of CaCl2 waste for the recovery of hydrochloric acid (HCl): Reaction pathways with the evolution of Ca(OH)Cl intermediate by experimental investigation and DFT modelling,” *J Hazard Mater*, vol. 439, p. 129620, Oct. 2022, doi: 10.1016/J.JHAZMAT.2022.129620.

[27] Y. Zhao, L. Wen, Y. Zhang, J. Wang, and Z. Yang, “Study on the pyro-hydrolysis of CaCl2 with steam and CO2 by experiments and DFT calculation,” *Colloids Surf A Physicochem Eng Asp*, vol. 683, p. 133075, Feb. 2024, doi: 10.1016/J.COLSURFA.2023.133075.

[28] N. Sophonrat *et al.*, “Ex Situ Catalytic Pyrolysis of a Mixture of Polyvinyl Chloride and Cellulose Using Calcium Oxide for HCl Adsorption and Catalytic Reforming of the Pyrolysis Products,” *Ind Eng Chem Res*, vol. 58, no. 31, pp. 13960–13970, Aug. 2019, doi: 10.1021/ACS.IECR.9B02299/ASSET/IMAGES/MEDIUM/IE-2019-02299M_M004.GIF.

[29] J. Mankasem, P. Prasertcharoensuk, and A. N. Phan, “Intensification of two-stage biomass gasification for hydrogen production,” *Int J Hydrogen Energy*, vol. 49, pp. 189–202, Jan. 2024, doi: 10.1016/J.IJHYDENE.2023.07.212.

[30] P. Prasertcharoensuk, S. J. Bull, and A. N. Phan, “Gasification of waste biomass for hydrogen production: Effects of pyrolysis parameters,” *Renew Energy*, vol. 143, pp. 112–120, Dec. 2019, doi: 10.1016/J.RENENE.2019.05.009.

6 Removal Mechanisms of Aqueous Phosphate by Ca-Biochar

6.1 Introduction

The work presented in this chapter builds on the results from Chapter 5, which examined the synergistic effects of chemical loading ratio (CLR) and pyrolysis temperature on the physicochemical properties and aqueous P-removal of Ca-decorated biochars. In the previous chapter, Ca-biochar samples synthesised were found to have a high potential for P removal (95-97 % at 20 mg_P/L, 74-79% at 200 mg_P/L) over a wide concentration range. Similar high P-removal rates (63-100 %) have been reported in the literature for other Ca-biochars, within the same concentration range, via adsorption of phosphate onto the surface of biochar, with a primary mechanism of surface precipitation along with secondary contributions from electrostatic attraction and ligand exchange [1], [2], [3].

Functionalised biochars used in the literature to remove aqueous P from simple phosphate solutions have been reported to, at times, leach the metals used to functionalise the biochar samples into solution [4], [5], [6]. If Ca-biochar were to leach Ca^{2+} ions to the bulk solution during P-removal, it is feasible that these Ca^{2+} could react with aqueous phosphates via bulk precipitation. This could occur when dissolved Ca^{2+} and phosphate species exceed the solubility product of calcium phosphate phases, initiating nucleation and growth of calcium phosphate minerals. The most common precipitates formed from the interaction of Ca^{2+} and phosphate ions in aqueous conditions are brushite, octacalcium phosphate, amorphous calcium phosphate, and hydroxyapatite with chemical reactions for each given in *Equations 6.1-6.4* respectively [7], [8], [9]. P-removal via bulk precipitation between metal ions and aqueous P is an effective process, which is commonly used in water treatment plants during chemical treatment of P-rich wastewaters with metal salts (including $CaCl_2$) to form metal phosphate precipitates[10], [11], [12]. Although activated carbons are not currently used in this wastewater chemical treatment process, free metal ions provided to a P-rich

solution from biochar could potentially also form precipitates, just as metal ions provided from metal salts do during conventional wastewater treatment processes.

$$Ca^{2+} + HPO_4^{2-} + 2H_2O \rightarrow CaHPO_4 \cdot 2H_20\ (s) \quad 6.1$$

$$8Ca^{2+} + 2HPO_4^{2-} + 4PO_4^{3-} + 5H_2O \rightarrow Ca_8(HPO_4)_2(PO_4)_4 \cdot 5H_20\ (s) \quad 6.2$$

$$3Ca^{2+} + 2PO_4^{3-} + nH_2O \rightarrow Ca_3(PO_4)_2 \cdot nH_20\ (s) \quad 6.3$$

$$5Ca^{2+} + 3PO_4^{3-} + OH^- \rightarrow Ca_5(HPO_4)_3OH\ (s) \quad 6.4$$

Despite the leaching of metal cations from biochar to solution previously reported in the literature, the potential role of bulk precipitation in P-removal between aqueous P and metal cations leached from biochar has not been examined. Chemical characterisation, presented in Chapter 5, confirmed the presence of Ca on the surface of biochars synthesised in this work in two main forms: $CaCl_2.4H_2O$ and $CaCO_3$. This chapter aims to investigate the P-removal mechanism of the biochar samples produced, with particular focus on the roles of adsorption and bulk precipitation, and provide an understanding of the role that different forms of Ca play in P-removal.

6.2 Methodology

The work presented in this chapter uses the same biochar samples synthesised in Chapter 5, as such the methodology for the production of Ca-biochar samples used can be found in *Section 5.2*. *Figure 6.1* provides an overview of the methodology used in this chapter to differentiate between the total P-removal (adsorption + bulk precipitation) potential of Ca-biochar and any adsorption-only potential. Where biochar samples are referred to as 'washed', this means functionalised biochar was stirred for 24 h in deionised (DI) water adjusted to pH 8 (using 0.1 M NaOH) at a dosage rate of 2 g/L and then dried in an oven. It is assumed that washing the biochar completely removed any Ca or Cl that would usually dissolve otherwise during P-removal experiments, leaving only $CaCO_3$; consequently, P-removal by washed biochar samples can be considered to be

due to adsorption alone. The Ca-biochar samples (*Figure 6.1a*) were rinsed with DI water prior to characterisation to remove any bulk precipitate coating the biochars surface, any P identified on the surface after rinsing was assumed to be adsorbed-P. To decouple the effects of adsorption and precipitation, the P-removal performance of washed (adsorption only) and unwashed (adsorption + precipitation) biochar samples is compared in this work.

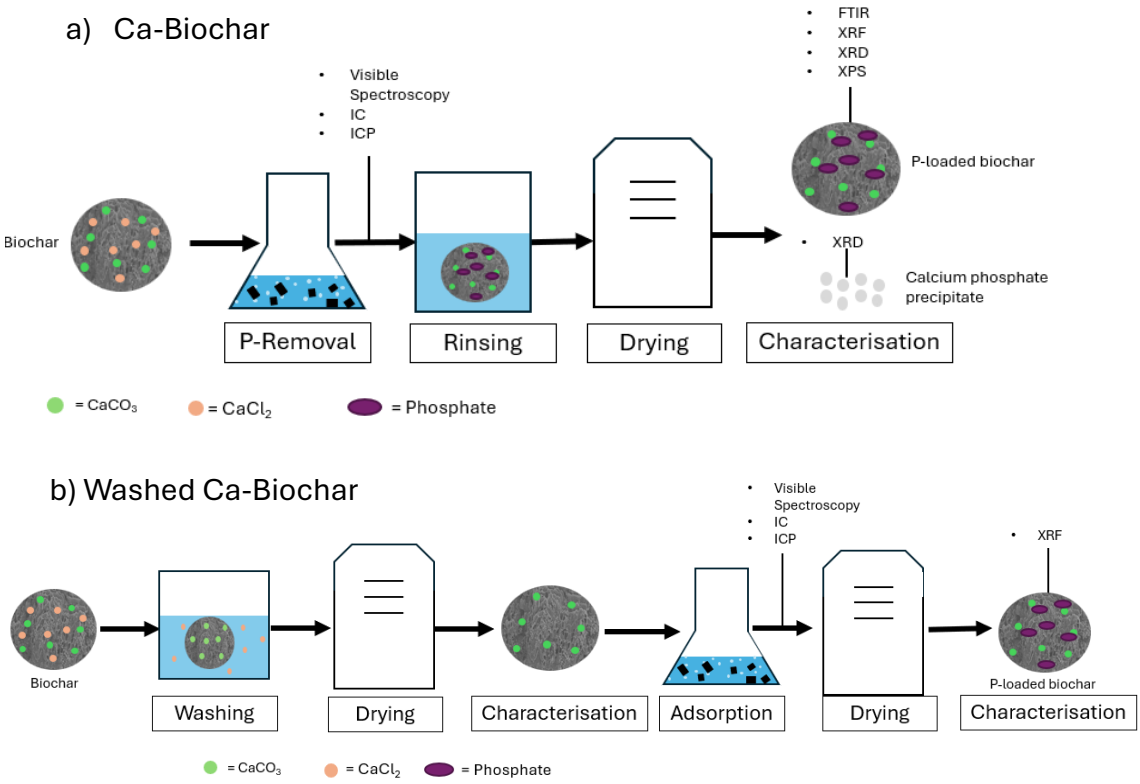

Figure 6.1: Flow diagram showing the methodology for analysis of a) total P-removal by Ca-biochar and b) P-adsorption by washed Ca-biochar.

6.3 Results and Discussion

6.3.1 Metal Dissolution from Biochar During Aqueous P-Removal

As displayed in *Figure 5.14*, *Section 5.5* biochar samples demonstrated excellent 24 h batch P-removal in 50 mL solutions, removing 95-97 % of P from a 20 mg_P/L solution and 74-79 % of P from a 200 mg_P/L solution.

To confirm the presence of P and other elements on biochar after 24 h removal at 20 mg_P/L, XRF analysis, the results of which are presented in *Table 6.1,* was carried out using Ca-1.75-T750 biochar samples, as an example, due to their high P-removal and position as DoE midpoint. The addition of P to unwashed biochar (*Figure 6.1a*) post P-removal confirms successful adsorption of phosphate by biochar. The Cl content of biochar after P-removal appeared to reduce significantly, indicating that there was release of Cl from the biochar into the solution. The Ca content of the biochar appeared to increase considerably after P-recovery, despite the biochar samples being the only source of Ca present, this is due to a significant loss of biochar mass during P-removal. To quantify this mass loss, Ca-1.75-T750 biochar samples were washed in DI water, adjusted to pH 8 to mirror the condition of P-removal experiments, with an average mass loss of 54.2 ± 4.4 %, indicating a net mass loss of Ca. XRD analysis (*Figure 5.13*) shows the presence of $CaCl_2.4H_2O$ on the biochars surface, assuming all Cl present in the biochar to be in the form of $CaCl_2.4H_2O$, loss of hydrated calcium chloride could feasibly account for approximately half of the observed mass loss. Significant carbon dissolution is unlikely for biochar samples produced high pyrolysis temperatures, such as those used in this work, where most labile carbon is volatilized during pyrolysis leaving a highly stable carbon matrix. Additional mass loss beyond the loss of $CaCl_2.4H_2O$ could result from the removal of other soluble mineral phases derived from feedstock ash, loss of water bound in other mineral phases, and dissolution of salts weakening the biochar matrix causing structural collapse and detachment of fine particles that are easily lost when collecting biochar after washing. These potential causes of additional mass loss beyond the loss of $CaCl_2.4H_2O$ would account for the net mass loss in the share of the biochar mass allocated to lightweight elements. The percentage weight of lightweight elements is calculated during XRF analysis by PCEDX-Navi software using a correction that assumes all unidentified mass belongs to elements with atomic numbers 12 or lower; in the case of biochar, this

is most likely a mixture of C, H, N, O, and small amounts of lightweight minerals such as Na and Mg.

Table 6.1: XRF results obtained for Ca-1.75-T750 (DoE2 midpoint) before and after 24 h batch P-removal (50mL solution, 2g/L biochar dosage, c_i=20 mg_P/L, 25°C, pH=8). Values given in the table are averages ± standard error.

Biochar Sample	Ca (wt%)	Cl (wt%)	P (wt%)	Lightweight Elements (wt%)	Trace Metals (wt%)
Ca-1.75-T750 (Pre P-removal)	5.8 ± 0.3	8.5 ± 0.3	-	85.0 ± 0.6	0.7 ± 0.01
Ca-1.75-T750 (Post P-removal)	10.8 ± 0.1	1.1 ± 0.1	2.1 ± 0.6	85.6 ± 0.9	0.5 ± 0.4

6.3.2 P-removal via Precipitation

XRF analysis results obtained for Ca-1.75-T750 are shown in *Table 6.1* and confirm adsorption of P onto the surface of the biochar; however, they also indicate dissolution of components from the biochar into solution, which could facilitate removal via precipitation. The influencing factors and the compounds being precipitated are further investigated in this section.

6.3.2.1 Factors Influencing Precipitation Detection

In the 50 mL batch experiments carried out to collect data used in the creation of *Figure 5.14*, no visible signs of precipitation were present at either low concentration (20 mg_P/L), or high (200 mg_P/L) concentration, as shown in *Figure 6.2a*. However, the small scale of these experiments and the consequently small number of crystals formed would make it difficult to distinguish between very small precipitate crystals and fine particulate powder of biochar when in solution. Additionally, the use of white filter paper may hinder the detection of any trace amounts of white-coloured precipitates. When both volume and P-concentration were increased during 24 h batch experiments, to 800 mL

solutions of 250 mg_P/L (pH_i 8), solid white precipitate was visibly present, as shown in *Figure 6.2b*.

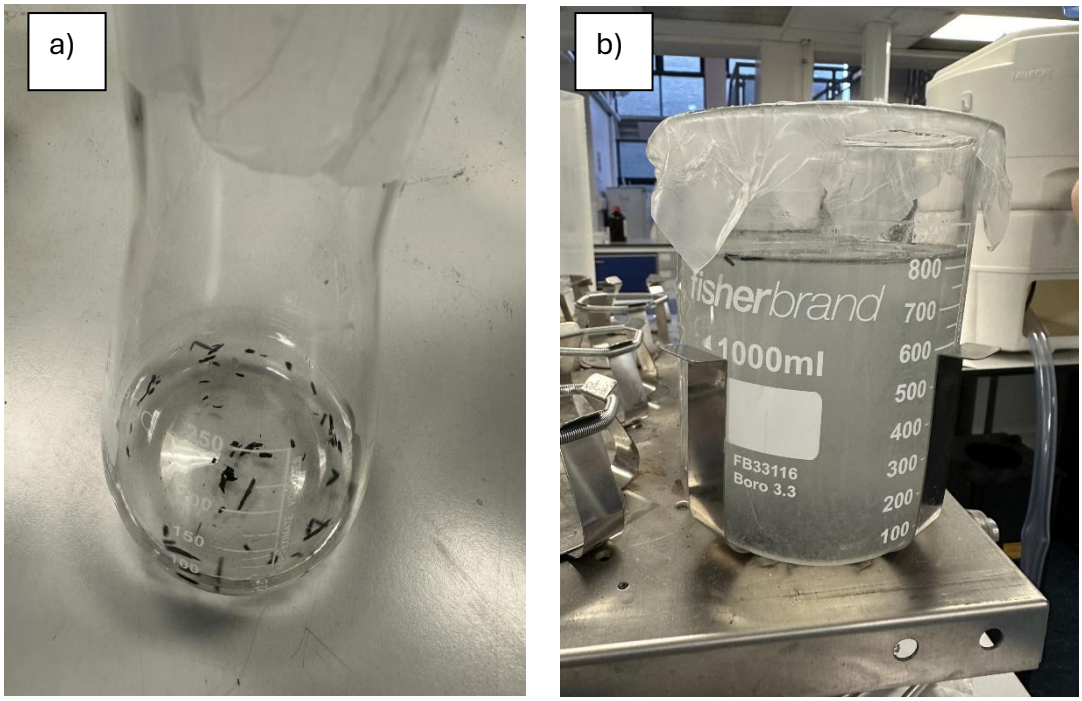

Figure 6.2:Comparison of 24 h batch P-removal experiment carried out using Ca-1.75-T750 biochar, synthesised in this work, using a) 50 mL of 200 mg_P/L solution and b) 800 mL of 250 mg_P/L solution.

6.3.2.2 Identification of Bulk Precipitate

The XRD pattern of the precipitate obtained during 800 mL batch P-removal experiments, using sample Ca-1.75-T750, is shown in *Figure 6.3*. The XRD pattern of the precipitate provides an excellent match to the known spectra for brushite ($Ca(HPO_4).2H_2O$), also shown in *Figure 6.3*. Some additional small peaks appear in the diffraction pattern of the precipitate compared to pure brushite, likely due to traces of impurities or biochar.

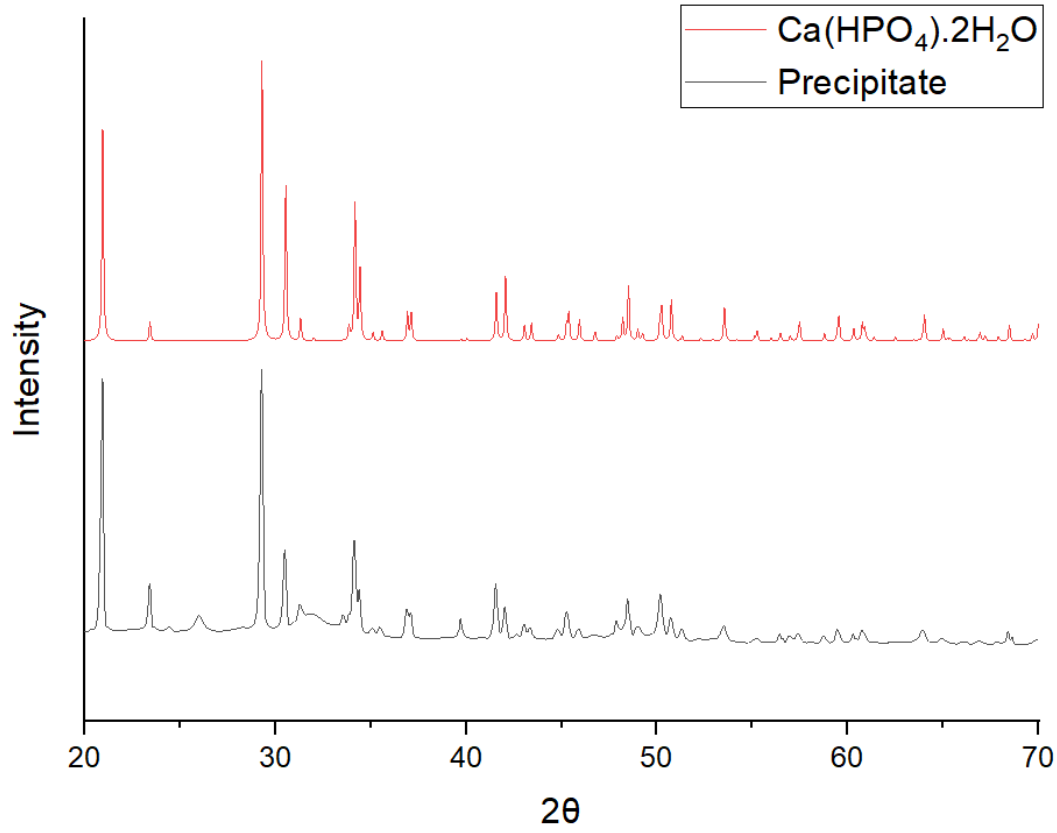

Figure 6.3:XRD pattern of precipitate obtained during batch P-removal (50mL solution, 2g/L biochar dosage, c_i=250 mg_P/L, 25°C, pH=8) by Ca-biochar (black) and known XRD spectra of brushite (red).

6.3.2.3 Dissolution of $CaCl_2$ During P-Removal

The formation of brushite during P-removal confirms that dissolution of Ca occurs from the biochar to solution. To determine whether Ca and Cl dissolution from biochar samples was caused by the aqueous environment or the presence of phosphate, the biochar was washed in DI water, adjusted to pH 8 to mimic conditions of phosphate solution without any P, and the washing eluent was then analysed. The Ca and Cl content of washing eluents for samples Ca-1.75-T600, Ca-1.75-T750, and Ca-1.75-T900 are listed in *Table 6.2*. Experiments were run in duplicate, and samples Ca-1.75-T600 and Ca-1.75-T900 were included in this analysis to assess whether increasing pyrolysis temperature enhanced the stability of Ca and Cl on biochar and, therefore, reduced dissolution. The results show that large amounts of Ca and Cl dissolve into solution in the absence of

phosphate, indicating that dissolution is caused by the aqueous environment rather than attraction to phosphate ions. The Cl concentrations in the eluent samples align well with the expected values, based on the Ca concentrations, for ions to originate from $CaCl_2$ dissolution. The average quantity of both Ca and Cl dissolved appeared to increase with higher pyrolysis temperature; however, since the error associated with a single sample was often larger than the variation between samples, the only reliable conclusion is that biochar pyrolysed at 900 °C dissolved more Ca than samples pyrolysed at 600 °C and 750 °C.

Table 6.2: Ca content (determined by ICP-AES) and Cl content (determined by IC) of eluent from washing of biochar samples synthesised in this work (washed in 800mL DI water altered to pH 8, biochar dosage 2g/L). Values are given as average ± standard error. Values for Cl content of eluent expected based on $CaCl_2$ release were calculated using average Ca values in eluent.

Sample Washed	**Ca in eluent (mg/L)**	**Cl in eluent (mg/L)**	**Cl expected based on $CaCl_2$ release**
Ca-1.75-T600	239 ± 5	397 ± 37	423
Ca-1.75-T750	232 ± 6	401 ± 13	410
Ca-1.75-T900	251 ± 3	440 ± 3	444

To further investigate the form of Ca dissolved from the biochar during washing, XRD analysis was carried out on the washed Ca-1.75-T750 sample, with the obtained diffraction pattern displayed in *Figure 6.4*. Characteristic peaks of both calcium chloride tetrahydrate ($CaCl_2.4H_2O$) and calcite ($CaCO_3$) are visible on the diffraction pattern of Ca-1.75-T750 biochar before washing; however, only peaks for calcite remain after washing, confirming that calcium chloride has been dissolved from the biochar into solution, likely due to calcium chloride being highly solubility in water [13].

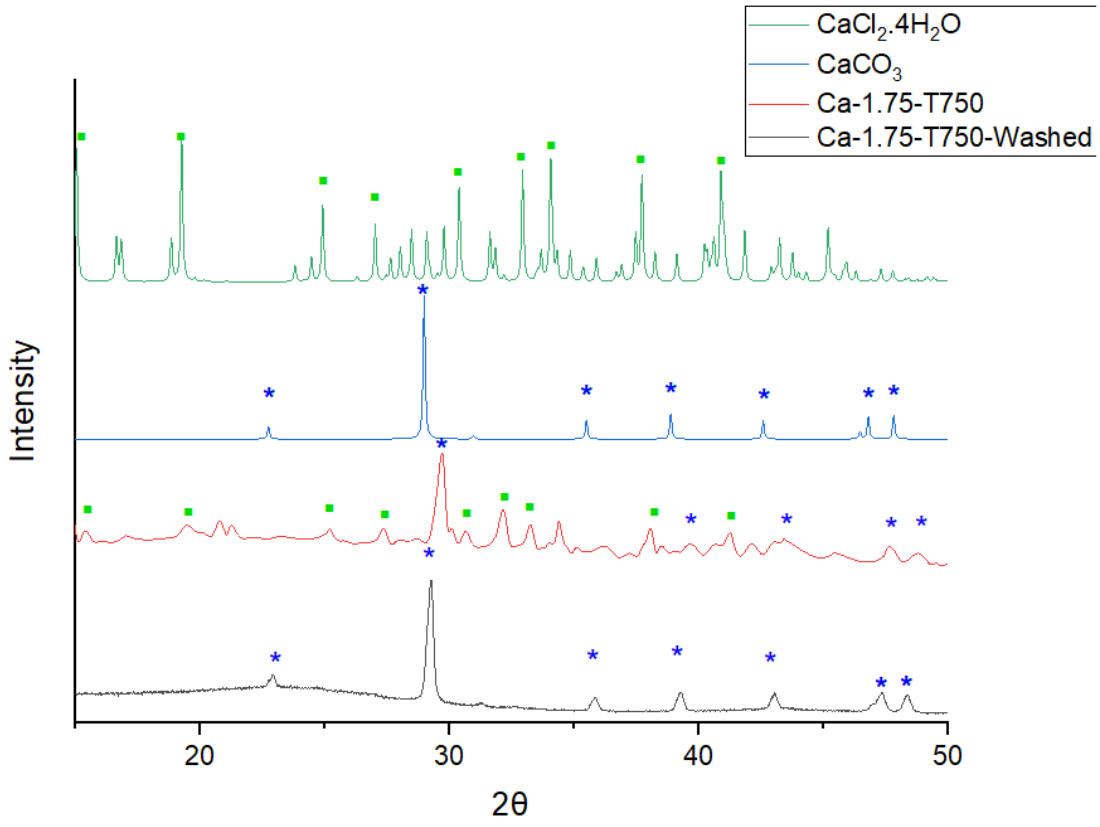

Figure 6.4:XRD patterns of Ca-1.75-T750 biochar synthesised in this work before washing (red), and after washing (black) with spectra of pure calcium chloride tetrahydrate (green) and calcite (blue). Washing carried out in 800mL of DI water altered to pH 8, biochar dosage 2g/L.

XRF analysis, the result of which are presented in *Table 6.3*, was carried out to examine the effects of washing on the chemical characteristics of biochar samples synthesised at various CLRs and pyrolysis temperatures. After washing, all biochar samples exhibited extremely similar compositions with 4.1-5.0 wt % Ca and 0.8-1.1 wt % Cl. The atomic ratio of Cl to Ca was far lower (0.18-0.29) than that of $CaCl_2$ (2), indicating only a very small proportion of Ca remaining in biochar could possibly be in the form $CaCl_2$. The atomic ratio of Cl:Ca appears to decrease as pyrolysis temperature increases, which is consistent with the findings presented in *Table 5.9*, *Section 5.4.4*.

*Table 6.3: XRF Compositional analysis of biochar samples synthesised in this work after washing.*Washing carried out in 800mL of DI water altered to pH 8, biochar dosage 2g/L.*

	Calcium (wt%)	Chlorine (wt%)	Lightweight Elements (wt%)	Trace Metals (wt%)	Atomic Ratio (Cl:Ca)
Ca-1.75-T600	4.1	0.9	94.5	0.5	0.25
Ca-1.57-T644	5.0	1.3	93.2	0.5	0.29
Ca-1.93-T644	4.3	1.1	94.2	0.4	0.29
Ca-1.5-T750	4.4	0.9	94.3	0.4	0.23
Ca-1.75-T750	4.8	1.0	93.6	0.6	0.24
Ca-2-T750	4.6	1.0	93.9	0.5	0.25
Ca-1.57-T856	4.8	0.9	93.9	0.4	0.21
Ca-1.93-T856	5.0	0.9	93.6	0.5	0.20
Ca-1.75-T900	4.9	0.8	93.7	0.6	0.18

*Expected atomic ratio of Cl:Ca in $CaCl_2$ =2

6.3.3 P-Removal Pathways: Adsorption and Precipitation

Considering data presented in *Table 6.1* confirming the adsorption of P on biochars surface, alongside *Figure 6.3* confirming bulk precipitation of $Ca(HPO_4).2H_2O$, P-removal can be considered to occur via a dual mechanism of precipitation and adsorption. However, the capacity for P removal through precipitation or adsorption alone remains unclear, this is investigated in this section to provide a better understanding of the P-removal process occurring.

6.3.3.1 P-removal Potential and P-adsorption Potential

Figure 6.5 shows the 24 h batch P-removal by unwashed (adsorption + precipitation) and washed (adsorption only) biochar samples from a 20 mg_P/L solution. For unwashed biochar samples, total P-removal ranged from 94.9% to 97.0%, while washed biochar samples adsorbed 16.5% to 43.7% of P. Values obtained are in good agreement with those reported in the literature for P-removal by Ca-rich biochars at similar P concentrations (64-100 %) [1], [2], [3].

In most cases, adsorption could account for approximately 38-45 % of P-removal, indicating that although precipitation appears to be the primary removal mechanism, adsorption can still play a significant role. It is important to note that the data presented likely do not reflect the actual balance between precipitation and adsorption during P-removal. Instead, they compare the potential of biochar samples to adsorb phosphate within 24 h with the total P-removal potential over 24 h. Unfortunately, it was not possible to determine the exact split of adsorption and precipitation as neither the collection and separation of the small quantity of precipitate crystals, mixed with dust particles of biochar, nor an accurate quantification of phosphate in the biochar was feasible to allow for a mass balance to be carried out at the scale of the experiment was undertaken.

The consistently high level of P-removal by unwashed biochar, even in samples with low adsorption potential (such as Ca-1.75-T600 and Ca-1.93-T644), suggests that sufficient $CaCl_2$ dissolves into the solution to offset poor adsorption performance. Although it is theoretically possible for all P removal to occur via precipitation, evidence presented in *Table 6.1* and *Section 6.3.3.3* indicates the presence of P on the biochar surface post-P-removal, negating this possibility.

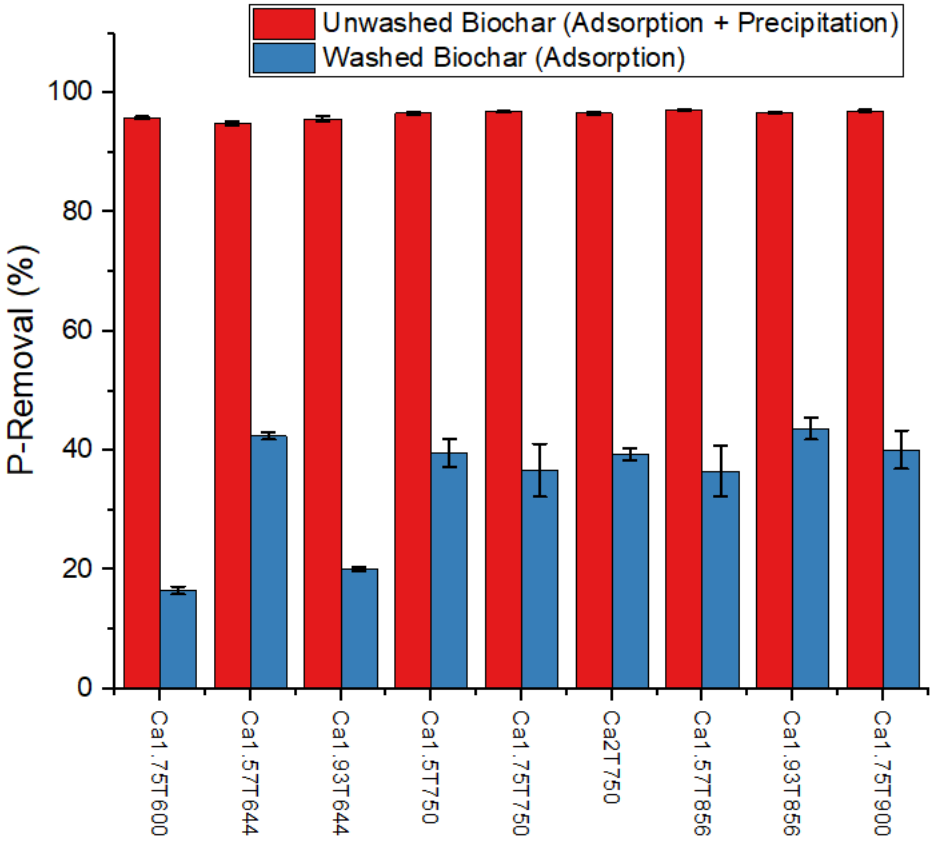

Figure 6.5: 24 h batch adsorption results of biochar samples synthesised in this work in 50mL of 20mg$_P$/L solution, biochar dosage of 2 g/L, 25 °C, pH=8. Washing carried out in 800mL of DI water altered to pH 8, biochar dosage 2g/L.

6.3.3.2 Effects of Phosphate Speciation on P-Removal Mechanisms

The P-removal capacities offered by unwashed biochar samples and the P-adsorption availabilities from washed biochars samples were studied across a range of pH (2-10), as shown in *Figure 6.7,* with the relationship between P-removal, P-adsorption, pH, and pH_{pzc} for midpoint sample Ca-1.75-T750 shown in *Figure 6.8*. This pH range was chosen to examine the effects of phosphate speciation for the two forms of phosphate known to be present in eutrophic water, i.e. $H_2PO_4^-$ and HPO_4^{2-}. The variation in phosphate speciation with pH is given in *Figure 6.6*. It should be noted that biochar samples, used to predict removal through adsorption across the stated pH range, were all washed at pH 8. Therefore, data for P-adsorption at pH values other than 8 may not accurately reflect the true adsorption potential of biochar samples at those pH values, as

biochar would be expected to dissolve different quantities of Ca and Cl when washed at different pH levels, with metal dissolution increasing with reducing pH [14]. Rather than represent an exact balance between adsorption and precipitation at various pH levels, this data aims to help understand the effects of phosphate speciation and biochar net surface charge on P-removal pathways.

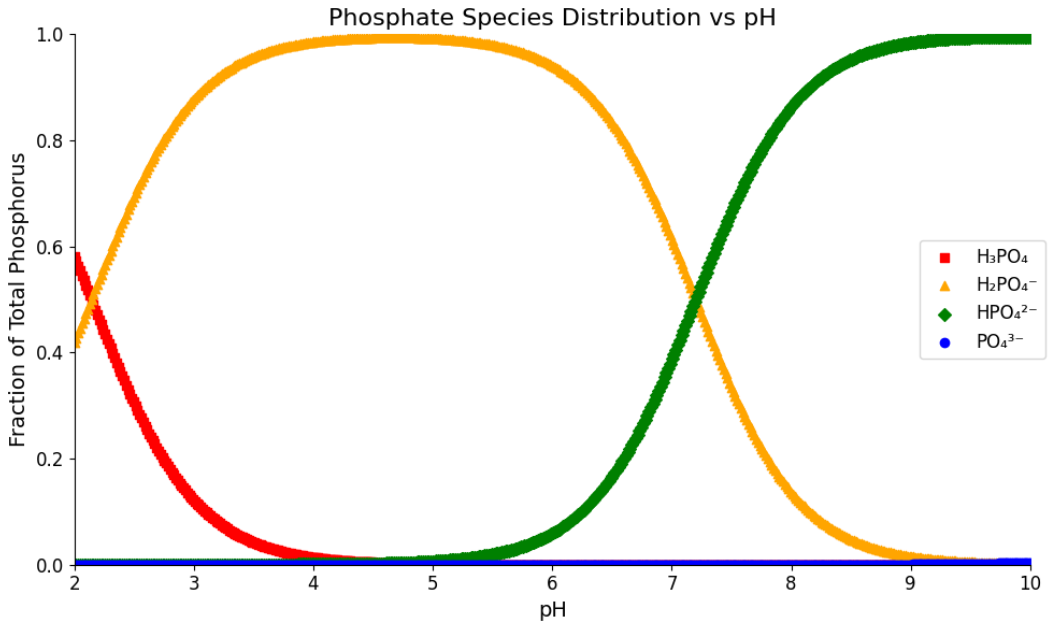

Figure 6.6: Diagram showing phosphate speciation in water as a function of pH, recreated and amended from [15] using generative AI (M365 Copilot) by inserting reference figure and using prompt: remake this image using different colours for each phosphorus species/shape and shorten the data range to be between pH 2-10.

A modest reduction in P-removal occurs for unwashed biochar samples when decreasing the pH from 6 to 4, with a significant decrease observed when lowering the pH further to 2, this can be primarily attributed to the reduced contribution of precipitation towards P-removal, as $Ca(HPO_4).2H_2O$ becomes increasingly soluble in water below pH 5, with a sharp increase in solubility below pH 4 [16], [17]. A similar decrease in P-adsorption is observed in washed biochar samples between pH 4 and 2; while a lower solution pH raises the net charge of the biochar surface, it also increases the proportion of phosphate present in the form of H_3PO_4 compared to $H_2PO_4^-$, thus reducing the amount of phosphate attracted to the increasingly positive biochar surface.

At pH 4, both P-removal and P-adsorption levels vary with the pyrolysis temperature and CLR used to produce the biochar, with the variations in P-removal generally following the same trend as those in P-adsorption, indicating that, as the solubility of $Ca(HPO_4).2H_2O$ decreases, the total P-removal capacity of a biochar is increasingly influenced by the adsorption capacity of the biochar. Adsorption uptake of P at pH 4 by washed biochar samples appears to increase with increasing pyrolysis temperature and increasing CLR, with the exception of samples synthesised at 856 °C, where error bars overlap. As can be seen from *Figure 6.6*, phosphate is expected to exist almost exclusively in the form of $H_2PO_4^-$ at pH 4, indicating that both pyrolysis temperature and CLR are influential in the recovery of dibasic phosphate.

At pH 2, precipitation is extremely unlikely, and P-removal can be considered to be due almost entirely to P-adsorption [16], [17]. At pH 2, P-adsorption on washed biochar samples appears to increase with increasing pyrolysis temperature, with samples synthesised above 644 °C removing more P from solution than unwashed biochar samples. Low pH has been shown to increase the dissolution of Ca from biochars, as such, biochar samples washed at pH 8 will likely release extra Ca at pH 2 [14]. A lower Ca^{2+} concentration in the phosphate solutions treated with washed biochars compared to unwashed biochars, due to a large proportion of soluble Ca already removed from the washed samples, could allow for a greater net dissolution of Ca from washed chars, reducing pore blockage and increasing available surface area for electrostatic interaction with aqueous P [18].

P adsorption appears to mainly decrease as pH rises from 6 to 8; however, for most samples, it is difficult to determine whether adsorption truly increases or decreases due to the overlapping error bars observed among the data points. Similarly, in most washed samples, it is challenging to ascertain whether P-adsorption truly increases or decreases as pH rises from 8 to 10. The point of zero charge (pH_{pzc}) of washed biochar samples ranged from 7.64 to 7.78 (see *Appendix A.4*). As pH increases past the pH_{pzc} of a sample, the char has an increasing

number of negative surface sites, which increases overall electrostatic repulsion between the biochar and phosphate particles. However, as pH rises from 6 to 8, the primary form of phosphate changes from $H_2PO_4^-$ to HPO_4^{2-}, increasing attraction between phosphate and the positive surface sites that remain. Similarly, as pH rises to 10, the biochar surface becomes increasingly net negative, and phosphate is almost exclusively in the form HPO_4^{2-} (see *Figure 6.6*). The inconsistency in the effects of solution pH between 6 and 10 on washed biochar samples is likely determined by the balance between increased tendency for repulsion of phosphate at the biochar surface and the greater affinity of phosphate for the remaining positive surface sites. When phosphate is present exclusively in the form HPO_4^{2-} (pH 10), adsorption can be seen to increase with increasing pyrolysis temperature.

The pH_{pzc} of unwashed biochars ranged from 7.2-7.3 (*Table 5.8*). P-removal can be seen to increase between pH 6-10 for unwashed biochar samples, despite increasing beyond the pH_{pzc} of the biochar samples, likely due to an increase in the proportion of phosphate in the form of HPO_4^{2-}, and decreased solubility of calcium phosphate, favouring precipitation.

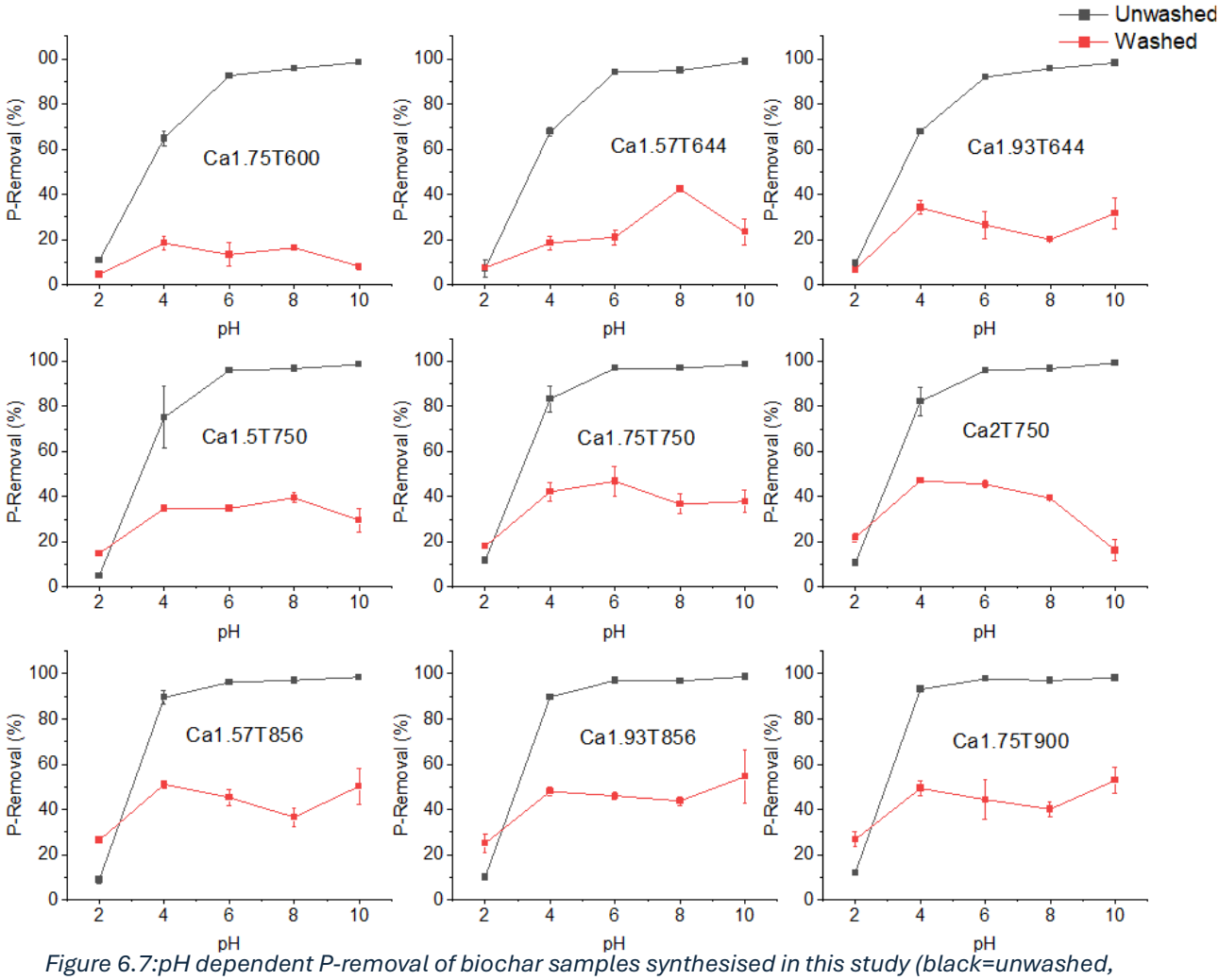

Figure 6.7:pH dependent P-removal of biochar samples synthesised in this study (black=unwashed, red=washed) in 24 h batch experiments using 50 mL of 20 mg_P/L solution, biochar dosage of 2g/L, 25 °C. Error bars are given for all data points, where error bars are not visible this is because error bars are smaller than the symbol size.

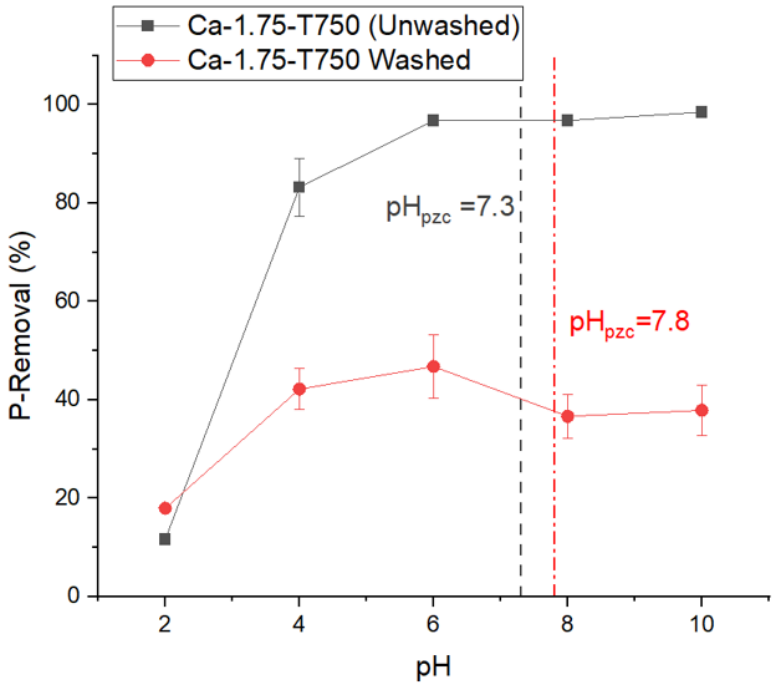

Figure 6.8: pH dependent P-removal and point of zero charge (pH_{pzc}) of biochar sample Ca-1.75-T750 synthesised in this study (black=unwashed, red=washed) in 24 h batch experiments using 50 mL of 20 mg_P/L solution, biochar dosage of 2g/L, 25 °C. Error bars are given for all data points, where error bars are not visible this is because error bars are smaller than the symbol size.

6.3.3.3 Post P-recovery Biochar Characterisation

Post P-removal analysis of unwashed biochar was carried out on sample Ca-1.75-T750 after 24 h batch adsorption in a 250 mg_P/L solution, pH 8. Sample Ca-1.75-T750 was chosen, as an example, due to high P-removal and position as DoE midpoint. Furthermore, large quantities of post-P-removal biochar produced at high P concentration allowed for easier detection of P during characterisation. The biochar sample was rinsed with DI water post P-removal, prior to characterisation, to ensure any bulk precipitate coating the biochar surface was removed.

Figure 6.9 shows the FTIR spectra obtained for Ca-1.75-T750 biochar before and after 24 h batch adsorption in a 250 mg_P/L solution, pH 8. After adsorption, a new peak can be seen at 1025 cm^{-1}, representing the bending vibration of P-O and confirming the presence of P on the biochar surface [19]. Characteristic peaks of

calcite (asymmetric stretching of the C-O bond at 1416 cm^{-1}, and out-of-plane bending of the C-O bond at 871 cm^{-1}) show reduced intensity post adsorption, indicating that calcite is involved in the adsorption process [20]. Post P-removal broadening, increased intensity, and red shift of the broad O-H stretch between 3700-2800 cm^{-1} indicate increased hydrogen bonding, with the peaks asymmetric shape suggesting hydrogen bonding to be occurring in a range of different environments [21], [22], [23].

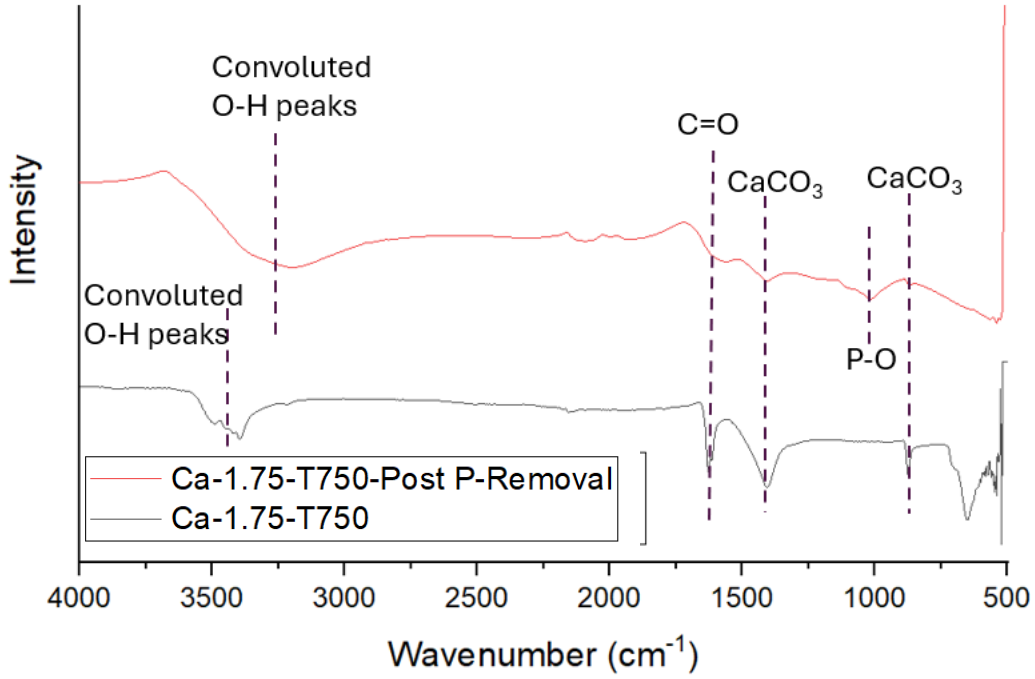

Figure 6.9: FTIR spectra of Ca-1.75-T750 biochar: pre-P removal (black) and post P-Removal (red).P-removal carried out in a 50mL solution, 2g/L biochar dosage, c_i=250 mg_P/L, 25°C, pH=8.

XRD patterns presented in *Figure 6.10,* show that post P-removal biochar loses characteristic peaks of $CaCl_2.4H_2O$ compared to pre P-removal biochar. The broad amorphous peak appearing after P-removal, centring around 27°, matches the diffraction patterns reported for amorphous calcium phosphate in the literature [24], [25]. No distinct peaks of crystalline calcium phosphate phases, such as brushite, monetite, or hydroxyapatite(HAP), can be seen. Amorphous calcium phosphate is a metastable precursor to HAP and brushite; as such, it would be expected, over time, to transform into more thermodynamically stable states [26]. The presence of amorphous calcium phosphate, without further

crystallisation, into forms such as HAP is likely due to insufficient time for transformation of amorphous calcium phosphate, and interactions with organic molecules on the biochar surface stabilising amorphous calcium phosphate [26], [27]. While some key intensity peaks of $CaCO_3$ are maintained after P-removal, they appear less sharp, with the large amorphous background making identification difficult. Alternative characterisation methods (FTIR and XPS) provide better evidence of the consistent presence of $CaCO_3$ on the surface of the biochars post P-removal.

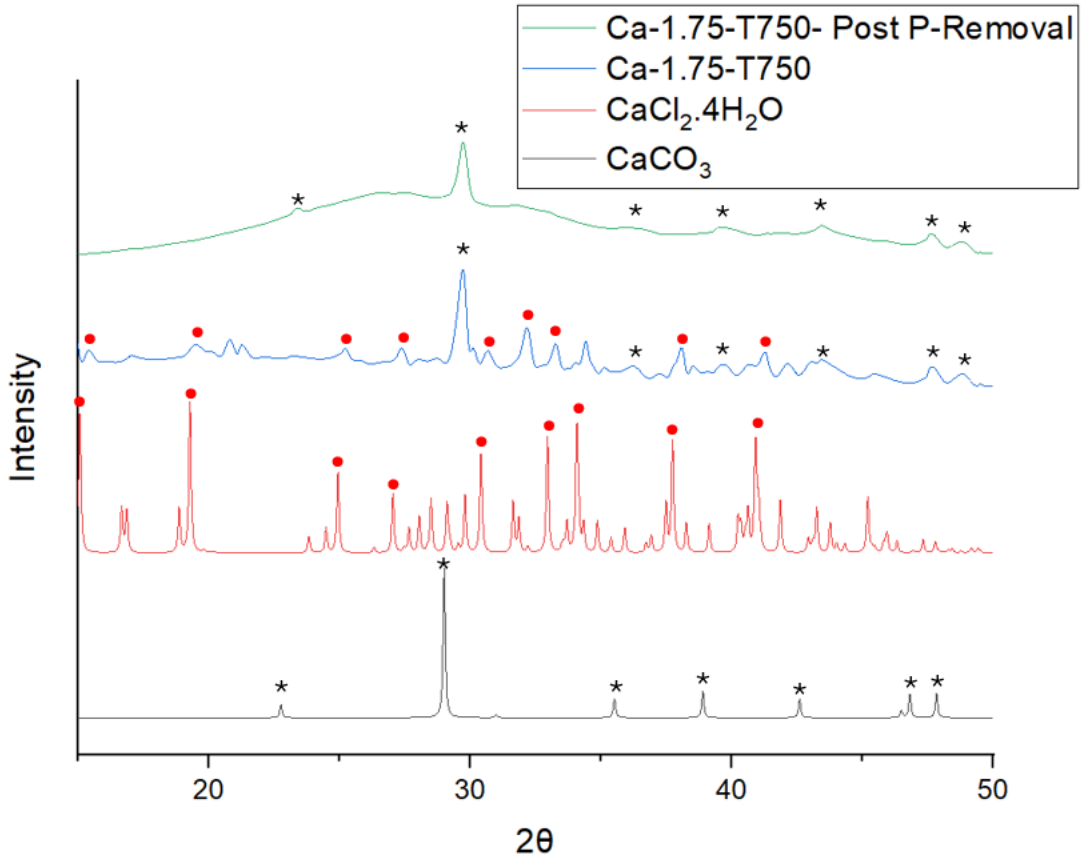

Figure 6.10:XRD patterns of Ca-1.75-T750 biochar synthesised in this work before P-removal (blue), and after P-removal (green) with spectra of pure calcium chloride tetrahydrate (red) and calcite (black).P-removal carried out in a 50mL solution, 2g/L biochar dosage, c_i=250 mg_P/L, 25°C, pH=8.

Tables 6.4 & 6.5 shows XPS data obtained for Ca-1.75-T750 biochar before and after P-removal with spectra displayed in *Figure 6.11*. The binding energies for some atomic species displayed slight increases compared to those typically

reported in the literature, likely due to a combination of factors including charging effects due to surface coverage with $CaCO_3$ and $CaCl_2$, sample heterogeneity, and the complex chemical environments present in the samples. Conventionally, adventitious carbon is used as a reference for charge correction; however, in the case of biochar, surfaces are dominated by intrinsic carbon [28]. As such, it is unlikely for the most intense peak to occur due to surface contamination; therefore, in this work, graphitic carbon was used as a reference [28], [29]. The surfaces of biochars are conductive and heterogeneous, with a primarily amorphous carbon structure comprising areas of local crystallinity, biochar samples in this work contain a high surface coverage of non-conductive $CaCO_3$ and $CaCl_2$ salts which can cause differential charging resulting in uniform or localised shifting of binding energies during XPS analysis— particularly in areas with high oxygen or mineral content [30], [31]. It was considered to use a specific element within the biochar as an internal reference to negate these effects; however, since all main components in the biochar sample have the potential to exist in multiple environments (eg, Cl^- in $CaCl_2$ and covalently bound Cl-C), this was not feasible.

Evidence of $CaCO_3$ and $CaCl_2$ on the biochar surface prior to P-removal can be observed from the XRD and FTIR results obtained for sample Ca-1.75-T750 (*Figures 6.4 & 6.9)*. XPS analysis of pre-P-removal Ca-1.75-T750 biochar further confirms this, with evidence of C 1s and O 1s peaks in metal carbonate at 289.8 and 532.1 eV, respectively [28], [29], [32]. Evidence of metal-chloride Cl 2p doublet peaks is also present at 199.28 and 200.98 eV [28], [33]. The Ca doublet peaks present at 348.2 and 351.7 eV likely contain contributions from Ca in both $CaCl_2$ and $CaCO_3$ [28]. The biochar surface composition of Cl was seen to significantly reduce after P-removal, with O and P content increasing, as shown in *Table 6.4*. In *Table 6.5*, the appearance of P 2p peaks at 134.49 and 136.20 eV after P-removal, alongside a new Ca 2p doublet at 349.3 and 352.8 eV, and slight increase in O 1s binding energies, indicates successful adsorption of phosphate species, likely forming surface-bound calcium phosphate [34], [35], [36].

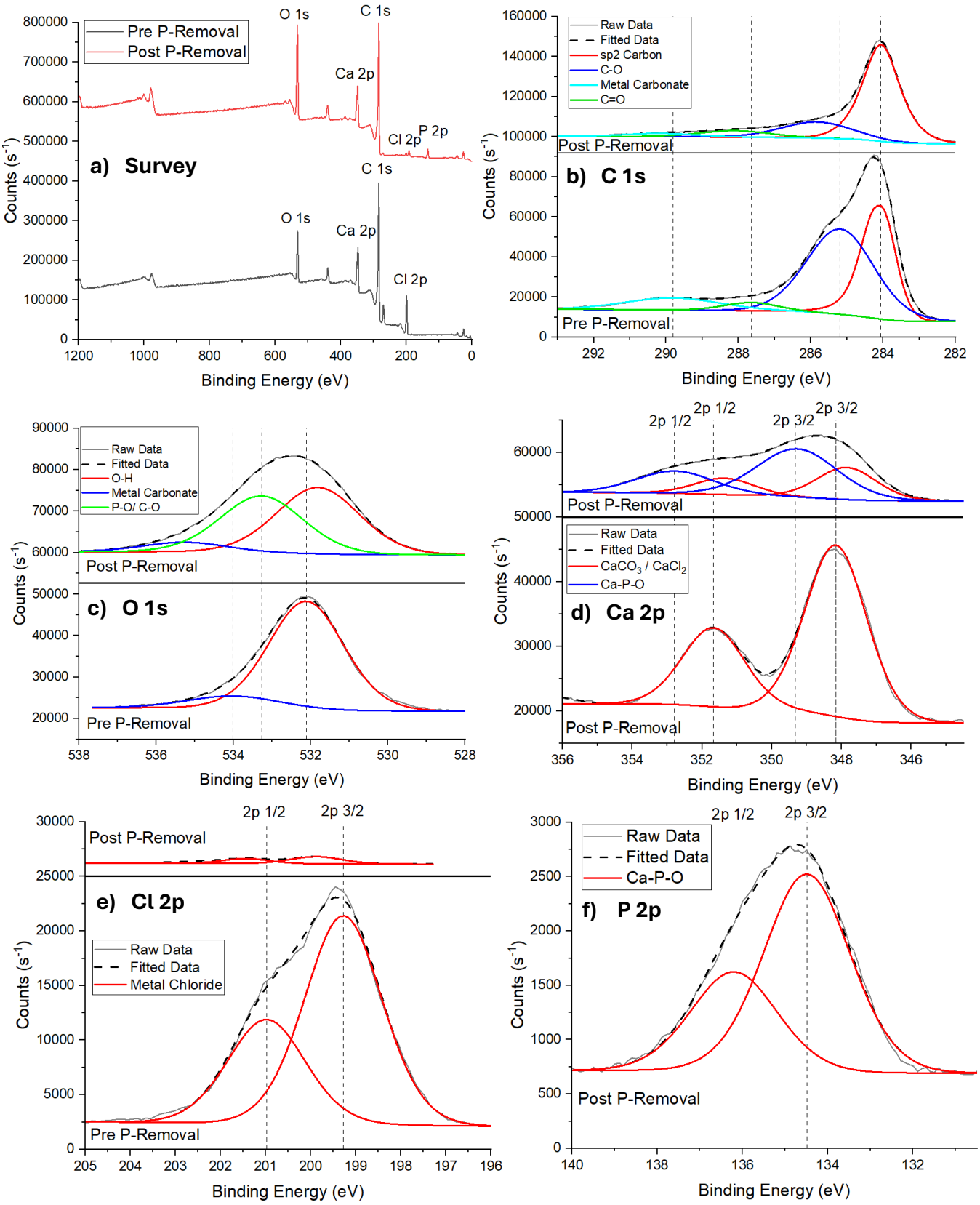

Figure 6.11:XPS a) survey, b) C 1s, c) O 1s, d) Ca 2p, e) Cl 2p, and f) P 2p spectra obtained for Ca-1.75-T750 biochar before and after P-removal. P-removal carried out in a 50mL solution, 2g/L biochar dosage, ci=250 mgP/L, 25°C, pH=8.

Table 6.4:Surface composition of Ca-1.75-T750 biochar synthesised in this work before and after P-removal, analysed using XPS.P-removal carried out in a 50mL solution, 2g/L biochar dosage, c_i=250 mg_P/L, 25°C, pH=8.

Element	Before P-Removal (atomic %)	After P-Removal (atomic %)
C	77.8	72.0
O	10.5	20.1
Ca	4.8	4.8
Cl	6.9	0.5
P	-	2.7

Table 6.5: XPS data obtained of Ca-1.75-T750 biochar before and after P-removal. P-removal carried out in a 50mL solution, 2g/L biochar dosage, c_i=250 mg_P/L, 25°C, pH=8.

C 1s								
Bonding	*Sp2 carbon*		*C-O*		*C=O*		*Metal carbonate*	
	BE(eV)	**%**	**BE(eV)**	**%**	**BE(eV)**	**%**	**BE(eV)**	**%**
Before P-Removal	284.06	27.4	285.18	39.5	287.64	7.8	289.81	3.0
After P-Removal	284.06	48.9	285.83	14.5	288.09	5.7	290.19	2.9
Reference	[29][28]							
O 1s								
Bonding	*Metal carbonate*		*P-O/ C-O*		*OH/ H_2O*			
	BE(eV)	**%**	**BE(eV)**	**%**	**BE(eV)**	**%**		
Before P-Removal	532.11	9.3			534.02	1.2		
After P-Removal	531.81	10.0	533.27	8.6	535.26	1.4		
Reference	[28], [32], [35]							
Ca 2p								
Bonding	*$CaCO_3$/ $CaCl_2$ ($2p_{3/2}$)*		*$CaCO_3$/ $CaCl_2$ ($2p_{1/2}$)*		*Ca-P-O ($2p_{3/2}$)*		*Ca-P-O ($2p_{1/2}$)*	
	BE(eV)	**%**	**BE(eV)**	**%**	**BE(eV)**	**%**	**BE(eV)**	**%**
Before P-Removal	348.16	3.3	351.67	1.5				
After P-Removal	347.85	1.1	351.35	0.6	349.27	2.2	352.77	1.0
Reference	[28], [37]				[34], [35], [36]			
Cl 2p								
Bonding	*Metal chloride (2p 3/2)*				*Metal chloride (2p 1/2)*			
	BE(eV)		**%**		**BE(eV)**		**%**	
Before P-Removal	199.28		4.6		200.98		3.3	
After P-Removal	199.87		0.3		201.43		0.2	
Reference	[33]							
P 2p								
Bonding	*Ca-P-O ($2p_{3/2}$)*				*Ca-P-O ($2p_{1/2}$)*			
	BE(eV)		**%**		**BE(eV)**		**%**	
Before P-Removal	-				-			
After P-Removal	134.49		1.8		136.20		0.9	
Reference	[34], [35], [36]							

6.3.4 Adsorption

Previous results presented in this chapter clearly demonstrate aqueous P-removal by Ca-decorated biochars synthesised to occur via a combination of bulk precipitation and adsorption. While precipitation accounts for the majority of P-removal, adsorption still has to potential to provide significant contribution. Understanding the adsorption behaviour is essential to clarify the overall removal pathways and for assessing the potential reversibility of adsorbed P (an important consideration if P-enriched biochar is intended for subsequent use as a soil amendment). This section focuses on the adsorption mechanisms occurring during P removal, including kinetic and isotherm analyses. Furthermore, a DoE analysis systematically evaluating the influence of biochar functionalisation conditions on P-adsorption performance in 24-hour batch experiments is presented.

6.3.4.1 Adsorption Mechanisms

Phosphorus removal by biochar involves both physical and chemical adsorption processes, each governed by distinct interaction pathways. The following section examines evidence from FTIR (*Figure 6.9*), XPS (*Table 6.5*) , and XRD (*Figure 6.10*) analyses to better understand the nature of adsorption interactions.

Physical Adsorption

Physical adsorption of phosphate onto the surface of biochar can occur through outer-sphere complexation and hydrogen bonding. Evidence of such hydrogen bonding was observed through the results obtained from FTIR and XPS analysis of sample Ca-1.75-T650 post P-removal (*Figure 6.9 & Table 6.5*). *Table 6.5* shows an increase in the binding energies of C-O and C=O peaks in the C1s spectra, indicating a reduction in electron density, consistent with C-O and C=O groups experiencing hydrogen bonding with phosphate ions after P-removal; this is further supported by the changes in the -OH region of the FTIR spectrum after P-removal [21], [38], [39].

Similarly, there is a significant increase in the binding energy of the high-energy O 1s peak (535.3 eV), likely indicating a combination of enhanced hydrogen

bonding in the biochar sample and increased hydration resulting from phosphate adsorption. As outer-sphere complexation would involve water molecules hydrogen-bonded to $CaCO_3$ also forming hydrogen bonds with phosphate, it is possible this increased hydration (indicated by the increase in the binding energy of the high-energy O 1s peak (535.3 eV)) could be a result of outer-sphere complexation between $CaCO_3$ and phosphate [40], [41]. However, outer-sphere complexation (in which $CaCO_3$ and phosphate are both directly bonded to water molecules opposed to each other) is unlikely to be a dominant adsorption mechanism between $CaCO_3$ and phosphate, as it is unlikely to cause the large increase in binding energy of the metal carbonate C 1s peak observed after P-removal.

Chemical Adsorption

In addition to physisorption, there is also evidence of chemical adsorption of phosphate onto the biochar surface, via inner-sphere complexation and surface precipitation. The new Ca 2p and P 2p peaks present in the data obtained from XPS analysis of post P-removal biochar confirm the presence of calcium phosphates on the biochar surface [34], [35], [36]. The appearance of P-O stretching bands in FTIR analysis after P-removal indicates phosphate binding, with the broad peak observed in the XRD pattern consistent with the formation of amorphous calcium phosphate, suggesting surface precipitation [19], [22], [24]. However, the absence of sharp crystalline calcium phosphate peaks in the XRD pattern indicates that surface precipitation is limited to amorphous forms or sub-monolayer coverage.

Surface precipitation of calcium phosphates may occur from the reaction of phosphate with Ca^{2+} ions free in solution (from dissolved $CaCl_2$) nucleating at the biochar surface, or from interactions between phosphate and Ca on the biochar surface, in which case consumption of compounds containing these Ca groups ($CaCO_3$) would be expected [19], [42], [43]. Although FTIR analysis indicates some loss of calcium carbonate, XPS analysis shows that peaks related to C 1s and O 1s bonds in metal carbonates remain mostly unchanged; additionally, XRD

analysis continues to display peaks characteristic of calcite, suggesting that inner-sphere complexation (which would not involve significant consumption of $CaCO_3$), between $CaCO_3$ and P, is a more dominant adsorption mechanism than surface precipitation. The decrease in binding energy of the metal carbonate C 1s peak after P-removal suggests interaction between metal carbonate and phosphate ions without depletion, reaffirming that inner-sphere complexation is the dominant form of chemisorption.

The area under the Ca 2p peaks attributed to a mixture of $CaCO_3$ and $CaCl_2$ decreases after P-removal; however, the reduced area and binding energy shift are likely mainly due to the loss of $CaCl_2$ during P-removal, rather than a significant loss of $CaCO_3$ [28]. The decrease in the area of C1s C-O and C=O peaks after P-removal, along with the increase in graphitic carbon peaks, is likely due to a combination of ligand exchange, displacing C-O and C=O, and dissolution of $CaCl_2$, which exposes more graphitic regions of the biochar.

6.3.4.2 Adsorption Modelling

Sample Ca-1.75-T900 was selected for further investigation due to the fact that it demonstrated the highest P-removal capacity across a wide pH range, as shown in *Figure 6.7*; therefore, an in-depth examination of adsorption kinetics and isotherms was conducted.

Adsorption modelling should only be performed using data where all P-removal is due to adsorption. Adsorption models assume that uptake results solely from surface interactions between the adsorbent and adsorbate; therefore, P-removal data that includes contributions from bulk precipitation violates this assumption, likely leading to incorrect model parameterisation, poor predictive performance, and potential misinterpretation of the adsorption mechanisms. The two mechanisms are not always decoupled in studies relating to phosphate removal, and various studies in the literature examining P-recovery by biochar may underestimate the role of bulk precipitation during P-removal [1], [44], [45]. In this work, adsorption modelling was conducted on washed biochar samples

(adsorption only) to accurately model adsorption behaviour, as well as unwashed samples (adsorption + precipitation) to provide comparison to the literature.

Adsorption Kinetics

Batch kinetic experiments were conducted in duplicate using 0.1 g of biochar in 50 mL of 20 mg_P/L phosphate solution. Pseudo-first-order, pseudo-second-order, and Elovich kinetic models were fitted to the data obtained for each biochar sample, as shown in *Figures 6.12a&b*, with the parameters obtained from the fits provided in *Table 6.6*. Error bars were considered when fitting models by using instrumental error weighting.

Pseudo-first-order kinetics provided the best fit for data obtained for both samples and predicted q_e well. Equilibration times of 24 h and 5 d were required for the unwashed and washed biochar samples, respectively, indicating adsorption to be a much slower process than precipitation; however, both samples achieved high P-removal at equilibrium, with 97% removal of P by the unwashed sample and 86% adsorption of P by the washed sample. Biochar with a dual P-removal mechanism may, therefore, be useful for applications in water bodies high in P where exposure to P-pollution sources is constant; precipitation would enable quick remediation of such water bodies, while adsorption allows for continuous maintenance.

Table 6.6:Kinetic model parameters and correlation coefficients obtained for fits of phosphate adsorption on selected biochars synthesised in this study. Experiments carried out in a 50mL solution, 2g/L biochar dosage, c_i=20 mg_P/L, 25℃, pH=8.

Washed Ca-1.75-T900, $q_{e\ (experimental)}$= 8.76					
	Parameter 1	**Parameter 2**	**R^2**	**Adjusted R^2**	**Reduced χ^2**
Pseudo-first-order	q_e=8.82	k_1=0.04	0.99	0.99	15.7
Pseudo-second-order	q_e=11.37	k_2=0.003	0.98	0.98	40.7
Elovich	α=0.47	β=1.19	0.93	0.93	164.5
Unwashed Ca-1.75-T900, $q_{e\ (experimental)}$= 9.69					
	Parameter 1	**Parameter 2**	**R^2**	**Adjusted R^2**	**Reduced χ^2**
Pseudo-first-order	q_e=9.67	k_1=0.40	0.96	0.96	18.5
Pseudo-second-order	q_e=10.14	k_2=0.06	0.95	0.94	27.3
Elovich	α=0.96	β=354.7	0.68	0.63	164.7

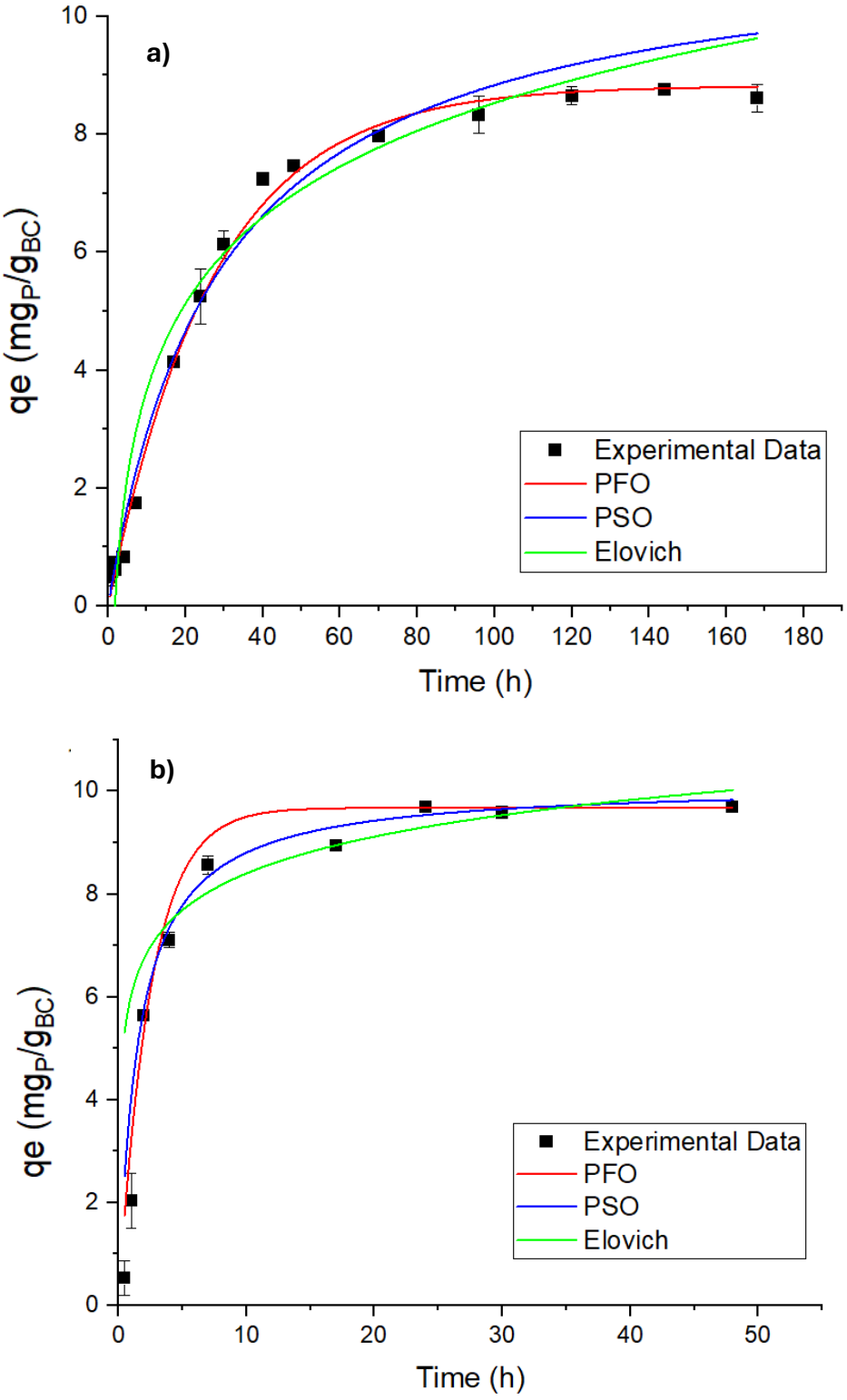

Figure 6.12:Time dependant adsorption of phosphate on a) washed Ca-1.75-T900 biochar and b) unwashed Ca-1.75-T900 biochar with kinetic model fittings: pseudo-first-order (PFO) (red), pseudo-second-order (PSO) (blue), and Elovich model (green). Experiments carried out in a 50mL solution, 2g/L biochar dosage, c_i=20 mg_P/L, 25°C, pH=8. Error bars are given for all data points, where error bars are not visible this is because error bars are smaller than the symbol size.

To examine the diffusion of phosphate from bulk solution to the biochar pores during P-recovery, the intraparticle diffusion model (IPD) was applied to kinetic data obtained for both washed and unwashed Ca-1.75-T900 samples, as shown in *Figure 6.13* with the parameters from the fits provided in *Table 6.7*.

Both samples displayed three distinct linear sections and non-zero values of c_i, indicating that P-removal is a multistep process. The first linear section of the IPD graphs represents bulk diffusion of P to the biochar surface. This stage is demonstrated to be slow for the washed biochar sample and fast for the unwashed sample, likely because this stage truly reflects a combination of bulk diffusion and precipitation for the unwashed sample, with P more likely to quickly come into contact with Ca^{2+} ions free in solution than to find favourable adsorption sites on the biochar surface in a similar timeframe. The c_1 value obtained for the unwashed biochar sample was negative, a physical impossibility; this is likely a consequence of this region including contributions from bulk precipitation instead of representing pure diffusion alone.

The second linear section represents film diffusion of P through the boundary layer; this stage is fast for both samples, being the quickest stage for washed char and the second fastest stage (after bulk diffusion/precipitation) for unwashed biochar. The c_2 value obtained for the washed biochar sample is negative; however, a negative boundary layer thickness is physically impossible, indicating that the model does not fully capture the reality of the system. This could indicate that the model assumption of a distinct film diffusion stage is oversimplified; this region may include contributions from early intraparticle diffusion, and the deviation may be exacerbated by sparse data points (caused by the constrained opening hours of the laboratory), limiting accurate segmentation of diffusion phases

Finally, the third linear section represents internal diffusion of P into the internal pore structure of the biochar samples; this section is slow for both samples,

likely due to restricted pore accessibility. During P removal by unwashed biochar, internal diffusion was the rate-controlling step, while during P adsorption by washed biochar, both bulk and internal diffusion equally controlled the adsorption rate.

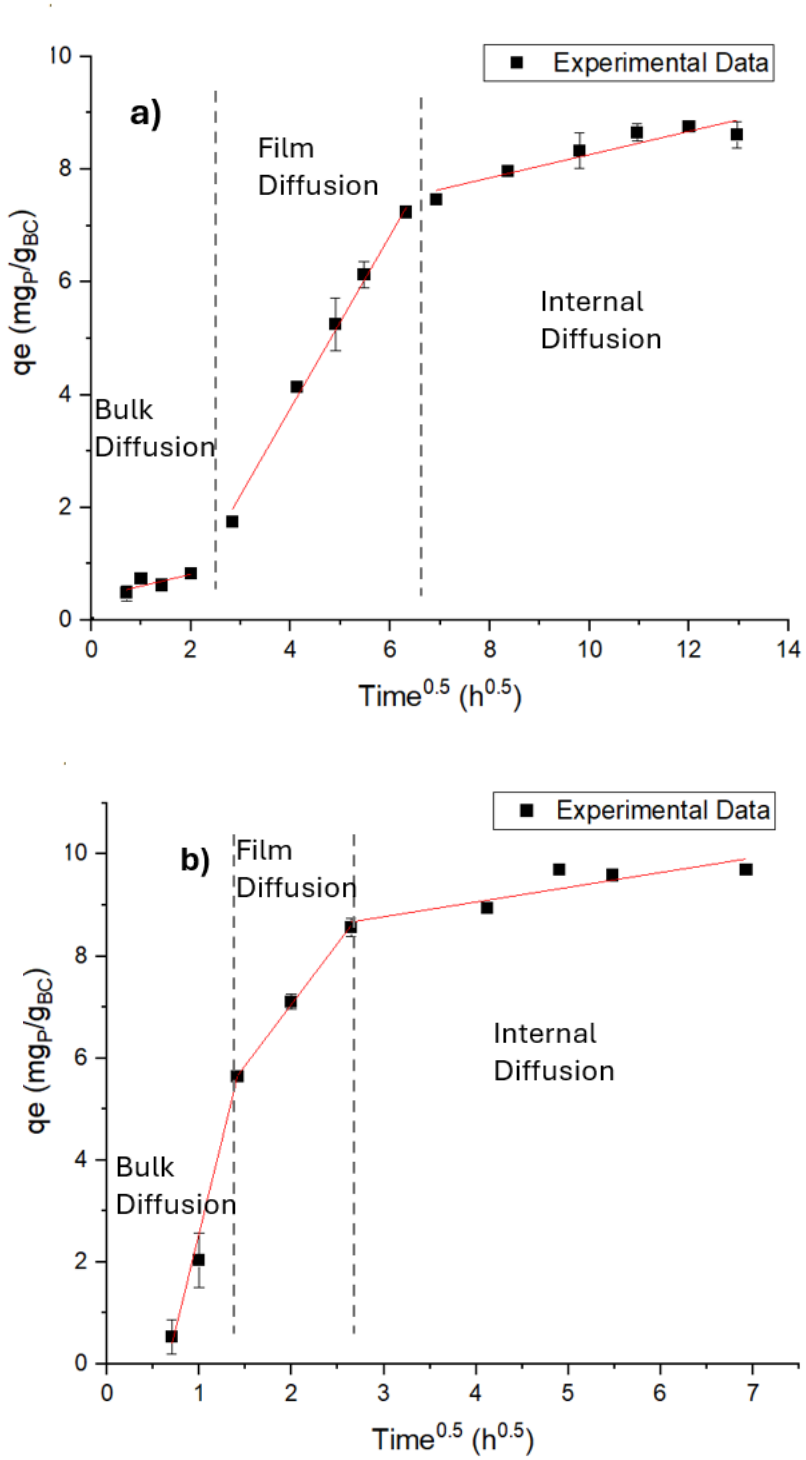

Figure 6.13:Time dependant adsorption of phosphate on a) washed Ca-1.75-T900 biochar and b) unwashed Ca-1.75-T900 biochar. Experiments carried out in a 50mL solution, 2g/L biochar dosage, c_i=20 mg_P/L, 25°C, pH=8. Fits obtained through application of the intra-particle diffusion model.

Table 6.7:Intraparticle diffusion model parameters and correlation coefficients obtained for phosphate removal on selected biochars synthesised in this study. Experiments carried out in a 50mL solution, 2g/L biochar dosage, c_i=20 mg_P/L, 25°C, pH=8.

Washed Ca-1.75-T900			
	k_{ip}	**c_i**	**R^2**
Section 1	k_{ip1}=0.21	c_1=0.40	0.61
Section 2	k_{ip2}=1.53	c_2= -2.37	0.99
Section 3	k_{ip3}=0.21	c_3=6.20	0.88
Unwashed Ca-1.75-T900			
	k_{ip}	**c_i**	**R^2**
Section 1	k_{ip1}=7.40	c_1= -4.83	0.99
Section 2	k_{ip2}=2.39	c_2=2.28	0.99
Section 3	k_{ip3}=0.29	c_3=7.91	0.78

Comparing the kinetic modelling results obtained for the unwashed biochar sample with those obtained for the washed biochar sample, shows that the contribution of precipitation to P-removal did not prevent the identification of the pseudo-first-order model as the best representative for P-removal kinetic behaviour. However, modelling of the unwashed biochar sample failed in identifying bulk diffusion as a rate-controlling step.

Adsorption Isotherms

Langmuir and Freundlich models were used to describe the adsorption performance of both washed and unwashed Ca-1.75-T900 samples, with the associated fits shown in *Figure 6.14*. The Freundlich isotherm model fitted the experimental data for the washed biochar sample very well, with an adjusted R^2 value of 0.97 and reduced χ^2 of 0.14, indicating multilayer adsorption on a heterogeneous surface. In the case of the unwashed biochar sample, neither Langmuir, Freundlich, nor Sips isotherm models fit the experimental data well (adjusted R^2 >0.7) with all model fitting resulting in low adjusted R^2 values and extremely high χ^2 values (> 6000). The cause of exceptionally large χ^2 values when fitting the isotherm models to data obtained for unwashed biochar can be considered to be systematic deviations between experimental data and model assumptions due to P-removal occurring not only through adsorption but also through bulk precipitation. Attempts were made to fit the Sips isotherm to both

data sets; however, in the case of the washed biochar sample, the model could not successfully converge without setting an upper limit for q_m, which the model would then always settle on. This suggests that the data does not saturate sufficiently to define a q_m. As the data was well described by the Freundlich model, the Sips isotherm model fitting was omitted for the washed biochar sample.

The value of 1/n, a constant obtained using the Freundlich equation for isotherm fitting, is representative of the favourability of an adsorption process; values between 0.1-0.5 suggest favourable adsorption, while values greater than 1 indicate unfavourable adsorption [46]. A 1/n value of 0.25 was determined for the fit of the data obtained for the washed biochar sample, indicating favourable adsorption. Washed and unwashed biochar samples exhibited Langmuir theoretical maximum adsorption capacities of 33.8 mg_P/L and 81.2 mg_P/L, respectively, both underestimating compared to experimental maximum adsorption capacities achieved (36.9 mg_P/L for washed biochar and 94.3 mg_P/L for unwashed biochar).

Table 6.8: Adsorption isotherm model parameters and correlation coefficients obtained for phosphate adsorption on selected biochars synthesised in this study. Experiments carried out in a 50mL solution, 2g/L biochar dosage, 25°C, pH=8, residence time washed biochar = 5 d, residence time unwashed biochar = 24 h

	Washed Ca-1.75-T900, ($q_{m\ (experimental)}$= 36.85)				
	Parameter 1	**Parameter 2**	**R^2**	**Adjusted R^2**	**Reduced χ^2**
Langmuir	q_m=33.8	k_l=0.08	0.73	0.69	1.55
Freundlich	1/n=0.25	k_f=9.21	0.98	0.97	0.14

	Unwashed Ca-1.75-T900, ($q_{m\ (experimental)}$= 94.28)					
	Parameter 1	**Parameter 2**	**Parameter 3**	**R^2**	**Adjusted R^2**	**Reduced χ^2**
Langmuir	q_m=81.2	k_l=0.17	-	0.70	0.66	6197.78
Freundlich	1/n=0.52	k_f=10.53	-	0.70	0.66	6143.66
Sips	q_m=118.3	K_s=0.05	n_s=0.73	0.71	0.62	6887.87

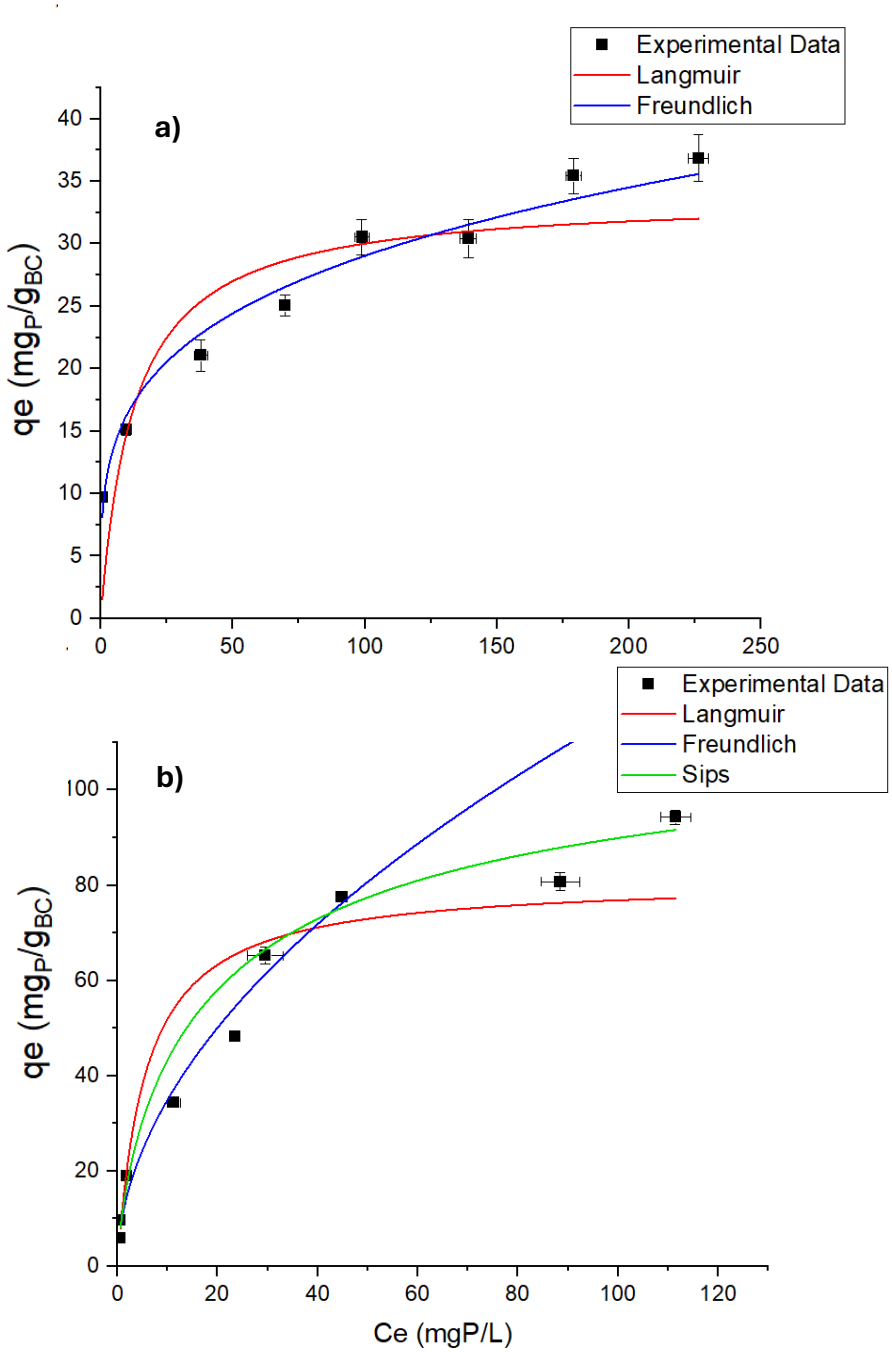

Figure 6.14:Equilibrium adsorption isotherms obtained for phosphate adsorption on a) washed Ca-1.75-T900 biochar and b) unwashed Ca-1.75-T900 biochar. Adsorption isotherm model fittings: Langmuir (red), Freundlich (blue), Sips (green).Experiments carried out in a 50mL solution, 2g/L biochar dosage, 25°C, pH=8, residence time washed biochar= 5 d, residence time unwashed biochar = 24 h. Error bars are given for all data points, where error bars are not visible this is because error bars are smaller than the symbol size.

6.3.4.3 DoE Analysis

The results presented in this chapter have established that aqueous P-removal by biochar samples occurs via a dual process of adsorption and bulk precipitation. As discussed in *Section 5.5,* no statistically significant relationship was found between P-removal (bulk precipitation + adsorption) and pyrolysis temperature or CLR. To investigate the relationship between P adsorption and functionalisation conditions, in order to optimise P-recovery, regression analysis was carried out.

Regression analysis was performed using data obtained for the 24 h batch adsorption capacities of washed biochar samples in 20 mg_P/L solutions (*Figure 6.5*) with temperature and CLR used as variables, and phosphate adsorption used as a response. StatEase360 software was used to fit linear, 2FI, quadratic, and cubic models to the data obtained, with the quadratic model providing the best fit. The quadratic model for the relationship between phosphate adsorption, pyrolysis temperature and CLR is given in *Equation 6.5* with the summary of statistical quantities presented in *Table 6.9*.

$$P - Adsorption = 37.23 + 9.03A - 2.69B + 14.75AB - 8.03A^2 + 3.12B^2 \quad (6.5)$$

Table 6.9:Summary statistics for quadratic fits of 24 h batch phosphate removal for Ca-biochars synthesised in this study.

Mean	Std. Dev	C.V. %	Adjusted R^2	Predicted R^2	Adequate Precision
36.00	2.74	7.61	0.86	0.40	16.40

The coefficient of variation (C.V.) is a measure of the reproducibility of data, calculated by taking a ratio of the standard deviation of a data set to the mean. A model is generally considered to be reproducible if the C.V. is less than 10%. Adequate precision is used by StatEase360 software as a measure of the signal to noise ratio in a dataset, with values above 4 being considered desirable. The

low C.V. and high adequate precision, as shown in *Table 6.9*, indicate that the data for P-adsorption by washed biochar samples are reproducible with a high signal-to-noise ratio. There is a notable difference between the adjusted R^2 and predicted R^2 values obtained; this could be due to outliers in the adsorption data or the need for model reduction. To further investigate, diagnostic plots presented in *Figure 6.13* below were analysed.

Diagnostic Plots

Description of the diagnostic plots used in *Figure 6.15* (normal plot, residual vs precited plot, predicted vs actual plot, and difference in fits (DFFITS) plot) including how they can be used to identify outliers in a data set is provided in *Section 3.3.6.3*.

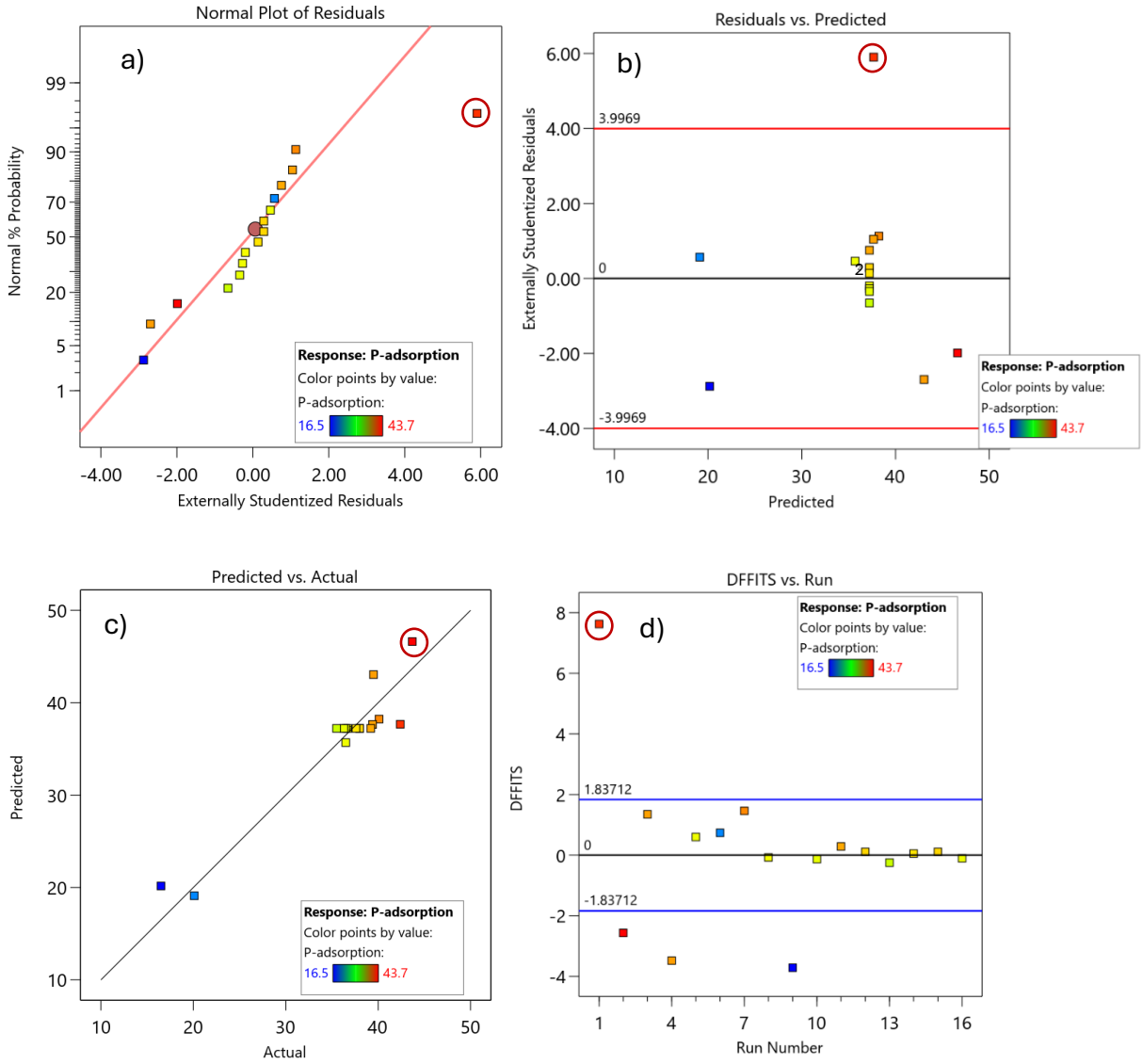

Figure 6.15:Diagnostic plots for the modelling of P-adsorption of biochar samples synthesised in this study with pyrolysis temperature and CLR, a) normal plot, b) residual vs predicted plot, c) predicted vs actual plot, d) difference in fits plot. The data point circled in red is run 1- an outlier.

The normal plot for surface area, shown in *Figure 6.13a*, highlights one clear outlier (circled in red, run 1- temperature=644 °C, CLR=1.57) whilst the rest of the data can be seen to adhere to a normal distribution. The residual versus predicted plot (*Figure 6.15b*) shows an even distribution of residuals around 0, with the exception of one data point—run 1 (circled red) —which exceeds the recommended cut-off value (shown by red horizontal lines). The predicted versus actual plot (*Figure 6.15c*) shows the model to predict data well—better than the predicted R^2 value suggests—indicating that the outlier data point (run 1) may be skewing these values. The DFFITS plot (*Figure 6.15d*) shows run 1 to be the most influential data point in the set; however, other diagnostic plots suggest this data point to be an outlier. Therefore, it was decided to omit run 1 from the data set. Omitting this data point from analysis gives the quadratic model presented in *Equation 6.6*, with the summary of statistical quantities presented in *Table 6.10*.

$$P - Adsorption = 37.22 + 11.26A - 0.4650B + 8.44AB - 9.6A^2 + 1.55B^2 \quad (6.6)$$

Table 6.10: Summary statistics for quadratic fits of 2 h batch phosphate removal for Ca-biochars synthesised in this study.

Mean	Std. Dev	C.V. %	Adjusted R^2	Predicted R^2	Adequate Precision
35.57	1.32	3.68	0.97	0.92	34.67

C.V. remained low, and adequate precision remained high, as desired. Values of adjusted and predicted R^2 are high and in relatively good agreement, suggesting the model is a reliable representation of the data.

Model Reduction

When carrying out ANOVA analysis for P-adsorption, not all model terms were found to be statistically significant within a 95% confidence interval. To refine the models, model reduction was carried out to test the effect on adjusted and predicted R^2 values.

*Table 6.11: ANOVA results for P-adsorption before and after model reduction, *non-significant*

	F-value	p-value	Adjusted R^2	Predicted R^2
Source				
		Original Model		
Model	86.15	<0.0001	***0.968***	***0.917***
A-Temperature (°C)	222.26	<0.0001		
B-CLR (wt:wt)	0.3791	0.5533*		
AB	25.01	0.0007		
A^2	99.48	<0.0001		
B^2	2.59	0.1422*		
Reduced Model				
Model	92.38	<0.0001	***0.963***	***0.934***
A-Temperature (°C)	201.46	<0.0001		
B-CLR (wt:wt)	0.1357	0.7203*		
AB	19.82	0.0012		
A^2	88.51	<0.0001		

Table 6.11 shows B and B^2 to be statistically insignificant model terms. When reducing the model and removing B^2, predicted R^2 increases (model term B was retained to maintain the model hierarchy). The reduced model has a high F-value of 92.38, indicating the model is significant with only a 0.01% chance of an F-value this high occurring due to noise. Temperature was the most influential parameter on the P-adsorption of washed biochar samples. While CLR exhibited the least influence on P-adsorption by a sample, interaction effects between CLR and pyrolysis temperature are influential, with statistically significant synergistic effects demonstrated between the two functionalisation parameters.

The surface of functionalised Ca-biochar samples produced in this work are decorated with $CaCl_2$ and $CaCO_3$ (Figure 5.13).Due to $CaCl_2$ on the biochars

surface dissolving in water (*Table 6.2* and *Figure 6.10*) and non-functionalised biochar failing to adsorb any phosphate (*Figure 4.4*), adsorption of phosphate onto the surface of Ca-decorated biochar can be assumed to be due to the interactions between phosphate ions and $CaCO_3$ on the biochars surface. During biochar production, $CaCl_2$ impregnated softwood reacts with pyrolysis vapours to form $CaCO_3$ on the resulting biochar surface, as explained further in Section 5.4.5. In brief, this transformation is governed by the availability of pyrolysis vapours, which act as the limiting reactant, while $CaCl_2$ remains in excess. Consequently, the extent of $CaCO_3$ formation depends primarily on pyrolysis temperature, as higher temperatures accelerate devolatilization and increase the quantity of pyrolysis vapours available for reaction. Simultaneously, rising temperature enhances the porosity and true surface area of the carbon matrix (even though measurable surface area by N_2 BET analysis may decline due to pore blockage at high CLRs).

The interactive effects of pyrolysis temperature and CLR are well illustrated by the contour plot shown in *Figure 6.16*. At low pyrolysis temperatures, P-adsorption increases when CLR is reduced due to a limited amount of pyrolysis vapours available to react with $CaCl_2$ constraining the formation of $CaCO_3$. Increasing CLR at these conditions increases pore blockage and reduces accessibility for phosphate ions. Therefore, a lower CLR minimises pore blockage without sacrificing the number of favourable adsorption sites.

At moderate temperatures, a medium CLR optimises P-adsorption due to higher pyrolysis temperatures increasing the production of pyrolysis vapours and the development of porosity within biochars carbon structure, allowing more $CaCl_2$ to convert into $CaCO_3$ without severe pore blockage. However, if CLR is too high, pore obstruction still occurs, so an intermediate CLR balances formation of $CaCO_3$ and accessibility of biochars porous structure.

At high temperatures, a high CLR enhances P-adsorption. At high temperature pyrolysis vapours are more abundant enabling efficient conversion of $CaCl_2$ into

$CaCO_3$ crystals. The increased porosity at high temperatures offsets potential increased pore blockage, and the greater $CaCO_3$ content provides more reactive sites for phosphate adsorption. Overall, P-adsorption increases with rising temperature, with optimal CLR also increasing with rising temperature. Therefore, the highest P-adsorption occurs at high temperature and high CLR.

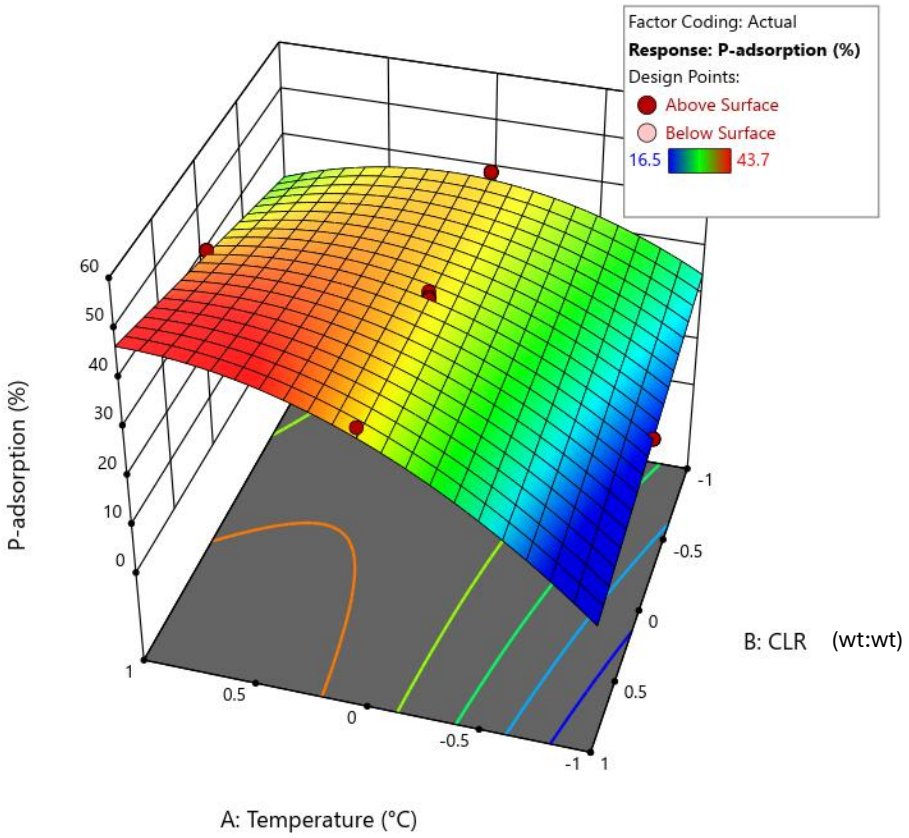

Figure 6.16:3D contour plot showing interactions of pyrolysis temperature and CLR on P-adsorption of Ca-biochar. Coded values are used with CLR ranging from -1 (1.5) to 1(2) and pyrolysis temperature ranging from -1 (600 °C) to 1 (900 °C).

Validation study

To validate the model and verify optimal conditions (highest P-adsorption) for pyrolysis temperature and CLR, StatEase 360 software was used to determine the functionalisation conditions with the highest desirability. When optimising parameters, goals can be set for all responses previously analysed using regression analysis, including yield, surface area, average pore size, Cl:Ca ratio, and P-adsorption. No goal was set for responses that had a relatively small range throughout the data set; as such no goal or boundaries were set for yield or total

P-removal. It was decided to maximise P-adsorption to optimise P-recovery. Surface area and average pore size were set to remain within the range of values in the experimental data set.

DoE validation experiments were among the final experiments conducted during this work. Unfortunately, the furnace used to synthesise biochars was damaged between the time of synthesising biochars used as input data for DoE and the synthesis of the optimal biochar as recommended by the model. The ceramic coating of the heating rods in the furnace had fractured and been compromised, reducing heat resistance through the rods and leading to inaccuracies in the temperature profile within the furnace. To gauge how much equipment damage may cause variation within a biochar sample, biochar under conditions of the DoE midpoint was synthesised and analysed to determine if the variation was outside the range obtained before the furnace was damaged.

Data presented in *Table 6.12* shows furnace damage resulted in values outside the expected variation for all responses except average pore size. A decrease in yield and an increase in surface area and P-adsorption, suggest increased temperature inside the furnace due to the loss of the ceramic coating on the heating rods. P-adsorption was most significantly impacted by the uncontrolled temperature rise within the furnace, followed by surface area, with a minor effect on yield. A relatively large effect on P-adsorption is expected considering the high influence of temperature on this response.

Table 6.12: Comparison of experimental values for biochar yield, surface area, average pore size, and P-adsorption synthesised in 'damaged' furnace compared to the previous range of samples synthesised in 'undamaged' furnace.

Pyrolysis Temperature (°C)	**CLR (wt: wt)**	**Yield (%)**		**Surface Area (m^2/g_{BC})**		**Average Pore Size (nm)**		**P-Adsorption (%)**	
750	1.75	Exp.	Range	Exp.	Range	Exp.	Range	Exp.	Range
		40.1	(40.7 - 47.3)	180	(149-168)	4	(4-5)	43.7	(35.5-39.5)

Data presented in *Table 6.13* shows that the experimental values obtained for the optimal biochar, as recommended by the StatEase software, demonstrate a poor match to predicted values. Yield decreased, while surface area and P-adsorption increased, as seen for the midpoint repetition, indicating that deviation from the model-predicted values was caused by increased temperature within the furnace.

Table 6.13: Comparison of experimental values and model-predicted values for biochar yield, surface area, average pore size, and P-adsorption for optimised biochar as suggested by the model.

Pyrolysis Temperature (°C)	**CLR (wt: wt)**	**Yield (%)**		**Surface Area (m^2/g_{BC})**		**Average Pore Size (nm)**		**P-Adsorption (%)**	
828	1.97	Exp.	Pred.	Exp.	Pred.	Exp.	Pred.	Exp.	Pred.
		43.0	48.4	94.4	86.8	7	8	52.1	44.3

Unfortunately, it was not possible to carry out a reliable validation study to verify the models obtained during DoE analysis. However, the synergistic relationship of CLR and pyrolysis temperature, represented by the influential interaction term (AB) in the quadratic model presented in *Equation 6.6*, could explain conflicting reports in the literature regarding the effect of increasing CLR on aqueous P-

adsorption alongside the trends in P-adsorption data reported in this work [47], [48]. As discussed in *Section 6.3.3.1* above, within the dual P-removal mechanism reported in this work, bulk precipitation is able to compensate for reductions in adsorption; this is likely why the synergistic effects of CLR and pyrolysis temperature could be clearly identified by StatEase360 software for P-adsorption data, but not P-removal data. Signs of bulk precipitation during P-removal by Ca-biochars is present in some of the literature but not all, an underestimation of the role of bulk precipitation in some studies but not others could also contribute to conflicting results reported on the effect of increasing CLR on aqueous P-adsorption [19], [44], [45], [49].

6.3.5 Proposed P-Removal Mechanisms

It is proposed that biochar synthesised in this work removes aqueous P through a dual removal process of adsorption and bulk precipitation, summarised in *Figure 6.17*, where bulk precipitation accounts for the majority of P removal in 24 h batch P-removal experiments with concentration ≥ 20 mg_P/L . It is also proposed that Ca-biochar, contains two key forms of Ca responsible for different removal pathways, the dissolution of $CaCl_2$ from biochar to solution facilitating bulk precipitation, and $CaCO_3$ remaining on biochar surface responsible for phosphate adsorption. Due to $CaCl_2$ on the biochars surface dissolving in water (*Table 6.2* and *Figure 6.10*) and non-functionalised biochar failing to adsorb any phosphate (*Figure 4.4*), adsorption of phosphate onto the surface of Ca-decorated biochar can be assumed to be exclusively due to the interactions between phosphate ions and $CaCO_3$ on the biochars surface.

Phosphorus adsorption onto Ca-decorated biochar is primarily governed by three mechanisms: hydrogen bonding, surface precipitation, and inner-sphere complexation. Hydrogen bonding occurs between the proton of the OH group in HPO_4^{2-} and the oxygen atoms of carbonate groups in $CaCO_3$, stabilising phosphate at the biochar surface. This is supported by FTIR shifts in the OH region and increased binding energies of C–O and C=O peaks in XPS, indicating reduced electron density on carbonate oxygens consistent with hydrogen bond

formation. Surface precipitation is evidenced by the appearance of P–O stretching bands in FTIR and broad Ca–P features in XRD, confirming the formation of amorphous calcium phosphate through interaction of Ca^{2+} ions with phosphate oxyanions. Inner-sphere complexation between $CaCO_3$ and phosphate ions is indicated by XPS shifts in carbonate-related C 1s and O 1s peaks, suggesting direct ligand exchange between carbonate oxygen atoms in $CaCO_3$ and the oxygen atoms of phosphate, forming stable Ca–O–P linkages without significant depletion of $CaCO_3$.

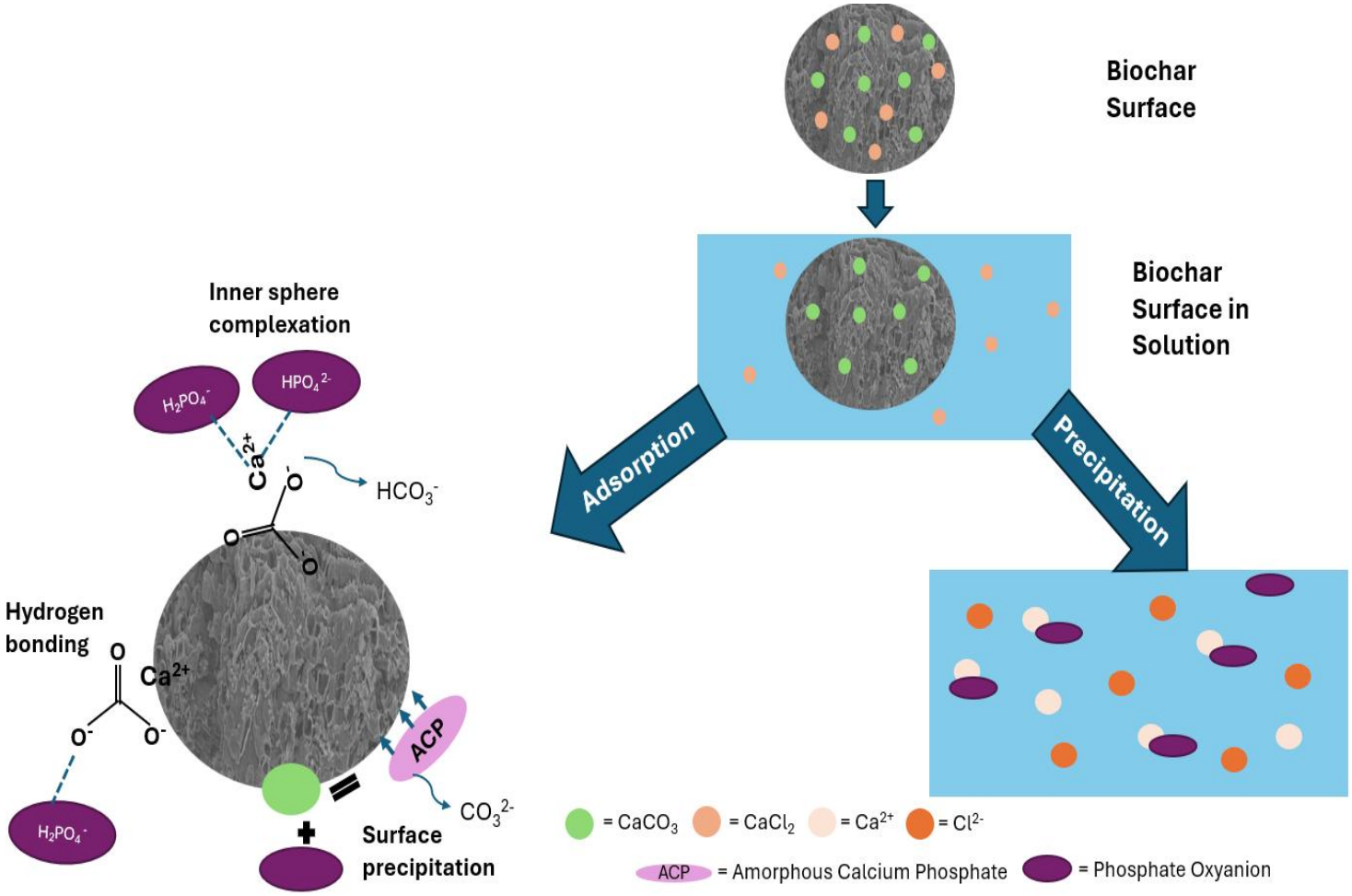

Figure 6.17: Diagram showing the various mechanisms of aqueous P-removal by biochar synthesised in this work.

Much work available in the literature presents P-adsorption via surface precipitation onto Ca-biochars surface as a primary mechanism of P-removal [50]; however, no current published work presents a dual P-removal mechanism of Ca-biochar with an attempt to decouple bulk precipitation and adsorption (as shown in *Figure 6.15*). It is standard practice in the literature to calculate the P-adsorption of a biochar sample by mass balance in which P-loss from solution is assumed equal to P-accumulation by the biochar, as is the method used in all literature cited in this thesis. However, these same adsorption experiments are usually carried out in low volumes, where small crystals produced via bulk precipitation could be easily missed in solution and during filtering. It is acknowledged that had batch adsorption experiments in this work not been up-scaled in both volume and concentration, bulk precipitation could have been easily missed and all P-removal assumed to be P-adsorption. As such, it is possible in work presented in the literature, where bulk precipitation may not be easily visible, that P-removal due to adsorption may be overestimated.

It is also possible that P-removal via bulk precipitation is sometimes mistaken in the literature for P-adsorption via surface precipitation and ion exchange. For example, Pan *et al*. produced biochar decorated with $CaCO_3$, $CaCl_2$, and CaO; the biochar possessed a high wt% of Ca and Cl which was significantly reduced after P-removal while the wt% of C was significantly increased [44]. All P-removed from solution was assumed to be adsorbed by the biochar, with reduction in Cl content attributed to ion exchange with phosphate; however, this fails to account for much of the large drop in Cl concentration and also neglects to explain the reduction in Ca and proportional increase in C content post adsorption. Dissolution of $CaCl_2$ would better explain the significant differences seen in the composition of the biochar before and after adsorption; however, the Ca and Cl concentration of the solution post adsorption was not presented – if Ca^{2+} were present as free ions in solution it is possible that bulk precipitation could have occurred.

Similarly, Li *et al*. theorised CaO_2-biochar successfully adsorbed P by CaO_2 dissolving in water and free Ca^{2+} ions forming brushite with HPO_4^{2-} ions, assuming all precipitate to deposit on the surface of the biochar [1]. However, while the presence of brushite and amorphous calcium phosphate was demonstrated on the biochar surface post adsorption, no quantitative data was provided to suggest all precipitation occurred at the surface of the biochar samples instead of in the bulk solution. Work in the literature, presenting biochar samples rich in Ca and Cl before P-removal, often assumes bulk precipitation to be negligible; however, these studies present neither the composition of the biochar samples nor the water post P-removal to prove this hypothesis [45] [19]. Similarly, much of the literature suggests surface precipitation as the primary P adsorption mechanism for Mg-rich biochar. However, although the release of Mg ions into solution is sometimes acknowledged, it is assumed that all precipitation occurs on the biochar surface rather than within the bulk solution, based solely on qualitative observations indicating that some precipitation occurs on the surface of the biochar [51],[52],[53],[54].

It should be noted that it is not the intent to state that bulk precipitation does occur in the works discussed, but instead to acknowledge that the data presented within the discussed studies suggest bulk precipitation is a possibility, without the presentation of sufficient data to rule it out. Some studies in the literature provide adequate evidence to indicate that bulk adsorption is not playing a significant role in P-removal. Ca-biochar produced via co-pyrolysis with oyster shell was shown to have a similar composition before and after adsorption, except for additional small amounts of P [19]. Similarly, when functionalised biochar produced using metal chlorides was thoroughly washed and dried after synthesis, enabling the potential pre-dissolution of metal chlorides, biochar composition exhibited little change before and after P-adsorption [49]. These examples vary from both the literature, as discussed in the previous paragraphs of this *Section 6.3.5,* and the work presented in this

thesis by synthesis methods that either facilitate pre-dissolution of metal groups from biochar or use lower CLRs.

If bulk precipitation is underestimated during P-removal it may lead to artificial inflation of theoretical maximum adsorption capacities, and subsequent total P-removal capacities.

6.4 Conclusions

This chapter presents evidence for the existence of a dual biochar P-removal mechanism of bulk precipitation and adsorption, suggesting that the role of bulk precipitation has been underestimated in several studies within the current literature for biochars with similar syntheses to those produced in this work.

Chemical analysis of biochar (FTIR, XRD, XRF, and XPS) post P-removal indicated multiple adsorption processes including: electrostatic attraction, hydrogen bonding, outer-sphere complexation, inner-sphere complexation, and surface precipitation of amorphous calcium phosphate. Data suggests hydrogen bonding and inner-sphere complexation to be the most dominant adsorption mechanisms. Adsorption of P by biochar exhibited pseudo-first-order kinetics. The adsorption data fit the Freundlich isotherm model well, indicating multilayer adsorption on a heterogeneous surface.

DoE analysis showed that P-adsorption by biochar is highly affected by pyrolysis temperature and is subject to the combined effects of CLR and pyrolysis temperature.

References

[1] X. Li *et al.*, “Enhanced phosphate removal from aqueous solution using resourceable nano-CaO2/BC composite: Behaviors and mechanisms,” *Science of the Total Environment*, vol. 709, Mar. 2020, doi: 10.1016/J.SCITOTENV.2019.136123.

[2] M. Feng *et al.*, “Oyster Shell Modified Tobacco Straw Biochar: Efficient Phosphate Adsorption at Wide Range of pH Values,” *International Journal of Environmental Research and Public Health 2022, Vol. 19, Page 7227*, vol. 19, no. 12, p. 7227, Jun. 2022, doi: 10.3390/IJERPH19127227.

[3] Y. Feng *et al.*, “Adsorption of Phosphate in Aqueous Phase by Biochar Prepared from Sheep Manure and Modified by Oyster Shells,” *ACS Omega*, vol. 6, no. 48, p. 33046, Dec. 2021, doi: 10.1021/ACSOMEGA.1C05191.

[4] Y. Zheng, A. R. Zimmerman, and B. Gao, “Comparative investigation of characteristics and phosphate removal by engineered biochars with different loadings of magnesium, aluminum, or iron,” *Science of The Total Environment*, vol. 747, p. 141277, Dec. 2020, doi: 10.1016/J.SCITOTENV.2020.141277.

[5] H. Samaraweera *et al.*, “Pyrolyzed Ca-impregnated lignite for aqueous phosphate removal: Batch and column studies,” *J Environ Chem Eng*, vol. 9, no. 5, p. 106077, Oct. 2021, doi: 10.1016/J.JECE.2021.106077.

[6] X. Zhang, X. Yuan, X. Yang, H. Zhang, and L. Han, “Environmental leaching of biochar: a full factorial analysis of composition and redundancy,” *Biomass Convers Biorefin*, vol. 15, no. 13, pp. 19993–20007, Jul. 2025, doi: 10.1007/S13399-024-06464-7/FIGURES/5.

[7] S. A. Parsons and J. A. Smith, “Phosphorus Removal and Recovery from Municipal Wastewaters,” *Elements*, vol. 4, pp. 109–112, Apr. 2008, Accessed: Sep. 08, 2025. [Online]. Available: https://www.ceas3.uc.edu/ret/archive/2018/ret/docs/readings/Project%201/Phosphorus%20removal%20and%20recovery%20from%20municipal%20wastewaters.pdf

[8] “Preparing for phosphorus removal in AMP 7 - AquaEnviro.” Accessed: Sep. 08, 2025. [Online]. Available: https://aquaenviro.co.uk/preparing-for-phosphorus-removal-in-amp-7/

[9] M. Preisner and M. Smol, “Investigating phosphorus loads removed by chemical and biological methods in municipal wastewater treatment plants in Poland,” *J Environ Manage*, vol. 322, p. 116058, Nov. 2022, doi: 10.1016/J.JENVMAN.2022.116058.

[10] L. M. Vrana, “Calcium Chloride,” in *Kirk-Othmer Encyclopedia of Chemical Technology*, John Wiley & Sons, Ltd, 2001. doi: 10.1002/0471238961.0301120318050904.A01.PUB2.

[11] C. Lievens *et al.*, “A case study: what is leached from mallee biochars as a function of pH?,” *Environ Monit Assess*, vol. 190, no. 5, pp. 1–12, May 2018, doi: 10.1007/S10661-018-6681-8/FIGURES/3.

[12] M. L. Free, “Speciation and Phase Diagrams,” *Minerals, Metals and Materials Series*, pp. 69–88, 2022, doi: 10.1007/978-3-030-88087-3_3/FIGURES/9.

[13] T. M. Gregory, E. C. Moreno, and W. E. Brown, “Solubility of CaHPO4 2H2O in the system Ca(OH)2-H3PO4-H2O at 5, 15, 25, and 37.5 C,” *J Res Natl Bur Stand A Phys Chem*, vol. 74A, no. 4, p. 461, Jul. 1970, doi: 10.6028/JRES.074A.036.

[14] E. C. Moreno, W. E. Brown, and G. Osborn, “Solubility of Dicalcium Phosphate Dihydrate in Aqueous Systems,” *Soil Science Society of America Journal*, vol. 24, no. 2, pp. 94–98, Mar. 1960, doi: 10.2136/SSSAJ1960.03615995002400020009X.

[15] P. Chikezie Ayogu, M. I. Ezugwu, and F. Ifeanyi Eze, “Principle of Common-ion Effect and its Application in Chemistry: a Review.,” *Journal of Chemistry Letters*, vol. 1, no. 2, pp. 77–83, Jul. 2020, doi: 10.22034/JCHEMLETT.2020.113421.

[16] Y. Xu *et al.*, “A Novel Ca-Modified Biochar for Efficient Recovery of Phosphorus from Aqueous Solution and Its Application as a Phosphorus Biofertilizer,” *Nanomaterials 2022, Vol. 12, Page 2755*, vol. 12, no. 16, p. 2755, Aug. 2022, doi: 10.3390/NANO12162755.

[17] A. Ojstršek and S. Gorgieva, “Cellulose Nanofibrils-Reinforced Pectin Membranes for the Adsorption of Cationic Dyes from a Model Solution,” *Polymers (Basel)*, vol. 16, no. 6, Mar. 2024, doi: 10.3390/POLYM16060724.

[18] P. E. Hansen and J. Spanget-Larsen, “NMR and IR Investigations of Strong Intramolecular Hydrogen Bonds,” *Molecules 2017, Vol. 22, Page 552*, vol. 22, no. 4, p. 552, Mar. 2017, doi: 10.3390/MOLECULES22040552.

[19] C. Scaggion *et al.*, “A fresh perspective on infrared spectroscopy as a prescreening method for molecular and stable isotopes analyses on ancient human bones,” *Scientific Reports 2024 14:1*, vol. 14, no. 1, pp. 1–14, Jan. 2024, doi: 10.1038/s41598-024-51518-5.

[20] A. B. D. Nandiyanto, R. Oktiani, and R. Ragadhita, “How to read and interpret ftir spectroscope of organic material,” *Indonesian Journal of Science and Technology*, vol. 4, no. 1, pp. 97–118, 2019, doi: 10.17509/IJOST.V4I1.15806.

[21] J. Zhao, Y. Liu, W. Bin Sun, and H. Zhang, “Amorphous calcium phosphate and its application in dentistry,” *Chem Cent J*, vol. 5, no. 1, p. 40, Jul. 2011, doi: 10.1186/1752-153X-5-40.

[22] L. Vecbiskena, K. A. Gross, U. Riekstina, and T. C. K. Yang, “Crystallized nano-sized alpha-tricalcium phosphate from amorphous calcium phosphate: microstructure, cementation and cell response,” *Biomedical Materials*, vol. 10, no. 2, p. 025009, Apr. 2015, doi: 10.1088/1748-6041/10/2/025009.

[23] A. J. Hoeher, S. T. Mergelsberg, O. J. Borkiewicz, and F. M. Michel, “Impacts of Initial Ca/P on Amorphous Calcium Phosphate,” *Cryst Growth Des*, Jun. 2021, doi: 10.1021/acs.cgd.1c00058.

[24] A. Indurkar *et al.*, “Small organic molecules containing amorphous calcium phosphate: synthesis, characterization and transformation,” *Front Bioeng Biotechnol*, vol. 11, p. 1329752, Jan. 2023, doi: 10.3389/FBIOE.2023.1329752/BIBTEX.

[25] J. F. Moulder, W. F. Stickle, P. E. Sobol, K. D. Bomben, and J. Chastain, *Handbook of X-ray Photoelectron Spectroscopy A Reference Book of Standard Spectra for Identification and Interpretation of XPS Data*. 1992.

[26] “Carbon | XPS Periodic Table | Thermo Fisher Scientific - UK.” Accessed: Sep. 01, 2025. [Online]. Available: https://www.thermofisher.com/uk/en/home/materials-science/learning-center/periodic-table/non-metal/carbon.html

[27] “UK Biochar Research Centre | What is Biochar?” Accessed: Sep. 03, 2025. [Online]. Available: https://www.biochar.ac.uk/what_is_biochar_technical.php

[28] V. G. Baldovino-Medrano, R. Ospina, and E. M. Gaigneaux, “Differential charging effects from impurities in pyrolytic graphite,” *Appl Surf Sci*, vol. 476, pp. 174–181, May 2019, doi: 10.1016/J.APSUSC.2018.12.269.

[29] “Oxygen | XPS Periodic Table | Thermo Fisher Scientific - UK.” Accessed: Sep. 03, 2025. [Online]. Available: https://www.thermofisher.com/uk/en/home/materials-science/learning-center/periodic-table/non-metal/oxygen.html

[30] “Chlorine | XPS Periodic Table | Thermo Fisher Scientific - UK.” Accessed: Sep. 03, 2025. [Online]. Available: https://www.thermofisher.com/uk/en/home/materials-science/learning-center/periodic-table/halogen/chlorine.html

[31] C. C. Chusuei and D. W. Goodman, “Brushite (CaHPO4·2H2O) by XPS,” *Surface Science Spectra*, vol. 8, no. 1, pp. 39–44, Jan. 2001, doi: 10.1116/11.20010501.

[32] G. N. Raikar, J. L. Ong, and L. C. Lucas, “Hydroxyapatite Characterized by XPS,” *Surface Science Spectra*, vol. 4, no. 1, pp. 9–13, Jan. 1996, doi: 10.1116/1.1247808.

[33] T. Roychowdhury, S. Bahr, P. Dietrich, M. Meyer, A. Thißen, and M. R. Linford, “Kidney stone, by near-ambient pressure XPS,” *Surface Science Spectra*, vol. 26, no. 1, Jun. 2019, doi: 10.1116/1.5052007/366929.

[34] “Calcium | Periodic Table | Thermo Fisher Scientific - UK.” Accessed: Sep. 03, 2025. [Online]. Available: https://www.thermofisher.com/uk/en/home/materials-science/learning-center/periodic-table/alkaline-earth-metal/calcium.html

[35] S. J. Kerber, J. J. Bruckner, K. Wozniak, S. Seal, S. Hardcastle, and T. L. Barr, “The nature of hydrogen in x-ray photoelectron spectroscopy: General patterns from hydroxides to hydrogen bonding,” 1996.

[36] J. F. . Watts and John. Wolstenholme, *An introduction to surface analysis by XPS and AES*. J. Wiley, 2003.

[37] S. Kumari, Y. Dong, and S. I. Safferman, “Phosphorus adsorption and recovery from waste streams using biochar: review of mechanisms, modifications, and agricultural applications,” vol. 15, p. 162, 2025, doi: 10.1007/s13201-025-02523-0.

[38] K. Nobaharan, S. B. Novair, B. A. Lajayer, and E. D. van Hullebusch, “Phosphorus Removal from Wastewater: The Potential Use of Biochar

and the Key Controlling Factors," *Water 2021, Vol. 13, Page 517*, vol. 13, no. 4, p. 517, Feb. 2021, doi: 10.3390/W13040517.

[39] J. A. Marshall, B. J. Morton, R. Muhlack, D. Chittleborough, and C. W. Kwong, "Recovery of phosphate from calcium-containing aqueous solution resulting from biochar-induced calcium phosphate precipitation," *J Clean Prod*, vol. 165, pp. 27–35, Nov. 2017, doi: 10.1016/J.JCLEPRO.2017.07.042.

[40] J. Yang, M. Zhang, H. Wang, J. Xue, Q. Lv, and G. Pang, "Efficient recovery of phosphate from aqueous solution using biochar derived from co-pyrolysis of sewage sludge with eggshell," *J Environ Chem Eng*, vol. 9, no. 5, p. 105354, Oct. 2021, doi: 10.1016/J.JECE.2021.105354.

[41] F. Pan *et al.*, "Phosphorus adsorption by calcium chloride-modified buckwheat hulls biochar and the potential application as a fertilizer," *J Clean Prod*, vol. 444, p. 141233, Mar. 2024, doi: 10.1016/J.JCLEPRO.2024.141233.

[42] S. B. Liu *et al.*, "Production of biochars from Ca impregnated ramie biomass (Boehmeria nivea (L.) Gaud.) and their phosphate removal potential," *RSC Adv*, vol. 6, no. 7, pp. 5871–5880, Jan. 2016, doi: 10.1039/C5RA22142K.

[43] R. L. Tseng and F. C. Wu, "Inferring the favorable adsorption level and the concurrent multi-stage process with the Freundlich constant," *J Hazard Mater*, vol. 155, no. 1–2, pp. 277–287, Jun. 2008, doi: 10.1016/J.JHAZMAT.2007.11.061.

[44] D. Ai, H. Ma, Y. Meng, T. Wei, and B. Wang, "Phosphorus recovery and reuse in water bodies with simple ball-milled Ca-loaded biochar," *Science of The Total Environment*, vol. 860, p. 160502, Feb. 2023, doi: 10.1016/J.SCITOTENV.2022.160502.

[45] S. Wang *et al.*, "Adsorption of phosphorus by calcium-flour biochar: Isotherm, kinetic and transformation studies," *Chemosphere*, vol. 195, pp. 666–672, Mar. 2018, doi: 10.1016/J.CHEMOSPHERE.2017.12.101.

[46] B. Biswas *et al.*, "Phosphorus adsorption using chemical and metal chloride activated biochars: Isotherms, kinetics and mechanism study," *Heliyon*, vol. 9, no. 9, p. e19830, Sep. 2023, doi: 10.1016/J.HELIYON.2023.E19830.

[47] T. Vijay *et al.*, “Scotland’s Rural College Phosphorus adsorption by functionalized biochar Phosphorus adsorption by functionalized biochar: a review,” *Environ Chem Lett*, doi: 10.1007/s10311-022-01519-5.

[48] Y. P. Gong, Z. Y. Ni, Z. Z. Xiong, L. H. Cheng, and X. H. Xu, “Phosphate and ammonium adsorption of the modified biochar based on Phragmites australis after phytoremediation,” *Environmental Science and Pollution Research*, vol. 24, no. 9, pp. 8326–8335, Mar. 2017, doi: 10.1007/S11356-017-8499-2/FIGURES/6.

[49] M. Zhang, B. Gao, Y. Yao, Y. Xue, and M. Inyang, “Synthesis of porous MgO-biochar nanocomposites for removal of phosphate and nitrate from aqueous solutions,” *Chemical Engineering Journal*, vol. 210, pp. 26–32, Nov. 2012, doi: 10.1016/j.cej.2012.08.052.

[50] Y. Yao, B. Gao, J. Chen, and L. Yang, “Engineered biochar reclaiming phosphate from aqueous solutions: Mechanisms and potential application as a slow-release fertilizer,” *Environ Sci Technol*, vol. 47, no. 15, pp. 8700–8708, Aug. 2013, doi: 10.1021/ES4012977/SUPPL_FILE/ES4012977_SI_001.PDF.

[51] K. Xu, F. Lin, X. Dou, M. Zheng, W. Tan, and C. Wang, “ Recovery of ammonium and phosphate from urine as value-added fertilizer using wood waste biochar loaded with magnesium oxide,” *Journal of Cleaner Production*, no. 187, pp. 205–214, Mar. 2018, Accessed: Sep. 05, 2025. [Online]. Available: https://doi.org/10.1016/j.jclepro.2018.03.206

7-Ca-biochar for P-recovery in Simulated Eutrophic Water and Application in Soil Systems

7.1 Introduction

Current policy and practice in the UK favours eutrophication control via prevention by reducing the input of nutrients to eutrophication-sensitive waterbodies [1], [2]. However, current methods have yielded little ecological benefit and fail to address issues associated with the release of legacy P from waterbed sediments [2]. As such, the use of biochar for the direct remediation of eutrophic waters should be considered alongside its potential for preventing eutrophication. There remains a lack of sufficient evidence for biochar's suitability for P-remediation in eutrophic waters. Current work available in the literature primarily focuses on P-removal in high concentration ranges (10-1000 mg_P/L), many orders of magnitude away from eutrophic concentrations (>0.035 mg_P/L) [3], [4], [5]. Furthermore, the literature primarily focuses on P removal in simple phosphate salt solutions, and there is a lack of consensus on the effects of coexisting ions (such as CO_3^{2-}, SO_4^{2-}, HCO_3^-, and NO_3^-) on biochars' aqueous P recovery in the available work [6], [7], [8]. Previous work presented in Chapters 4-6 of this thesis demonstrates the excellent P-recovery of biochars synthesised in this work in simple phosphate salt solutions across a wide range of concentrations commonly used in the literature (10-300 mg_P/L). The work presented in this chapter will address the aforementioned gaps by testing biochars' aqueous P removal under environmentally relevant pH levels, concentrations, and in the presence of coexisting ions to better understand how these environmental conditions affect biochars P-removal performance in real eutrophic and waste waters.

Just as testing P-removal in conditions reflective of real waters is essential, another relevant real-world assessment would be evaluating the effect of P-charged biochar on plant growth. Initial research into the use of P-laden biochar

for enhanced plant growth is promising; however, in the literature, only limited pot trials have been carried out, typically lasting no longer than a month, which limits findings to effects on germination and initial growth rates [9], [10], [11], [12]. In this Chapter, pot trials with P-laden biochar were carried out to provide longer-term (65 days) plant growth data than currently available, and to examine the effect of biochar on the bioavailability of P in soil.

7.2 Methodology

7.2.1 Biochar Production

The work presented in this chapter builds on results presented in Chapters 5 and 6, investigating the effects of pyrolysis temperatures and chemical loading rate (CLR) on biochars' physiochemical characteristics and aqueous P-recovery using DoE methodology; as such, details for the selection of pyrolysis temperatures and CLRs used are discussed in *Section 5.2* of this thesis.

Three types of biochar are defined in this chapter, which are functionalised biochar (Ca-biochar), washed biochar, and P-laden biochar. To produce functionalised biochar, softwood wood chips were ground to flakes of 1-2 mm, and then gently stirred for 24 h in a solution of $CaCl_2$ with CLR given in *Table 7.*1, dried in an oven at 100 °C for 24 h, and pyrolysed at temperatures in *Table 7.1*, following the DoE methodology set out in Chapter 5.

Table 7.1: Pyrolysis temperature and functionalisation CLR used for the synthesis of biochars produced in this work.

Ca-modified									
Temperature (°C)	600	644	644	750	750	750	856	856	900
CLR (wt:wt)	1.75	1.57	1.93	1.5	1.75	2	1.57	1.93	1.75

Washed biochar refers to functionalised biochar that was further stirred for 24 h in deionised (DI) water adjusted to pH 8 using 0.1M NaOH, at a dosage rate of 2 g/L, and then dried at 100 °C for 24 h in an oven.

P-laden biochar refers to biochar containing adsorbed P. This biochar was obtained by conducting 24 h batch P-removal experiments on Ca-biochar in a 250 mg_P/L solution, adjusted to pH 8 using 0.1M NaOH, at a dosage rate of 2 g/L, the biochar sample was then subsequently rinsed with DI to remove any bulk precipitated P coating its surface, and finally dried in an oven at 100 °C for 24 h. P-laden biochar + P-precipitate refers to P-laden biochar which was not rinsed after P-removal and remained coated in precipitate. P-precipitate refers to brushite ($CaHPO_4.2H_2O$) produced during P-removal experiments.

Note, all aqueous P-removal experiments in this chapter were conducted in solutions made in the lab to simulate specific characteristic of eutrophic water, however no real eutrophic water was used in this work.

7.2.2 Pot Trials

Pot trials were conducted according to the methodology detailed in *Section 3.3.13*. In brief, two rounds of pot trials were carried out; beans were planted by placing one seed in a plastic flowerpot, 9 cm H x 9 cm D, filled with one of the soil treatments specified below, with five replicates of each scenario:

1. Soil (control)
2. Soil + washed biochar (s + wc)
3. Soil + P-laden biochar (s + pc)
4. Soil + P-laden biochar + P-precipitate (s +prec)

Biochar was added to soil at an application rate of 1 wt%, to match application rates commonly used in the literature [13], [14]. As noted in *Section 3.3.13*, the first attempt to grow beans was not successful, and so the experiment was repeated. Round 2 of pot trials involved taking the five pots from each treatment

scenario in Round 1, removing any plant material, mixing the contents, and redistributing them into five new plant pots. Runner beans (Scarlet Emperor) were potted, and the plants received 15-30 mL of deionised water three times a week. They were harvested 65 days after sowing the seeds. The plants were grown in the lab on a window sill from the last week of March to the final week of May, using natural sunlight.

All biochar used for pot trials were samples Ca-1.75-T750, this sample was chosen as a large volume of biochar was required to carry out pot-trials, as such it was decided to use the DoE midpoint conditions (where repeats were already required) to reduce the number of additional furnace runs required to produce enough biochar.

7.3 Results and Discussion- Simulated Eutrophic Water

7.3.1 Influence of solution pH on P-removal

Eutrophic water bodies most commonly exist in a slightly alkaline state with a pH between 7 and 9; however, can experience a range of pH levels, with pH typically rising during the day and falling at night [15], [16]. To evaluate the performance of biochar at pH levels typical in eutrophic water, P-removal was studied in solutions with an initial pH of 6-10 [17], [18],[19]. Batch P-removal experiments were carried out for 24 h in 50 mL of 20 mg_P/L solution with a biochar dosage rate of 2 g/L.

As shown in *Figure 7.1*, all biochar samples demonstrated high P-removal (>91%) within the tested pH range, and P-removal was observed to increase with rising pH. At an initial solution pH of 10, the P-removal performance of the different biochar samples was nearly identical, ranging from 98.3-99.1 %; however, this range was observed to widen as pH decreased. At pH 6, P-removal ranged from 92.0-97.7 %, with a general trend that biochar performance improved as pyrolysis temperature increased.

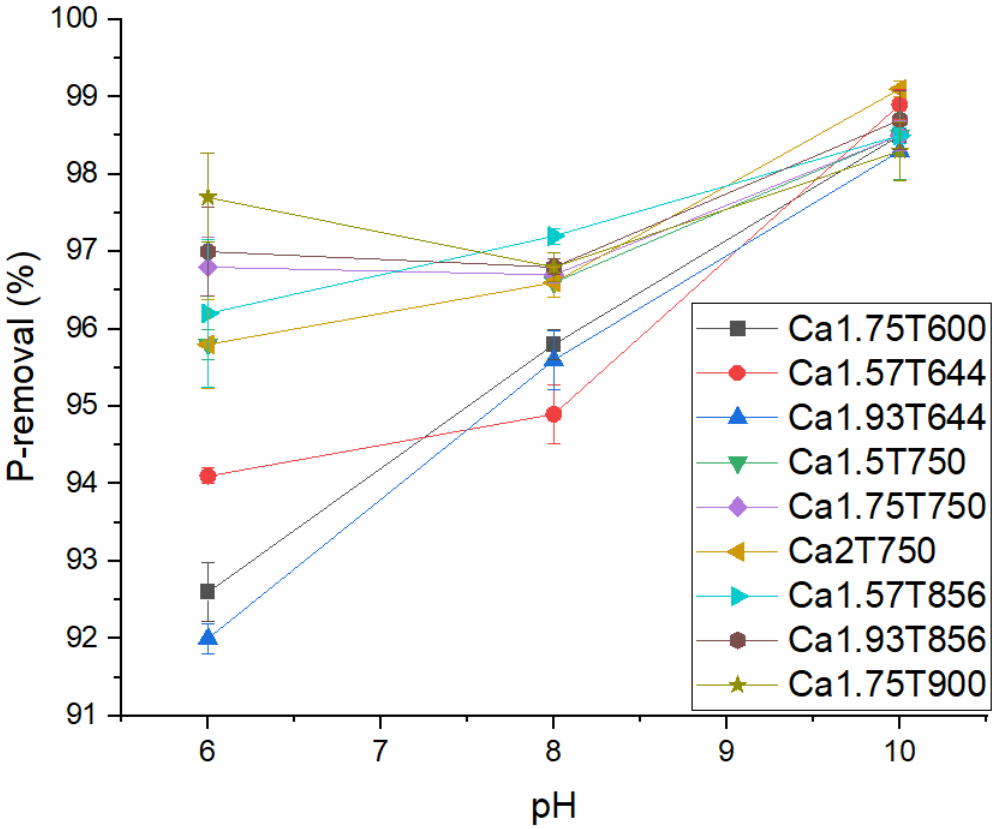

Figure 7.1:Effects of initial solution pH on the P-removal of biochar samples synthesised in this work. Batch P-removal experiments were carried out for 24 h in 50 mL of 20 mg_P/L solution with a biochar dosage rate of 2 g/L, 25°C.

7.3.2 Influence of low P concentration

To examine the effects of low initial concentration, batch P-removal experiments were performed in duplicate for 24 h in 50 mL of 1 mg_P/L solution, adjusted to pH 8, with a biochar dosage of 2 g/L. An initial concentration of 1 mg_P/L was selected to align with the EU limit for discharge into water bodies sensitive to eutrophication [20].

As shown in *Figure 7.2*, P-removal drops significantly when the initial P concentration decreases from 20 mg_P/L (94.9-97.0% P-removal) to 1 mg_P/L (13.1-26.6% P-removal). As discussed in detail in Chapter 6, phosphate is removed through a dual mechanism involving bulk precipitation of brushite, resulting from the reaction between leached Ca^{2+} and HPO_4^{2-} ions, and adsorption. The

solubility product (Ksp) of brushite at 25 °C is 2.45 x10^{-7}, precipitation is only thermodynamically favourable if the ionic product of reacting ions exceeds this Ksp [21] . Taking the Ca concentration in solution as 251 mg/L (*Table 6.2*, *Section 6.3.2.3*), the ionic product of Ca^{2+} and HPO_4^{2-} ions will not exceed the Ksp of brushite below 1.21 mg_P/L; thus, it can be inferred that bulk precipitation no longer contributes to P removal at low concentrations (<1.21 mg_P/L), and all P-removal is due to adsorption only. As shown in *Figure 7.2*, biochar samples demonstrated lower P-removal rates in 1 mg_P/L solutions (adsorption only) compared to P-adsorption rates in 20 mg_P/L solutions. As discussed in Chapter 6, adsorption behaviour was well described by pseudo-first-order kinetics. Pseudo-first-order kinetics assume that the concentration gradient between the adsorbate in solution and on the adsorbent acts as the driving force for adsorption; consequently, a low bulk concentration of phosphate would be expected to reduce the rate of diffusion of P from the bulk solution to the biochar surface.

The reduction in P-removal with decreasing initial P concentration highlights the need for further research in the literature to evaluate biochars' performance at environmentally relevant P levels for eutrophic water, and that significant variations in P concentration could influence P-removal mechanisms. Rapid Small Scale Column Testing (RSSCT) was conducted to determine if a fixed bed setup could enhance the mass transfer of P from solution to biochar at low concentrations (1 mg_P/L). Unfortunately, the column tests were unsuccessful, and no P was removed from the solution, indicating that the biochar samples produced are only suitable for use in batch systems at low concentrations. Results of RSSCT can be found in *Appendix A.5*.

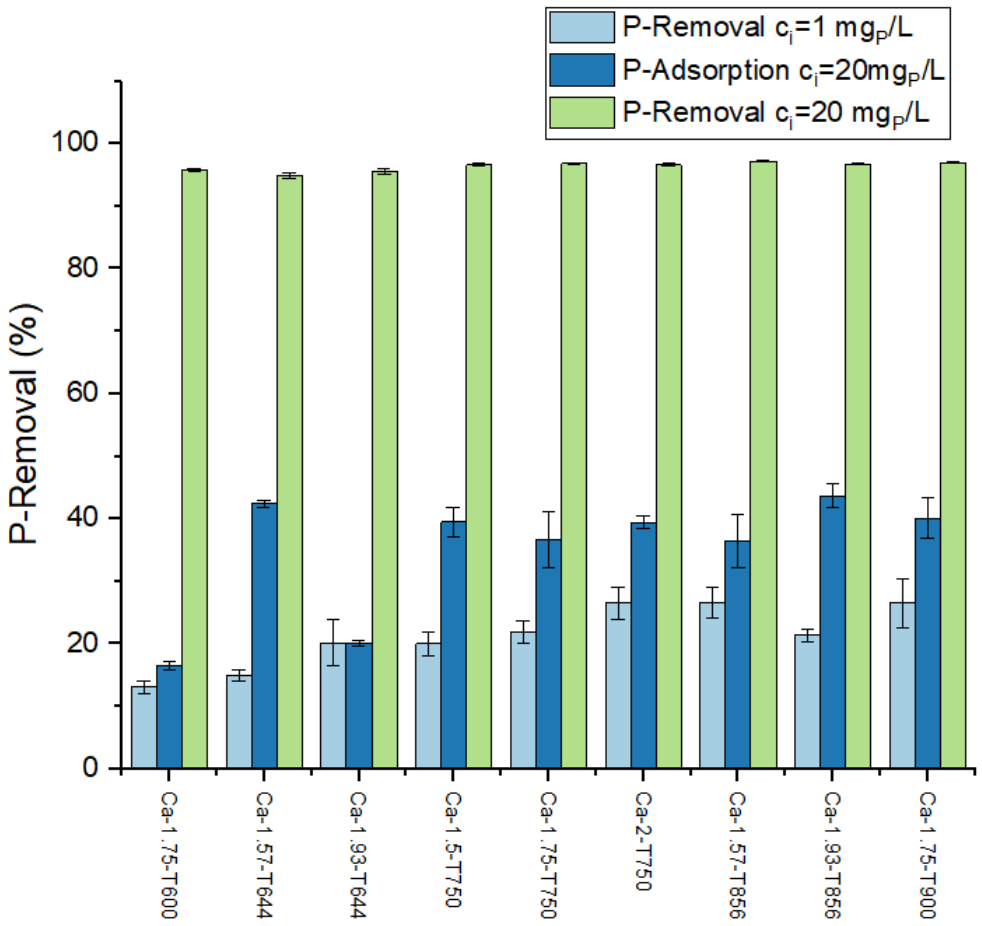

Figure 7.2: Comparison of P-removal achieved by biochars synthesised in this study at initial P concentrations of 1 mg_P/L (light blue) and 20 mg_P/L (total P removal-green, adsorption only- dark blue). All experiments were carried out in batch configuration for 24 h in a 50 mL solution, adjusted to pH 8, at 25 °C, with a biochar dosage rate of 2 g/L.

7.3.3 Coexisting Ions

To investigate the influence of commonly coexisting ions on phosphate removal by biochar samples, 20 mg_P/L solutions of KH_2PO_4 were mixed in a 1:1 ratio with 20 mg_C/L, 20 mg_N/L, and 20 mg_S/L solutions of Na_2CO_3, $NaNO_3$, and K_2SO_4, respectively [22], [23]. Batch P-removal experiments were conducted in triplicate for 24 h in 50 mL of 10 mg_P/L solution, adjusted to pH 8, with a biochar dosage of 2 g/L. P-removal was also tested in tap water with 10 mg_P/L of KH_2PO_4 added to the solution; the concentration of anions in the P-tap water solution is provided in *Table 7.2*. The biochar sample Ca-1.75-T900 was selected for coexisting ion

experiments because of its high P removal over a wide pH range, as demonstrated in *Section 7.3.1*.

Table 7.2: Concentration of anions in P-tap water before treatment with biochar.

Anion	**Concentration (mg/L)**
P-PO_4	17.1
Cl	10.1
N-NO_3	0.8
S-SO_4	4.3

As shown in *Figure 7.3*, P-removal demonstrated by biochar samples remained largely unaffected by the presence of coexisting ions, with a slight increase in P removal in solutions containing carbonate and nitrate. This small rise in P removal is likely due to the presence of Na^{2+} ions aiding P-recovery. Biochar samples did not remove any coexisting ions during P-removal experiments.

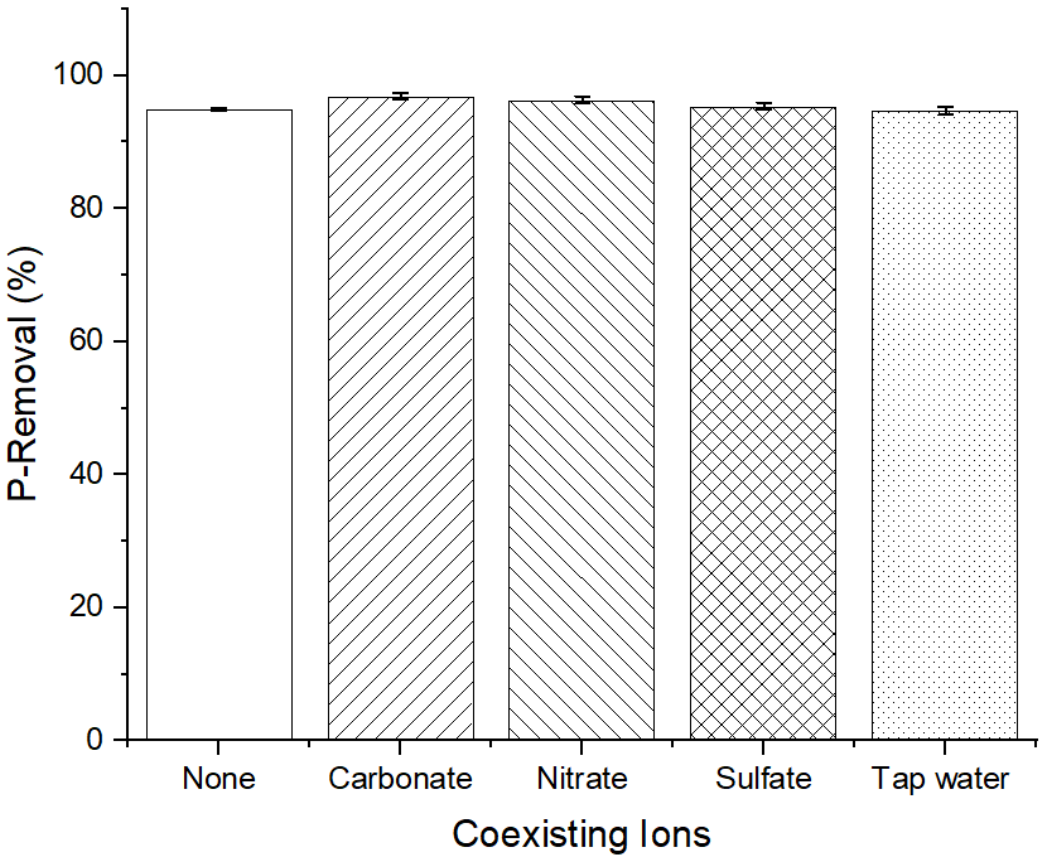

Figure 7.3: Comparison of P-removal achieved by biochars synthesised in this study in the presence of different coexisting ions. All experiments were carried out in batch configuration for 24 h in a 50 mL solution, adjusted to pH 8, 25 °C, with a biochar dosage rate 2 g/L.

7.4 Results and Discussion-Pot Trials

7.4.1 Plant Growth

7.4.1.1 Germination

Results for the germination rates of plants are shown in *Figure. 7.4*, where the time for germination was taken to be the number of days for a shoot to first be visible above the soil surface. Unfortunately, plant growth was not successful in pots with the treatment s+pc, with only one of five pots successfully germinating, and not until day 23; as such, this treatment was omitted from the analysis of amendments' effects on germination rate. The poor performance of samples with the s+pc treatment was unexpected, especially considering that samples with the s+wc and s+prec treatments performed so well, indicating that neither the

presence of biochar nor additional phosphorus had a negative effect on germination.

Figure 7.4a shows consistently high germination rates, with pots containing biochar exhibiting a higher success rate (100%) compared to control samples with soil only (60%). Germination was also observed to occur more quickly in treatments containing biochar, with an average germination time of 12.3, 11.4, and 10.6 days for soil, s+wc, and s+prec treatments, respectively. Large error bars present in *Figure 7.4b* are representative of the high standard deviation and wide variability seen within samples of the same treatment. No significant difference in germination rate was present at a 90 % confidence level using a t-test.

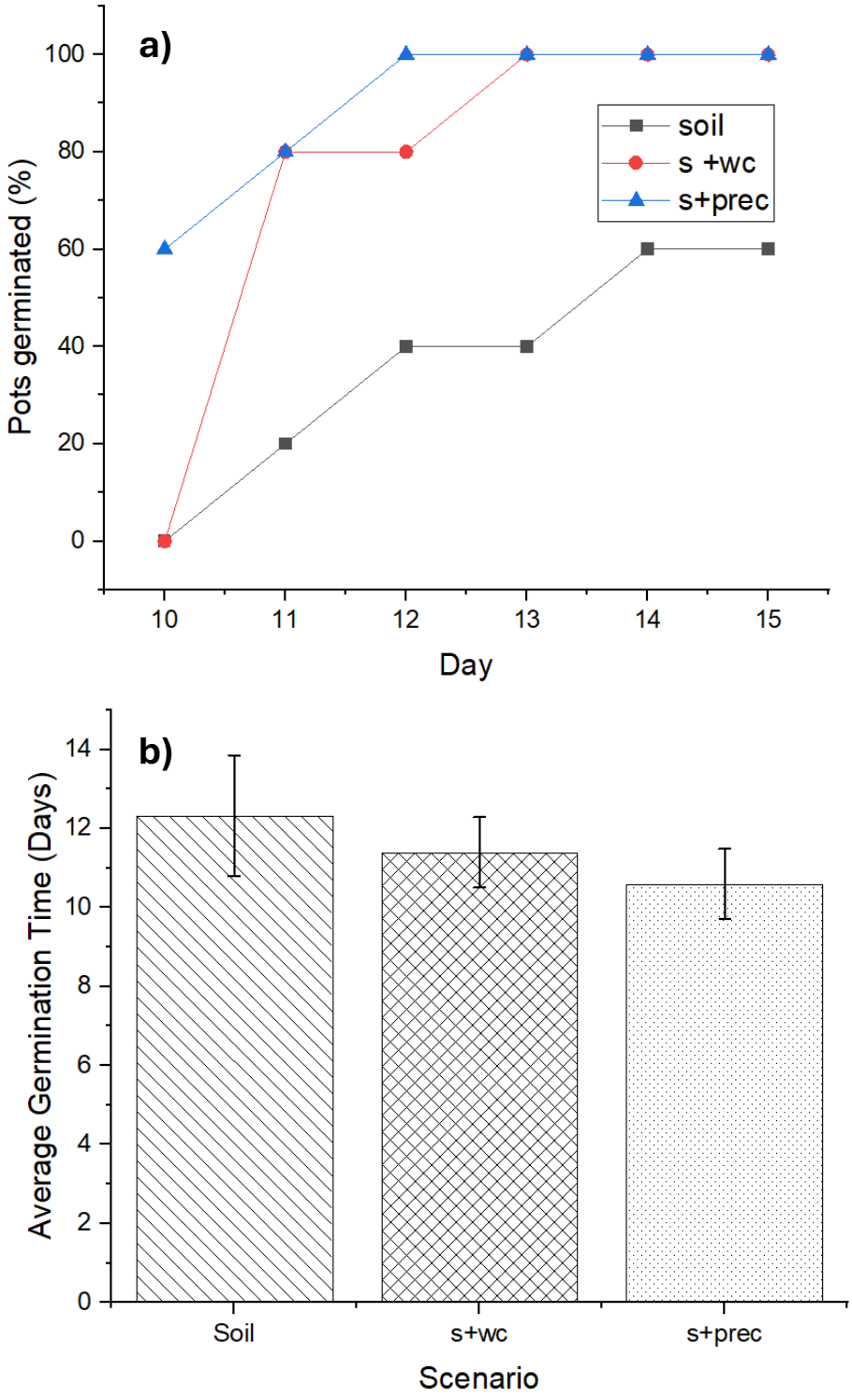

Figure 7.4:a) Germination rate of plants grown in different soil treatments in this work. b) Average germination time of plants grown in different soil treatments in this work.

7.4.1.2 Plant Height

Plants' shoots were allowed to grow to an above-soil height of 85 cm, at which point they were pinched just below their top bud. The pinching encourages growth in width rather than height and prevents plants from becoming overwhelmingly tall. *Figure 7.6* compares the rate of plants growth in height with different soil treatments; once again, the s+pc treatment was omitted from the results. Overall, plants treated with s+prec appeared to grow the most rapidly, exhibiting the highest average height during the first 40 days. While the average height of plants with the control treatment was greater than that of plants treated with s+wc, this truly reflects a wider variation in the s+wc sample (where more plants successfully germinated) rather than faster growth. As seen in *Figure 7.6b*, treatments with soil and s+wc had the same number of plants pinched between days 25 and 36, and both took 42 days for 100% of plants to reach pinching height, indicating their growth rates were similar. Since the presence of biochar itself did not appear to increase plant growth rates, the enhanced growth observed in plants treated with s+prec can be attributed to the presence of $CaHPO_4.2H_2O$. Images of plants fully grown after 65 days can be seen in *Figure 7.5*.

Soil

s + wc

s + pc

s + prec

Figure 7.5: Images of plants grown in different scenarios in this work.

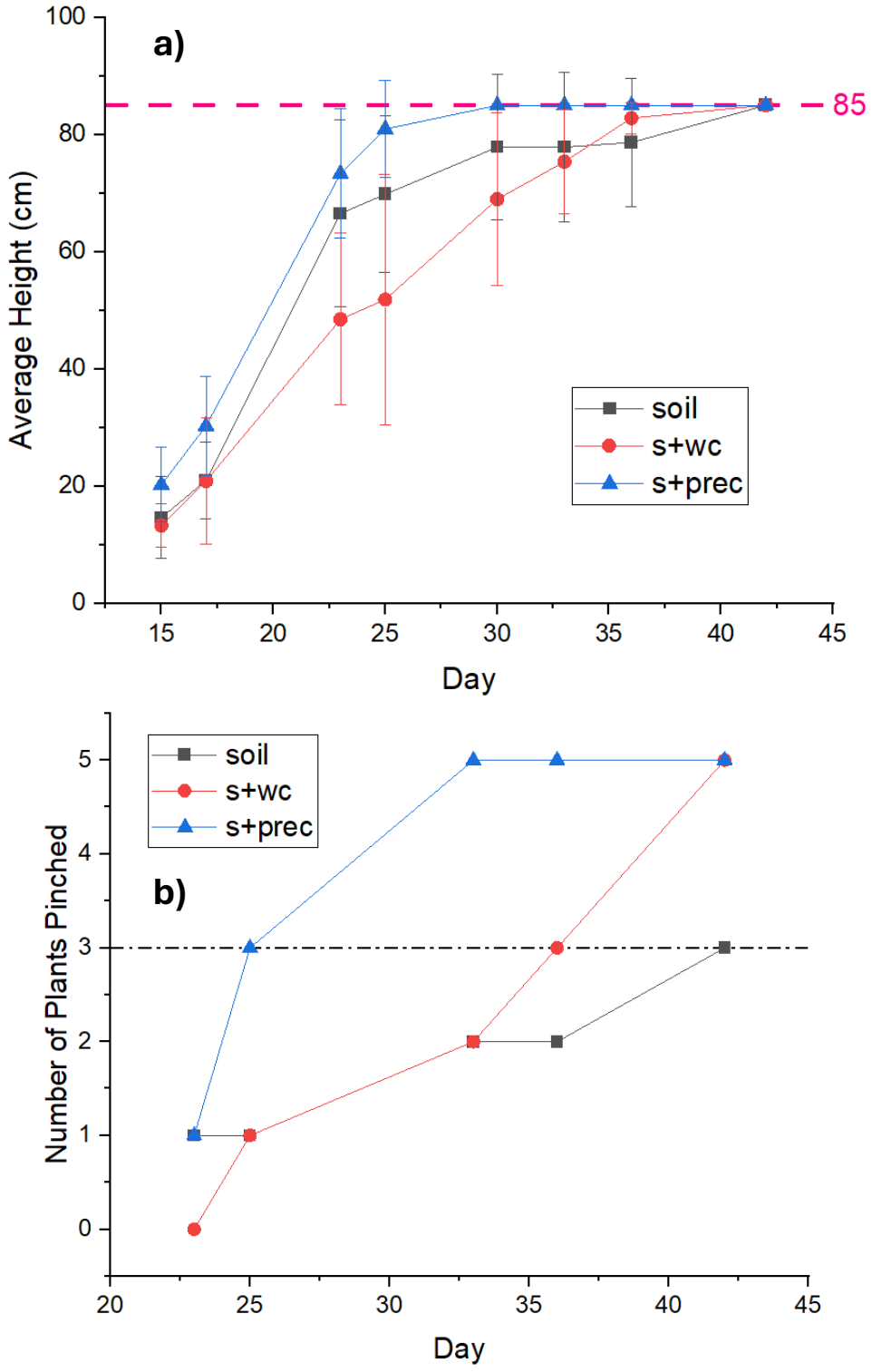

Figure 7.6: a) Average heights of plants grown in different soil treatments in this work. b) Time until pinching for plants of different soil treatments grown in this work, where the dashed black line represents the total number of germinated pots for the soil-only (control) treatment.

7.4.1.3 Plant Weight and Width

The average fresh weight (FW) and dry weight (DW) of shoots and leaves of plants grown using different soil treatments, along with the standard deviation in the sample results, are presented in *Table 7.3*. The moisture content of the plant matter produced remained unaffected by soil treatments. Unamended soil produced the greatest biomass, followed by soil treated with precipitate and then soil treated with washed biochar. However, only DWs of plants produced using s+wc and s+prec treatments were found to be significantly different using a t-test, at a 90 % confidence level using t-testing. While samples grown with the s+prec amendment appeared to grow faster, they did not exhibit overall enhanced growth. It was unexpected for biochar to reduce plant growth, as much of the literature demonstrates biochar to increase biomass production [24], [25]. Although research on the specific effects of P-rich biochar on plant growth is limited, general agreement exists that P-rich biochar can enhance plant growth; however, much of the available literature is comprised of short-term studies focusing on the first 30 days of growth [9], [10], [11], [12]. The variation in study durations may account for the differing results. Considering the data presented in *Figure 7.6a*, it is probable that if the work presented in this thesis had been limited to the first 30 days, similar findings to the literature would have been observed. *Figure 7.7* illustrates the relationship between average FW and average plant width for different soil treatments; variation in height between amendments appears to reflect variation in plant width, as expected due to pinching of plants.

*Table 7.3: Average fresh weight and dry weights of plants grown in this work using different soil treatments. Values given as average ± standard deviation.**

Treatment	Average Fresh Weight (g)	Average Dry Weight (g)
Soil	20.3 ± 4.8	2.03 ± 0.50
s+wc	15.4 ± 2.3	1.50 ± 0.23
s+pc	11.6	1.21
s+prec	16.7 ± 2.5	1.79 ± 0.23

**n=5 for s+wc and s+prec treatments, n=3 for soil treatment, and n=1 for s+pc treatment.*

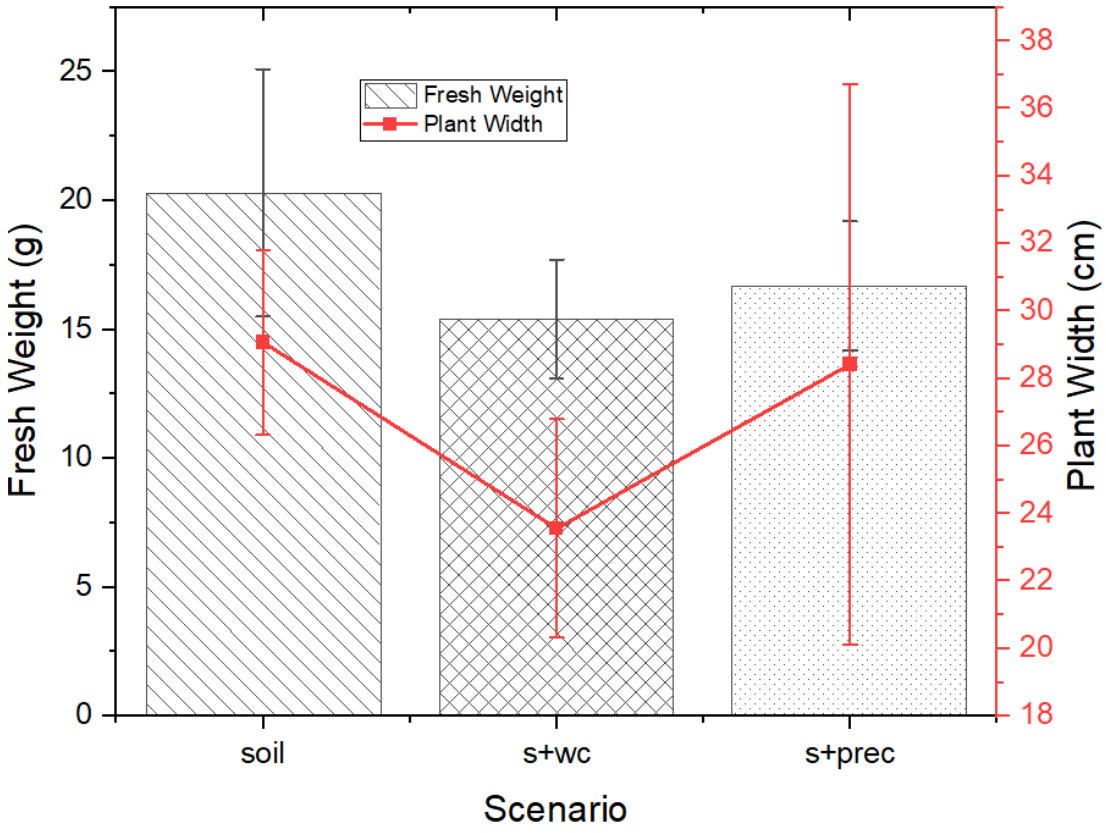

Figure 7.7:Average fresh weight (bars) and plant width (line) of plants grown in different soil amendments in this work.

7.4.2 Nutrient Content of Soil and Plant Matter

Table 7.4 displays the mass of bioavailable P in soil before and after plant growth in various soil treatments, as well as the average mass of P and Ca in the plants grown. Initial bioavailable P contents were taken from each of the amendment mixtures before they were divided into the five different pots; no replicates were carried out due to limited material. The final characteristics were measured for each pot individually, with an average value and standard deviation provided. Biochar was observed to increase the initial content of bioavailable P in the soil treatment mixtures. The higher level of initial bioavailable P in the s+wc soil mixture compared to the control sample is counterintuitive since biochar in the s+wc samples had not been previously treated with phosphate; however, this could be attributed to P already present in the biochar from softwood feedstock. Based on the analysis presented in *Chapter 6* showing that adsorption kinetics are governed by physisorption, a reversible process, it was expected that at least some P present in P-laden biochar would be available to plants; however, pots treated with s+pc demonstrated the lowest initial bioavailable P content. It should be noted that as initial measurements of bioavailable P could not be replicated, the variation within samples is unknown, and for scenarios where the values obtained are close together, such as s+wc and s+pc, it is not possible to determine which scenario truly contained more bioavailable P. The highest initial bioavailable P content was seen in s+prec treated soil, indicating the $CaHPO_4.2H_2O$ precipitate to be partially bioavailable.

Considering data presented in *Table 7.4*, the bioavailable P content of soil amendment mixtures appeared to increase after plant growth in control-treated pots, remain mostly unaffected in s+wc-treated pots, and decrease in s+prec-treated pots. A much larger variation in final bioavailable P was seen in samples treated with s+prec compared to other treatments, partially influencing the large difference between average final bioavailable P contents. The bioavailability of soil amendment mixtures can be enhanced by the solubilisation of P by microbes in the soil. As plants absorb P, microbes solubilise non-bioavailable P to maintain

equilibrium between the concentration of soluble P in the soil and the P concentration in the plants [26]. Control pots, samples treated with the s+wc mixture, and the sample treated with the s+pc mixture all exhibit similar final bioavailable P content, potentially indicative of the equilibrium state between P uptake by plants and P solubilisation by microbes. Using a t-test, the final bioavailable P of soil samples with s+prec treatment was found to be significantly different from s+wc and control treatments at a 90 % confidence level.

Plant samples grown in the s+prec treatment showed lower P content than the control treatment, indicating that the reduction in final bioavailable P in the soil mixture is not due to increased plant uptake. Furthermore, although biochar possesses the potential to adsorb P present in the soil, this is unlikely to account for the observed decrease in bioavailable P, since adsorption would also be expected to occur in other treatments with biochar amendments, particularly in the s+wc treatment, where the biochar was not previously saturated with P prior to mixing soil. Various forms of Ca have been reported to reduce P-solubilisation by different microbes [27], [28]. Over time, as $CaHPO_4.2H_2O$ partially dissolves in the soil matrix, it may increase the activity of Ca^{2+} ions and promote reprecipitation as less soluble, more thermodynamically stable compounds like hydroxyapatite, thereby reducing the concentration of bioavailable P, reducing the effectiveness of P-solubilising microbes [29], [30]. As expected, the trend in the total mass of phosphorus and calcium in plant samples reflected the trend in the mass of biomass produced. Using a t-test, both the P and Ca content of plant matter grown in s+wc treatment mixture can be deemed significantly different from plant matter grown in control and s+prec treatments at a 90% confidence level. However, no statistically significant difference exists between control and s+prec treatments.

Overall, neither the initial nor the final average bioavailable P content of the soil treatment mixtures appeared to correlate with the overall average growth or P content of plant material grown under different treatments. The strong growth of plants observed with the control treatment emphasises the ample quantity of P

in the high-quality commercial topsoil used. It is therefore likely that increasing the nutrient surplus in the soil did not impact plant growth. However, since P in biochar was shown to be bioavailable, this study should be repeated in P-depleted soil to investigate the effects of biochar in systems where the soil is not already nutrient-rich.

*Table 7.4: Nutrient content (P and Ca) of soil samples and plant matter grown in this work with different soil treatments. Values given as average ± standard deviation.**

Treatment	Bioavailable P in soil mixtures (mg)		P content of plant (leaves & stems) (mg)	Ca content of plant (leaves & stems) (mg)
	initial	final		
Soil	21.1	25.7 ± 2.7	4.36 ± 0.58	7.12 ± 0.24
S+wc	25.2	24.7 ± 3.0	3.14 ± 0.23	6.42 ± 0.26
S+pc	24.8	25.8	1.94	4.15
S+prec	27.1	11.8 ± 10.7	3.94 ± 0.45	7.40 ± 0.27

**n=5 for s+wc and s+prec treatments, n=3 for soil treatment, and n=1 for s+pc*

7.4.3 Soil Characteristics

Table 7.5 displays the characteristics of soil treatments before and after plant growth. Initial characteristics were taken from the amendment mixtures before they were divided into the five different pots, and final characteristics were measured for each pot individually, with an average value and standard deviation provided. All soil treatments exhibited a high organic matter content, with a slight increase in amendments containing biochar. All soil treatments, excluding s+pc, initially had a mildly alkaline pH of 8.1; the initial pH of the s+pc treatment was marginally lower. Throughout plant growth, the pH of samples without precipitate increased by approximately 0.1, while the pH of soil containing precipitate increased slightly more, by approximately 0.2—likely due to the liming effect of $CaHPO_4.2H_2O$. Using a t-test, the difference in final soil pH of samples treated with s+prec was found to be significantly different from control samples and those treated with s+wc at a 95% confidence level. Samples containing biochar

showed increased water retention, gaining moisture from the initial conditions, while control samples lost moisture. Biochar is well known for enhancing the water-holding capacity of soil [31]. Water retention appeared to increase with rising P and Ca content in biochar. Calcium has been shown to improve soil structure by promoting aggregate formation, increasing soil porosity, and enhancing water retention [32], [33]. Using a t-test, the final moisture content of soil under control, s+wc, and s+prec treatments was found to be significantly different from each other at 95% confidence levels. Increased moisture in soil has been linked to a higher germination rate in various crops—potentially explaining the improved performance of amended pots compared to the control samples [14], [34]. Results presented demonstrate the suitability of biochar for use in soils affected by drought.

*Table 7.5: Characteristics of different soil amendments before and after plant growth. Values for after plant growth are given as average± standard deviation.**

Treatment	**pH**		**Moisture Content (%)**		**Organic matter content (%)**
	initial	final	initial	final	
Soil	8.12	8.22 ± 0.02	27.1	22.8 ± 3.0	18
S+wc	8.12	8.21 ± 0.06	26.8	29.2 ± 1.9	21
S+pc	8.03	8.1	25.1	31	18
S+prec	8.13	8.32 ± 0.05	25.6	35.62 ± 1.7	19

**n=5 for s+wc and s+prec treatments, n=3 for soil treatment, and n=1 for s+pc*

7.5 Biochar-Based Circular Approach

The use of Ca-biochar for the capture of aqueous bioavailable orthophosphate is a promising strategy for integrating waste valorisation, water remediation, and soil amendment into a circular nutrient management system that helps recover P and prevent water eutrophication [3], [35]. Remediation of current eutrophic

water bodies is necessary; however, current policy and practice in the UK primarily favour prevention—reducing nutrient inputs to eutrophication-sensitive waterbodies— as the primary approach to eutrophication control [1], [2]. Functionalised biochar produced in this work may offer a dual-function solution capable of both remediation by removing dissolved P from water bodies and prevention by intercepting high P concentration waste streams before environmental discharge. A summary of the circular biochar process proposed in this work, detailing potential uses of biochar for P-recycling in water and soil systems, is illustrated in *Figure 7.8*.

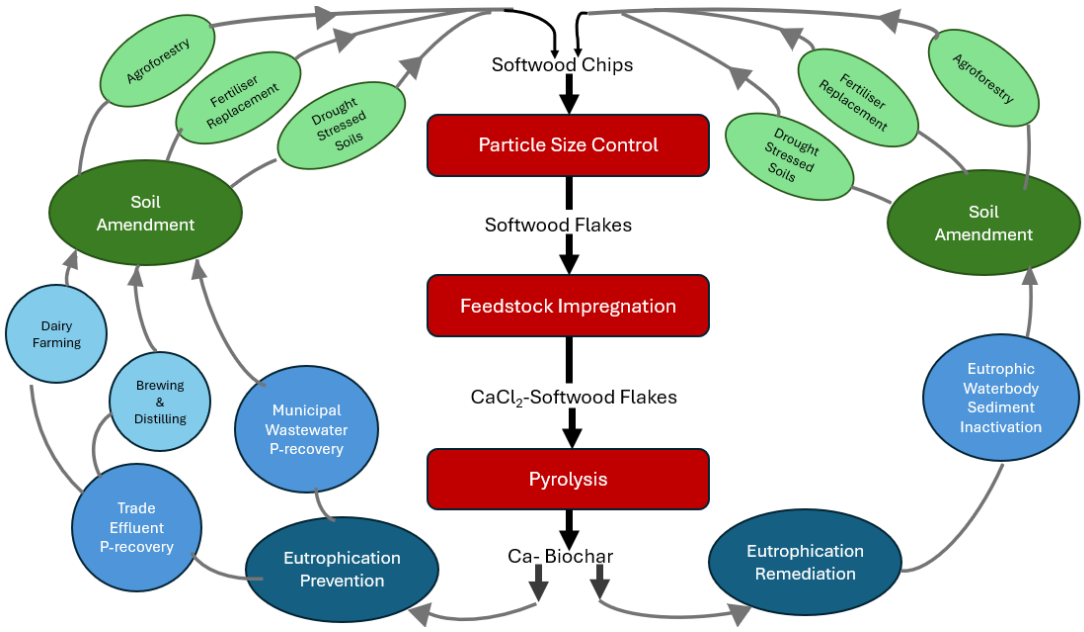

Figure 7.8: Butterfly diagram illustrating potential circular approaches for Ca-biochar synthesised in this work, integrating waste utilisation, water remediation, and soil amendment to recover and recycle P within the environment.

7.5.1 Eutrophic Water Remediation

Current remediation methods of eutrophic waterbodies include the removal of algae— removing the P absorbed by algae as they grow and preventing release of P back into the water body when they die— and sediment drudging or inactivation [36], [37]. Even after external P inputs are reduced, P stored in waterbed sediments may release into the overlying water for decades—a process known as internal loading [38], [39]. Sediment inactivation refers to the chemical stabilisation of P stored in the waterbed, at the sediment–water interface, via

precipitation with metal salts ($Al_2(SO_4)_3$, iron salts, or calcium salts) or modified clays (La-bentonite), the precipitates formed are left in the water as a P-sink [40], [41], [42]. In contrast, sediment dredging involves the removal of phosphorus-rich sediments and is invasive, costly, and can disturb habitats[37],[43] .

Concentrations of orthophosphate-P at the sediment-water interface are significantly higher than in the bulk solution, commonly varying from 0.1-9 mg_P/L, with values up to 29 mg_P/L reported in the literature [44], [45], [46], [47]. Due to the moderate P concentrations at the sediment-water interface, Ca-biochar synthesised in this work may be a highly effective alternative to current sediment inactivation materials, allowing for adsorption of P onto biochar's surface alongside the more traditional approach of precipitation with calcium phosphate-based salts. Recovery of biochar, to utilise its circular economy potential, without sediment dredging would be challenging. Further research should be conducted into the deployment of biochar in bags, mats, or geotextile carriers capable of remaining in the sediment-water interface and recovery without waterbed disturbance [48], [49]. Over time, using Ca-biochar for sediment inactivation, alongside control of external P inputs, will allow for a gradual decline in P concentration as algae consume current P.

As discussed in *Section 7.3.1* above, in a low concentration solution (<1.21 mg_P/L), Ca-biochar no longer removes P via a dual mechanism of adsorption and precipitation; instead, only adsorption occurs. Furthermore, adsorption is governed by physisorption, with low concentrations leading to slow kinetics and less favourable adsorption. As such, Ca-biochar synthesised in this work may be less suitable for the immediate remediation of bulk solution, as opposed to sediment inactivation, in eutrophic waterbodies (0.035-0.1 mg_P/L) [5].

7.5.2 Prevention of Eutrophication

Wastewater streams include: municipal waste (urban and commercial sewage), industrial waste, agricultural waste, and trade effluent. In England, phosphorus

pollution to river water bodies is attributed to be 60-70 % from sewage treatment works, 25 % from agriculture, and 7 % from diffuse urban sources [2].

Treatment of municipal wastewater to reduce P-concentration and prevent eutrophication is generally carried out using chemical removal (precipitation using metal salts) as a primary removal mechanism, and biological P removal (using cells to take up P and then removing cells as a sludge) as a secondary treatment [50], [51]. Tertiary removal/polishing may be used where necessary. Following polishing, sludges produced for different stages in the wastewater treatment process commonly undergo anaerobic digestion, producing a liquor high in P concentration (up to 167 mg_P/L) [52], [53], [54]. This digestate liquor is often recycled back to the input stream to be treated.

Moderate orthophosphate concentrations of municipal wastewater typically vary between 4-12 mg_P/L, making it suitable for treatment with Ca-biochar synthesised in this work [50], [55]. Since standard treatment methods of these waste streams often involve chemical precipitation, Ca-biochar produced in this work has the potential to replace the salts added during this process step, fitting into existing infrastructure and allowing for both bulk precipitation and adsorption to occur. However, the presence of pollutants in municipal wastewater, such as pathogens and organic micropollutants, may pose challenges for circular reuse due to potential soil contamination [56]. To make the use of biochar suitable for land application, P-charged spent biochar would have to be shown to meet regulatory standards by either thermal sanitation of spent biochar or proving it to be sufficiently low in pollutants of concern [57]. Digestate liquor is generally lower in pathogens and other pollutants of concern; as such, P recovery from this stream may face fewer issues meeting regulatory standards [58]. Additionally, Ca-biochar produced in this work has demonstrated excellent P-removal at the high concentrations of digestate liquor streams.

Although not one of the most prominent causes of waterbody P pollution, trade effluent streams may still benefit from the recovery of P by Ca-biochar

synthesised in this work and contribute towards P recycling and reduced fertiliser use. Trade effluent streams which would be strong candidates for biochar-supported P-recycling are brewing/distilling waste streams (30-100 mg_P/L), and wastewater from dairy processing (25-100 mg_P/L)[59], [60], [61], [62].

Functionalised biochar produced in this work may not be particularly suitable to treat P from diffuse agriculture due to low P concentration of these streams (0.1-1.5 mg_P/L) [63], [64]. However, the circular use of P-charged biochar as a soil amendment and fertiliser replacement has the potential to indirectly reduce diffuse agricultural pollution via the adoption of green farming methods. While biochar facilitated adsorption for P-recovery from wastewater may not yet rival conventional remediation in scale or speed, its compatibility with circular strategies makes it a compelling tool for eutrophication prevention and phosphorus recovery.

7.6 Conclusions

The work presented in this chapter highlights the importance of testing biochars' aqueous P removal at environmentally relevant conditions. Biochar was seen to perform well across a pH range typical of eutrophic water and in the presence of coexisting ions. However, initial P concentration was found to influence the P-removal mechanisms of biochar, preventing precipitation and reducing adsorption.

Pot trials demonstrated that amendment with P-laden biochar + $CaHPO_4.2H_2O$ increased the initial rate of growth of plants but decreased overall biomass production. Biochar was seen to improve germination rates of plants due to its ability to enhance soil moisture retention and soil aeration, allowing for better oxygen availability and moisture balance which creates favourable conditions for seed growth. The presence of $CaHPO_4.2H_2O$ also appeared to inhibit the solubilisation of P. However, this did not affect plant growth. Results presented suggest the suitability of biochar to support plant growth in soil systems

undergoing stress from nutrient deficiency, drought, or in agroforestry applications.

Biochar synthesised in this work is appropriate for use in a circular economy. Pending future work, biochar has the potential to help combat eutrophication by remediating eutrophic water bodies via sediment inactivation. Water treatment with biochar has the potential to fit into existing infrastructure, treating waste streams such as municipal wastewater or trade effluent. Subsequently, P-charged biochar is suitable for use in soil systems.

References

[1] "Nutrient pollution: reducing the impact on protected sites - GOV.UK." Accessed: Sep. 14, 2025. [Online]. Available: https://www.gov.uk/government/publications/nutrient-pollution-reducing-the-impact-on-protected-sites/nutrient-pollution-reducing-the-impact-on-protected-sites

[2] "Phosphorus-challenges-for-the-water-environment.odt," Dec. 2022. Accessed: Sep. 09, 2025. [Online]. Available: https://view.officeapps.live.com/op/view.aspx?src=https%3A%2F%2Fassets.publishing.service.gov.uk%2Fmedia%2F64b50abe0ea2cb001315e366%2FPhosphorus-challenges-for-the-water-environment.odt&wdOrigin=BROWSELINK

[3] I. W. Almanassra, G. Mckay, V. Kochkodan, M. Ali Atieh, and T. Al-Ansari, "A state of the art review on phosphate removal from water by biochars," *Chemical Engineering Journal*, vol. 409, p. 128211, Apr. 2021, doi: 10.1016/J.CEJ.2020.128211.

[4] L. Ghodszad, A. Reyhanitabar, M. R. Maghsoodi, B. Asgari Lajayer, and S. X. Chang, "Biochar affects the fate of phosphorus in soil and water: A critical review," Nov. 01, 2021, *Elsevier Ltd*. doi: 10.1016/j.chemosphere.2021.131176.

[5] Scottish Environmental Protection Agency (SEPA), "Annex E: Classification for Scotland's Standing Waters." Accessed: Jul. 21, 2025. [Online]. Available: https://www.sepa.org.uk/media/38358/loch-water-quality-classification-scheme.pdf

[6] J. Yang, M. Zhang, H. Wang, J. Xue, Q. Lv, and G. Pang, "Efficient recovery of phosphate from aqueous solution using biochar derived from co-pyrolysis of sewage sludge with eggshell," *J Environ Chem Eng*, vol. 9, no. 5, p. 105354, Oct. 2021, doi: 10.1016/J.JECE.2021.105354.

[7] R. Li *et al.*, "Enhancing phosphate adsorption by Mg/Al layered double hydroxide functionalized biochar with different Mg/Al ratios," *Science of*

The Total Environment, vol. 559, pp. 121–129, Jul. 2016, doi: 10.1016/J.SCITOTENV.2016.03.151.

[8] O. Alagha, M. Saood Manzar, M. Zubair, I. Anil, N. Dalhat Mu'azu, and A. Qureshi, "Comparative Adsorptive Removal of Phosphate and Nitrate from Wastewater Using Biochar-MgAl LDH Nanocomposites: Coexisting Anions Effect and Mechanistic Studies", doi: 10.3390/nano10020336.

[9] Y. Xu *et al.*, "A Novel Ca-Modified Biochar for Efficient Recovery of Phosphorus from Aqueous Solution and Its Application as a Phosphorus Biofertilizer," *Nanomaterials 2022, Vol. 12, Page 2755*, vol. 12, no. 16, p. 2755, Aug. 2022, doi: 10.3390/NANO12162755.

[10] D. Ai, H. Ma, Y. Meng, T. Wei, and B. Wang, "Phosphorus recovery and reuse in water bodies with simple ball-milled Ca-loaded biochar," *Science of The Total Environment*, vol. 860, p. 160502, Feb. 2023, doi: 10.1016/J.SCITOTENV.2022.160502.

[11] Y. Yao, B. Gao, J. Chen, and L. Yang, "Engineered biochar reclaiming phosphate from aqueous solutions: Mechanisms and potential application as a slow-release fertilizer," *Environ Sci Technol*, vol. 47, no. 15, pp. 8700–8708, Aug. 2013, doi: 10.1021/ES4012977/SUPPL_FILE/ES4012977_SI_001.PDF.

[12] B. Arwenyo, J. J. Varco, A. Dygert, and T. Mlsna, "Phosphorus availability from magnesium-modified P-enriched Douglas fir biochar as a controlled release fertilizer," *Soil Use Manag*, vol. 38, no. 1, pp. 691–702, Jan. 2022, doi: 10.1111/SUM.12751.

[13] F. Wali *et al.*, "Effect of Consecutive Application of Phosphorus-Enriched Biochar with Different Levels of P on Growth Performance of Maize for Two Successive Growing Seasons," *Sustainability 2022, Vol. 14, Page 1987*, vol. 14, no. 4, p. 1987, Feb. 2022, doi: 10.3390/SU14041987.

[14] D. Hou *et al.*, "Effects of Soil Moisture Content on Germination and Physiological Characteristics of Rice Seeds with Different Specific

Gravity," *Agronomy 2022, Vol. 12, Page 500*, vol. 12, no. 2, p. 500, Feb. 2022, doi: 10.3390/AGRONOMY12020500.

[15] X. Ji, J. M. H. Verspagen, M. Stomp, and J. Huisman, "Competition between cyanobacteria and green algae at low versus elevated CO2: who will win, and why?," *J Exp Bot*, vol. 68, no. 14, p. 3815, Jun. 2017, doi: 10.1093/JXB/ERX027.

[16] J. A. Raven, C. J. Gobler, and P. J. Hansen, "Dynamic CO2 and pH levels in coastal, estuarine, and inland waters: Theoretical and observed effects on harmful algal blooms," *Harmful Algae*, vol. 91, p. 101594, Jan. 2020, doi: 10.1016/J.HAL.2019.03.012.

[17] L. Carvalho *et al.*, "Sustaining recreational quality of European lakes: Minimizing the health risks from algal blooms through phosphorus control," *Journal of Applied Ecology*, vol. 50, no. 2, pp. 315–323, Apr. 2013, doi: 10.1111/1365-2664.12059;SUBPAGE:STRING:FULL.

[18] J. M. H. Verspagen, D. B. Van De Waal, J. F. Finke, P. M. Visser, E. Van Donk, and J. Huisman, "Rising CO2 Levels Will Intensify Phytoplankton Blooms in Eutrophic and Hypertrophic Lakes," *PLoS One*, vol. 9, no. 8, p. e104325, Aug. 2014, doi: 10.1371/JOURNAL.PONE.0104325.

[19] R. B. Wallace, H. Baumann, J. S. Grear, R. C. Aller, and C. J. Gobler, "Coastal ocean acidification: The other eutrophication problem," *Estuar Coast Shelf Sci*, vol. 148, pp. 1–13, Jul. 2014, doi: 10.1016/J.ECSS.2014.05.027.

[20] EUW Directive -Off. J. Eur.Communities, "Council Directive of 21. May 1991 concerning urban waste water treatment (91/271/EEC)," 1991. Accessed: May 22, 2025. [Online]. Available: https://scholar.google.com/scholar?q=EU%2C%20Council%20Directive%2091%2F271%2FEEC%2C%20%E2%80%9CUrban%20Waste%20Water%20Treatment%20(OJ%20L%20135%2C%2030.5.1991).

[21] "Solubility Product Constants Ksp at 25°C." Accessed: Aug. 06, 2025. [Online]. Available: https://www.aqion.de/site/16

[22] M. N. Afridi, W. H. Lee, and J. O. Kim, “Effect of phosphate concentration, anions, heavy metals, and organic matter on phosphate adsorption from wastewater using anodized iron oxide nanoflakes,” *Environ Res*, vol. 171, pp. 428–436, Apr. 2019, doi: 10.1016/J.ENVRES.2019.01.055.

[23] Y. Zhu, X. Yue, and F. Xie, “Adsorptive removal of phosphate by a Fe–Mn–La tri-metal composite sorbent: Adsorption capacity, influence factors, and mechanism,” *Adsorption Science and Technology*, vol. 38, no. 7–8, pp. 254–270, Oct. 2020, doi: 10.1177/0263617420942709/ASSET/C478C2D3-5514-405A-8960-4E16EDE18713/ASSETS/IMAGES/LARGE/10.1177_0263617420942709-FIG11.JPG.

[24] X. Zhang, X. Feng, N. Chai, Y. Kuzyakov, F. Zhang, and F. M. Li, “Biochar effects on crop yield variability,” *Field Crops Res*, vol. 316, p. 109518, Aug. 2024, doi: 10.1016/J.FCR.2024.109518.

[25] J. O. Ighalo *et al.*, “Biochar for ameliorating soil fertility and microbial diversity: From production to action of the black gold,” *iScience*, vol. 28, no. 1, p. 111524, Jan. 2025, doi: 10.1016/J.ISCI.2024.111524.

[26] M. C. Ogwu, M. E. Patterson, and P. A. Senchak, “Phosphorus mining and bioavailability for plant acquisition: environmental sustainability perspectives,” *Environ Monit Assess*, vol. 197, no. 5, p. 572, May 2025, doi: 10.1007/S10661-025-14012-7.

[27] J. Musarrat and M. S. Khan, “Factors affecting phosphate-solubilizing activity of microbes: Current status,” *Phosphate Solubilizing Microorganisms: Principles and Application of Microphos Technology*, pp. 63–85, Jul. 2014, doi: 10.1007/978-3-319-08216-5_3/TABLES/2.

[28] K. Bai *et al.*, “Effects of phosphorus-solubilizing bacteria and biochar application on phosphorus availability and tomato growth under phosphorus stress,” *BMC Biol*, vol. 22, no. 1, pp. 1–20, Dec. 2024, doi: 10.1186/S12915-024-02011-Y/FIGURES/7.

[29] M. S. A. Johnsson and G. H. Nancollas, “The role of Brushite and octacalcium phosphate in apatite formation,” *Critical Reviews in Oral Biology and Medicine*, vol. 3, no. 1–2, pp. 61–82, 1992, doi: 10.1177/10454411920030010601,.

[30] R. Štulajterová and Ľ. Medvecký, “Effect of calcium ions on transformation brushite to hydroxyapatite in aqueous solutions,” *Colloids Surf A Physicochem Eng Asp*, vol. 316, no. 1–3, pp. 104–109, Mar. 2008, doi: 10.1016/J.COLSURFA.2007.08.036.

[31] F. Razzaghi, P. B. Obour, and E. Arthur, “Does biochar improve soil water retention? A systematic review and meta-analysis,” *Geoderma*, vol. 361, p. 114055, Mar. 2020, doi: 10.1016/J.GEODERMA.2019.114055.

[32] M. Huang *et al.*, “Effects of Soil Exchangeable Calcium in Promoting the Accumulation of Soil Organic Carbon by Karst Vegetation Restoration,” *J Soil Sci Plant Nutr*, vol. 24, no. 1, pp. 843–854, Mar. 2024, doi: 10.1007/S42729-023-01589-6/FIGURES/4.

[33] M. C. Rowley, S. Grand, and É. P. Verrecchia, “Calcium-mediated stabilisation of soil organic carbon,” *Biogeochemistry*, vol. 137, no. 1–2, pp. 27–49, Jan. 2018, doi: 10.1007/S10533-017-0410-1/FIGURES/3.

[34] L. D. Doneen and J. H. MacGillivray, “Germination (Emergence) of Vegetable Seed as Affected By Different Soil Moisture Conditions,” *Plant Physiol*, vol. 18, no. 3, pp. 524–529, Jul. 1943, doi: 10.1104/PP.18.3.524.

[35] T. Vijay *et al.*, “Scotland’s Rural College Phosphorus adsorption by functionalized biochar Phosphorus adsorption by functionalized biochar: a review,” *Environ Chem Lett*, doi: 10.1007/s10311-022-01519-5.

[36] G. Zeng *et al.*, “Comparison of the Advantages and Disadvantages of Algae Removal Technology and Its Development Status,” *Water 2023, Vol. 15, Page 1104*, vol. 15, no. 6, p. 1104, Mar. 2023, doi: 10.3390/W15061104.

[37] M. Riza, M. N. Ehsan, M. N. Pervez, M. M. O. Khyum, Y. Cai, and V. Naddeo, “Control of eutrophication in aquatic ecosystems by sustainable

dredging: Effectiveness, environmental impacts, and implications," *Case Studies in Chemical and Environmental Engineering*, vol. 7, p. 100297, Jun. 2023, doi: 10.1016/J.CSCEE.2023.100297.

[38] M. Søndergaard, J. P. Jensen, and E. Jeppesen, "Role of sediment and internal loading of phosphorus in shallow lakes," *Hydrobiologia*, vol. 506–509, no. 1, pp. 135–145, Nov. 2003, doi: 10.1023/B:HYDR.0000008611.12704.DD/METRICS.

[39] O. Tammeorg, J. Horppila, P. Tammeorg, M. Haldna, and J. Niemistö, "Internal phosphorus loading across a cascade of three eutrophic basins: A synthesis of short- and long-term studies," *Science of The Total Environment*, vol. 572, pp. 943–954, Dec. 2016, doi: 10.1016/J.SCITOTENV.2016.07.224.

[40] A. Bańkowska-Sobczak, A. Blazejczyk, E. Eiche, U. Fischer, and Z. Popek, "Phosphorus Inactivation in Lake Sediments Using Calcite Materials and Controlled Resuspension—Mechanism and Efficiency," *Minerals 2020, Vol. 10, Page 223*, vol. 10, no. 3, p. 223, Feb. 2020, doi: 10.3390/MIN10030223.

[41] N. B. Pallí, "A comparison of two methods to reduce internal phosphorus cycling in lakes: Aluminium versus Phoslock", Accessed: Sep. 08, 2025. [Online]. Available: http://stud.epsilon.slu.se/

[42] L. Zisen *et al.*, "In-situ Technologies for Controlling Sediment Phosphorus in Eutrophic Shallow Lakes: A Review," *Journal of Earth Science 2025 36:1*, vol. 36, no. 1, pp. 113–133, Feb. 2025, doi: 10.1007/S12583-024-0118-9.

[43] "Floods and dredging: explaining the Environment Agency's approach – Creating a better place." Accessed: Sep. 08, 2025. [Online]. Available: https://environmentagency.blog.gov.uk/2021/12/23/floods-and-dredging/

[44] K. Kowalczewska-Madura and R. Gołdyn, "Spatial and seasonal variability of pore water phosphorus concentration in shallow Lake Swarzędzkie,

Poland," *Environ Monit Assess*, vol. 184, no. 3, pp. 1509–1516, Mar. 2012, doi: 10.1007/S10661-011-2056-0/METRICS.

[45] M. B. de Toledo and H. M. Baulch, "A landscape limnology approach to assessing controls on soluble reactive phosphorus in sediment porewater and internal loading risk," *Science of The Total Environment*, vol. 953, p. 176012, Nov. 2024, doi: 10.1016/J.SCITOTENV.2024.176012.

[46] W. Förster *et al.*, "Phosphorous Supply to a Eutrophic Artificial Lake: Sedimentary versus Groundwater Sources," *Water (Basel)*, vol. 13, no. 563, 2021, doi: 10.3390/w13.

[47] E. J. Palmer-Felgate, M. J. Bowes, C. Stratford, C. Neal, and S. MacKenzie, "Phosphorus release from sediments in a treatment wetland: Contrast between DET and EPC0 methodologies," *Ecol Eng*, vol. 37, no. 6, pp. 826–832, Jun. 2011, doi: 10.1016/J.ECOLENG.2010.12.024.

[48] "High-tech mats for water treatment biochar | Blog PYREG." Accessed: Sep. 08, 2025. [Online]. Available: https://pyreg.com/high-tech-mats-for-water-treatment-filled-with-biochar/

[49] "Using an Ancient Technology in a New Way: Removing Nutrients in a Lake with Biochar - PRINCETON HYDRO." Accessed: Sep. 08, 2025. [Online]. Available: https://princetonhydro.com/biochar/

[50] S. A. Parsons and J. A. Smith, "Phosphorus Removal and Recovery from Municipal Wastewaters," *Elements*, vol. 4, pp. 109–112, Apr. 2008, Accessed: Sep. 08, 2025. [Online]. Available: https://www.ceas3.uc.edu/ret/archive/2018/ret/docs/readings/Project%201/Phosphorus%20removal%20and%20recovery%20from%20municipal%20wastewaters.pdf

[51] "Preparing for phosphorus removal in AMP 7 - AquaEnviro." Accessed: Sep. 08, 2025. [Online]. Available: https://aquaenviro.co.uk/preparing-for-phosphorus-removal-in-amp-7/

[52] R. Kleemann, J. Chenoweth, R. Clift, S. Morse, P. Pearce, and D. Saroj, "Evaluation of local and national effects of recovering phosphorus at

wastewater treatment plants: Lessons learned from the UK," *Resour Conserv Recycl*, vol. 105, pp. 347–359, Dec. 2015, doi: 10.1016/J.RESCONREC.2015.09.007.

[53] S. Kato and Y. Kansha, "Comprehensive review of industrial wastewater treatment techniques," *Environ Sci Pollut Res Int*, vol. 31, no. 39, p. 51064, Aug. 2024, doi: 10.1007/S11356-024-34584-0.

[54] F. Simoes, R. Colston, C. Rosa-Fernandes, P. Vale, T. Stephenson, and A. Soares, "Predicting the potential of sludge dewatering liquors to recover nutrients as struvite biominerals," *Environmental Science and Ecotechnology*, vol. 3, p. 100052, Jul. 2020, doi: 10.1016/J.ESE.2020.100052.

[55] S. Guida, G. Rubertelli, B. Jefferson, and A. Soares, "Demonstration of ion exchange technology for phosphorus removal and recovery from municipal wastewater," *Chemical Engineering Journal*, vol. 420, no. 1, p. 129913, 2021, doi: 10.1016/j.cej.2021.129913.

[56] M. Dong *et al.*, "Challenges in safe environmental applications of biochar: identifying risks and unintended consequence," *Biochar*, vol. 7, no. 1, pp. 1–20, Dec. 2025, doi: 10.1007/S42773-024-00412-4/FIGURES/7.

[57] "The UK research exploring how to make sewage sludge safer and more sustainable - CIWEM." Accessed: Sep. 09, 2025. [Online]. Available: https://www.ciwem.org/news/uk-research-exploring-how-to-make-sewage-sludge-safer?utm_source=chatgpt.com

[58] Q. Zhao and Y. Liu, "Is anaerobic digestion a reliable barrier for deactivation of pathogens in biosludge?," *Sci Total Environ*, vol. 668, p. 893, Jun. 2019, doi: 10.1016/J.SCITOTENV.2019.03.063.

[59] P. Lejwoda, B. Białecka, and M. Thomas, "Removal of phosphate from brewery wastewater by cerium(III) chloride originating from spent polishing agent: Recovery and optimization studies," *Science of The Total Environment*, vol. 875, p. 162643, Jun. 2023, doi: 10.1016/J.SCITOTENV.2023.162643.

[60] A. Gebeyehu, N. Shebeshe, H. Kloos, and S. Belay, “Suitability of nutrients removal from brewery wastewater using a hydroponic technology with Typha latifolia,” *BMC Biotechnol*, vol. 18, no. 1, p. 74, Nov. 2018, doi: 10.1186/S12896-018-0484-4.

[61] P. O. Bickers, R. Bhamidimarri, J. Shepherd, and J. Russell, “Biological phosphorus removal from a phosphorus-rich dairy processing wastewater,” *Water Science and Technology*, vol. 48, no. 8, pp. 43–51, Nov. 2003, doi: 10.2166/WST.2003.0451.

[62] B. Gil-Pulido *et al.*, “Evaluation of dairy processing wastewater biotreatment in an IASBR system: Aeration rate impacts on performance and microbial ecology,” *Biotechnology Reports*, vol. 19, p. e00263, Sep. 2018, doi: 10.1016/J.BTRE.2018.E00263.

[63] J. Cloy *et al.*, “A state of knowledge overview of identified pathways of diffuse pollutants to the water environment,” 2021.

[64] S. Harrison, C. McAree, W. Mulville, and T. Sullivan, “The problem of agricultural ‘diffuse’ pollution: Getting to the point,” *Science of The Total Environment*, vol. 677, pp. 700–717, Aug. 2019, doi: 10.1016/J.SCITOTENV.2019.04.169.

8 Conclusions and Future Work

This research aimed to develop a proof of concept for a biochar circular process which integrates waste utilisation, water remediation, and soil amendment to both recover and recycle phosphorous (P) within the environment. This chapter summarises the key findings of this thesis, highlights the original contributions to knowledge, and reflects on the impact of the work presented. Limitations of the work are acknowledged, and potential directions for future work are proposed.

8.1 Conclusions

To effectively utilise biochar for P recovery and reuse, it was essential to evaluate its capabilities in different applications. To better understand the optimal route for the creation of functionalised biochar for aqueous P-removal, the performance of two high-performing functionalisation agents (Ca and Mg) was compared at various CLR and pyrolysis temperatures, with Ca-biochar found to display a higher P-removal than Mg-biochar. DoE optimisation of functionalisation conditions (pyrolysis temperature and CLR) found that Ca-biochars and Mg-biochars respond to variations in functionalisation conditions differently, highlighting the importance of using a range of functionalisation conditions when comparing different functionalisation agents.

The effects of two different particle size control methods (wood grinding and biochar grinding) were examined, with pre-pyrolysis particle size control (wood grinding) found to increase biochar samples' aqueous P-removal compared to biochar particle size control— this was attributed to an increased uptake of functionalisation agent during feedstock impregnation. Similarly, when softwood feedstock was impregnated with $CaCl_2$ pre-pyrolysis, P-removal was enhanced compared to the impregnation of biochar with CaOH or $CaCO_3$ post-pyrolysis. This was attributed to increased uptake of functionalisation agent by softwood compared to biochar. Overall, when optimising Ca-biochars production for high aqueous P recovery, process decisions which favoured increased functionalisation agent uptake enhanced aqueous P removal. Optimal P recovery

was achieved when impregnating particle-size-controlled wood flakes pre-pyrolysis with $CaCl_2$. Work carried out in this thesis to optimise the process of functionalised biochar production provides novel contributions to current knowledge by comparing the effect of pre vs post pyrolysis particle size control, and pre vs post pyrolysis impregnation, to create metal oxide/carbonate decorated biochar, for the first time in the literature. This work provides key insights into the effects of the functionalisation process on biochars' physicochemical properties and aqueous P-removal, contributing towards the overall aim of this thesis by establishing best practice, which is essential for identifying the potential of biochar in the application of wastewater treatment.

The effects of temperature and CLR on biochars' physicochemical characteristics and P uptake have not been well understood, with conflicting reports in the existing literature. For the first time in the literature, a DoE methodology was used in this thesis to analyse the effects of CLR and pyrolysis temperature on biochars physicochemical properties and P-adsorption. Regression analysis was successfully used to determine quadratic equations capable of describing the relationships of pyrolysis temperature and CLR with four physicochemical properties response variables (yield, surface area, average pore volume, and mass ratio of Cl:Ca). All response variables exhibited a higher dependence on temperature than CLR and displayed no statistically significant interaction effects, failing to prove that any synergistic effects were present. Evidence was provided of the presence of $CaCO_3$ and $CaCl_2{\cdot}4H_2O$ on the surfaces of Ca-biochar samples. A mechanism for the transformation of $CaCl_2$ during pyrolysis was proposed, suggesting $CaCl_2$ to react with pyrolysis vapours (predominantly H_2O and CO_2) during pyrolysis to form $CaCO_3$, with excess $CaCl_2$ remaining on the biochar surface and absorbing water from the atmosphere to form $CaCl_2.4H_2O$.

All Ca-biochar samples produced demonstrated excellent 24 h batch phosphate removal, achieving up to 97% removal from a 20 mg_P/L solution and 79% from a 200 mg_P/L solution. Evidence of a dual P-removal mechanism of bulk

precipitation and adsorption was provided, suggesting the role of bulk precipitation (responsible for the majority of P-removal) has been significantly underestimated (and the role of surface precipitation overestimated) in the current literature for biochars with a synthesis similar to that produced in this work. It was proposed that the two different forms of Ca present on the biochar's surface each played a different role in P-removal, with $CaCl_2$ facilitating bulk precipitation and $CaCO_3$ facilitating adsorption.

Adsorption was able to remove up to 43.7% of P within 24 h batch experiments, with regression analysis successfully used to determine a quadratic relationship between P-adsorption and functionalisation conditions. P-adsorption by biochar was shown to be highly affected by pyrolysis temperature and subject to, statistically significant, large and positive combined effects of CLR and pyrolysis temperature— indicating synergistic effects on aqueous P-adsorption. Optimal CLR for high P-adsorption is seen to increase with increasing pyrolysis temperature; this is attributed to greater functionalisation agent content without increased pore blockage. Chemical analysis of biochar after P-removal showed that adsorption happens through multiple processes, including electrostatic attraction, hydrogen bonding, outer-sphere complexation, inner-sphere complexation, and surface precipitation of amorphous calcium phosphate. The adsorption of P by biochar followed pseudo-first-order kinetics, suggesting that physisorption governs the process. The adsorption data fitted the Freundlich isotherm well, indicating multilayer adsorption on a heterogeneous surface.

DoE analysis conducted in this work provides new insights into the influence of functionalisation conditions (pyrolysis temperature and CLR) on biochars' yield, surface area, average pore volume, transformation of $CaCl_2$ during pyrolysis, and P-adsorption. It provides mathematical relationships that can be used to predict biochar properties and produce tailor-made biochars within the tested design space. The DoE analysis conducted allows for an understanding of how different key characteristics are affected by functionalisation parameters. As biochar application often determines the most influential characteristics, this is

essential for use in circular systems. Analysis of P-removal mechanisms provides some of the key novel scientific contributions in this work, discussing a dual mechanism in which bulk precipitation is a significant factor for the first time in the literature. Analysis of the adsorption mechanisms also provides essential insight into the reversibility of P-uptake by biochar, a critical factor in the suitability of biochar as a P-source in soil.

Biochar was shown to maintain an excellent P-removal over a range of pH levels typical of eutrophic water and wastewaters (up to 97.7-99.1 % between pH 6-10) and displayed no reduction in P-removal in the presence of co-existing anions. However, initial P concentration was found to influence the P-removal mechanisms of biochar samples, with removal dropping to 13.1-16.6 % at an initial concentration of 1 mg_P/L. Low concentration (<1.21 mg_P/L) was seen to prevent precipitation from occurring and reduce adsorption in 24 h batch experiments.

Pot trials conducted demonstrated that amendment of soil with P-laden biochar + $CaHPO_4.2H_2O$ successfully increased the initial rate of growth of plants (runner beans (scarlet emperor)) but decreased overall biomass production. The presence of biochar was shown to improve germination rates of plants and enhance soil moisture retention, however the presence of $CaHPO_4.2H_2O$ appeared to inhibit the solubilisation of P. Results obtained indicate the suitability of biochar for agroforestry applications or to support plant growth in soil systems with nutrient deficiency or drought.

Work demonstrating the performance of biochar under environmentally relevant conditions and within soil systems demonstrates biochars potential suitability for use in real water systems and in supporting plant growth. This successfully provides proof of concept for biochar applicability in a circular process which recovers and recycles phosphorous while utilising waste, remediating water, and amending soil.

8.2 Future Work

This research has demonstrated the suitability of biochar for use in phosphorus recycling within a circular process. This research has provided new insights into: the optimisation of Ca-decorated biochars functionalisation process; effects of functionalisation conditions on Ca-biochars physicochemical properties and aqueous P-recovery; the mechanism of aqueous P-removal by Ca-biochar; the effect of environmental conditions such as pH, coexisting ions, and P-concentration on biochars aqueous P-removal; and spent biochars suitability in crop producing soil systems. However, further research is needed to overcome the limitations of this and facilitate scale-up of the proposed process.

Evidence of P-removal occurring via both precipitation and adsorption was provided, alongside the total P-removal potential and total P-adsorption potential of biochar samples under various experimental conditions. However, further research should be conducted into the true split of P removed via precipitation compared to adsorption during P-removal.

It was proposed in this work that $CaCl_2$ present on the feedstock reacts with pyrolysis vapours (predominantly H_2O and CO_2) to form $CaCO_3$, with excess $CaCl_2$ remaining on the biochar surface. An attempt was made to determine the ratio of Ca in $CaCl_2$ to $CaCO_3$ in different biochar samples to analyse how this ratio may change with changes to functionalisation conditions; however, this was not possible with the experimental techniques available. To provide further evidence of the transformation process of $CaCl_2$ during pyrolysis, further quantitative analysis of the forms of Ca on the biochar's surface should be carried out. Analysis of biochars surface before and after washing and P-removal would also provide further evidence for the hypothesis that precipitation occurs due to the presence of $CaCl_2$ while adsorption occurs due to the presence of $CaCO_3$. Furthermore, this would create a launchpad for further research into controlled design of Ca groups on biochar's surface, varying the quantities of

$CaCl_2$ and $CaCO_3$ for the desired proportions of precipitation and adsorption, respectively.

Relatively large quantities of $CaCl_2$ were used to functionalise biochar, with all Ca-biochars showing very similar total P-removal. While the amounts of functionalisation agent used are commonly seen in the literature, this may increase the cost of large-scale production and reduce the sustainability of the process. Furthermore, a much higher Ca concentration than necessary for even complete precipitation was observed in solution from $CaCl_2$ leaching of biochar. The effects of lowering both CLR and pyrolysis temperature on overall P-removal should be considered, with investigation into how to utilise the dual P-removal mechanism best to facilitate this.

Low initial concentration experiments were seen to have less favourable adsorption than moderate and high concentration experiments, likely due to kinetic factors. Kinetic modelling of Ca-biochar samples across the ultra-low concentration range of eutrophic waterbodies should be carried out to investigate the potential for use of biochar to be deployed in these water bodies for long periods for successful remediation or maintenance. Methods of collection of biochar used in real water systems should also be investigated. Specifically, the deployment of biochar in bags, mats, or geotextile carriers for ease of recovery should be considered.

Biochar samples were seen to maintain an excellent P-removal in the presence of coexisting ions such as chloride, sulphate, nitrate, and carbonate. A wider range of anions should be tested, as well as cations and organic matter, to better understand how other components of eutrophic and wastewater systems may affect biochars' P-removal performance.

This work demonstrated the presence of biochar during pot trials to enhance the moisture content, germination rate, and growth rate of plants; however, it showed no improvement in overall biomass production. This is likely due to the use of high-quality soil in which the extra P provided by biochar was not necessary. Pot

trials should be repeated in soil systems experiencing stress from nutrient deficiency or drought. Pot trials in nutrient-deficient soils should compare the performance of biochar to a traditional fertiliser to better understand its commercialisation potential. The use of spent biochars for land management to rehabilitate degraded soils should be investigated to test its suitability in applications such as agroforestry.

Finally, further research should be undertaken to better understand the suitability of biochars in soil systems at a larger scale. Field trials should be conducted to test the effects of spent biochar in less tightly controlled conditions as well as on insects and pests. Furthermore, field trials should aim to provide an understanding of how many crop growth cycles biochar can undergo before needing to be replaced.

Appendices

Chapter 3

A1- Calibration Curve for Phosphate Determination

This appendix presents the calibration curve used for visible spectroscopic determination of P concentration for solutions, with statistical data for the linear fit given in *Table A.1*. Visible spectroscopy was used for solutions with initial P concentration 5-300 mg_P/L, where the initial concentration was over 20 mg_P/L these solutions were diluted before measurement. Visible spectroscopy was also used to measure P concentration in rapid small scale column experiments.

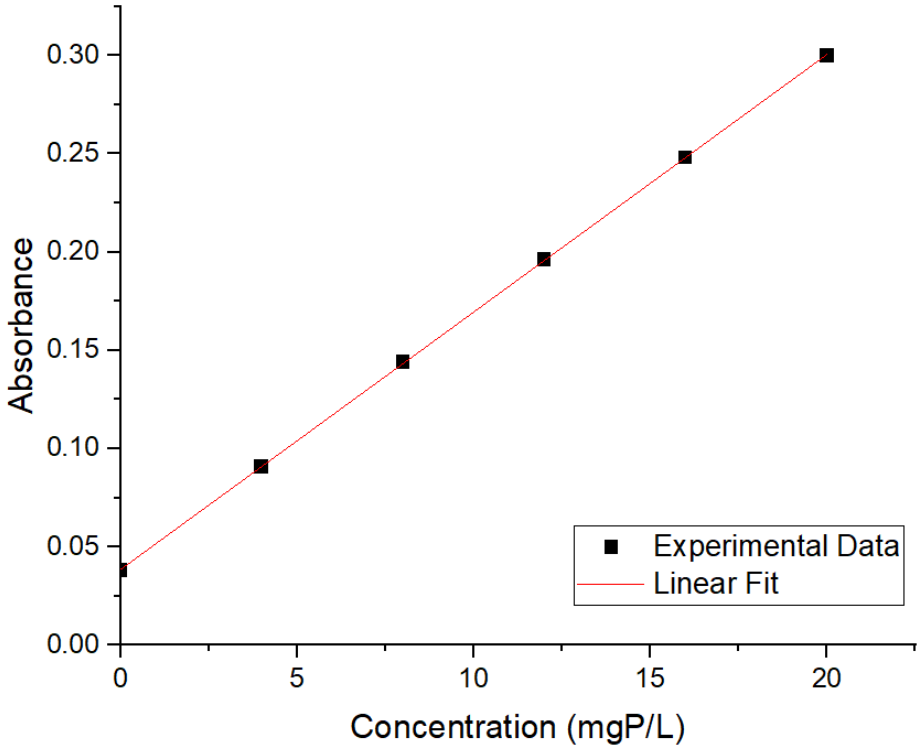

Figure A.1: Calibration curve for the determination of phosphate by ammonium molybdate vanadate solution, concentration range 0-20 mg_P/L.

Table A.1:Parameter of the linear fit of data in the calibration curve for the determination of phosphate by ammonium molybdate vanadate solution.

Gradient	**Intercept**	**R^2**
0.01309	0.03857	0.99998

Chapter 5

A.2 XRD Patterns of Ca-Biochars

This appendix presents the XRD patterns of Ca-biochars synthesised in *Chapter 5* of this work. The XRD patterns of samples Ca-1.5-T750, Ca-1.75-T750, and Ca-2-T750 are presented in *Figure 5.13*, *Section 5.4.5*.

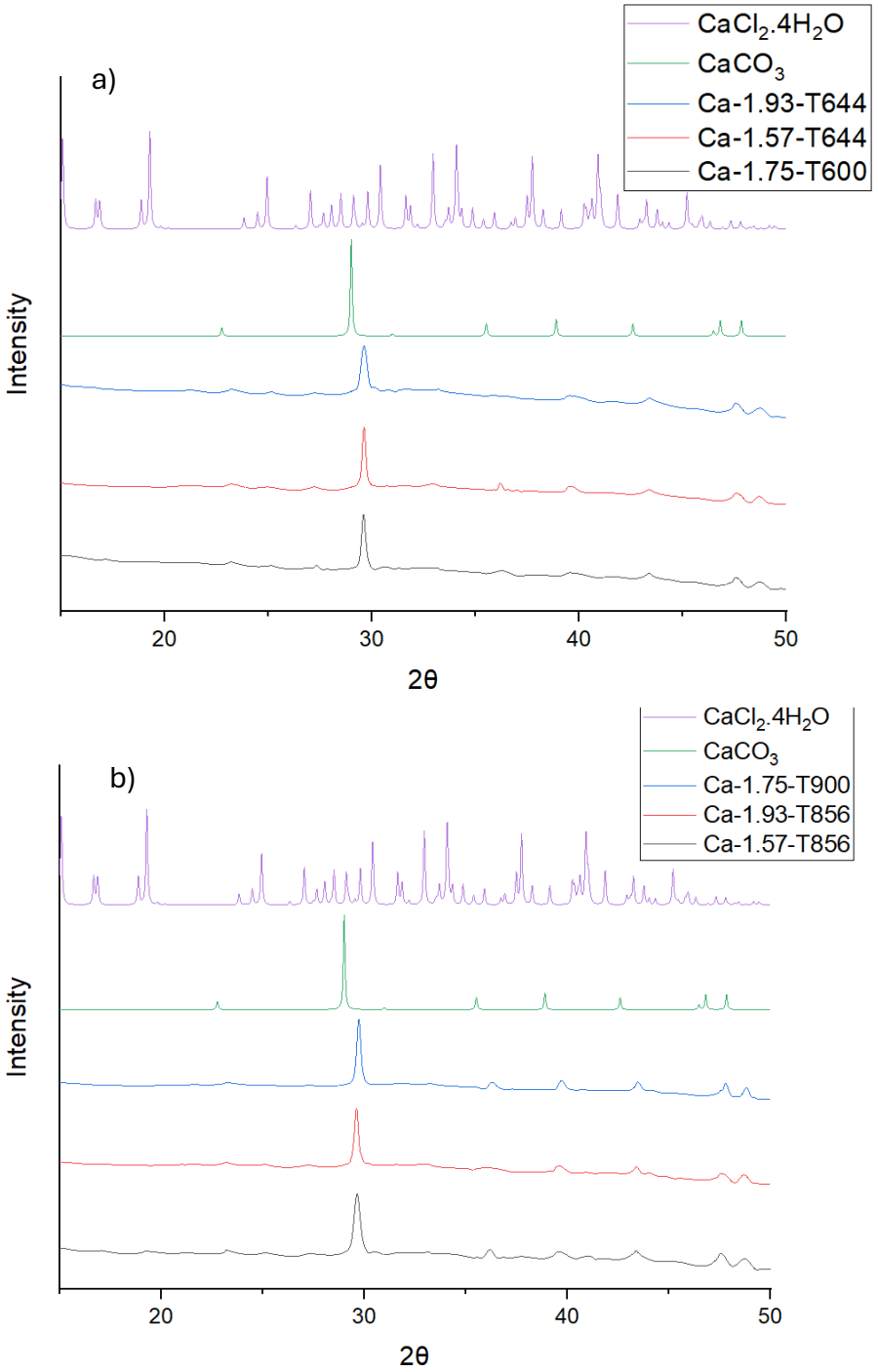

Figure A.2:XRD patterns of biochars synthesised in this work at pyrolysis temperatures a) 600 and 644 °C and b) 856 and 900 °C.

Chapter 6

A.3 Physical Characteristics of Washed Biochar Samples

This appendix presents the yield and physical characteristics of Ca-biochar samples, synthesised in *Chapter 5* of this work, after washing in DI water (adjusted to pH 8) for 24 h. Samples were dried in an oven at 100 °C for 24 h before measurements were taken.

Table A.2: Physical characteristics of washed Ca-biochars synthesised in this work.

Biochar Sample washed	**Surface Area (m^2/g)**	**External Surface Area (m^2/g)**	**Pore Volume (cm^3/g)**	**Average pore size (nm)**
Ca-1.75-T600	402	183	0.39	6
Ca-1.57-T644	410	214	0.35	4
Ca-1.93-T644	407	171	0.47	9
Ca-1.5-T750	421	236	0.41	5
Ca-1.75-T750	389	226	0.42	5
Ca-2-T750	378	200	0.45	7
Ca-1.57-T856	406	215	0.45	6
Ca-1.93-T856	321	198	0.39	6
Ca-1.75-T900	362	221	0.40	5

A.4 Point of Zero Charge- Washed Ca-Biochar Samples

This appendix presents the point of zero charge of Ca-biochar samples synthesised in *Chapter 5* of this work, after washing in DI water (adjusted to pH 8) for 24 h. Samples were dried in an oven at 100 °C for 24 h before measurements were taken.

Table A.3: Point of zero charge of washed Ca-biochar samples synthesised in this work.

Samples	pHpzc
Ca-1.75-T600	7.70
Ca-1.57-T644	7.64
Ca-1.93-T644	7.75
Ca-1.5-T750	7.71
Ca-1.75-T750	7.78
Ca-2-T750	7.79
Ca-1.57-T856	7.78
Ca-1.93-T856	7.76
Ca-1.75-T900	7.75

Chapter 7

A.5 Rapid Small Scale Column Tests

This appendix presents the results of unsuccessful rapid small scale column tests carried out at low P concentration using biochar sample Ca-1.75-T900.

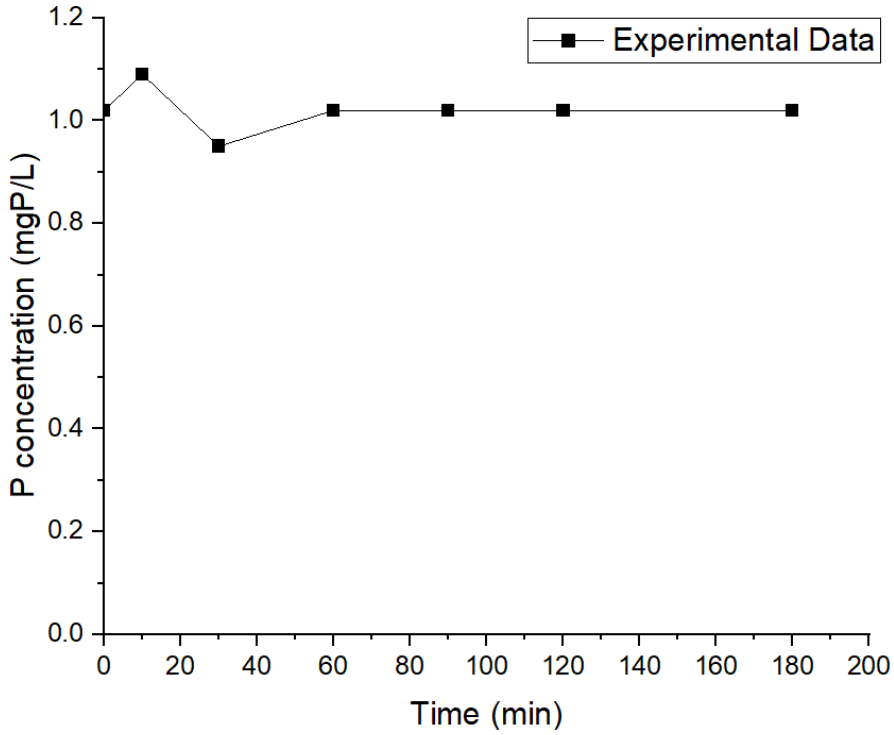

Figure A.3: Results of variation of P-concentration with time for rapid small scale column P-removal test carried out using Ca-1.75-T900. Bed length= 15 cm, internal diameter= 8 mm, flow rate= 5 mL/min, biochar particle size= 1-2 mm. Phosphate solution 1mg$_P$/L, pH 8.